

Università degli Studi di Palermo (UNIPA),  
Dipartimento di Energia, Ingegneria dell'Informazione e Modelli Matematici (DEIM)  
Université du Québec  
Institut National de la Recherche Scientifique (INRS)  
Centre Énergie, Matériaux et Télécommunications (EMT)

# **ULTRA-BROADBAND COHERENT DETECTION OF TERAHERTZ PULSES VIA CMOS- COMPATIBLE SOLID-STATE DEVICES**

by

Alessandro Tomasino

Thesis or dissertation submitted to obtain the double Degree of  
Philosophy Doctor (Ph.D.)  
in Energy and Materials Science (EMT), Varennes, Quebec  
and  
in Energia e Tecnologie dell'Informazione (DEIM), Palermo, Italy

## **Jury d'évaluation**

Président du jury	Prof. Alessandro Busacca University of Palermo, Italy
Examineur interne	Prof. Roberto Morandotti INRS-EMT, Québec, Canada
Examineur externe	Prof. Gianluca Giustolisi University of Catania, Italy
Directeur de recherche	Prof. Roberto Morandotti INRS-EMT, Québec, Canada
Codirecteur de recherche	Prof. Alessandro Busacca University of Palermo, Italy

© Rights reserved (*Alessandro Tomasino*), year 2018.



*This thesis is dedicated to*

*my parents,*

*my sister,*

*and all my family,*

*who are my life.*



# Acknowledgments

I am really fortunate and grateful for the chance to have known my advisors, Prof. Alessandro Busacca at the University of Palermo and Prof. Roberto Morandotti at INRS-EMT, who have been foremost my mentors and inspiring figures. They taught me how to be not only a good scientist but also a well-rounded and eager to learn person, who firmly keeps in mind his targets. Thanks to them, I had the great opportunity to work on some very important and timely projects with the freedom to pursue some of my own ideas. Their unique insight into the concepts and their professional guidance have been continuously inspiring. The passion for science they demonstrated has addicted me and is responsible for my initial interest in the terahertz area.

A special acknowledgment goes to Dr. Salvatore Stivala, who taught me numerous useful and practical skills, while I was taking the first steps within the experimental Optics, at the beginning of my Ph.D. studies. I also want to thank him for his valuable support and precious help in many others academic concerns.

I would like to thank Prof. Marco Peccianti for all those times we had very fruitful discussions, for his incredible open minded and creative approach, which has strongly amplified my excitement in chasing my objectives. His advice and help have been definitely invaluable.

I wish to thank my colleagues, at both INRS-EMT and UNIPA, for their friendship and the great time we spent together in the last five years. Many pleasurable and thought-provoking discussions with them have served as a nucleation site for many new ideas and personal growth. I will treasure these memories and all the unforgettable experiences, for a lifetime.

I am grateful to those people who have been particularly close to me during the whole doctorate path and who have always encouraged and pushed me to give my best.

I also desire to dedicate a cordial thank to those who have left me an indelible memory, even though they either had to move away because of diverse reasons or simply wanted to drift apart eventually.

Last but not least, I wish to thank my parents and all my family, without whom my whole path would have been purposeless and meaningless.

This work is dedicated to each of them.



# Abstract

In this dissertation, we develop and demonstrate an innovative and fully integrated technique aimed at the coherent detection of terahertz (THz) radiation, i.e., electromagnetic waves whose frequency content conventionally falls in the spectral window ranging between  $0.1\text{-}10 \times 10^{12}$  Hz. We named such a detection technique *solid-state biased coherent detection* (SSBCD), since it is based on a solid-state medium and allows simultaneously recording both the amplitude and phase information of ultrashort THz pulses, i.e. featuring ultra-broadband spectra ( $> 10$  THz). As such, our technique can be successfully used in those systems where THz pulses are employed as either diagnostic tool or signal carriers, such as in the areas of time-resolved spectroscopy and imaging or signal processing. SSBCD is based on platform fully compatible with the CMOS process, i.e. a microfabrication technology commonly employed for the realization of miniaturized electronics circuits (*chips*), thus being cost-effective and particularly reliable for the production of a great number of devices. Hence, its affordability makes it attractive for both a broad scientific and industrial audience. Indeed, the fundamental advantage of the technique presented here is the unlimited operating bandwidth in the whole THz range (allowed via interaction with ultrashort pulse durations), thus potentially addressing many of the issues and constraints of those THz solutions where the detection scheme represents a bottleneck in terms of the entire system frequency response.

Following a brief introduction regarding state-of-the-art of the THz technology and its different spectral regimes of operation, we will mainly review those detection techniques, which have been lately demonstrated to achieve the exact reconstruction of ultrashort THz transients. In particular, we will focus on those methods, which allow the detection of THz radiation, the spectrum of which covers the entire THz domain or even beyond (namely, the ultra-broadband regime). We will see that such particular techniques are essentially gas-based and rely on a similar concept, since the so far available solid-state methods, representing the state-of-the-art

in the THz detection area, are not suitable in the ultra-broadband regime, since they suffer a limited frequency response. Then, we will pass to the detailed description of mainly three different approaches, highlighting both advantages and drawbacks or limitations, eventually focusing our attention on the air-biased coherent detection (ABCD) technique. Indeed, we will show that our novel approach essentially overcomes some of the crucial issues of the ABCD method, by adopting particular, yet very common solid-state media (glasses) and plain integrated structures. ABCD exploits the nonlinearity of air and therefore operates at optical probe energies in the order of microjoules and bias voltages as high as several kilovolts. This restricts its application to expensive, bulky amplified ultrafast laser systems, and slow, high voltage amplifiers, which limit the noise performance and imply health hazard (electrical shocks). On the contrary, we show how the employment of CMOS-compatible dielectrics as nonlinear media, allows to dramatically decrease not only the requirement of optical energy to the level of nanojoules but also to greatly shrink down the size of the interaction region between the THz and optical pulses, with respect to the case of air. This results in the possibility to perform the THz detection in a compact structure, by using orders of magnitudes lower bias voltages, comparable to those regularly employed for photoconductive antennas. Such results pave the way to the realization of a unique and portable device that can be potentially driven by laser oscillators (featuring very good beam stability) and low-voltage amplifier, operating at much higher repetition rates and modulation frequencies, which will result in the significant increase of both dynamic range and signal-to-noise ratios.

# Sommario

Il presente lavoro di tesi presenta e dimostra una tecnica innovativa e completamente integrata dedicata alla rilevazione coerente di radiazioni a frequenze Terahertz (THz), cioè di onde elettromagnetiche il cui contenuto frequenziale cade convenzionalmente nella finestra spettrale compresa tra  $0.1-10 \times 10^{12}$  Hz. Tale tecnica è stata battezzata col nome di *solid-state-biased coherent detection* (SSBCD), dal momento che essa sfrutta le proprietà di un mezzo a stato solido e consente di ricostruire simultaneamente l'informazione sulla fase e sull'ampiezza degli impulsi THz, anche nel caso in cui quest'ultimi siano dotati di spettri a banda cosiddetta "ultra larga" ( $> 10$  THz). Tale metodo di rivelazione può essere utilizzato con successo in quei sistemi in cui gli impulsi THz vengono comunemente impiegati come strumento diagnostico o come portanti di segnali a banda stretta, per esempio nelle aree della spettroscopia nel dominio temporale e nell'elaborazione di immagini o segnali, rispettivamente. La tecnica SSBCD si basa su una piattaforma completamente compatibile con il ben noto processo CMOS, cioè una tecnologia di micro fabbricazione comunemente impiegata per la realizzazione di circuiti elettronici miniaturizzati (*chips*), essendo quindi economicamente conveniente e particolarmente affidabile per la produzione di un gran numero di dispositivi per singolo processo produttivo. Queste caratteristiche rendono il metodo SSBCD particolarmente attraente per un ampio pubblico sia strettamente accademico sia industriale. Infatti, il suo principale vantaggio è rappresentato da una risposta spettrale estremamente larga, così da coprire l'intera gamma del dominio THz (qualora la durata temporale dell'impulso ottico lo consenta), permettendo potenzialmente di risolvere gran parte dei problemi e dei limiti che caratterizzano le attuali tecniche di rivelazioni, le quali rappresentano invece il collo di bottiglia di molti sistemi che operano a frequenze THz.

Di seguito, dopo una breve panoramica sulla tecnologia THz ed i diversi regimi spettrali di funzionamento, esamineremo le principali tecniche di rilevazione, che sono state recentemente

dimostrate per ricostruire nel modo più fedele possibile impulsi THz ultra corti. In particolare, ci concentreremo su quei metodi che consentono di ricostruire la forma di impulsi i cui spettri coprono l'intero dominio THz e anche oltre (vale a dire, il regime *ultra-broadband*). Vedremo che tutte queste tecniche sono essenzialmente basate sull'impiego di gas, sfruttando sostanzialmente lo stesso fenomeno fisico, dal momento che le configurazioni basate sui materiali a stato solido e che rappresentano lo stato dell'arte nell'area della rivelazione THz, non sono adatte per operare nel regime *ultra-broadband*, essendo caratterizzate da una limitata risposta in frequenza. Pertanto, passeremo alla descrizione in dettaglio di tre approcci diversi, evidenziandone vantaggi e inconvenienti, concentrando infine l'attenzione su un metodo di rivelazione detto *air-biased coherent detection* (ABCD). In effetti, mostreremo che il nostro nuovo approccio supera essenzialmente alcune problematiche cruciali della tecnica ABCD, grazie all'utilizzo di materiali alquanto usuali (essenzialmente dei vetri) e un'unica semplice struttura integrata. Infatti, il meccanismo intrinseco nell'ABCD sfrutta la non linearità dell'aria, richiedendo perciò energie ottiche dell'ordine dei microjoule e tensioni di polarizzazione pari a diversi kilovolt. Ciò restringe la sua applicazione da un lato a sistemi laser amplificati, che sono costosi e voluminosi, e dall'altro ad amplificatori ad alta tensione, che funzionano a basse frequenze di modulazione (onde quadre), limitando le prestazioni in termini di rumore, nonché comportando rischi per la sicurezza dell'operatore. Al contrario, mostreremo come il metodo SSBCD consente di ridurre drasticamente non solo il fabbisogno di potenza ottica al livello dei nanojoule, ma anche le dimensioni fisiche della regione di interazione fra impulsi THz ed ottici, rispetto al caso dell'ABCD, permettendo così l'utilizzo di livelli di tensione di polarizzazione paragonabili a quelli utilizzati regolarmente per le antenne fotoconduttrici. Tali risultati spianano la strada alla realizzazione di un dispositivo unico e portatile che può essere potenzialmente pilotato da oscillatori laser (che generano fasci laser di migliore stabilità ma a ben più basse energie) e amplificatori a bassa tensione, operanti a frequenze di modulazione molto più elevate, portando così ad un significativo aumento della dinamica dei segnali rivelati e dei loro rapporti segnale-rumore.

# Résumé

Dans cette thèse, nous développons et démontrons une nouvelle technique entièrement intégrée ayant pour but de détecter la cohérence des rayons TéraHertz (THz), c'est-à-dire des ondes électromagnétiques dont le contenu spectral est compris dans la fenêtre spectrale comprise entre  $0.1-10 \times 10^{12}$  Hz. Nous avons appelé cette technique de détection solid-state-biased coherent detection (SSBCD) puisqu'elle est basée sur un état solide et permet d'enregistrer simultanément des informations d'amplitude et de phase d'impulsions THz, même dans le cas de spectres avec ultra-large bande ( $> 10$  THz). En tant que telle, elle peut être potentiellement utilisée dans les systèmes où les impulsions THz servent d'outil de diagnostic ou de supports de signaux, comme dans les domaines de la spectroscopie à résolution temporelle et de l'imagerie, ou encore du traitement du signal. La technique SSBCD est basée sur une plate-forme entièrement compatible avec un processus CMOS. CMOS est une technologie de micro-fabrication couramment utilisée pour la réalisation de circuits électroniques miniaturisés (chips), donc rentables et particulièrement fiables pour la production d'un grand nombre de dispositifs. Par conséquent, son accessibilité rend cette technologie attrayante à la fois pour le public scientifique et industriel. L'avantage principal de la technique présentée ici est la bande passante illimitée dans toute la zone THz (pour une durée d'impulsion laser fixée), permettant ainsi de résoudre tous les problèmes et contraintes de ces solutions THz où l'étape de détection limite principalement les performances du système entier. Après une brève introduction sur la technologie THz et ses différents régimes spectraux, nous passerons en revue toutes les techniques de détection qui ont été récemment démontrées pour obtenir la reconstruction exacte d'états transitoires THz ultra-courts. En particulier, nous nous concentrerons sur les méthodes qui permettent la détection de rayons THz dont les spectres couvrent tout le domaine THz, ou même au-delà (à savoir, le régime de bande ultra-large, c'est-à-dire plus de deux décades). Nous verrons que toutes ces techniques sont essentiellement basées sur les gaz et reposent sur un concept similaire, puisque

les configurations à l'état solide, représentant jusqu'ici la fine pointe du domaine de la détection THz, ne sont pas appropriées dans le régime de bande ultra-large, car elles souffrent d'une réponse en fréquence limitée. Ensuite, nous passerons à la description détaillée de trois approches différentes principalement, en soulignant les avantages ou les inconvénients et les limitations, et en concentrant finalement l'attention sur la technique appelée air-biased coherent detection (ABCD). En effet, nous montrerons que notre approche novatrice résout fondamentalement certaines des questions cruciales de la méthode ABCD, en adoptant des matériaux communs à l'état solide (verres) et des structures intégrées particulières. ABCD exploite la non-linéarité de l'air et fonctionne donc à l'énergie de la sonde optique de l'ordre du microjoule et de la tension de polarisation jusqu'à plusieurs kilovolts. Ceci limite son application à des systèmes laser ultra-rapides amplifiés coûteux et volumineux et à des amplificateurs à haute tension lents, qui limitent les performances de bruit et pourraient impliquer un danger pour la santé. Au contraire, nous montrons comment l'utilisation d'un matériau à l'état solide en tant que moyen non-linéaire permet de réduire considérablement non seulement l'exigence d'énergie optique au niveau des nanojoules, mais aussi la taille de la région d'interaction, par rapport à la technique basée sur l'air. Ceci engendre la possibilité d'effectuer la détection THz dans une structure confinée en utilisant des ordres de grandeur de tensions de polarisation inférieure, comparables à celles couramment utilisées pour les antennes photoconductrices. De tels résultats ouvrent la voie à la réalisation d'un dispositif unique et portable pouvant être piloté par des oscillateurs laser (très bonne stabilité du faisceau) et des amplificateurs basse tension, fonctionnant à des fréquences de modulation et de répétition beaucoup plus élevées, qui se traduira par l'augmentation significative de la gamme dynamique et des rapports signal sur bruit.

# Content

Acknowledgments.....	5
Abstract .....	7
Sommario.....	9
Résumé.....	11
Chapter 1 .....	2
Introduction to THz radiation.....	2
<b>1.1 Background.....</b>	<b>2</b>
<b>1.2 THz spectral regimes .....</b>	<b>4</b>
<b>1.3 Motivation .....</b>	<b>7</b>
Chapter 2 .....	10
Ultra-broadband THz coherent detection techniques.....	10
<b>2.1 Dynamic Range and Signal-to-Noise Ratio.....</b>	<b>11</b>
<b>2.2 Nonlinear interaction of THz radiation and optical beams in gas media .....</b>	<b>15</b>
<b>2.2.1 Terahertz-Field-Induced Second Harmonic Generation.....</b>	<b>15</b>
<b>2.2.2 Phase-matching and Gouy phase shift.....</b>	<b>18</b>
<b>2.3 Air-breakdown coherent detection .....</b>	<b>21</b>
<b>2.4 Optically-biased coherent detection.....</b>	<b>25</b>
<b>2.4.1 Analytical model.....</b>	<b>25</b>
<b>2.4.2 Experimental results .....</b>	<b>27</b>
<b>2.5 Air-biased coherent detection .....</b>	<b>30</b>

<b>2.5.1</b>	<b>General aspects</b> .....	30
<b>2.5.2</b>	<b>Phase matching constraint</b> .....	33
<b>2.5.3</b>	<b>Analysis of the Gouy phase shift in the ABCD method</b> .....	35
<b>2.5.4</b>	<b>Dependence on the gas parameters</b> .....	37
<b>2.5.5</b>	<b>Plasma absorption</b> .....	40
<b>2.5.6</b>	<b>Dependence on the beam intensity profile</b> .....	42
<b>2.5.7</b>	<b>Balanced air-biased coherent detection</b> .....	43
<b>2.6</b>	<b>Noise evaluation in the ABCD technique</b> .....	48
	Chapter 3 .....	54
	Silica-based Solid-State-Biased Coherent Detection of ultra-broadband THz pulses .....	54
<b>3.1</b>	<b>Limitation of the ABCD technique</b> .....	55
<b>3.2</b>	<b>Previous demonstration of TFISH in solid materials</b> .....	56
<b>3.3</b>	<b>A CMOS process-compatible material: Silica</b> .....	60
<b>3.3.1</b>	<b>Simulations of the static electric field</b> .....	63
<b>3.3.2</b>	<b>SSBCD device microfabrication</b> .....	66
<b>3.4</b>	<b>Ultra-broadband THz time-domain spectroscopy set-up</b> .....	67
<b>3.5</b>	<b>Characterization of the first generation of SSBCD devices</b> .....	71
<b>3.5.1</b>	<b>Bias voltage dependence</b> .....	72
<b>3.5.2</b>	<b>Probe energy dependence</b> .....	75
<b>3.6</b>	<b>Characterization of the second generation of SSBCD devices</b> .....	77
<b>3.6.1</b>	<b>Four-wave mixing in silica with THz radiation</b> .....	79
<b>3.6.2</b>	<b>Dependence on the slit width and electrode size</b> .....	82
<b>3.6.3</b>	<b>Spectral response</b> .....	86
<b>3.7</b>	<b>Comparison between SSBCD and EOS</b> .....	87
<b>3.8</b>	<b>Application: Ultra-broadband Time-Domain Spectroscopy</b> .....	94

<a href="#">Equation Chapter (Next) Section 1</a> .....	96
Chapter 4 .....	96
Beyond silica: Silicon nitride-based solid-state-biased coherent detection .....	96
<b>4.1 SiN properties: differential THz-time domain spectroscopy</b> .....	97
<b>4.2 Four-wave mixing in silicon nitride</b> .....	101
<b>4.2.1 Fabrication of the SiN-based SSBCD device</b> .....	103
<b>4.3 Comparison with the ABCD technique</b> .....	104
<b>4.4 Characterization of the SiN-based SSBCD devices</b> .....	104
<b>4.4.1 Simulation of the field enhancement</b> .....	104
<b>4.4.2 Bias voltage dependence</b> .....	110
<b>4.4.3 Direct estimation of the THz electric field peak in the slit</b> .....	113
Conclusions .....	116
Conclusions .....	122
Appendix A .....	128
<b>Two-color plasma THz sources</b> .....	128
Appendix B .....	136
A.1 List of articles published in scientific journals.....	136
A.2 List of conference proceedings.....	137
References .....	142
List of Figures .....	154
List of Tables.....	164



# Chapter 1

## Introduction to THz radiation

### 1.1 Background

Beyond its physical meaning as a frequency unit of measurement, with the term “terahertz radiation” we indicate electromagnetic waves the spectral content of which belongs to the intermediate portion between the highest region of the microwaves (millimeter and sub-millimeter waves) and the lowest part of the optical domain (far-infrared, FIR) [1], [2]. Alternatively, they are sometimes called T-ray, in analogy with X-rays, and conventionally their spectra span the two-decade wide range  $0.1\text{-}10 \times 10^{12}$  Hz (see Fig. 1.1), which corresponds to the wavelength range of  $30\text{-}3000 \mu\text{m}$  in vacuum (wavenumber spanning the range  $3.3\text{-}333.3 \text{ cm}^{-1}$ ). However, it is worth mentioning that some authors still talk about terahertz (THz) radiation, even though they deal with waves featuring frequencies partially covering the FIR (10-30 THz), just because such waves are being generated and detected via extremely wideband (several octaves) THz sources and detectors [1].

Although THz radiation constantly permeates our daily surrounding environment, due to the fact that it is incoherently emitted as part of the black-body radiation spectrum from any object with a temperature greater than few tens of Kelvin [3]–[5], we cannot directly experience its presence, because the interaction with matter is generally very poor. Indeed, THz radiation easily penetrates several optically opaque dry materials, whereas its photon energy ( $\sim 4.1 \text{ meV}$ ) is too low for the typical energy transition mechanism (semiconductor band-gap based detection) exploited in optical technologies, which makes its handling quite cumbersome. For these reasons, this part of the electromagnetic spectrum was the least explored in the past, even though the very first experiment involving THz transients generated in quartz crystals [6] can be dated to the same period in which the second harmonic generation demonstrated in lithium

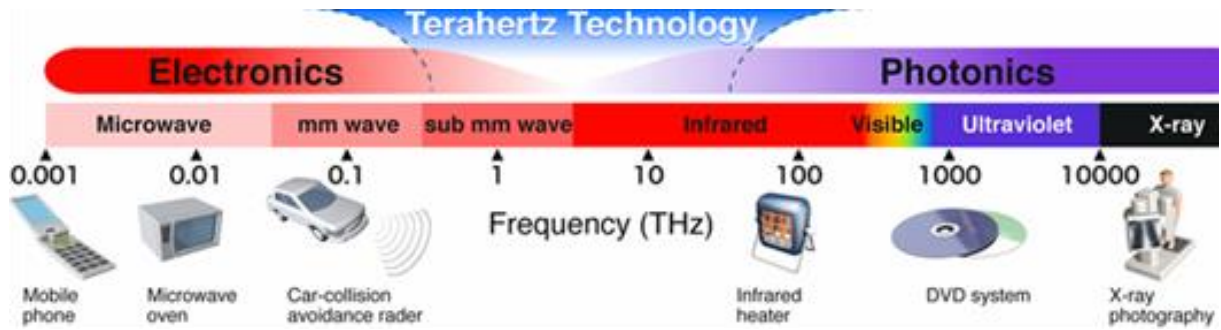


**Figure 1.1** Subdivision of the electromagnetic spectrum. The THz domain is situated between microwaves and mid-infrared radiation (Optics).

niobate crystals, i.e. right after the laser was demonstrated (the 1960s). After that, the THz domain was mostly set aside for several decades and essentially no significant works appeared in scientific journals. This was mainly due to the poor interest and the bare knowledge of the actual mechanism behind such a type of radiation, with respect to the emerging optical domain, boosted instead by the development of the laser technology. Therefore, the previous lack of any reliable device operating in the THz range led to the expression “THz-gap”, to indicate the inability to realize standalone systems able to either efficiently generate or detect and in general manipulate information carried by THz radiation. Nevertheless, in the last two decades (roughly from the 1990s), tremendous effort has been made in the development of the THz technology [7] and its growth was so impressive that it rapidly resulted in a noticeable decrease and almost closure of such a gap. As a matter of fact, nowadays we better refer to it as “THz frontier”. The rapid advances in THz research can be attributed to the ongoing and parallel development of the field of optoelectronics and in particular of ultrafast chirped pulsed laser systems, able to emit optical pulses with femtosecond duration (down to the few cycles regime, Nobel prize in Physics 2018) [8]–[10]. A plethora of new and exciting opportunities in the area of the THz science and technology have soon emerged in many research areas, spanning from imaging and spectroscopy to microelectronics and telecommunications [11]–[14]. In addition, since THz radiation is recognized to be non-ionizing, THz technology has been arousing an ever-increasing interest in important fields such as (bio-) chemical sensing, monitoring, quality control, characterization of semiconductors and high-temperature superconductors, as well as medicine, forensic science, defence and security [11], [12]. In each of these research areas, THz

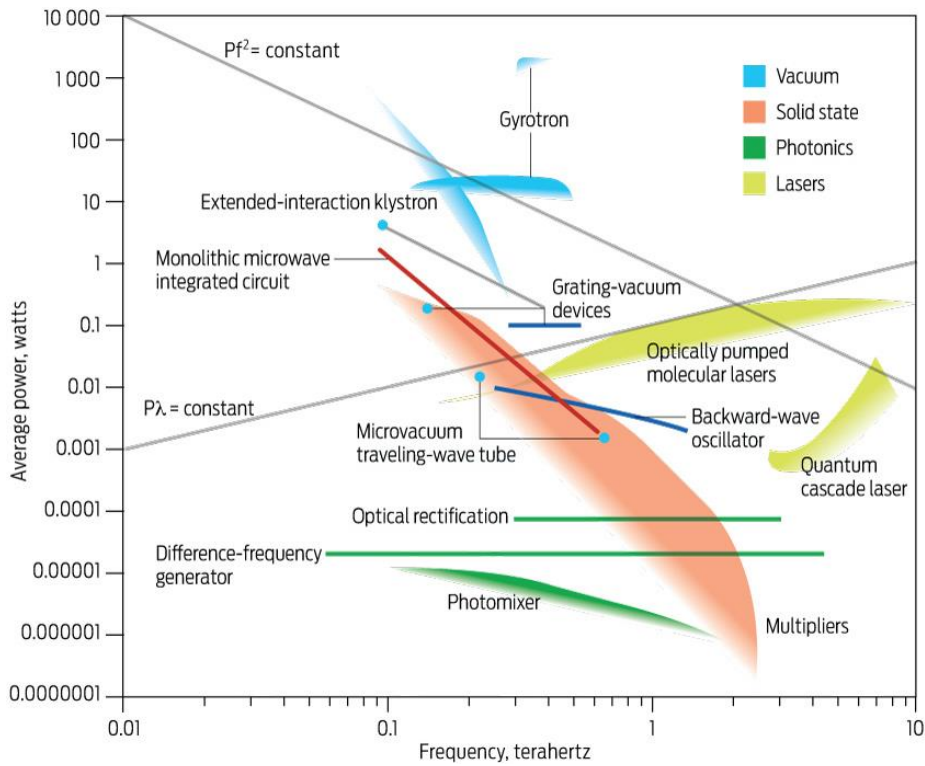


**Figure 1.2.** Chart of the THz generation techniques deployed as a function of the THz spectral emission and available average power. Compact terahertz sources exhibit low power and conversion efficiencies of much less than 1% in nearly every case, as the frequency rises into the terahertz range, the source output power plummets. Here, the  $Pf^2 = \text{constant}$  line (being  $P$  the power and  $f$  the frequency), is the sort of power-frequency slope one would expect to see in a more mature RF device, while the  $P\lambda = \text{constant}$  line (being  $\lambda$  the wavelength), is the expected slope for some commercial lasers. Higher frequencies are accessible by means of laser techniques only. (Figure adapted from Ref. [15]).

sources and detectors have been employed according to the specific application, in order to better accomplish the requested tasks. Historically, this has led to a natural differentiation of the THz products, mainly divided into pulsed and continuous wave (CW) solutions. This is explained in more details in the following sections.

## 1.2 THz spectral regimes

We typically distinguish among three THz spectral regimes of operation [1], depending on the main approaches that have been adopted so far in order to obtain efficient THz generation and detection, i.e. the frequency multiplication of microwaves occurring in nonlinear devices and

nonlinear optical methods involving ultrashort laser pulses [13], [14], as generally shown in Fig. 1.2. The type of classification that we are going to present is pretty useful in order to better comprehend the goals of this doctoral project. While THz radiation obtained by means of microwave techniques (*up-conversion*) results in a nearly single (sinusoidal) frequency (suitable, for instance, as a carrier in transceiver systems), optical techniques (*down-conversion*) usually allow for the generation and manipulation of coherent broadband THz pulses. Therefore, all the techniques find a place in the following three macro-categories:

*Narrowband/Continuous Wave.* High harmonic waves in diodes with strong nonlinear current-voltage characteristics have also been demonstrated to be suitable for single-frequency radiation manipulation in the THz region (Fig. 1.3(a)). Quantum cascade lasers (QCLs), realized by the mutual coupling of multiple quantum wells are a common example for narrowband CW THz generation [16] (Fig. 1.3(b)). The quantum cascade arises from electrons tunneling between adjacent quantum wells. These electronic (intraband) transitions lead to the emission of photons with energies falling into the THz range. To date, QCLs have been the only feasible realization of the so-called “THz laser”, analogous to the optical counterpart. For sake of completeness, we mention that CW THz radiation can also be obtained via the nonlinear beating of two laser beams with slightly different central frequencies in suitable second-order material. The resulting beating envelope oscillates at a frequency equal to the difference between the two carrier beams, which falls in the THz range (Fig. 1.3(c)).

*Broadband (0.1-4 THz).* In contrast to the case of CW radiation, THz pulses featured by a wideband spectrum (i.e. whose central frequency is of the same order of magnitude of its linewidth) can be generated (detected) through optical down (up) conversion of ultrashort laser pulses, whose temporal duration is sub-picosecond. Such a type of radiation is characterized by pulse durations of few picoseconds and typical quasi-single cycle temporal shape. They can be regarded as sinusoids modulated (i.e., *apodized*) by a short Gaussian envelope, which limits the number of cycles of the sinusoidal carrier. The larger the bandwidth, the shorter the Gaussian envelope and the lower the number of cycles of the THz carrier within the pulse duration. In this case, the most widespread generation techniques are optical rectification in quadratic media and photoconductive switches, whereas for detection, electro-optic sampling (EOS) [17]–[21]

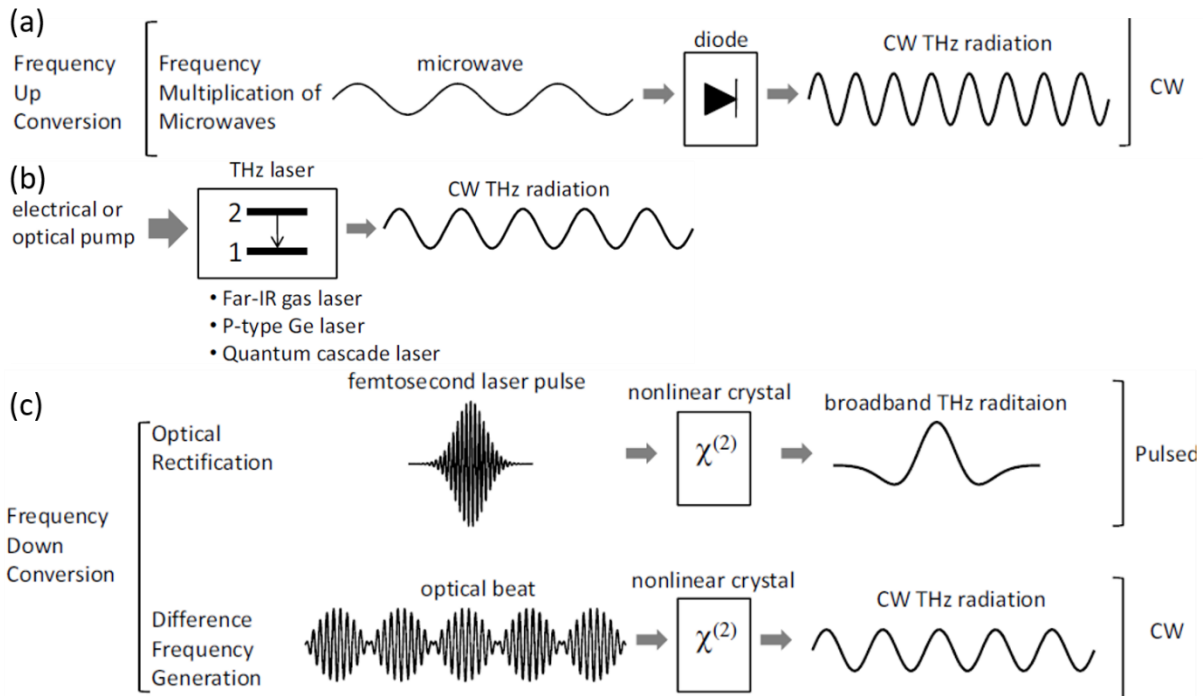


**Figure 1.3** Subdivisions of the THz generation methods. Continuous wave radiation featured by a multicycle shape can be achieved via either (a) microwave harmonic generation in nonlinear devices (mixer) or (b) integrated devices based on semiconductor nanostructured lattices (QCL). (c) Down-conversion from the optical domain in second-order materials, allow the generation or both pulsed and CW THz radiation. (Figure adapted from Ref. [1])

and photoconductive sampling (PCS) [22]–[29] represent the state-of-the-art techniques. (Fig. 1.2(c)).

*Ultra-broadband (bandwidth larger than 10 THz).* Beyond the regime of broadband radiation, there is a relatively recent emerging area, where all the efforts are devoted to the handling of so-called single-cycle THz pulses. Essentially, such type of THz pulses are featured by exactly one carrier cycle, because of the extremely narrow temporal extension of the relative Gaussian envelope, hence the name ultrashort THz pulses. Their pulse duration is in the range of few hundreds of femtosecond or less and their spectral width can extend into the multi-THz regime. Indeed, in this case, the carrier frequency is lower in value than its linewidth (total bandwidth). For sake of completeness, it should be mentioned that similarly to the case of ultrashort lasers, the *envelope* of a single cycle THz pulse could be defined up to a phase term named pulse *chirp*

[8]. Ultrashort THz pulses are difficult to manage, because, as soon as they travel through the free space, the several absorption lines of the water molecules distort the pulse shape, which then shows long-lasting residual oscillations. Moreover, most of the common techniques prevent achieving a pure single-cycle THz pulse, because of some inherent and detrimental interactions with the nonlinear materials involved in either the generation or detection scheme, as will be better explained in the following sections. Particularly, it is worth highlighting that, currently, there is no metrological system, which allows to directly access the actual form of the THz pulses as emitted by a particular source. Indeed, any detection method features a precise frequency response, which is not simply flat all over the bandwidth, thus affecting the reconstructed THz spectrum and the associated THz transient shape. For this reason, we would like to clarify that with the term *ultra-broadband* THz pulses, which all along underlines this thesis work, we strictly indicate those techniques which reduce as much as possible any spectral artefact, thus allowing the retrieving of THz spectra which are virtually modulation-free and continuous, i.e. do not show notch frequencies or stop bands. Nowadays, plasma-based techniques are mainly exploited in the ultra-broadband regime for both generation and detection [30]–[42].

### 1.3 Motivation

To date, effective methods have been developed for the cases (i) and (ii), which allow for the manipulation of THz sources [7-12]. Various promising solutions for the generation of high power broadband THz pulses have been proposed, differing in their complexity, THz bandwidth, efficiency, and footprint. However, the realization of a practical ultra-broadband detector in the THz domain is still a key challenge. Commonly, direct detectors based on thermal absorption have been employed, such as helium-cooled silicon and germanium bolometers [1]. Most of these solutions require elaborate cooling systems to reduce thermal background. However, more importantly, they are incoherent detectors, i.e. not sensitive to the waveform of the THz radiation. This limits their use in field-resolved experiments, such as time-domain spectroscopy. EOS and PCS are both able to simultaneously recover the amplitude and phase, but their deployment is limited to the broadband regime only. This is because they require the use of solid-state materials, particularly compound semiconductors, which unavoidably suffer

detrimental phenomena such as non-negligible free-carrier lifetimes, phonon resonances, phase-mismatch and etalon effects within the THz domain. These concomitant effects can lead to significant dips in the spectrum, thus resulting in the detection of suitable THz bandwidths of only a few THz (mainly 0.1-4 THz in state-of-the-art systems) [19], [25], [43]–[48]. The need for a robust detection paradigm able to address all the above-mentioned issues and which could represent an ultimate solution for many THz systems, currently seems to be highly pressing and demanding. Indeed, the ultra-broadband regime is particularly attractive due to the advantages which such a wide spectral range has with respect to conventional THz systems [49]. On one side, a 10 THz-wide radiation lasts only a few hundreds of femtosecond (full width at half maximum), enabling high-resolution time-of-flight measurement for, e.g., 3D THz imaging of multilayered structures [50] or thickness evaluation of thin films [51], [52]. On the other side, many substances such as semiconductors [53], liquid crystals [54], chemicals, like drugs and explosives [55], and biopolymers like proteins and DNA [56], [57], possess specific roto/vibrational modes above 2 THz. Therefore, the possibility of providing ultra-broadband detection capabilities is essential for their complete investigation in a wider THz spectral window [58]. Most of the detection methods able to properly operate in the ultra-broadband regime are mainly gas-based techniques, which imply the use of experimental scheme and equipment relatively more complex and expensive with respect to those employed in either PCS or EOS techniques. In this work, we present all the efforts made in the development of a compact, standalone, solid-state device, which can be easily realized and employed as general purpose THz detector, in both broadband and ultra-broadband regimes.



# Chapter 2

## Ultra-broadband THz coherent detection techniques

In the second chapter of this dissertation, we will review the most important techniques proposed until now for the ultra-broadband coherent detection of THz pulses. As we have already mentioned in the first Chapter, although EOS and PCS are considered the state-of-the-art in the THz detection area, they do not allow for ultra-broadband operation according to the definition previously given. Therefore, here we will not detail the working principles of such detection methods, referring the interested reader to the specific literature [1], [17], [18], [24]. Instead, we will mainly focus the attention onto gas-based techniques. Gases show resonant-free frequency response even in the THz domain, due to the lack of any periodic arrangement of the constituting particles. Moreover, a gas continuously regenerates itself due to the random movements of the molecules, thus allowing for nonlinear interaction among high-intensity laser beams, without the risk of permanent damage. Air is usually the most common employed gas, because of immediate availability and very low chromatic dispersion, which is a desirable property while handling ultra-broadband radiation. In addition, since air is composed of 78% of nitrogen, it already exhibits remarkable performance in the detection of THz pulses. However, higher efficiencies can be achieved by using other types of gases such as pure nitrogen, argon, xenon, and krypton, as will be discussed in the following. All the gas-based schemes share the same background mechanism, which somehow resembles the so-called electric-field-induced second harmonic (EFISH) generation [59]–[62], occurring in centrosymmetric media, which will be described in more details in a dedicated section. However, since the nonlinear interaction between an optical beam and a traveling THz electric field wave results in crucial differences

with respect to the case of a purely static electric field, such a phenomenon is more correctly referred to as Terahertz-Field Induced Second Harmonic Generation (TFISH). Before starting with an overview regarding the current THz detection techniques, it is essential to discuss the concepts of dynamic range and signal-to-noise ratio, which will be recalled several times throughout the text. These two parameters are the most widespread noise figures employed for an exhaustive description of the quality of a THz-TDS system, yet there is a quite great confusion in literature regarding the real meaning and the difference between these two quantities.

## 2.1 Dynamic Range and Signal-to-Noise Ratio

Since the efficiency of the typical THz generation and detection methods is still far from the theoretical quantum limit reachable in the mechanisms involving optical beams ( $\sim 10^{-2}$ ) [63], the noise affecting the detection of THz radiation plays a crucial role in the ultimate determination of the performance of THz-TDS solutions. Among others, the main parameter often provided with THz systems is the dynamic range (DR). Another important parameter, somehow similar to the DR and aimed at describing the quality of a reconstructed THz pulse, is the signal-to-noise ratio (SNR). However, there are few considerations to point out before directly passing to the operating definition of both parameters. First, given the confusion that certain authors working in the THz community have raised until now, it is worth clarifying that DR and SNR are not the same parameter and do not exactly return the same type of information. Likewise, typical values for the two quantities are generally much different in terms of order of magnitude. Two more appropriate general definitions have been given by Naftaly *et al.* [64], as stated by the following sentences:

- *The DR describes the maximum quantifiable signal change.*
- *The SNR indicates the minimum detectable signal change.*

The two definitions above can be interpreted in a more practical way. The DR expresses how much we can attenuate the signal and still be able to resolve it from the noise floor. The SNR, instead, expresses how much we can distinguish between the signal changes and the fluctuations induced by the noise. In light of these definitions, it is clear that the two parameters aim to

characterize the measured data in two different, yet complementary, ways. Another main point to highlight is that for a typical THz-TDS system (and, in general, also for other systems) both DR and SNR are not properly defined for either one single generation or detection scheme. Those values depend on the particular combination of source and detector, since the performance obtained for the same generation technique can be different if the associated detection approach is varied, and vice versa. Quantitatively, DR and SNR are evaluated as [64]:

$$\text{DR}(t) = \frac{\text{max of the temporal amplitude}}{\text{RMS of noise floor}} \quad (3.1)$$

$$\text{SNR}(t) = \frac{\text{mean value of temporal amplitude}}{\text{RMS of the temporal amplitude}} \quad (3.2)$$

where RMS stands for root-mean-square. When analyzing a typical THz waveform, it is found out that both DR and SNR are not constant as a function of time, but they are usually higher for those time instants where the signal assumes its maximum value. Therefore, as suggested in [64], in order to evaluate optimum parameters, which can well reproduce the quality of the measurements, Eqs. (2.1) and (3.2) should be evaluated at the peak of the THz waveform. The strategy is the following:

- **DR:** the delay between the two pulses is varied in such a way to record the noise floor before the arrival of the THz transient. Then, the peak (either positive or negative) of the THz waveform is measured and is then divided by the RMS of the noise floor.
- **SNR:** the delay is fixed on the time position corresponding to the peak of the THz waveform. Several data points are acquired (in a number of ten or more) and by applying statistical methods to this dataset, the mean value of the peak and its standard deviation are evaluated. The ratio between such two quantities returns the SNR value.

As an example, these two procedures were used to analyze the dataset provided in Fig. 2.1(a). While one scan is in principle enough to evaluate the DR, it is necessary to iterate the measurement several times in order to access the SNR information. Therefore, the main THz

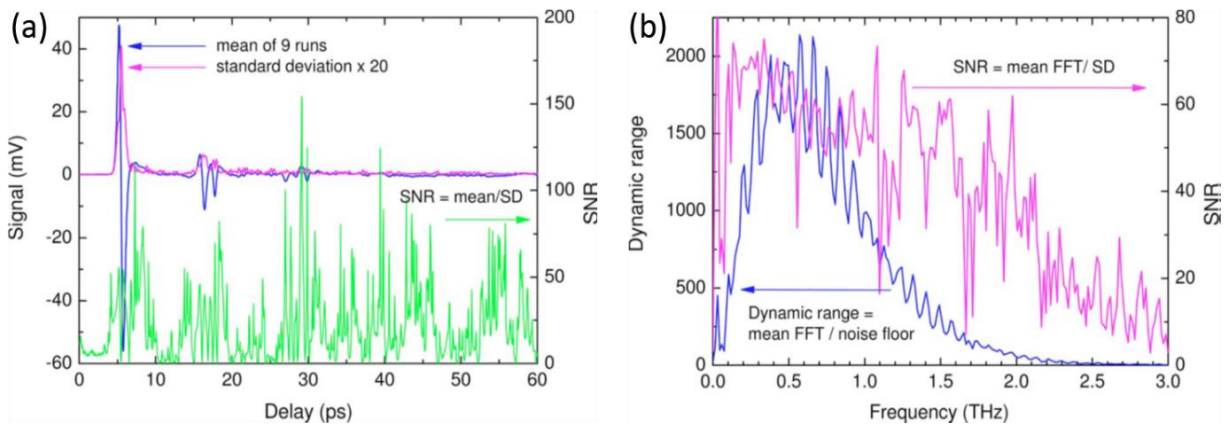


**Figure 2.1** (a) Typical THz time domain waveform (blue line) reconstructed as the mean of nine consecutive temporal scans (left vertical axis). The standard deviation of such measurements is plotted as the purple line. The green curve represents the SNR plotted as a function of time (right vertical axis). (b) DR (blue curve, left vertical axis) and SNR (purple curve, right vertical axis) evaluated in the frequency domain. Note the different scale of the two vertical axes. (Figure adapted from Ref [64]).

waveform shown in the figure is actually the mean of nine consecutive scans. The purple line shows the standard deviation (STD) of the set of data multiplied by 20, revealing that while STD assumes negligible values before the arrival of the THz transient, it greatly varies once the THz pulse shows up, assuming the highest value when the signal approaches its maximum amplitude (negative, in this case). The resulting DR is equal to  $\sim 10000$  for this measurement. Moreover, the point-to-point ratio between the blue and purple curve returns the SNR as a function of time (green curve), with a maximum around 150. It is worth stressing that the two numbers are profoundly different ( $DR/SNR \sim 80$ ), thus indicating that they represent different features of the measured THz waveform.

The definitions given above allow evaluating the DR and SNR in the time domain. Nevertheless, it is possible to retrieve the same parameters in the frequency domain as well. However, it is important to highlight that there is not a specific relationship between temporal and spectral DR and SNR, and most importantly, they assume different values for the same THz system. Since in a THz-TDS system, we can actually retrieve the temporal waveform only, whereas the spectra are subsequently calculated by numerical Fourier Transformation (FFT), the procedure for the evaluation of DR and SNR in the frequency domain is the following. First, one calculates the FFT of a dataset of measurements (in a number of tens or more). Then, statistical methods are

employed to evaluate its mean value (and the corresponding noise floor) as well as the standard deviation. As before, in principle, one measurement is sufficient for DR evaluation only. Finally, the following formulas are used:

$$\text{DR}(f) = \frac{\text{mean FFT amplitude}}{\text{noise floor}} \quad (3.3)$$

$$\text{SNR}(f) = \frac{\text{FFT mean value}}{\text{STD}} \quad (3.4)$$

By again considering the previous example, the application of Eqs. (2.3) and (3.4) leads to the curves plotted in Fig. 2.1(b). The DR as a function of the frequency closely reproduces the shape of the actual THz spectrum (note the natural scale on the left vertical axis). The maximum DR is around 2000. Conversely, the maximum SNR is around 70. As stated before, such numbers are not related to the homologous retrieved in the time domain. In addition, the ratio  $\text{DR}/\text{SNR} \sim 30$  reiterates the fact that the two parameters point out a different type of information. To this point, Fig. 2.1(b) helps in the proper interpretation of DR and SNR, as anticipated in the notes before. Indeed, on the one hand, the DR features a bell-shaped curve, centered on 0.5 THz, which quickly decays to values lower than 200 for frequencies higher than 1.5 THz. This means that the THz system under characterization is more sensitive to the frequencies nearby those corresponding to the maximum DR. In other words, if the THz signal is attenuated by around 2000 times, at least that frequency region can be still extracted from the noise and detected. On the other hand, the SNR shows a flatter frequency response and it is interesting to observe that its values are still close to the maximum ( $\sim 60$ ) at frequencies for which, instead, the DR is already one order of magnitude lower than its peak. Therefore, the SNR does not really depend on the DR and vice versa, which implies that if one attenuates the signal strength, its DR range changes, yet the SNR remains essentially unvaried. We also note that, once the DR approaches values two orders of magnitude smaller than its peak, the SNR is still around 25% of such a value. This means that this particular THz system is able to effectively resolve small variation of the signal over noise fluctuations, in the portion of the spectrum where the signal itself has a poor frequency content.

We finally mention that, in the following sections, we will extensively use the concept of DR

only to characterize the noise performance of our ultra-broadband set-up, when detection is performed via either ABCD or our new technique. This because the SNR is greatly affected by the stability of the THz source for the time instants where the THz pulse is present, due to the averaging among several contiguous measurements. On the contrary, the DR can be evaluated by knowing only one temporal waveform and the stability on the THz source does not play a crucial role, thus allowing to better highlight the properties of the detector stage.

## 2.2 Nonlinear interaction of THz radiation and optical beams in gas media

### 2.2.1 Terahertz-Field-Induced Second Harmonic Generation

Detection based on a centrosymmetric ( $\chi^{(3)}$ ) material, as for the case of EOS, consists in the up-conversion of the THz frequencies to the optical domain, via the THz-driven frequency doubling of an optical probe beam. The so-generated new optical beam encodes the information carried by the THz wave and can be easily recorded via standard optical detectors, thus overcoming the difficulties affecting direct detection of THz radiation. As previously mentioned, TFISH essentially works as EFISH. In the latter case, a static electric field breaks the symmetry of the centrosymmetric medium, thus inducing an electrically-driven second-order behavior. Under this condition, an optical probe pulse propagating through such a symmetry-broken material, experiences a frequency doubling via the effective second-order coefficient driven by the static electric field ( $\chi_{\text{eff}}^{(2)} = \chi^{(3)} E_{DC}$ ). Similarly, in the TFISH case, since the THz electric field can be regarded as static within a complete cycle of the optical wave ( $\omega_{THz} \ll \omega_P$ ), when the THz beam is overlapped in both time and space with the probe, a third beam *approximately* at the second harmonic (SH) frequency of the probe beam is generated [65]–[67]. This SH beam can be acquired, after proper probe filtering through a narrow-band filter (NBF), for example by means of a photodiode or a photomultiplier tube (PMT), as sketched in Fig. 2.2(a). In a practical case, a femtosecond NIR probe beam ( $\lambda_P = 800$  nm) is approximately converted via TFISH into a  $\lambda_{SH} \sim 400$  nm (blue) beam. In such a framework, the SH electric field  $E_{SH}^{THz}$  and the corresponding intensity  $I_{SH}^{THz}$  of the THz-induced SH beam change proportionally to the THz electric field strength  $E_{THz}$  and its intensity  $I_{THz}$ , respectively, according to the following two relations:

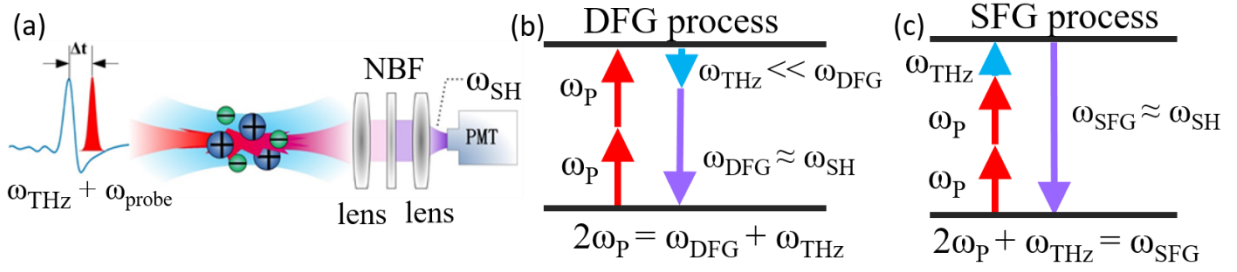


**Figure 2.2** (a) TFISH generation in air: the probe pulse is frequency-doubled when the THz beam is strongly focused around the focal spot of the optical beam. A photomultiplier tube acquires the filtered second harmonic beam. Simplified diagram representing the two possible energy transitions taking place in the four-wave mixing process giving rise to (b) difference frequency generation (DFG) and (c) sum frequency generation (SFG).

$$E_{SH}^{THz} = \chi^{(3)} E_P E_P E_{THz} \quad (3.5)$$

$$I_{SH}^{THz} = \left( \chi^{(3)} I_P \right)^2 E_{THz}^2 \quad (3.6)$$

where  $E_P$  and  $I_P$  are the probe electric field and intensity, respectively. For the sake of completeness, it is worth mentioning that the process described by Eq. (2.5) and (3.6) is an approximation valid in the weak probe intensity regime only, since for higher intensities many others nonlinear phenomena could occur (such as multiphoton absorption, probe spectrum broadening, and others). Moreover, the Kerr coefficient itself could manifest a certain dependence on the optical energy. Such effects could give rise to a saturation of the actual  $I_{SH}^{THz}$  trend, which eventually results deviating from the predicted quadratic dependence on the THz electric field. Another great simplification in writing Eqs. (3.5) and (3.6) arises from assuming that we deal with a nonlinear interaction taking place among plane waves, in the absence of any phase-matching condition. Indeed, since the bandwidth of the THz pulse is not negligible, above all for ultrashort pulses, the generated TFISH beam is not exactly oscillating at the SH frequency. Rather, the overall interaction can be better explained in terms of a four-wave mixing (FWM) process driven by the third-order susceptibility (Kerr). Theoretically, as shown in Fig. 2.2(b)-(c), two possible FWM mechanisms could occur, i.e. either a difference frequency process (DFG) or a sum frequency generation (SFG). In the former case, two probe photons combine together to generate one THz photon and one photon at the DFG frequency

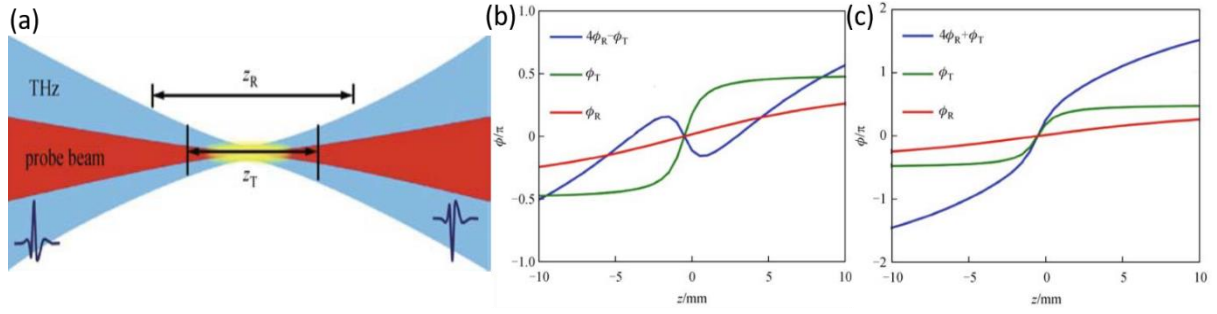


**Figure 2.3.** (a) Gouy phase shift experienced by the THz beam while crossing the focal point. The  $\pi$ -rotation results in a flip of the polarity of the THz pulse.  $z_T$  and  $z_R$  are the Rayleigh lengths of THz and probe beam, respectively. Gouy phase shift for the case (b) DFG and (c) SFG generation process, along the propagation direction  $z$  with origin on the focal plane, evaluated for the case of  $z_T = 0.8$  mm and  $z_R = 4.8$  mm. While for the DFG the total phase change (blue curve) never overcomes the value of  $\pm\pi$ , thus promoting the coherent summation of the contributions to the total DFG beam in a wide range of propagation values, for the SFG case, the total phase change overcomes  $\pm\pi$ -rotation for values relatively close to the focus, thus limiting the total conversion efficiency. (Figure adapted from Ref. [35]).

( $\omega_{\text{DFG}} + \omega_{\text{THz}} = 2\omega_p$ ), whereas in the latter case, two probe photons and one THz photon combine together to generate one SFG photon ( $\omega_{\text{SFG}} = 2\omega_p + \omega_{\text{THz}}$ ). It is worth noticing that both the DFG and SFG frequencies are actually quite close in value to the SH of the probe beam, because  $\omega_{\text{THz}} \ll \omega_p$ , but the phase-matching conditions for the two cases are profoundly different. Indeed, it is well known that when a tightly focused Gaussian beam travels for several Rayleigh lengths ( $z_R = kW^2/2$ , where  $k$  is the wave vector and  $w$  the beam waist on the focal spot) across its focus, it experiences an additional phase rotation of  $\pi$  radians with respect to a propagating plane wave featured by the same wavelength. Such an effect is known as Gouy phase shift [68] and essentially leads to a flip of the THz pulse polarity, as schematically depicted in Fig. 2.3(a). As will be better clarified in the next notes, this further phase contribution favors the DFG process against the SFG when air or other gases are employed as nonlinear materials, because of the long interaction length, necessary to achieve sufficient EFISH power conversion [37]. Therefore, from now on, the SFG will be totally neglected within the text. Moreover, since the THz bandwidth is generally much smaller than that of optical frequencies, it results  $\omega_{\text{SH}} \approx \omega_{\text{DFG}}$ , therefore we will often use equally the term DFG or SH to refer to the intensity of the TFISH beam.

### 2.2.2 Phase-matching and Gouy phase shift

In order to understand how the focusing of both probe and THz beams affects the overall efficiency of the DFG process, we assume that their electric field functions are well described by standard Gaussian profiles, which are expressed, in cylindrical coordinates, by the following relations:

$$E_P(r, z) = \frac{E_P(z)}{1 + iz/z_R} \exp\left\{-\frac{r^2}{w_P^2(1 + iz/z_R)}\right\}, \quad (3.7)$$

$$E_{THz}(r, z) = \frac{E_{THz0}}{1 + iz/z_{THz}}, \quad (3.8)$$

where,  $r$  and  $z$  are the transversal and longitudinal coordinates, and the terms  $E_P(z)$ ,  $E_{THz0}$  and  $z_R$ ,  $z_{THz}$  are the longitudinal amplitude profiles and the Rayleigh lengths of the probe and THz beam, respectively. Therefore, the Gouy phase shifts of the two beams are given by:

$$\phi_{THz}(z) = -\arctan\left(\frac{z}{z_{THz}}\right), \quad \phi_R(z) = -\arctan\left(\frac{z}{z_R}\right) \quad (3.9)$$

Since common values for the THz spot size are in the order several hundreds of micrometers, with respect to the few tens of micrometers for the probe beam, the transversal dependence of the THz beam upon  $r$  can be neglected in Eq. (2.8) with a good approximation. Considering the slowly varying envelope approximation, the second harmonic beam featured by the electric field  $E_{SH}$  is generated according to the following nonlinear Helmholtz equation:

$$2ik_{SH} \frac{\partial E_{SH}}{\partial z} + \nabla_T^2 E_{SH} = -\frac{16\pi\omega^2}{c^2} \chi_{eff}^{(2)} E_P^2 \exp\{-i\Delta kz\}, \quad (3.10)$$

where,  $\Delta k = 2k_P - k_{SH}$  is the wave vector mismatch between the probe and SH beams, which is inherently negative ( $\Delta k < 0$ , as it can be easily understood by looking at the typical dispersion relations). Here, the THz-induced effective second-order susceptibility is expressed by:

$$\chi_{eff}^{(2)} = \chi^{(3)} E_{THz}^* + c.c. \quad (3.11)$$

where the asterisk sign stands for the complex conjugate of the THz electric field (DFG). The trial solution for  $E_{SH}$  is determined for similarity to the fundamental field (Eq. (3.7)) as:

$$E_{SH}(r, z) = \frac{E_{SH}(z)}{1 + iz/z_R} \exp\left\{-\frac{2r^2}{w_p^2(1 + iz/z_R)}\right\}. \quad (3.12)$$

By inserting Eqs. (3.12), (3.7) and (3.8) in Eq. (3.10), it is found out:

$$E_{SH}(z) = \frac{i4\pi\omega}{n_p c} \chi^{(3)} E_p^2 E_{THz}^* J(\Delta k, z), \quad (3.13)$$

where  $n_p$  is the refractive index at the probe frequency, whereas the term  $J(\Delta k, z)$  has the form:

$$J(\Delta k, z) = \int_{-\infty}^{+\infty} \frac{\exp(i\Delta k z')}{(1 + iz'/z_R)(1 - iz'/z_T)} dz', \quad (3.14)$$

and can be easily evaluated with a contour integration (Jordan's Lemma, 2<sup>nd</sup> formulation) [69].

Finally, Eq. (3.13) becomes:

$$E_{SH}^{THz}(r, z) = \frac{i8\pi^2\omega}{n_p c} \chi^{(3)} E_p^2 E_{THz} \frac{z_R z_{THz}}{z_R + z_{THz}} \exp\{-\Delta k z_{THz}\}, \quad (3.15)$$

while the total Gouy phase shift which  $E_{SH}$  undergoes is given by:

$$\phi_{SH}(z) = 4\phi_R(z) \pm \phi_{THz}(z), \quad (3.16)$$

where the double sign identifies the DFG (-) or SFG (+) generation process, respectively. Figures 2.3(b)-(c) show the phase trends expressed by Eq. (3.16) for the case of  $z_T = 0.8$  mm and  $z_R = 4.8$  mm, which are typical focusing conditions of the THz and probe beams. We are now able to comprehend while the Gouy phase shift favors DFG against SFG. Indeed, while the two propagating pulses nonlinearly interact to generate  $I_{DFG}$ , the total phase change  $\phi_{DFG}(z) = 4\phi_R(z) - \phi_{THz}(z)$  does not reach the value of  $\pm\pi$  in a long range of propagation (~cm). This means that each contribution to  $I_{DFG}$  is accordingly summed in phase, leading to a constructive interference, which enhances the DFG yield. Conversely, for the SFG case,  $\phi_{DFG}(z) = 4\phi_R(z) + \phi_{THz}(z)$  overcomes the  $\pm\pi$  rotation for propagation distance  $z$  quite close

to the focal plane ( $\sim$ mm), beyond which the polarity of the THz pulse is reversed. This leads to a destructive interference, which effectively limits the total  $I_{SFG}$ . By carefully examining Eq. (3.15), we can notice that the total strength of the SH electric field depends not only on the THz strength and probe intensity but also on the interplay between the THz and probe Rayleigh lengths as well as the phase-matching condition between the probe and the SH frequencies. It is worth noticing that the Rayleigh length of the probe beam does not directly affect the phase-matching condition. In order to minimize the effect of phase-mismatch, the exponential term in Eq. (3.15) suggests that  $z_{THz}$  should be as short as possible. However, due to the long wavelengths associated with the THz frequencies, this value has a relatively high lower limit ( $\sim$ 1 mm), which eventually could result in poor conversion efficiencies. On the other hand, since  $z_R$  is generally much larger than  $z_T$ , the second ratio in Eq. (3.15) has an asymptotic limit equal to  $z_T$  itself, thus leading to an opposite trend with respect to the exponential term. Hence, a trade-off clearly exists. Additional considerations about this point will be presented in the following sections, where other parameters playing a role in the overall detection will be taken into account. For example, as better explained later in the text, while the Gouy phase shift is actually limiting the performance of gas-based techniques, it does not play any particular role in our solid-state detection technique, yet based on the TFISH process. This is because, in the latter case, the interaction is limited to a region extremely close to the focal plane (in the best case, only a few micrometers), before the THz pulse could undergo polarity inversion. As already stated in Eq. (3.6), it is clear how the PMT readout signal, which is sensitive to  $I_{SH}$  only, scales with the square of  $E_{THz}$ . This means that at this point, THz pulse detection is still incoherent, i.e. the phase information is lost. Since most of the pulsed THz systems are based on the simultaneous detection of both amplitude and phase of the THz transient, i.e. coherent detection, several efforts have been devoted to the extraction of the phase information from the TFISH signal. Three main solutions have been proposed across the years, which somehow relies on a unique idea: the TFISH electric field beats with a so-called local oscillator  $E_{LO}$ , i.e. a further electric field oscillating at the same frequency of the probe SH, and then the cross term is isolated and detected. At first instance, such techniques essentially differ in the strategy adopted to generate the local oscillator and are named: air-breakdown coherent detection, optically-biased coherent detection, and air-biased coherent detection. It is worth mentioning that a specific feature

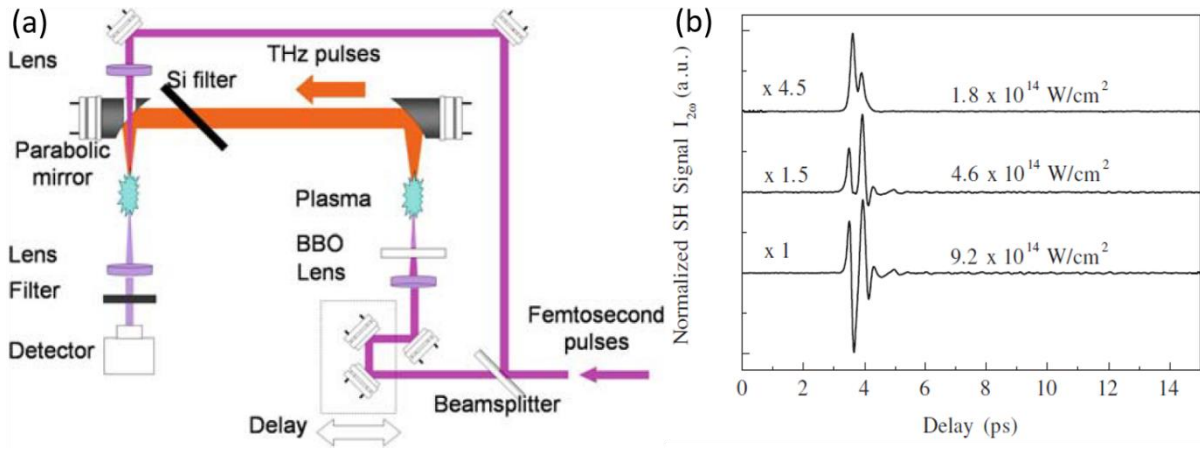


**Figure 2.4** (a) Sketch of the experimental set-up employed in Ref [70]. The THz wave is generated by the nonlinear mixing of the fundamental and its second harmonic beams occurring on the first plasma channel. A couple of 90 off-axis mirror collimates and (after separation from the optical beams), focuses the THz beam in air together with the probe beam. The latter is focused via an optical lens and passes through a hole made in the middle of the mirror. The EFISH beam is hence formed and acquired by a PMT, after filtering the remaining probe power. (b) Time-resolved EFISH transients measured at three different probe intensities (increasing moving from the upper to the lower):  $1.8 \times 10^{14} \text{ W/cm}^2$ ,  $4.6 \times 10^{14} \text{ W/cm}^2$ ,  $9.2 \times 10^{14} \text{ W/cm}^2$ . Gradual conversion of the transient from unipolar to bipolar is observed. (Figure adapted from Ref [70]).

actually underlies the last technique, i.e. the heterodyne scheme, which provides a unique advantage against the other two methodologies, in terms of both noise figure and fidelity of the reconstructed coherence, as detailed in the following.

### 2.3 Air-breakdown coherent detection

Perhaps the very first attempt of implementing a gas-based ultra-broadband detection scheme, the air-breakdown coherent detection method was demonstrated both analytically and experimentally by Dai *et al.* [14-15]. In such a work, authors generated a train of ultra-wideband THz pulses via a two-color plasma technique (see Appendix A), realized by focusing a 800 m, 120 fs, 800 uJ, 1 kHz pump beam with its second harmonic, the latter achieved in a 100- $\mu\text{m}$ -thick beta barium borate ( $\beta$ -BBO) type-I crystal, as sketched in Fig. 2.4(a). The THz wave is separated from the pump by interposing a silicon wafer -acting as a long pass filter- and then

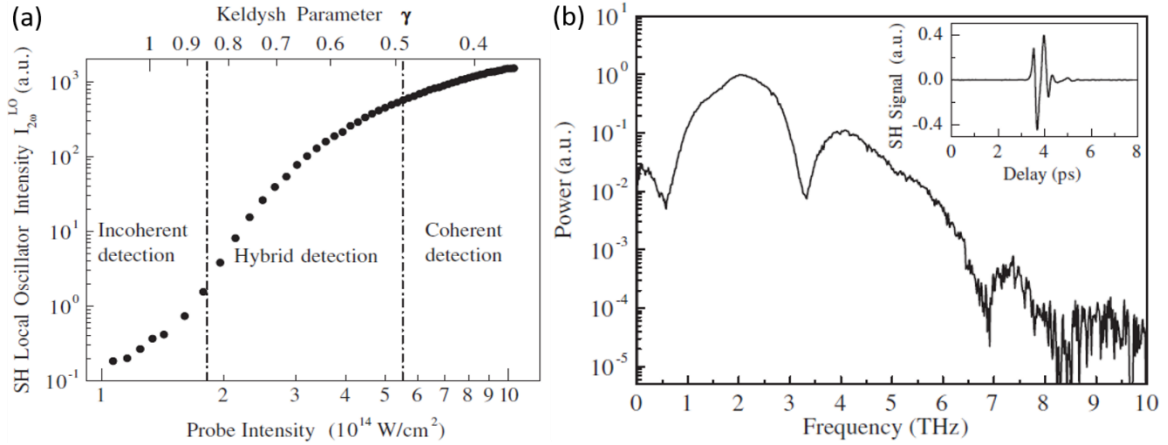


**Figure 2.5.** (a) Intensity of the local oscillator  $I_{LO}^{SH}$  as a function of the probe intensity (black dots). Note that both the scales are logarithmic. The corresponding Keldysh parameter is shown on the top x-axis. It is possible to identify three main regions, separated by the vertical dashed lines, which indicate the probe intensity values for which the incoherent, hybrid and coherent detection regime are achieved, respectively. (b) Power spectrum of the THz waveform recorded in a nitrogen environment for a probe intensity of  $9.2 \times 10^{14} \text{ W/cm}^2$  (shown in the inset). Some spectral artefacts appear in the spectrum, the actual origin of which is not totally understood. (Figure adapted from Ref [70]).

tightly refocused by a  $90^\circ$  off-axis parabolic mirror. A probe beam (obtained by splitting part of the main beamline and the polarization of which can be controlled by means of a half plate) is propagated through a hole made in the center of the last parabolic mirror. It is then focused through a lens the focus of which is placed on the same focal point of the parabolic mirror, thus being spatially overlapped with the THz spot. By scanning the time delay between the THz and the probe beam, it was possible to reconstruct the waveform of the SH intensity readout by means of the PMT. The results are shown in Fig. 2.4(b). While the intensity of the probe beam was below the value of  $1.8 \times 10^{14} \text{ W/cm}^2$ , the authors observed the detection of the TFISH beam only, i.e. a signal shaped as the intensity of the THz waveform. However, as the probe intensity increased, they first noticed a change of the THz waveform from a unipolar to a hybrid bipolar curve for intermediate probe intensity in the order of  $3.3 \times 10^{14} \text{ W/cm}^2$ . This eventually turned into a bipolar THz transient for intensities greater than  $5.5 \times 10^{14} \text{ W/cm}^2$ , which somewhat resembles the typical few-cycle waveform recorded through EOS in ZnTe crystals. Such experimental results can be explained with the aid of a simple mathematical model. We recall

that the readout signal of the PMT when only the THz pulse is present, is expressed by Eq. (2.1), which results in the upper transient in Fig. 2.4(b). However, when the probe beam becomes more intense, it starts to ionize air, giving rise to white light as results of self-phase modulation and self-steeping. The electric field associated to the frequency component at the second harmonic of the probe beam-induced plasma then acts as local oscillator (LO)  $E_{LO}^{SH}$ , which beats with the TFISH term. Such a mixing gives rise to a total DFG intensity, which consists of three main contributions:

$$I_{DFG} \propto \left(E_{total}^{SH}\right)^2 = \left(\chi^{(3)} I_P\right)^2 E_{THz}^2 + 2\left(\chi^{(3)} I_P\right)^2 E_{THz} E_{LO}^{SH} \cos(\theta) + \left(E_{LO}^{SH}\right)^2 \quad (3.17)$$

where  $\theta$  is the phase difference generally present between the TFISH term and the LO component, which can be considered approximately constant since the only source for the LO field is the white light generated by the probe beam. We notice that the cross term in Eq. (3.17) is linearly dependent on the THz electric field, thus constituting the key factor for the detection of the full THz waveform. The third term is an offset contribution from the LO term and is easily filtered out by carrying out the detection via a lock-in amplifier synchronized with the chopping frequency of the THz beam. Therefore, Eq. (3.17) simplifies in:

$$I_{DFG} \propto \left(\chi^{(3)} I_P\right)^2 E_{THz}^2 + 2\left(\chi^{(3)} I_P\right)^2 E_{THz} E_{LO}^{SH} \cos(\theta) \quad (3.18)$$

By means of Eq. (3.18), we are now able to understand the reason behind the change of the waveform nature presented in Fig. 2.4(b). Indeed, below the plasma threshold  $I_P^{th}$ , the contribution of LO to the total SH intensity is negligible and Eq. (3.18) reduces to Eq. (3.6). However, once the intensity of the probe beam is high enough to generate plasma, the cross term becomes dominant with respect to the pure TFISH term, resulting in:

$$I_{DFG} \xrightarrow{I_P \gg I_P^{th}} 2\left(\chi^{(3)} I_P\right)^2 E_{THz} E_{LO}^{SH} \cos(\theta) \quad (3.19)$$

Therefore, in the limit of a very high probe intensity, the readout signal of the PMT linearly scales with the THz electric field and the detection scheme becomes quasi-coherent. The latter condition explains the appearing of negative lobes in the intermediate curve in Fig. 2.4(b), which becomes more prominent in the lowest transient. The transition from the incoherent to the

coherent detection regime can be identified by taking into account the Keldysh parameter  $\gamma$ , which indicates the type of ionization process (either multiphoton or tunneling) occurring for a certain optical intensity. In particular, by measuring only the background offset intensity of the local oscillator  $I_{LO}^{SH} \propto (E_{LO}^{SH})^2$  as a function of the probe intensity (recorded by modulating the probe beam and blocking the THz beam), it is possible to build the graph shown in Fig. 2.5(a). Three main regions can be recognized, as highlighted by the vertical dashed lines, corresponding to the regimes of incoherent, hybrid and quasi-coherent detection, each of them characterized by different slopes. For low intensities, the probe beam generates no significant blue light (LO). As soon as the intensity overcomes the value of  $\sim 1.8 \times 10^{14}$  W/cm<sup>2</sup> (roughly the plasma formation threshold),  $I_{LO}^{SH}$  starts to dramatically increase of several orders of magnitude, because of the multiphoton ionization, until approximately  $5.5 \times 10^{14}$  W/cm<sup>2</sup>. Beyond such a value, the further increase of the plasma carrier density is dominated by tunneling ionization (as pointed out by the condition  $\gamma < 0.5$ , holding for femtosecond laser pulses) and correspondingly the increase of  $I_{LO}^{SH}$  slows down. Under this condition, the plasma blue component is so strong that totally dominates over TFISH, and Eq. (3.19) can be satisfied. The coherence of this type of ultra-broadband detection method strongly depends on the amount of probe intensity available in the experiments. In particular, a fully coherent THz transient can be achieved at the expense of a significant portion of optical power split from the main beamline, necessary to induce the tunneling ionization regime. Moreover, such high probe intensities do not allow to hold the approximation of four-wave mixing (FWM) process in order to exhaustively describe the detection mechanism. Indeed, although the linear dependence on the THz electric field expressed by Eq. (3.19) maintains in a relatively large range of THz strength values (0-10 kV/cm), it has been demonstrated that the PMT signal recorded for increasing probe intensity significantly deviates from the theoretical quadratic trend. Rather, it shows a sort of saturation for the intensities able to trigger the tunneling ionization. Besides the nonlinear absorption induced by highly dense plasma channels, this effect can be ascribed to the fact that  $\chi^{(3)}$  could not be considered constant for such high values, thus degrading the efficiency of the FWM process. Additionally, the requirement of elevated  $I_{LO}^{SH}$  in order to ensure the coherent detection, seriously limits the noise performance of the detection method because of the tremendous

increase of the background component from the white light, which must be filtered out from the actual signal. Since the lock-in amplifier operates at the same relatively low repetition rate of the laser (1 kHz), its filtering action worsens as the probe intensity increases, thus degrading the dynamic range, which indeed did not overcome the value of  $10^3$  (in power). As a final note, Fig. 2.5(b) shows the THz power spectral density (PSD) of the signal recorded for a probe intensity equal to  $9.2 \times 10^{14} \text{ W/cm}^2$  in a nitrogen ambient, evaluated via Fast Fourier Transformation (FFT) of the corresponding waveform shown in the inset. The bandwidth extends up to 8 THz only, which is quite narrower than that ( $> 12 \text{ THz}$ ) expected from a THz two-color plasma source driven by a 120 fs optical pump pulse. Moreover, the spectrum is heavily modulated by three main spectral features located around 0.5, 3.25 and 7 THz, which show relatively deep ( $>10 \text{ dB}$ ) linewidths. These notches result in the multi-cycle nature of the THz transient, which greatly differs from the single-cycle shape expected from the ultra-broadband plasma source. The origin of such notches is still under debate. Although the above-mentioned issues, it is worth mentioning that such a technique enables to locally detect THz radiation before it could propagate along very long distances and undergo severe absorption. Indeed, quite bright plasma can be generated much far from the operator, by focusing powerful laser beams via optical components (such as mirrors, lenses) having very long focal lengths, thus exploiting the particularly low losses featuring standard air atmosphere at optical wavelengths. The plasma then interferes with the backscattered THz wave and generates a second harmonic beam, the free space propagation of which is less affected by air molecules than the THz beam [38].

## **2.4 Optically-biased coherent detection**

### **2.4.1 Analytical model**

Besides the requirement of very high probe energy in order to carry out the air-breakdown coherent detection technique, another main –still unsolved– issue is the lack of control on the phase and polarization of the second harmonic component in the supercontinuum exploited as LO, thus preventing from optimizing the detection mechanism. Such an issue can be addressed by sending into the interaction region between the probe and THz beams, a third beam, achieved, by frequency doubling the probe beam into a beta-borate ( $\beta$ -BBO) crystal. The latter

plays the role of LO, in a similar manner to the previous scheme, yet it is featured by the advantage to properly adjust its intensity, phase and polarization, thus also allowing field- and

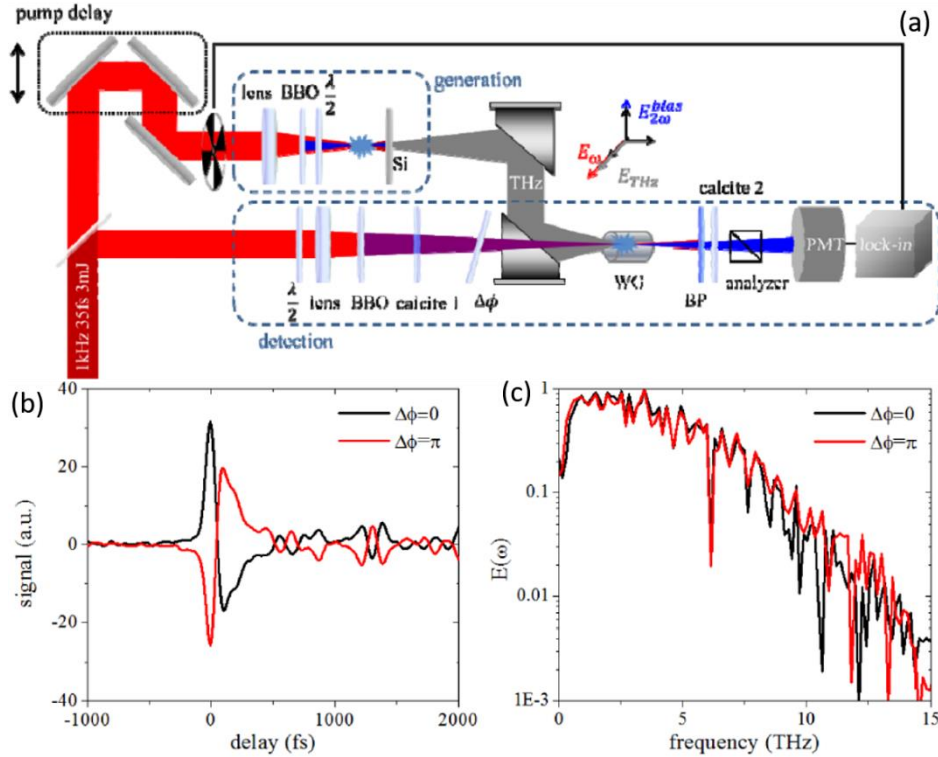


**Figure 2.6.** (a) Sketch of the experimental set-up implementing the OBCD technique. THz pulses are emitted from the two-color plasma generated by focusing the pump beam and its second harmonic achieved in a BBO crystal. On the detection arm, the probe beam is frequency-doubled in a second BBO crystal and finally focused together with its SH and the THz beam inside a metallic hollow fiber, thus forming a plasma channel. The nonlinear interaction generates the fourth beam with a central frequency slightly lower than that of the probe SH, which is proportional to the THz waveform. The output total beam is filtered from the probe fundamental frequency and acquired by a PMT. (b) THz transients recovered via OBCD for the case of  $\Delta\phi = 0$  (black line) and  $\Delta\phi = \pi$  (red line). (c) Corresponding electric field THz spectra of the waveforms in (b). (Figure adapted from Ref [71]).

polarization-resolved measurements. Since the so-achieved SH beam acts as a bias field for the plasma generated by the fundamental frequency of the probe beam (which somehow resembles the dual process involved in the two-color plasma source), such a technique is also known as Optically-Biased Coherent Detection, briefly OBCD [71],[47]. By using a more rigorous formalism for the TFISH generation process, i.e. by taking into account the complex nature of

the electric fields and the finite duration of the probe beam, the total PMT readout signal is actually proportional to the cross-correlation between the THz and probe beam as expressed by the following:

$$S_{TFISH}^{PMT}(\tau) \propto \int |E_{\omega}^2(t+\tau) E_{THz}^2(t)|^2 dt \propto I_{2\omega}(\tau), \quad (3.19)$$

which is valid when only the THz beam is present. As before, if we include the second harmonic term  $E_{LO}^{SH}$  in the interaction, the total SH intensity is given by:

$$I_{2\omega}(\tau) \propto |\chi^{(3)} E_{\omega}^2 E_{THz} + E_{2\omega}^{LO}|^2 = |\chi^{(3)} E_{\omega}^2 E_{THz}|^2 + |E_{2\omega}^{LO}|^2 + 2 \operatorname{Re} \{ \chi^{(3)} E_{\omega}^2 E_{THz} E_{2\omega}^{LO*} \} \quad (3.20)$$

where a cross term proportional to the first power of the THz electric field appears. Again, in order to make the mechanism fully coherent,  $E_{LO}^{SH}$  has to be chosen high enough to hide the contribution of the first quadratic term, while the second term – resulting in a constant background signal – can be easily rejected by the filtering action of the lock-in amplifier synchronized with the repetition rate of the THz beam. Therefore, Eq. (3.20) reduces to:

$$S_{TFISH}^{PMT}(\tau) \propto \operatorname{Re} \left\{ \int E_{\omega}^2(t+\tau) E_{2\omega}^{LO*}(t) E_{THz}(t) dt \right\} = \cos(\Delta\phi) \int I_{\omega}^2(t+\tau) E_{THz}(t) dt \quad (3.20)$$

where,  $\Delta\phi = 2\phi_{\omega} - \phi_{2\omega}$  is the phase difference between fundamental and SH beams. Here, compared to the case of air-breakdown coherent detection, it is possible to control the phase displacement between the two beams by placing dispersive optics in the propagation path shared by the probe and SH beams, thus maximizing the sensitivity of the method whenever the condition  $\Delta\phi = m\pi$ , with  $m$  integer, is satisfied.

#### 2.4.2 Experimental results

The experimental set-up employed to demonstrate the OBCD method is presented in Fig. 2.6(a). The laser source consists of 800 nm, 3.5 mJ, 35 fs, 1 kHz optical pulses and is split into two arms so to form the pump and probe beams. The pump is frequency-doubled in a 30- $\mu$ m-thick type-I BBO crystal and then tightly focused in order to generate a two-color plasma emitting ultra-broadband THz pulses. A true-zero-order half-wave plate is placed after the BBO in order

to ensure parallel polarization between fundamental and SH, which results in the maximum THz energy yield. The THz pulses are then collected by a first parabolic mirror and separated from

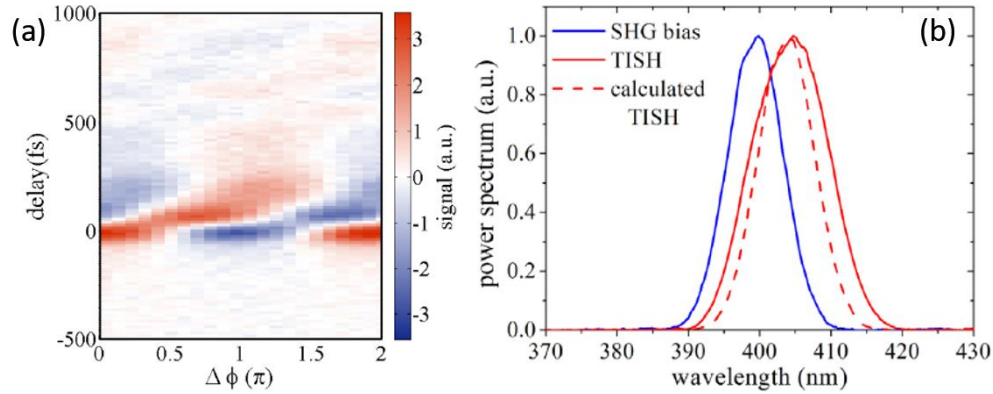


**Figure 2.7.** (a) Cross correlation signal  $S(\tau, \Delta\phi)$  measured as a function of the delay and the phase displacement between fundamental and SH probe frequencies in the range  $\Delta\phi = 0-2\pi$ . (b) Comparison between the simulated TFISH spectrum (red dashed line) and that retrieved experimentally (red solid line). The spectrum of the probe SH (local oscillator) is also reported (blue solid line) for comparison purpose. All the curves are normalized to their own maxima. (Figure adapted from Ref [71]).

the pump beam by means of a high-resistivity silicon wafer. Finally, a second parabolic mirror focuses the THz beam, thus reaching the peak value of  $\sim 1$  MV/cm on the focal spot. The 50- $\mu$ J-probe beam travels through a half-wave plate and then is focused by a 125-mm-lens (passing through a hole made in the parabolic mirror) in the same focal spot of the THz beam, thus generating a plasma channel. In order to improve the phase-matching between the long THz wavelengths and the probe carrier, a 5-mm-long metallic cylindrical waveguide with an inner diameter of 200  $\mu$ m is placed close to the focus position of the parabolic mirror. The local oscillator is generated by interposing along the focusing path of the probe beam, a second 10- $\mu$ m-thick type-I BBO crystal, which gives rise to a cross-polarized SH beam, whose phase delay with respect to the fundamental can be adjusted by means of the birefringent calcite plate. Moreover, the latter allows to temporally advance the SH beam and preventing from distortion of the recovered THz waveform, due to the two different group velocities inside the plasma channel. The interference signal generated by the nonlinear interaction between the three waves into the waveguides, is filtered by a 400-nm passband filter and acquired by a PMT, while a lock-in amplifier synchronized with the chopping frequency of the THz beam, reads the

electrical signal, which is then recorded as a function of the time delay added to the pump beam arm. Figure 2.6(b) shows the typical THz waveforms acquired via OBCD, while Fig. 2.6(c) shows the corresponding FFT-evaluated electric field spectra. For the values of probe energy and THz strength mentioned above, the authors claim to be able to reach a SNR of 40 when setting a time constant of 100 ms in the lock-in, synchronized at 370 Hz. In particular, both the cases of phase delay  $\Delta\phi = 0$  and  $\pi$  are investigated, achieved by properly rotating the calcite plate. It results that while the absolute maximum peak amplitude is obtained for zero phase delay, a  $\pi$ -rotation simply flips the polarity of the transient (without affecting the bandwidth), thus confirming the four-wave mixing nature of the detection mechanism. However, the signal does not present a node (i.e., does not nullify at any temporal instant) for  $\Delta\phi = \pi/2$ , as one would expect from Eq. (3.20). Indeed, Fig. 2.7(a) shows the entire mapping of the cross correlation signal in the complete range of phase delay values  $0-2\pi$ , which highlights the presence of a non-zero signal around  $0.5\pi$ . This discrepancy with the simple model of Eq. (3.20) could be explained by the fact that the TFISH spectrum is not centered at the SH frequency of the probe beam. Rather, it is slightly red-shifted as shown in Fig. 2.7(b), as a consequence of the phase-matching condition which favors the difference-frequency generation process (DFG), i.e.  $\omega_{TFISH} = 2\omega_p - \omega_{THz}$ , for the case of Gaussian beams tightly focused, which experiences a significant Gouy phase shift in small regions (see previous section). Therefore, a revised analytical description of the TFISH process, corrected so to take into account its detuning with respect to the SH, has the form:

$$S_{TFISH}^{PMT}(\tau) \propto \int_{-\infty}^{+\infty} I_{\omega}^2(t+\tau) E_{THz}(t) \cos(\Delta\phi + \Delta\omega t) dt \quad (3.21)$$

where this time the cosine term is time-dependent through  $\Delta\omega$ , which is the frequency mismatch between TFISH and SH bias frequencies. Therefore, Eq. (3.21) claims that such a detuning frequency ( $\Delta\omega$ ) induces a further time-dependent phase contribution in the nonlinear mixing, preventing from a perfect cancellation of the  $S_{TFISH}^{PMT}(\tau)$  signal, when the phase displacement becomes an odd multiple of  $\pi/2$ , i.e.  $\Delta\phi = (2m+1)\pi/2$ , with  $m$  integer. However, the authors point out that the red-shift minimally affects the OBCD readout signal for diphas

values far from the condition above, and in particular near  $\Delta\phi = m\pi$ , where Eq. (3.21) assumes its maximum. This consideration keeps as long as  $\Delta\omega$  is narrower than the FWHM spectrum

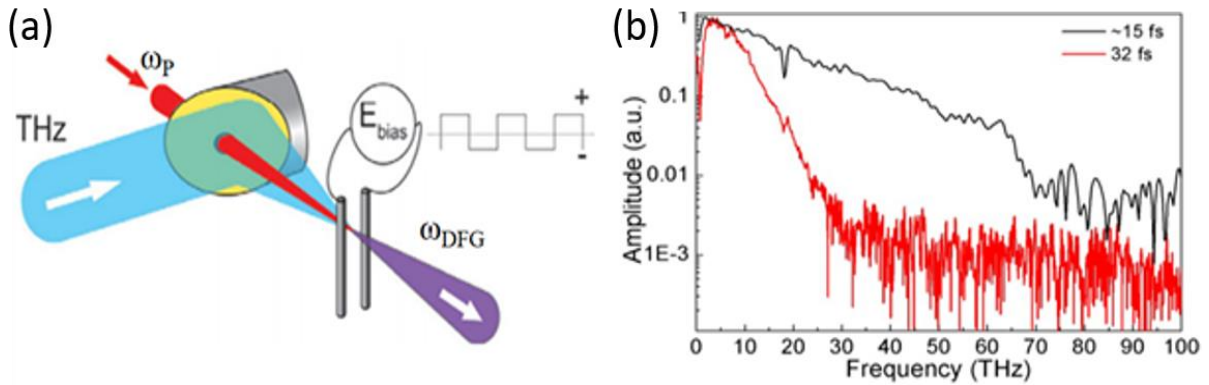


**Figure 2.8.** (a) Sketch of the ABCD technique. A square wave bias voltage is applied to the focal plane of the off-axis parabolic mirror. The modulation frequency of the voltage is half of the repetition rate of the THz pulse train. The result of the interaction among the three electric fields is directed towards the photomultiplier. (b) Typical THz spectra acquired via ABCD. The bandwidth depends on the optical pulse duration only. If the probe pulse duration is halved, the bandwidth doubles accordingly. The difference in the noise floor is due to a different repetition rate of the two fs lasers used to carry out the detection via lock-in amplifier. The notch around 18.5 THz in both spectra is due to a two-phonon absorption effect in the silicon wafers used to separate the pump and THz beams at the generation stage. (Figures adapted from Ref. [35]).

of the SH local oscillator, in order not to result in a distortion of the reconstructed THz pulse coherence.

## 2.5 Air-biased coherent detection

### 2.5.1 General aspects

The third method routinely employed as an ultra-broadband THz detection scheme is named air-biased coherent detection (ABCD), first introduced by Karpowicz *et al.* [72] as a convenient strategy to overcome the limitations imposed by the quasi-coherent detection seen for the air-breakdown coherent detection technique (see section 2.4). In such a case, the local oscillator is obtained by superimposing an additional static (i.e., a DC bias) electric field,  $E_{bias}^{DC}$ , to the interaction region between the probe and THz beams. Therefore, the total intensity of the DFG

beam generated as results of the degenerative four-wave mixing is due to the resultant of the two electric fields, and Eq. (3.6) becomes:

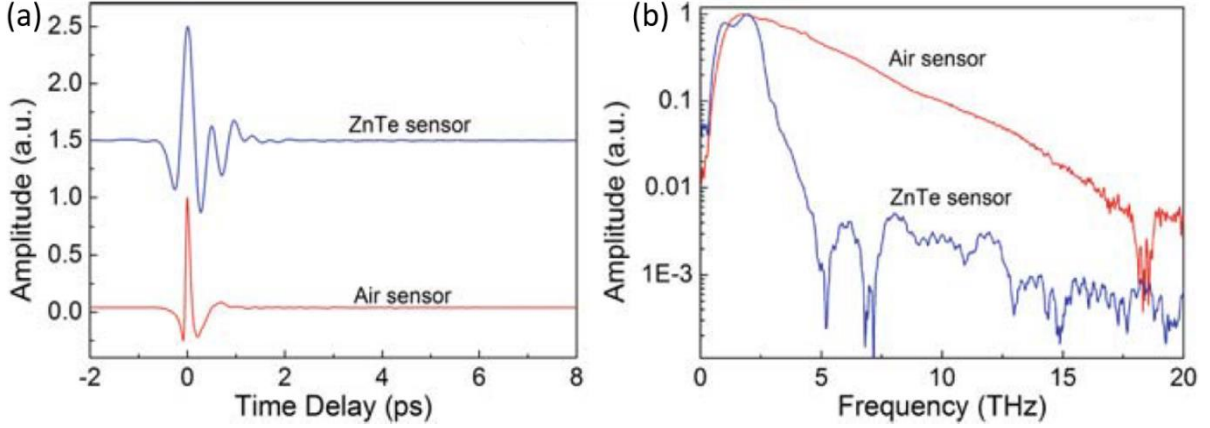


**Figure 2.9.** Comparison between the THz waveforms (a) and relative FFT-evaluated bandwidth (b) emitted by a two-color plasma source driven by an 85 fs optical pulse. These are retrieved via both EOS in a thin ZnTe crystal (blue curve) and ABCD technique (red curve). (Figure adapted from Ref. [58]).

$$I_{DFG}^{total} \propto (E_{DFG}^{total})^2 = (\chi_{xxxx}^{(3)} I_P)^2 (E_{THz} \pm E_{bias}^{DC})^2 = (\chi_{xxxx}^{(3)} I_P)^2 \left[ E_{THz}^2 + (E_{bias}^{DC})^2 \pm 2E_{THz} E_{bias}^{DC} \right], \quad (3.22)$$

where, the double sign depends on the phase difference between the THz and bias electric fields and  $\chi_{xxxx}^{(3)}$  represents the third-order susceptibility for the case of all the three waves (probe, THz, SH) having the same polarization along the x-axis (that is the highest in value among all the other homologous nonlinear coefficients). We note that Eq. (3.22) is composed by three main terms. The first quadratic term is the usual incoherent TFISH, which has the same repetition rate of the laser pulses, the second one acts as a constant offset, while the third term is directly proportional to THz electric field. The latter represents the key factor enabling the possibility to perform pure coherent detection. Now, if the bias electric field is modulated with a modulation frequency different from the repetition rate ( $f_r$ ) of the THz electric field (usually half,  $f_r/2$ ), namely  $E_{bias}^{AC}$ , the second term in Eq. (3.22), being proportional to the square of the bias electric field, will oscillate with a modulation frequency equal to  $2 \times f_r/2 = f_r$ , see Fig. 2.8(a). Therefore, by carrying out the detection via a lock-in amplifier synchronized to the bias

modulation frequency  $f_r/2$ , the two incoherent terms in Eq. (3.22) can be rejected and only the cross term is effectively reconstructed:

$$I_{DFG}^{heterodyne} \propto 2 \left( \chi_{xxxx}^{(3)} I_\omega \right)^2 E_{bias}^{AC} E_{THz}. \quad (3.23)$$

Equation (3.23) ensures the coherence of the detection process, as the waveform featuring the cross term reproduces the THz transient. Since, in order to record the signal expressed by Eq. (3.23), the lock-in amplifier must be locked to the *bias modulation frequency* rather than the THz repetition rate, it is used to say that this method exploits a *heterodyne scheme*, in contrast with the others presented before, which instead employed *homodyne schemes*. The heterodyne detection brings about some important advantages with respect to the homodyne counterpart. First, the full coherence of the method is immediately accomplished for any bias voltage value allowing to resolve the cross term from the noise floor. Indeed, Eq. (3.23) does not predict any threshold that the bias voltage must overcome to accurately reconstruct the phase of the THz pulse and, hence, no hybrid detection regime exists. In addition, the strength of the  $I_{DFG}^{heterodyne}$  signal can be easily increased by modifying the bias electric field rather than the probe intensity. This means that a significant amount of optical power can be moved from the probe beam to the pump arm (thus enhancing the source throughput), since probe energies required to operate ABCD are typically much lower than 100  $\mu\text{J}$ . Such a relatively low value greatly reduces the white light generated in the plasma region, as air has to be only weakly ionized, resulting in a lower background noise acquired by the PMT and a more effective filtering action operated by the lock-in amplifier. Indeed, a dynamic range as high as 3000 has been reported by employing a 50- $\mu\text{J}$ -probe beam and 2.5 kV bias voltage. Since no distortion is introduced in the retrieved THz waveforms, single-cycle THz pulses can be detected via ABCD. This is due to the very low dispersion which characterizes air at the operating optical frequencies, and the lack of a lattice structure resonating with the THz wavelengths. Indeed, Fig. 2.8(b) shows how ABCD allows recording THz electric fields with extremely large bandwidths, which is simply doubled by accordingly halving the pulse duration of the probe beam. The spectral feature at around 18 THz manifested in both the curves is only due to the two-phonon absorption line of the silicon wafer employed to separate the THz and pump pulses at the generation stage. No other

parameters play any particular role in the ultimate determination of the detected bandwidth which is only limited by the probe pulse duration, as verified for THz spectra as large as 100 THz. Figure 2.9 shows the difference between a pure coherent ultra-broadband detection method -as it is ABCD- and the state-of-the-art of the solid-state methods, i.e. electro-optic sampling (EOS) in a 20- $\mu\text{m}$ -thick ZnTe crystal, while ultrashort THz pulses are emitted by a two-color plasma source in both the cases. It can be clearly seen that the waveform retrieved through the EOS is featured by a multi-cycle nature and lasts more than 3 ps, whereas the ABCD transient is almost single cycle and lasts less than 1 ps (see Fig. 2.9(a)). Correspondingly, the bandwidth reconstructed via ABCD is uniform (i.e. notch-free, apart from the usual feature at around 18 THz) and indeed represents the best reconstruction of the THz pulse emitted by the source (Fig. 2.9(b)). On the other hand, the spectrum retrieved via EOS is heavily modulated by the frequency response of the ZnTe lattice structure, which introduces several artefacts. First, the continuous bandwidth is limited to roughly 5 THz, since the first transversal phonon resonance of ZnTe is located around 5.32 THz and causes an abrupt roll out of the spectrum due to the strong dispersion and absorption occurring around that frequency. Another notch is observed around 7 THz due to the appearing of a longitudinal phonon resonance. However, we note that the spectrum reaches the noise floor level only around 15 THz, when the mismatch between the optical and THz refractive indices is too high to guarantee an efficient interaction between the probe and THz beams.

### 2.5.2 Phase matching constraint

As already introduced in Section 2.2, Eq. (3.23) is valid under the hypothesis of plane wave approximation and ideally perfectly satisfied phase matching. In order to model a more realistic scenario, it is therefore necessary to account for the Gaussian profile of the beams, the real electric bias field distribution and the dispersion relation of the medium, similarly to the strategy followed to determine Eq. (3.15). First, the analytical expression for the longitudinal distribution of the DC electric field generated by two cylindrical wires placed as in Fig. 2.8(a) and biased with a voltage  $V$ , is given by [37]:

$$E_{DC}(z) = \frac{2V}{d \cosh^{-1}(l/2a)} \cdot \frac{1}{1 + (2z/d)^2}, \quad (3.24)$$

where  $a$  is the radius of the wire,  $l$  is the spacing between them and the  $d$  is a geometrical parameter defined in such a way that  $d^2 = l^2 - 4a^2$ . Such a parameter will result useful in investigating the properties of the total second harmonic beam. By inserting Eq. (3.24) in Eq. (3.10), it is possible to determine the second harmonic electric field generated by the bias:

$$E_{SH}^{DC}(r, z) = \frac{i8\pi^2\omega}{n_p c \cosh^{-1}(l/2a)} \chi^{(3)} E_P^2 V \frac{z_R}{2z_R + d} \exp\left\{-\frac{\Delta k d}{2}\right\}, \quad (3.25)$$

It is interesting to note the similarity between Eqs. (3.15) and (3.25). The parameter  $d$  plays a similar role to that of the THz Rayleigh length, as it is present in the exponential term accounting for the phase-matching condition. The smaller  $d$ , the higher the conversion efficiency. Since  $d$  decreases as  $l$  decreases and  $a$  increases, larger radii and narrower gaps between the two wires promote a more efficient generation process. However, the THz spot size imposes a lower limit to the distance between the wires. Eventually, the limit  $d \rightarrow 0$  corresponds to the DC electric field within an infinite parallel plate capacitor. Now, for the case of ABCD (heterodyne detection), the actual readout signal is then given by the cross term (Eq. (3.23)), i.e. the product between the electric fields in Eqs. (3.15) and (3.25). Therefore, Eq. (3.23) can be more accurately rewritten as:

$$I_{DFG}^{heterodyne} \propto E_{DFG}^{THz} E_{DFG}^{DC} \propto \left(\chi^{(3)} I_P\right)^2 E_{THz} V \frac{z_R^2 z_T}{(z_R + z_T)(2z_R + d)} \exp\left\{-\Delta k (z_T + d/2)\right\}, \quad (3.26)$$

where only the main factors have been reported. Equation (3.26) reveals that the combination of the DC and THz contributions to the total second harmonic intensity slightly modifies the phase matching constraint with respect to that appearing in Eq. (3.15), as the parameter  $d$  is now included in the exponential term. This has to be expected since, while the THz wave propagates, the Gouy phase shift introduces a phase inconsistency along the longitudinal coordinate  $z$ , which is missing for the DC contribution. For a too long electrode width (namely longer than the THz Rayleigh length), the phase change experienced by the THz contribution could eventually result in cross-phase with respect to the DC field, thus nullifying the total DFG intensity. However, a too short region where the DC electric field is distributed can cause an insufficient accumulation of the signal read by the PMT due to a lower interaction length, thus limiting the achievable

maximum strength and the dynamic range. A reasonable trade-off could be reached by imposing  $d \ll 2z_T$ , which results in the choice of two wires with relatively large diameter, according to Eq. (3.26), as the THz spot-size fixes the minimum spacing between them.

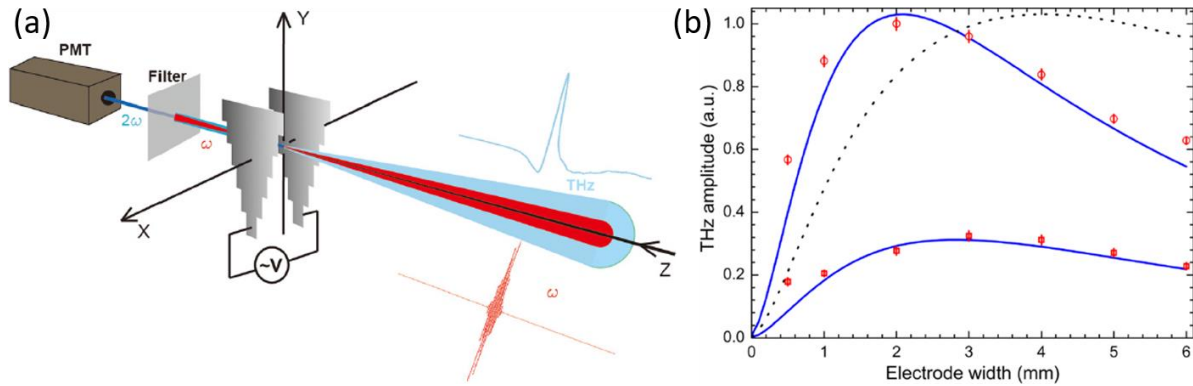


**Figure 2.10.** (a) Experimental set-up for the study of the Gouy phase shift effect on the ABCD technique. The electrodes consist of a stair-shaped stack, which is vertically shifted to change the effective width of the biased region. (b) THz electric field strength (red dots) experimentally retrieved as a function of the electrode width for the two cases of 35-mm-diameter (upper curve) and 20-mm-diameter (lower curve) THz beam. The blue solid line shows the simulation results. The dotted black line represents the simulation result for the case of a plane wave. Curves and data are normalized to the corresponding maximum values, respectively. (Figures adapted from Ref. [73]).

### 2.5.3 Analysis of the Gouy phase shift in the ABCD method

The condition of choosing small-sized electrical contacts with respect to the THz Rayleigh length so to bias the interaction between THz and probe beam, could be better achieved by completely replacing the electrodes with a different shape, e.g. two parallel metal plates. In particular, He *et al.* [73] demonstrated that by properly positioning such metal plates along the focal point, it is possible to compensate the two concurrent effects (i.e., larger interaction length vs phase-matching) thus allowing a significant (at least two-fold) improvement of the total DFG throughput and dynamic range. To pursue such an investigation, the authors employed the experimental set-up sketched in Fig. 2.10(a). An amplified laser system provides ultra-fast optical pulsed beam of 800 nm, 50 fs, 1.4 mJ, 3 kHz, which are split into two arms. The 1.3-mJ-pump beam drives a two-color plasma source to generate THz pulses, while the 16- $\mu$ J-probe beam is focused through a 150-mm-lens (resulting in a probe Rayleigh length of  $z_R = 100 \mu\text{m}$ )

together with the THz beam in the middle of the 1.5-mm-spaced, 1.5-kV-biased electrodes, so to perform the ABCD technique. At the detection stage, the polarizations of probe, THz and bias electric fields are parallel and horizontally oriented. The electrode structure consists of a stack of stair-shaped plates, whose width changes vertically. In this way, it is possible to change the length of the biased interaction region, by shifting the whole structure along the vertical axis ( $y$ ). The stage can also be moved along the  $z$ -direction in order to optimize the overlap of the THz beam with the bias electric field in time and space. The second harmonic beam emerging from the electrodes is then sent to a PMT, placed behind an optical bandpass filter centered at the second harmonic frequency. The Rayleigh length of the THz beam ( $z_T$ ) was varied by changing the diameter of the collimated beam through an iris. In particular, two cases were studied, i.e. for the values of  $z_T = 1.6$  mm and 4.8 mm. These correspond to a beam diameter of 35 mm and 20 mm, respectively, at the frequency of 1 THz. By fixing  $z_T$ , the THz waveform is experimentally reconstructed for each electrode width. Then, the THz peak values (red dots) are plotted as a function of the width in the range 1-6 mm, as shown in Fig. 2.10(b). Additionally, the case of wire electrodes for both  $z_T$  is reported in correspondence of the 0.5 mm point (most left), for comparison purpose. We note that the values for the case of  $z_T = 1.6$  mm are always larger than those at  $z_T = 4.8$  mm and that the ratio between two points retrieved for the same electrode width satisfies the relation  $(35/20)^2 \approx 3$ , given by the square of the ratio between the corresponding THz beam diameters. Moreover, it results that, as expected, there exists an optimum electrode width leading to the highest TFISH yield. Interestingly, such an optimum value is dependent on the THz Rayleigh length and, in particular, it moves from 2 mm for  $z_T = 1.6$  mm to 3 mm for  $z_T = 4.8$  mm. This means that the competing effects of accumulation and phase-cancellation reach the optimum when the electrode width is roughly close to  $z_T$ . Indeed, an empirical formula, which gives a good estimation of the optimum electrode width ( $W$ ) to employ in the detection, has the form:

$$W_{optimum} \approx \frac{\pi z_T}{1 - 2\pi z_T \Delta k}. \quad (3.27)$$

Numerical simulation results shown in Fig. 2.10(b) as blue dotted line, reveal a good agreement with the experiments for electrode widths larger than 2 mm, whereas for smaller values a slight

discrepancy is observed. This has to be ascribed to the fact that when the length of the electrodes approaches the gap separation, the bias electric field generated by the capacitor-like structure assumes a wider extension in the surrounding space, due to the fringing effect [74]. Finally, in order to understand how crucial the inclusion of the Gouy phase shift in the calculation is, the

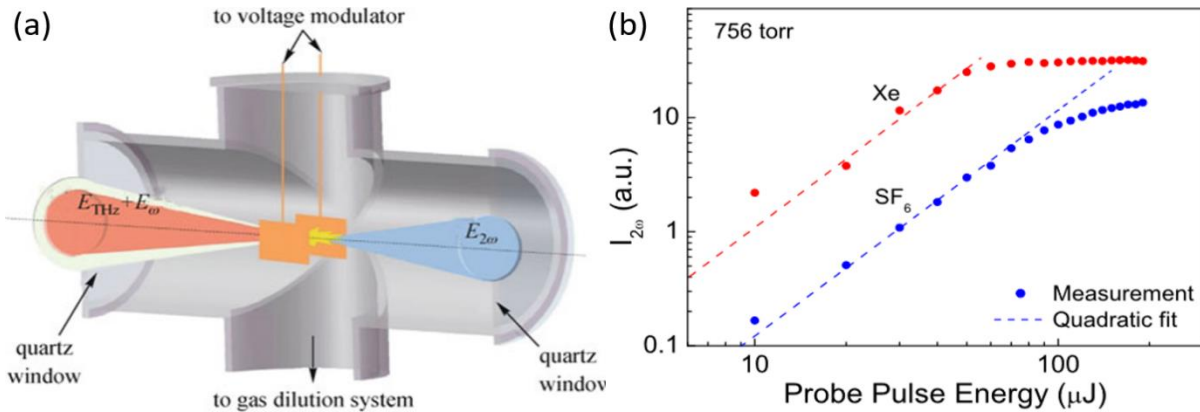


**Figure 2.11.** (a) Sketch of the vacuum cell employed in the study of the ABCD performance as a function of the type of gas. The apparatus consists of a stain steel chamber fed by a gas dilution system, which allows varying the gas pressure inside. Two fused quartz windows at the entrance and exit (2 and 3-mm-thick, respectively) of the cell are relatively transparent to the incoming probe and outgoing second harmonic. THz frequencies beyond 5 THz are highly attenuated by the large thickness of the glass. (b) Second harmonic intensity generated from the ABCD mechanism as a function of the probe energy for two different gases at the pressure of 1 atm ( $\sim 760$  torr): Xenon (red dots) and sulfur hexafluoride ( $\text{SF}_6$ , blue dots). The dashed lines are quadratic fits. (Figures adapted from Ref. [75]).

black dotted line shows simulation results when the Gouy effect is not included in the interaction and the phase cancellation is supposedly due to dispersion only, occurring between the fundamental and second harmonic frequencies in the gas medium. As it can be clearly seen, the expected trend reaches the highest values for electrode widths much longer than for the real case, because the phase change induced by dispersion is generally slower than that introduced by the Gouy effect.

#### 2.5.4 Dependence on the gas parameters

In order to gain more knowledge from Eq. (3.26), it is convenient to study the phase-matching condition as a function of the dispersion of the nonlinear medium, the latter being air in the case

of standard ABCD. However, for sake of completeness, we will consider the case of a generic gas at the pressure  $p$  (expressed in atmospheres). Indeed, the refractive index of a gas varies with pressure (i.e., the density of the particles), which in turn affects the phase-mismatch term  $\Delta k$ . Therefore, we could formally write such dependence as:

$$\Delta k = -p \cdot dk = -2\pi p \frac{\Delta n_0}{\lambda_{SH}} \quad (3.28)$$

where  $\lambda_{FH}$  and  $\lambda_{SH}$  are the fundamental (FH) and second harmonic (SH) wavelengths,

$$dk = 2k_{FH} - k_{SH} = \frac{4\pi n_{FH}}{\lambda_{FH}} - \frac{4\pi n_{SH}}{\lambda_{SH}} = 2\pi \frac{\Delta n_0}{\lambda_{SH}}$$

is the phase-mismatch at one atmosphere (atm) and

$\Delta n_0 = n_{SH} - n_{FH}$  is the refractive index difference between the two wavelengths. In addition, the third-order nonlinear susceptibility is pressure-dependent, according to:

$$\chi^{(3)}(p) = \chi_0^{(3)} p \quad (3.29)$$

where  $\chi_0^{(3)}$  is the nonlinear susceptibility at 1 atm. By inserting Eqs. (2.29) and (3.29) in Eq. (2.27), it is possible to explicit the dependence of the DFG intensity upon the pressure:

$$I_{DFG}^{heterodyne} \propto \frac{z_R^2 z_T}{(z_R + z_T)(2z_R + d)} \left( \chi_0^{(3)} p \right)^2 \exp\{-dkp(z_T + d/2)\}. \quad (3.30)$$

From Eq. (3.30), the pressure value which maximizes the total intensity yield is:

$$p_{MAX} = \frac{2}{(z_T + d/2)dk}. \quad (3.31)$$

For such a value, Eq. (3.31) simply becomes:

$$I_{DFG}^{heterodyne} \propto \frac{z_R^2 z_T}{(z_R + z_T)(2z_R + d)(z_T + d/2)^2} \left( \frac{\chi_0^{(3)}}{dk} \right)^2 \quad (3.32)$$

We note that the exponential term accounting for the phase-matching has been replaced by the expression in parenthesis, which uniquely depends on the nonlinear coefficient of the gas employed for detection and its dispersion characteristics. The latter quantity can be regarded as

a figure of merit, which helps in determining the performance of the particular gas sensor employed as the nonlinear medium. In order to study the effectiveness of the model expressed by Eqs. (2.31) and (3.32), Lu *et al.* carried out a series of experiments by modifying the experimental set-up as seen in Fig. 2.8(a), so to include a 50-mm-long stain steel gas cell, which

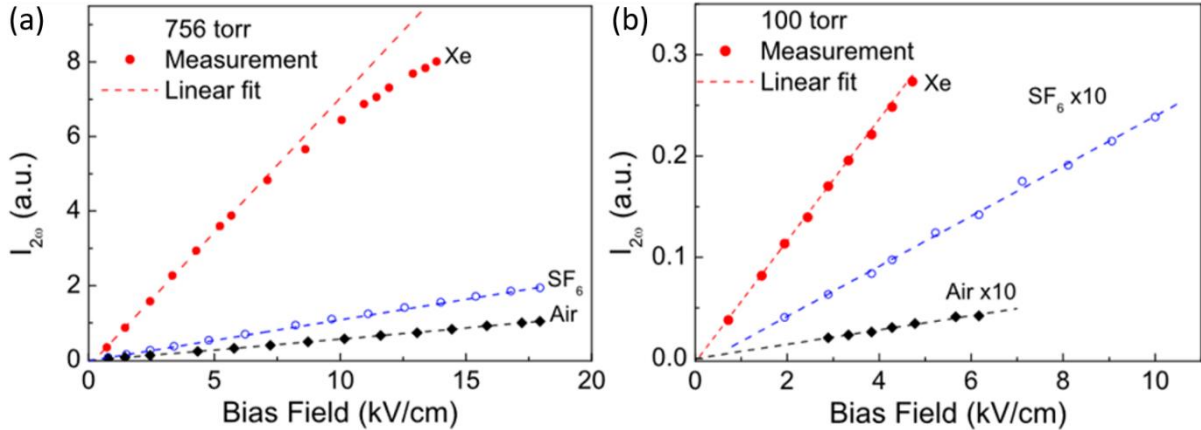


**Figure 2.12** EFISH intensity generated in the ABCD mechanism as a function of the bias electric field for three different gases, Xenon (red full dots), sulfur hexafluoride ( $\text{SF}_6$ , blue dots), and Air (black diamonds) at the pressure of (a) 1 atmosphere (756 torr) and (b) 100 torr. Dashed lines are quadratic fits. (Figures adapted from Ref. [75]).

embodies the detection stage, as sketched in Fig. 2.11(a). The optical and THz beams are focused inside the cell, by traveling through a 2-mm-thick fused quartz window, where two electrodes forming a gap of 1 mm are placed at the focus position. The outgoing DFG beam passes through a second 3-mm-thick quartz window and is then sent to the PMT. The gas cell can be pumped from vacuum ( $< 20$  mtorr) to the desired pressure level of the gas under study. Figure 2.11(b) reports the data acquired as a function of the probe energy when two particular gases were employed instead of common air: Xenon (Xe) and sulfur hexafluoride ( $\text{SF}_6$ ), which shows a low (12.13 eV) and high (15.7 eV) ionization energy [76], respectively. The ionization energy indicates the minimum amount of energy required to extract an electron from a neutral atom [77]. For comparison, the ionization potential of nitrogen is 15.58 eV. Therefore, it is expected that the formation of a plasma at the focus position should occur at much lower probe energies in Xe atmosphere, with respect to the  $\text{SF}_6$  gas. Indeed, it can be seen that higher signal intensities are achieved in presence of Xe, since its  $\chi^{(3)}$  value is higher than that of  $\text{SF}_6$ , according

to Eq. (3.32). Interestingly, for both cases, it is possible to recognize two regimes: a monotonic trend at low probe energy, as highlighted by the quadratic fit (note the logarithmic scale on the vertical axis), and a saturation region where the SH signal does not significantly increase with the probe energy, because of the formation of plasma, which clamps the peak value. However, the threshold between the two regimes is reached at different probe energies, i.e.,  $\sim 50 \mu\text{J}$  for Xe, and  $\sim 75 \mu\text{J}$  for  $\text{SF}_6$ . This fact is indeed consistent with the observations at different ionization potentials. Once the threshold is overcome, the noise in the detection waveform suddenly increases because of the high level of plasma fluorescence background. However, no minimum probe energy is required to reach the coherent detection with the heterodyne scheme underlying ABCD. Therefore, for the best operation scenario, probe energies slightly lower than the threshold are recommended. Figure 2.12 shows the trend of the SH intensity as a function of the bias electric field for a fixed probe energy of  $50 \mu\text{J}$ , (a) for the case of atmospheric pressure and (b) at the lower pressure of 100 torr (b). Data reveal that the trend is linear for the case of  $\text{SF}_6$  and air, with slightly higher values for the former gas (mainly due to the absence of water molecules absorbing the THz radiation). Since the dielectric strength of Air is relatively low ( $\sim 30 \text{ kV/cm}$ , at 1 atm), bias electric fields higher than  $20 \text{ kV/cm}$  were not applied in all the experiments. This in order to avoid detrimental effects, which occur when Air starts to be slightly ionized. Instead, the dielectric strength of  $\text{SF}_6$  is  $\sim 90 \text{ kV/cm}$ , therefore  $\text{SF}_6$  could withstand higher biases. Although the values for the case of Xe are one order of magnitude higher than the Air case, data show a different behavior for such a case, since the SH intensity saturates soon after  $7 \text{ kV/cm}$ , most likely due to the high pressure, which induces complicated aside effects and hides the main SH generation process. Indeed, the measurements performed at a lower pressure ( $\sim 100 \text{ torr}$ ), reveal that all gases fulfill the linear trend predicted by Eq. (3.32). We recall that the breakdown voltage of a gas decreases at lower pressure, which explains the reason why the bias electric fields applied in Fig. 2.12(b) were lower than those at the atmospheric pressure (Fig. 2.12(a)). Noteworthy, in this case, the values acquired in presence of Xe are more than two orders of magnitude larger than those taken in air.

### 2.5.5 Plasma absorption

In the previous section, it has been shown that when the probe intensity at the focal point overcomes the plasma generation threshold, the detection scaling mechanism deviates from the expected parabolic trend, resulting in a saturation of the SH intensity. At first instance, this is due to the fact that the plasma generation causes the clamping of the probe intensity, due to defocusing, which prevents a further increase of the detection efficiency. If detection is carried

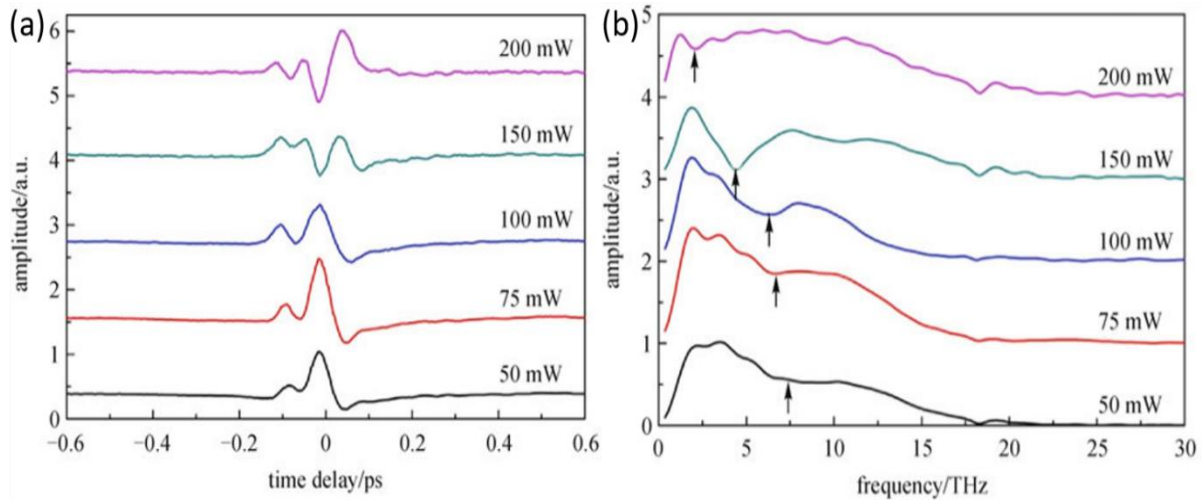


**Figure 2.13** Second harmonic intensity generated from the ABCD mechanism as a function of the bias electric field for three different gases, Xenon (red full dots), sulfur hexafluoride ( $\text{SF}_6$ , blue dots), and Air (black diamonds) at the pressure of (a) 1 atmosphere (756 torr) and (b) 100 torr. The dashed lines are quadratic fits. (Figures adapted from [35]).

out with particularly short pulses ( $< 100$  fs) in order to enlarge the ABCD frequency response, such a drawback limits, even more, the overall performance because more carriers are generated in the plasma. Moreover, plasma itself is not completely transparent to the THz radiation, rather it shows some natural resonant frequencies, which affects the frequency response of ABCD. Indeed, Figure 2.13 shows (a) the waveforms and (b) the corresponding FFT-evaluated spectra, retrieved when the ABCD technique is performed with a 35-fs-long probe pulse, the power of which varies in the range 50-200 mW. It can be seen that when passing from low to high optical power, the THz transient undergoes a significant reshaping, showing an increasing number of cycles as the power increases. By looking at the spectra, it is clear that the single-cycle nature of the THz waveform is lost because of the appearance of a cut-off frequency in the higher part of the THz spectrum. However, the position of such a frequency (pointed out by the vertical

black arrows) moves towards lower frequencies as the power increases, revealing an unexpected dependence on the probe intensity. Indeed, an increase of the plasma carrier density should result in a blue-shift of the absorption line, which is not the case here. Rather, different reasons were proposed in order to explain the observed behavior. Among others, one motivation could be related to resonances in the waveguide-like structure made up by the plasma channel, which confines the THz radiation. Since the channel length and width proportionally scale with the laser power, a possible resonance should inversely scale with the frequency. Another possible explanation is that for higher powers, the interaction region (proportional to the plasma length) between THz and probe becomes so long to result in a destructive interference of the FWM process for frequencies as much lower as the channel length increases. Incidentally, we recall that in section 2.3, we have already shown how the air-breakdown coherent detection method suffered from some artefacts in the retrieved THz spectrum, since the typical optical probe powers employed to operate that technique were in the same order of magnitude of those employed for this investigation. A clear interpretation of this behavior is still not fully provided.

### **2.5.6 Dependence on the beam intensity profile**

The analytical model discussed in Section 2.5.2 was developed under the hypothesis of constant intensity along the propagation, similarly to the case of a plane wave, while the only effect of strong THz and optical beam focusing considered, was the Gouy phase shift. However, we recall that the diffraction limit imposes that a generic beam cannot be focused to a spot size smaller than its wavelength. Since the optical frequencies are two orders of magnitude higher than the THz ones, it results that the spot size of the THz beam will be much larger than that of the optical probe beam. Moreover, for an ultra-broadband THz pulse, the spot size (and correspondingly the Rayleigh length  $z_T$ ) is strongly frequency-dependent, and cannot be neglected. Therefore, we can revise that model in order to include the focusing effect of both the beams and explicit such a dependence in terms of beam parameters. In particular, by introducing the THz ( $P_{THz}$ ) and probe ( $P_P$ ) power, the intensity and the electric field of the two beams can be expressed as:

$$I_{THz(P)} = \frac{2P_{THz(P)}}{\pi w_{THz(P)}^2} = \frac{P_{THz(P)}}{z_{THz(P)} \lambda_{THz(P)}} \quad (3.32)$$

$$E_{THz(P)} = \sqrt{\frac{2I_{THz(P)}}{\epsilon_0 c}} \quad (3.33)$$

Therefore, by inserting Eqs. (2.33) and (3.33) in Eq. (2.27), after some simplifications, we have:

$$I_{DFG}^{heterodyne} \propto A(P_{THz}, P_P, \lambda_{THz}, \lambda_P) \frac{\sqrt{z_T}}{(z_R + z_T)(2z_R + d)} (\chi_0^{(3)} P)^2 \exp\{-dkp(z_T + d/2)\}, \quad (3.34)$$

where the coefficient  $A$  is now dependent upon the powers of the two beams and their wavelengths. By evaluating the optimum pressure by means of Eq. (3.34), it is found that:

$$I_{DFG}^{heterodyne} \propto A(P_{THz}, P_P, \lambda_{THz}, \lambda_P) \frac{4\sqrt{z_T}}{(z_R + z_T)(2z_R + d)(z_T + d/2)^2} \left( \frac{\chi^{(3)}}{dk} \right). \quad (3.35)$$

In the hypothetical case of optimum pressure, Eq. (3.35) suggests that in order to maximize the signal, both beams (and especially the probe beam) should be focused as tightly as possible, since  $z_R$  is only present at the denominator. However, when the THz beam is tightly focused, its Rayleigh length can become so short that the optimum pressure, according to Eq. (3.35), will be pushed towards very high values, potentially too far from the pressure under operation, thus hampering the performance. Therefore, acting on the optical beam focusing represents an easier task to accomplish in order to maintain the performance reasonably high.

### 2.5.7 Balanced air-biased coherent detection

The previous sections were devoted to the implementation of methods and procedure aimed at the enhancement of the amplitude response of the ABCD technique. These schemes can boost the ABCD throughput in terms of second harmonic intensity generated through the FWM mechanism. Therefore, the performance of the THz detection scheme was better described in terms of DR, which involves the measurement of the THz waveform amplitude. The problems related to the noise contribution were only barely mentioned and marginally investigated, e.g. in terms of SNR. We recall that in the ABCD technique, the introduction of the heterodyne

scheme allows achieving a pure coherent detection by relying on the filtering action of the lock-in amplifier, which rejects any incoherent term that does not appear at the same modulation frequency of the bias voltage. However, such incoherent terms are always read by the lock-in amplifier, bringing about more noise contribution and possibly resulting in saturation of the instrument. Therefore, one manner to further increase the DR and SNR is the implementation of a revised scheme, which could suppress useless contributions to the total signal. Inspired by

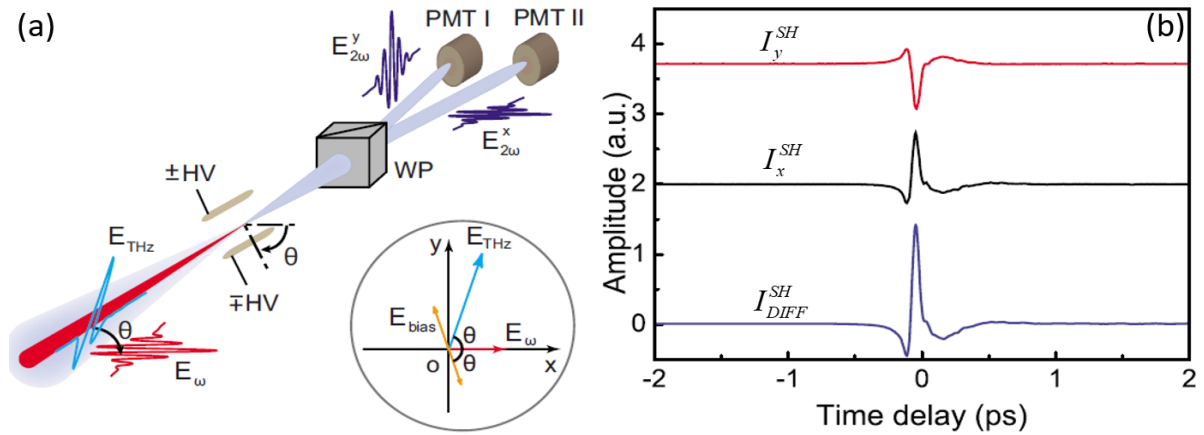


**Figure 2.14** (a) Sketch of the modified detection stage to operate the balanced ABCD technique. The THz and static electric field polarizations form an angle  $\theta$  with the optical probe beam ( $E_\omega$ ). A Wollaston prism separates the two orthogonal components, which are then sent to two different PMTs. (b) THz waveforms detected by each single PMT (first and second curve starting from the top). The lowest curve represents the actual signal from the lock-in amplifier, given by the difference of the two curve above. (Figures adapted from Ref. [40]).

the differential scheme underlying EOS, Lu *et al.* developed the so-called balanced-ABCD, which exploits the tensor property of the third-order susceptibility  $\chi^{(3)}$  of gases to generate two cross-polarized SH beams and reconstruct the THz waveform as the difference between these two signals. The idea behind the implementation of this approach is sketched in Fig. 2.14(a). The THz and probe beams are still focused together within two metal wires, which deliver the proper bias. However, with respect to conventional ABCD, the THz and probe electric fields are not parallel with each other, but they form an angle  $\theta$ . Moreover, the wires are rotated with respect to the horizontal direction so to form the same angle with the probe beam, but with opposite sign ( $-\theta$ ). The inset in Fig. 2.14(a) depicts the orientation of all the electric fields. As

will be explained in the following notes, such a configuration leads to the generation of two orthogonal second harmonic components (namely,  $E_x^{SH}$  and  $E_y^{SH}$ ), which are separated by a Wollaston prism and acquired by two PMTs. The reason why the FWM process involving such a scheme generates two orthogonal components, can be explained if we take into account that in an isotropic medium, like a gas, the  $\chi^{(3)}$  tensor has only three independent non-vanishing components [63], i.e.  $\chi_{yyxx}^{(3)}, \chi_{xyxy}^{(3)}, \chi_{xyyx}^{(3)}$ , whereas  $\chi_{xxxx}^{(3)} = \chi_{yyxx}^{(3)} + \chi_{xyxy}^{(3)} + \chi_{xyyx}^{(3)}$ . The subscription indicates the polarization orientation of four electric fields, i.e. SH, either THz or DC, and two probe (degenerate case), respectively. The geometry depicted in Fig. 2.14(a), allows selecting two components, i.e.  $\chi_{xxxx}^{(3)}$ , where all electric fields are x-polarized and  $\chi_{yyxx}^{(3)}$ , which involves SH and THz polarizations along the y-axis, while the probe beam is x-polarized. In this way, the nonlinear interaction occurring in conventional ABCD gives rise to one x- and one y-polarized SH components, which could be quantified by means of the following relations:

$$E_x^{SH} = \left(E_{THz}^{SH}\right)_x \pm \left(E_{bias}^{SH}\right)_x \propto \chi_{xxxx}^{(3)} I_\omega E_{THz} \cos \theta \pm \chi_{xxxx}^{(3)} I_\omega E_{bias} \cos \theta \quad (3.36)$$

$$E_y^{SH} = \left(E_{THz}^{SH}\right)_y \mp \left(E_{bias}^{SH}\right)_y \propto \chi_{xxxx}^{(3)} I_\omega E_{THz} \sin \theta \mp \chi_{xxxx}^{(3)} I_\omega E_{bias} \sin \theta, \quad (3.37)$$

where,  $E_x^{SH}$  and  $E_y^{SH}$  are the x and y components of the total SH electric field,  $I_\omega$  is the probe intensity,  $E_{bias}$  is the static electric field. The double sign in Eqs. (2.37) and (3.37) is due to the fact that, since the bias field is modulated at a frequency equal to the half of the THz repetition rate, the resulting  $E_{THz}^{SH}$  and  $E_{bias}^{SH}$  could be either in phase or have a  $\pi$  phase difference. Moreover, since the angles between the pair THz and probe fields vs bias and probe fields, are opposite in sign, the two SH components experience an additional  $\pi$  rotation with respect to each other, which explains the opposite double signs in Eqs. (2.37) and (3.37). According to the heterodyne scheme, the actual signal read by the lock-in amplifier from each PMT channel is proportional to the intensity of the SH components:

$$I_x^{SH} \propto \left( \chi_{xxx}^{(3)} I_\omega \cos \theta \right)^2 \left( E_{THz} \pm E_{bias} \right)^2, \quad (3.38)$$

$$I_y^{SH} \propto \left( \chi_{yyx}^{(3)} I_\omega \sin \theta \right)^2 \left( E_{THz} \mp E_{bias} \right)^2. \quad (3.39)$$

Now, in order to perfectly balance the detection, the coefficients in Eqs. (2.39) and (3.39) must be equal, i.e. they have to satisfy the following condition:

$$B = \chi_{xxx}^{(3)} I_\omega \cos \theta = \chi_{yyx}^{(3)} I_\omega \sin \theta \Rightarrow \tan \theta = \frac{\chi_{xxx}^{(3)}}{\chi_{yyx}^{(3)}}. \quad (3.40)$$

By means of Eq. (3.40), we can rewrite Eqs. (2.39) and (2.40) as:

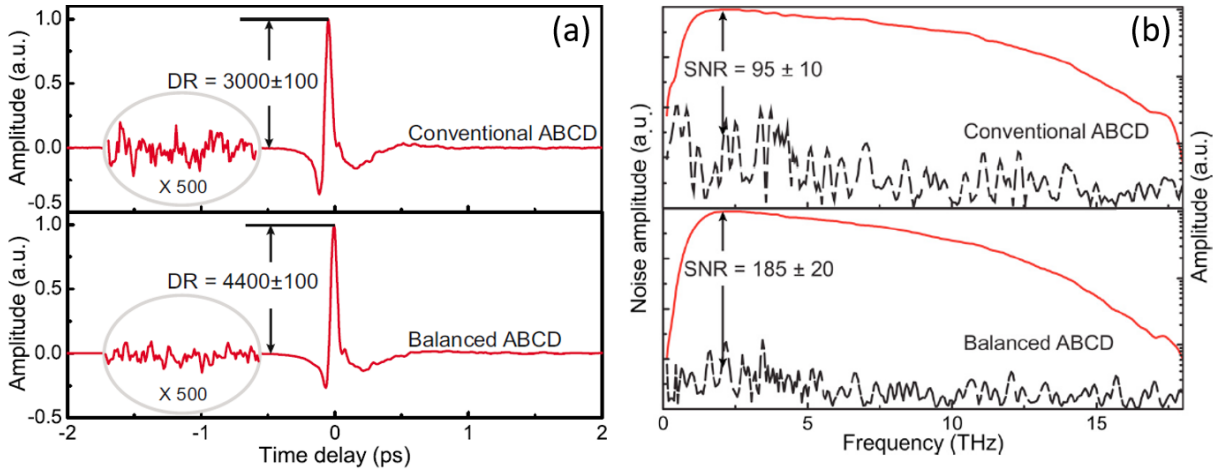


**Figure 2.15.** Comparison between conventional and balanced ABCD techniques in terms of (a) waveforms and DR and (b) spectra and SNR. (Figures adapted from Ref. [40]).

$$I_x^{SH} \propto I_\omega^2 B^2 \left( E_{THz} \pm E_{bias} \right)^2, \quad I_y^{SH} \propto I_\omega^2 B^2 \left( E_{THz} \mp E_{bias} \right)^2, \quad (3.41)$$

and by performing the difference between the components in Eq. (3.41), it is found that:

$$I_{DIFF}^{SH} = I_x^{SH} - I_y^{SH} \propto \pm 4 I_\omega^2 B^2 E_{THz} E_{bias}. \quad (3.42)$$

By comparing Eq. (2.23) with Eq. (3.42) ruling standard ABCD, it turns out that if we perform the detection in the differential configuration, the input signal for the lock-in amplifier is directly proportional to the cross term only. No other contributions are present. This circumstance is expected to greatly enhance the noise performance, because the filtering action performed by

the lock-in amplifier is relieved by the difference in between the two channels, which inherently suppresses the offset terms. The price to pay is that, with respect to Eq. (3.42), the amplitude of the readout signal is now reduced by a factor  $B^2/2$ , which depends on the properties of the selected gas. Such a value can be experimentally estimated by measuring the intensity of the two SH beam components induced by the bias electric field only (i.e., when the THz beam is blocked), as a function of the angle. Otherwise, since for most of the gases,  $\chi_{xxxx}^{(3)} \approx 3\chi_{yyyy}^{(3)}$  [78], [79], we can evaluate with good approximation an angle of  $\theta_{DIFF} \approx 71^\circ$  (by directly solving Eq. (3.42)) Figure 2.14(b) shows the experimentally reconstructed THz waveforms at each PMT channel (red and black curve), and their difference (blue curve), when both the THz polarization and orientation of the electrode are rotated by the angle  $\theta_{DIFF}$ . Further details of the experimental set-up can be found in [35], [40]. We note that each channel is actually a single-ended (i.e., one arm) detection and already allows to record the THz transient (apart from the opposed phase, which results in the flipping of the waveform). However, the amplitude of the differential signal achieved in the case of the balanced scheme (i.e., double arm) appears larger by a factor of  $4 \times \sin^2(\theta_{DIFF})/2 = 4 \times 3 \times \cos^2(\theta_{DIFF})/2 \approx 1.77$ , accordingly to the theoretical prediction. Besides the slightly lower peak amplitude achieved with respect to the case of conventional ABCD, the comparison in terms of dynamic range reveals the potential of the differential scheme. To this end, Fig. 2.15(a) shows the comparison between the THz waveforms recorded in both cases. The DR increases from the value of around 3000 in the case of single-ended ABCD to around 4400 for the balanced version, without appreciably affecting the shape of the THz transient. It is worth highlighting that the DR does not simply double, because of the small attenuation of the THz peak with respect to the conventional case. Different experimental conditions in terms of either type of gas or pressure, which allows setting  $\theta \approx 45^\circ$ , could further boost performances. Correspondingly, from Fig. 2.15(b), the spectral noise floor (evaluated by Fourier transforming the waveform recorded when the THz beam is blocked), is decreased by a factor of two, which results in a 2-fold improvement of the SNR, from 95 of the conventional case to 185 of the balanced scheme. As will be analytically demonstrated in the following section, improvement is indeed due to the noise cancellation enabled by the differential scheme.

## 2.6 Noise evaluation in the ABCD technique

Based on the relation given in the previous section, we will now provide a quantitative description of the noise underlying the conventional ABCD technique, with the aim to explain the behavior of DR and SNR, only qualitatively described so far. To this end, we start from the analytical form of the total SH intensity generated by the nonlinear interaction between THz probe beams under a generic bias field, given by Eq. (3.42), and here reported for simplicity:

$$S_{TOT} = \left( \chi^{(3)} I_P \right)^2 \left( E_{THz} \pm E_{DC} \right)^2. \quad (3.43)$$

However, due to the heterodyne mechanism, the lock-in amplifier (LA) will detect only the signal at the same modulation frequency of the bias voltage, used as its synchronism, that is:

$$S_{LA} = 2 \left( \chi^{(3)} I_P \right)^2 E_{THz} E_{DC}. \quad (3.44)$$

To evaluate the DR, we have to estimate the contributions to the total background noise ( $N$ ), i.e. recorded when the THz electric field is not reaching the detector, that is:

$$N = S_{TOT} (E_{THz} = 0) = \left( \chi^{(3)} I_P E_{DC} \right)^2 \quad (3.45)$$

The noise is essentially due to three main contributions: the fluctuations of laser intensity ( $\delta I_P$ ) and bias electric field ( $\delta E_{DC}$ ), and the noise equivalent power (NEP) of the PMT. In order to analytically determine the forms of such contributions, we will exploit the results of the standard noise theory [80], considering additive noise contributions. Therefore, we can write:

$$\frac{\partial N}{\partial I_P} \delta I_P = 2 I_P \left( \chi^{(3)} E_{DC} \right)^2 \delta I_P = 2 \left( \chi^{(3)} I_P E_{DC} \right)^2 N_P \quad (3.46)$$

$$\frac{\partial N}{\partial E_{DC}} \delta E_{DC} = 2 E_{DC} \left( \chi^{(3)} I_P \right)^2 \delta E_{DC} = 2 \left( \chi^{(3)} I_P E_{DC} \right)^2 N_{DC} \quad (3.47)$$

where, we have defined the quantities  $N_P = \frac{\delta I_P}{I_P}$  and  $N_{DC} = \frac{\delta E_{DC}}{E_{DC}}$  as the percentage of the laser and bias fluctuations, usually provided by the supplier of the instruments. For the SNR, we have to evaluate the fluctuations of the total signal  $S_{TOT}$  (at its peak) around its average value, due to

the noise. We highlight that, even though the LA is returning the heterodyne signal only (i.e. Eq. (3.47)), the noise is actually due to all the contributions to the total SH intensity, including the incoherent terms. This is indeed the main drawback of the single-ended technique, as we will clarify later. Thus, we find for the two contributions:

$$\frac{\partial S_{TOT}}{\partial I_P} \delta I_P = 2I_P (\chi^{(3)})^2 (E_{DC} \pm E_{THz})^2 \delta I_P = 2(\chi^{(3)} I_P)^2 (E_{DC} \pm E_{THz})^2 N_P, \quad (3.48)$$

$$\frac{\partial S_{TOT}}{\partial E_{DC}} \delta E_{DC} = 2(E_{DC} \pm E_{THz}) (\chi^{(3)} I_P)^2 \delta E_{DC} = 2(\chi^{(3)} I_P)^2 (E_{DC} \pm E_{THz} E_{DC}) N_{DC}. \quad (3.49)$$

Therefore, the complete expressions for DR and SNR, involving all the main parameters, are:

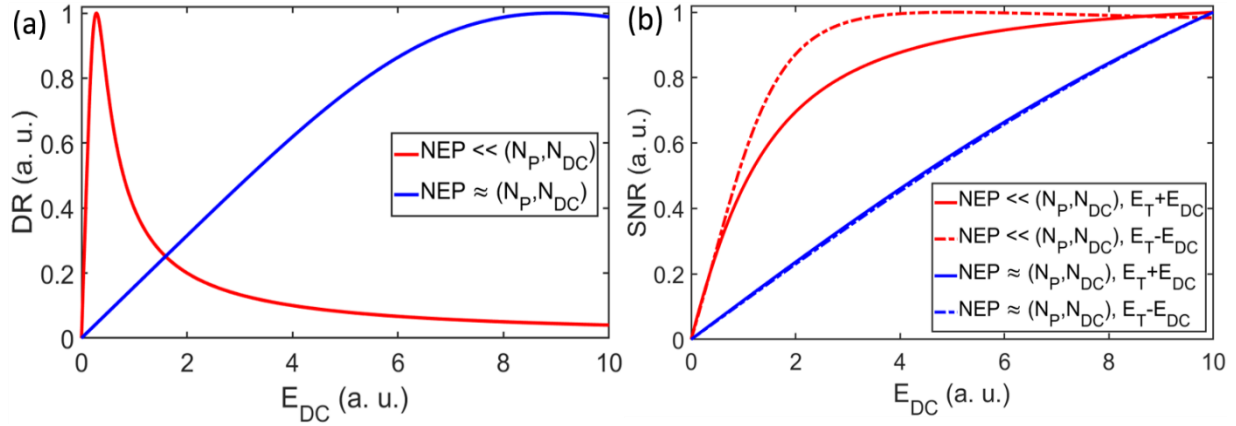


**Figure 2.16.** Dependence of the (a) DR and (b) SNR upon the bias electric field. In both graphs, the red curves indicate the regime of ideal PMT, whereas the blue curves represent the case of NEP comparable with the fluctuation introduced by the laser and bias sources. Note that for the SNR, both cases of in-phase (solid curves) and out of phase (dashed lines)  $E_{THz}$  and  $E_{DC}$  are depicted. All the curves are normalized to their own maxima.

$$DR = \frac{S_{LA}}{\sqrt{\left(\frac{\partial N}{\partial I_P} \delta I_P\right)^2 + \left(\frac{\partial N}{\partial E_{DC}} \delta E_{DC}\right)^2 + NEP^2}} = \frac{2(\chi^{(3)} I_P)^2 E_{THz} E_{DC}}{\sqrt{4(\chi^{(3)} I_P E_{DC})^4 (N_{DC}^2 + N_P^2) + NEP^2}} \quad (3.50)$$

$$\begin{aligned}
SNR &= \frac{S_{LA}}{\sqrt{\left(\frac{\partial S_{TOT}}{\partial I_P} \delta I_P\right)^2 + \left(\frac{\partial S_{TOT}}{\partial E_{DC}} \delta E_{DC}\right)^2 + NEP^2}} = \\
&= \frac{2\left(\chi^{(3)} I_P\right)^2 E_{THz} E_{DC}}{\sqrt{4\left(\chi^{(3)} I_P\right)^4 \left(E_{THz} \pm E_{DC}\right)^2 \left[\frac{N_{DC}^2}{\left(1 \pm E_{THz} / E_{DC}\right)^2} + N_P^2\right] + NEP^2}} \quad (3.51)
\end{aligned}$$

It is worth mentioning that Eqs. (2.51) and (3.51) represent a first-order approximation model, which could well describe the noise affecting the detection process, when the contributions from all the other equipment (mostly electronics noise) can be completely neglected. At first instance, we observe that if all the fluctuations decrease, both DR and SNR increase, as intuitively expected. However, depending on the NEP of the PMT, we could distinguish two noise regimes. Let us first neglect the NEP. Then, Eqs. (2.51) and (3.51) simplify as:

$$DR|_{NEP \ll N_{DC}, N_P} \approx \frac{E_{THz}}{E_{DC} \sqrt{\left(N_{DC}^2 + N_P^2\right)}}, \quad (3.52)$$

$$SNR|_{NEP \ll N_{DC}, N_P} \approx \frac{E_{THz}}{\sqrt{N_{DC}^2 + N_P^2 \left[\frac{E_{THz}}{E_{DC}} \pm 1\right]^2}}. \quad (3.53)$$

We note that for the case of ideal PMT, both DR and SNR can be improved by simply increasing the strength of the THz field. This can be achieved by tightly focusing the THz beam, which is a condition already explored in section 2.6.6. However, the dependence on the bias electric field strength is different for the two cases, as depicted in Fig. 11. Indeed, on one side, the DR appears to diminish as the bias increases (see Fig. 2.16(a), red curve), because it acts as an amplification term for all the noise contributions. Instead, for the SNR, the behavior is somewhat more complex because of the double sign in Eq. (3.53). If the THz and bias fields are in phase, the term in squared parenthesis is always greater than one, thus resulting in an amplification of the laser fluctuations and consequently in a decrease the SNR (solid red curve in Fig. 2.16(b)).

Conversely, if  $E_{THz}$  and  $E_{DC}$  are out of phase, the term in parenthesis is greater than the unity only for bias strengths lower than  $E_{THz}/2$ , when it reaches its maximum. Beyond such a value, the laser fluctuations are demagnified and the SNR is only limited by the quality of the bias electric field source (i.e.,  $N_{DC}$  starts to dominate over  $N_P$ , dashed red curve in Fig. 2.16(b)). The slightly better performance achieved for those time intervals when the fields are out of phase ( $E_{THz}-E_{DC}$ ), finds an explanation in the fact that noise is unipolar and positive, being due to the offset (i.e., incoherent) terms, which are always proportional to the square of the fluctuations. Therefore, in the case of ideal PMT, it results relatively easier to resolve the signal from the noise, when the product  $E_{THz}E_{DC}$  has an opposite sign with respect to the incoherent terms. The regime stated by Eqs. (2.53) and (3.53) is not practically addressable, because the PMT always introduces a strong noise contribution to the detected waveforms. However, when the NEP is included, the dependence of the noise figures on the DC field becomes more complicated. We recall that, in a PMT, the optical signal is converted into an electrical current, which is amplified by the avalanche process occurring when the gain is applied to the device through a power supply. It is possible to identify three different operating regions as a function of the gain: below the threshold of the avalanche (no gain), linear gain and field effect region [81]. Each region is featured by a different type of noise. It has been shown [35] that, for the ABCD technique, DR and SNR do not show the same trend as a function of the gain. In particular, the optimum DR is achieved for values slightly larger than those of the avalanche threshold. On the contrary, the SNR linearly scales with the gain in the linear region, reaching the optimum value just before entering the field-effect mode region. The reason behind the different behavior featuring SNR and DR could be explained by simply considering once again Eq. (2.53) and (3.53). Higher gains increase the detection yield in terms of  $S_{TOT}$ , which also includes the offset terms responsible for the noise floor  $N$ . Therefore, the gain favors the DR enhancement only for those values, which do not excessively amplify the background noise  $N$ , compared to the emphasis on the LA readout signal  $S_{LA}$ . Since larger gains make the PMT more sensitive to spurious light and other perturbations present within the environment, the noise increase rate may become faster than that of the actual signal, soon lowering the DR. Instead, very high gain values generally favor the SNR, because strong signal peaks are relatively less affected by fluctuations, until the noise induced by the PMT itself becomes giant, once the Geiger mode region has been

reached. The overall trend of the DR and SNR when the NEP is not negligible with respect to  $N_P$  and  $N_{DC}$ , are indicated by the blue curves in Fig. 2.16(a) and (b), respectively. As expected for this case, both noise figures increases as the bias electric field strengthens. On the one hand, we notice that the DR could theoretically saturate for very high DC values, i.e. when the  $N_P$  and  $N_{DC}$  dominate over the NEP, reproducing the condition pointed out by the red curve. However, it is worth highlighting that, for the case of ABCD, the bias field resulting in the saturation DR is not practically reachable, because it would be much higher than the dielectric strength of air (30 kV/cm), and only the linear regime (i.e., the blue curve for low DC values) has been experimentally observed (see Fig. 2.12(b)). Conversely, we anticipate that the SSBCD technique allows applying much higher bias electric field, which accordingly reflects in the DR trend of Fig. 2.16(a). On the other hand, the graph of the SNR reveals that the difference between THz and DC fields in/out of phase is totally negligible when the noise of the PMT is included in the model. Let us consider now the case of differential ABCD (briefly named  $\hat{\partial}ABCD$  in the following notes). In this case, the total SH intensity is exactly equal to the heterodyne signal read by the LA (i.e., the cross term, Eq. (3.53)):

$$S_{TOT}^{\hat{\partial}ABCD} = S_{LA}^{\hat{\partial}ABCD} = 4I_P^2 B^2 E_{THz} E_{DC}. \quad (3.54)$$

Moreover, since the differential signal is based on the balancing of the background levels coming from the two PMT channels (which we assume to be identical), the overall fluctuations should mostly cancel out each other. Therefore, ideally, it results that  $N^{\hat{\partial}ABCD} \rightarrow 0$ , whereas Eqs. (2.49) and (2.50) become:

$$\frac{\partial S_{TOT}^{\hat{\partial}ABCD}}{\partial I_P} \delta I_P = 8I_P B^2 E_{DC} E_{THz} \delta I_P = 8I_P^2 B^2 E_{DC} E_{THz} N_P = 2S_{LA}^{\hat{\partial}ABCD} N_P, \quad (3.55)$$

$$\frac{\partial S_{TOT}^{\hat{\partial}ABCD}}{\partial E_{DC}} \delta E_{DC} = 4I_P^2 B^2 E_{THz} \delta E_{DC} = 4I_P^2 B^2 E_{THz} E_{DC} N_{DC} = S_{LA}^{\hat{\partial}ABCD} N_{DC}. \quad (3.56)$$

Finally, DR and SNR are given by:

$$DR^{\hat{\partial}ABCD} = \frac{S_{LA}^{\hat{\partial}ABCD}}{\text{RMS}(N^{\hat{\partial}ABCD})} \rightarrow \infty, \quad (3.57)$$

$$\begin{aligned}
SNR^{\hat{\partial}ABCD} &= \frac{S_{LA}^{\hat{\partial}ABCD}}{\sqrt{4(S_{LA}^{\hat{\partial}ABCD} N_P)^2 + (S_{LA}^{\hat{\partial}ABCD} N_{DC})^2 + NEP_{diff}^2}} = \\
&= \frac{1}{\sqrt{4N_P^2 + N_{DC}^2 + \frac{NEP_{diff}^2}{(S_{LA}^{\hat{\partial}ABCD})^2}}}. \tag{3.58}
\end{aligned}$$

Interestingly, Eq. (2.58) states that the DR for the  $\hat{\partial}ABCD$  tends, at least theoretically, to the infinitive, since the noise floor is automatically canceled out by the differential scheme. However, we recall that there are other sources of noise not included in the model presented so far, which practically limit the experimental DR for this technique, to a finite value. Moreover, the perfect cancellation of the background noise is never completely observed, due to some unavoidable differences in the levels of the two PMT channels. Nevertheless, DRs 1.5 times higher than for standard ABCD have been demonstrated, as already described in section 2.5.7. With regards to the SNR, we note that in writing Eq. (3.58), we introduced a term named  $NEP_{diff}$  which could be considered as the residual noise contribution to the differential signal, somehow related to the two  $NEPs$  affecting each PMT. Those, for sake of generality, are in principle different, even though provided by the same supplier. However, the parameter  $NEP_{diff}$  is generally smaller than either  $N_P$  or  $N_{DC}$  and its contribution quickly roll down as the signal increases. Therefore, for sufficiently high  $S_{LA}^{\hat{\partial}ABCD}$ , SNR becomes virtually independent from the absolute value of either the bias electric field or the laser power, which represents a valuable advantage of the differential scheme technique against the single-ended version. Indeed, SNR could be easily improved by simply adopting low-noise bias sources and more intensity-stable laser pulses.

# Chapter 3

## **Silica-based Solid-State-Biased Coherent Detection of ultra-broadband THz pulses**

In the third chapter of this dissertation, we will provide a detailed description of the main topic of this research project. Starting with a brief overview on the limitations underlying the ABCD technique, we will explain the strategy adopted in order to overcome such issues, thus implementing a revised detection method, which results in a completely new technique. This innovative paradigm somewhat resembles and borrows some concepts of the ABCD scheme, such as the TFISH generation in a third-order medium and the heterodyne scheme, yet moves away from ABCD technique, due to some crucial differences. Indeed, our approach consists in the confinement of the nonlinear interaction, which gives rise to the TFISH term, within a standalone and integrated device, based on a solid-state material. For the first two generations of our technique, object of this chapter, the entire structure relies on a silica platform, provided with a couple of metallic contacts, which serve to deliver the bias voltage required to operate

the heterodyne mixing. Therefore, the resulting devices assume the form of a real compact and portable THz detector, which can be realized by means of a widespread fabrication technique, nowadays routinely employed in the manufacturing of commercial electronics, i.e. the CMOS process. This paves the way for a novel and unprecedented integrated approach to the ultra-broadband coherent detection of THz pulses, so far restricted to gas-based techniques. For these reasons, we have named our new method *solid-state bias coherent detection* (SSBCD), while for simplicity, we will refer to the integrated structures as SSBCD devices, whose features and potentialities will be presented in-depth in the following sections.

### 3.1 Limitation of the ABCD technique

In the previous Chapter, we have extensively described the ABCD technique and some of its variants. We recall that such a technique allows for the detection of extremely wideband THz pulses, since the upper cut-off frequency of the ABCD spectral response is only related to the pulse duration of the pulsed probe beam. Such a feature was achieved by exploiting the disordered particle structure of air, which, with respect to semiconductor materials commonly employed in previously reported solid-state techniques, does not show any particular resonance in the THz region, apart from the absorption lines of water vapor, unavoidably present under standard atmosphere conditions. Besides the basic mechanism occurring in the ABCD technique, we have shown some approaches aimed to boost the detection performance. On the one hand, in order to improve the yield of nonlinear FWM, i.e. the conversion efficiency between the THz and optical beams (without introducing artefacts in the reconstructed THz spectrum), the use of other types of gas was explored. It has been found out that long organic molecules (i.e. featuring long chains of carbon-hydrogen groups), under precise pressures and beam focusing, can enhance the SH intensity generation by a factor of 230. On the other hand, the introduction of the balanced scheme resulted in the almost 2-fold improvement of both DR and SNR. However, overall, ABCD still remains a relatively low efficient detection technique, mainly because it relies on the third-order susceptibility ( $\chi^{(3)}$ ) of gas media, which is recognized to be particularly low ( $< 10^{-23} \text{ m}^2/\text{V}^2$ ) [75]. If we consider the product of  $\chi^{(3)}$  by the THz electric field, the resulting effective second-order susceptibility  $\chi_{\text{eff}}^{(2)} = \chi^{(3)} E_{\text{THz}}$  still results in values

which are a few orders of magnitude lower than the homologous nonlinear coefficient of many solid-state materials. This explains why ABCD typically requires relatively high probe energies ( $\sim 100 \mu\text{J}$ ), as air is a weak nonlinear medium ( $\chi_{air}^{(3)} \sim 1.68 \times 10^{-25} \text{ m}^2/\text{V}^2$ , [82]). Such optical energies are extremely high when compared to those employed in either EOS or PCS, which are in the order of  $\sim 1 \text{ nJ}$  or even less [17]. Moreover, the relatively large focusing region in air ( $\sim 1.5\text{-mm}$ -wide) requires the use of kV sources in order to generate sufficiently high bias field strengths across the contacts, in such a way to result in a detected waveform with reasonable DR. Indeed, we have seen that the DR linearly scales with the bias electric field, but it is ultimately limited by the relatively low dielectric strength of air ( $\sim 30 \text{ kV/cm}$ ) [77]. As before, higher bias field values are only possible by employing gases with high ionization potential. However, since the interaction region cannot be thinner than a few times the THz beam spot size, elevated bias fields could be generated at the expenses of sophisticated electronics able to switch huge bias voltages at a rate of hundreds of Hz. Hence, the best performance achievable when such gases are employed as a nonlinear medium, has the drawback to imply possible health hazards (very high voltage!) and require bulky non-optical components, such as gas cells and dilution systems, which eventually are particularly cost-demanding and not easy access to. These factors limit the development of the ABCD method as a standalone application operated via a unique integrated device.

### 3.2 Previous demonstration of TFISH in solid materials

In order to highlight the breakthroughs which the SSBCD technique brings about to the solid-state THz detection area, we start by considering again Eq. (3.58), which expresses the relation between the readout signal of the lock-in amplifier (i.e., the intensity of the DFG beam) and the other main parameters playing a role in the ABCD mechanism, here reported for simplicity:

$$I_{DFG}^{heterodyne} \propto 2 \left( \chi^{(3)} I_{\omega} \right)^2 E_{bias}^{AC} E_{THz}. \quad (3.58)$$

We notice that the product  $\chi^{(3)} I_{\omega}$  acts as the real kernel of the detection mechanism. Indeed, in the previous section, we have shown that, accordingly to Eq. (3.58), most of the efforts devoted to the enhancement of the ABCD amplitude response have been focused in replacing air with

other gases, featuring higher  $\chi^{(3)}$ . This because the strength of the bias and THz electric fields are not (usually) real free parameters, since they have to fulfill other requirements related to the focusing geometry. At the same time, since gases are continuously renewed, there is no risk of possible damage in the nonlinear medium. Hence, the probe beam intensity can be tuned in a wide range of high values, at least up to the plasma triggering, which would ruin the ABCD spectral response. Differently, the main objective we want to accomplish via the SSBCD technique is not only the achievement of a highly efficient TFISH generation, but also to cut down the requirement of high probe energies, which so far have limited the operation of

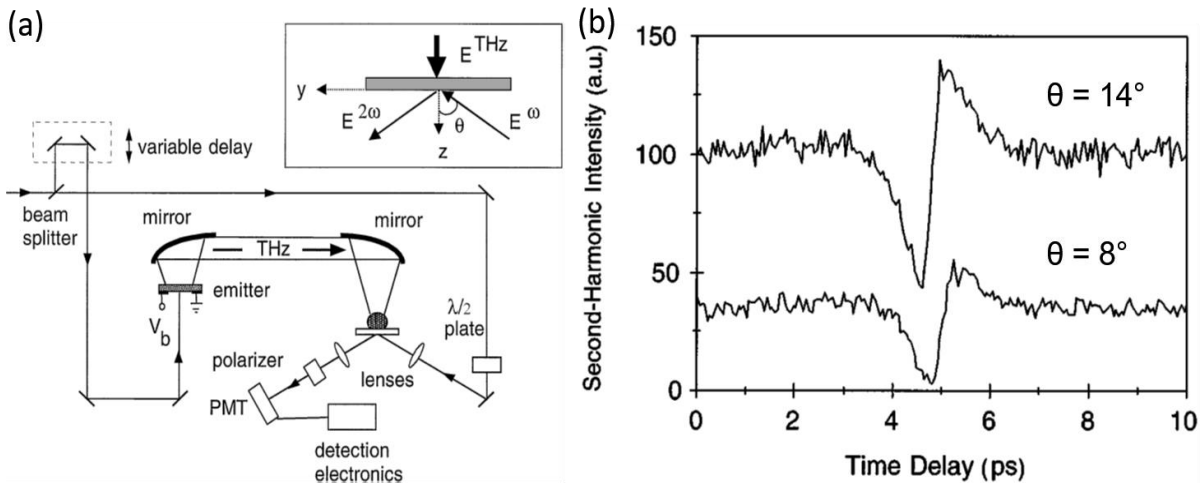


**Figure 3.1.** (a) Sketch of the experimental set-up employed to demonstrate TFISH in amorphous silicon. Note in the inset the geometrical orientation of the THz, probe and SH beams. (b) Reconstructed bipolar THz waveform retrieved by means of the set-up in (a), for two different values of the angle  $\theta$ . (Figure adapted from Ref [66]).

this type of detection scheme driven by amplified laser systems only, which emit optical pulses with energy in the range 0.1-10 mJ. In order to pursue this target, we have first exploited the much higher third-order susceptibility featured by centrosymmetric solid materials, known to be up to six orders of magnitude larger than for common gases [63]. It is worth recalling that the very first experiment of optical second-harmonic generation induced by THz waves was presented by Nahata *et al.* in 1998 [66], followed by Cook *et al.* in 1999 [83]. However, while Cook *et al.* only reported incoherent TFISH generation achieved in thin pellicle of liquids embedded within pairs of glass or polymeric windows, Nahata's work is somehow more

impactful. Indeed, they demonstrated TFISH generation from an amorphous silicon film deposited on a crystalline silicon substrate. In that experiment, due to the very good transparency of silicon, they sent the THz beam from the rear of the sample, while the probe beam was launched with a certain angle towards its top surface, as shown in Fig. 3.1(a). A further beam at the SH of the probe central frequency was then observed emerging from such a surface, modulated by the THz intensity. Furthermore, they were also able to reconstruct a bipolar THz transient, through the nonlinear mixing between the pure TFISH term and the background SH generated on the surface of the amorphous silicon [84], resulting in a homodyne mechanism similar to the one underlying the OBCD technique (see section 2.4). However, the detection was extremely limited in terms of SH intensity, THz bandwidth and SNR (see Fig. 3.1(b)), because of an insufficient interaction length, the latter occurring just near the surface of the sample and estimated to be narrower than 100 nm, i.e. close to the escape depth of the SH beam in silicon. For sake of completeness, we also cite that, Cornet *et al.* [85] demonstrated the possibility to induce TFISH in second-order materials, like ZnTe (which instead is commonly employed for EOS), via a phenomenon called Pockels-effect-induced second harmonic generation. This was achieved by a cascading process between the Pockels effect and the SH generation, which are both driven by the non-vanishing  $\chi^{(2)}$  coefficient associated to ZnTe crystals. However, this technique was still hampered by the same problems of EOS, i.e. the limited and heavily modulated spectral response of ZnTe crystals in the whole THz range.

The two examples of TFISH based on a solid-state material given above, introduce the main nontrivial issue that we also had to overcome while implementing our solid-state technique, i.e. the choice of a suitable nonlinear material. In fact, in order for the TFISH to be really efficient, the chosen material must be reasonably transparent to mainly three different frequencies: the fundamental and SH of the probe beam and that of the THz radiation. The fulfillment of this condition is challenging, because such frequencies fall in spectral ranges, which are quite apart from each other, where generally materials manifest different properties and frequency responses. This circumstance becomes even more crucial if we consider that an ultra-broadband THz radiation corresponds to a spectrum covering more than two decades, where usually materials do not show a constant frequency response. In 2013, Clerici *et al.* [86]–[88] demonstrated TFISH generation in both single- and polycrystalline bulk diamond samples, the

thicknesses of which were varied in the range 50-500  $\mu\text{m}$ , in both a co- and counter-propagating geometry (referred to the traveling directions of THz and probe beams). In that work, they observed the occurrence of FWM between the THz and the NIR beams even for the case of collimated rather than tightly focused optical beams (see Fig. 3.2(a)), thus showing the occurrence of the nonlinear interaction in a solid-state material for much lower NIR peak intensities than those employed in the air case. Moreover, the absence of lattice resonances in diamond allowed for the unperturbed retrieving of THz pulses with spectra covering bandwidths as wide as 20 THz. Nevertheless, all these experiments only concerned the achievement of

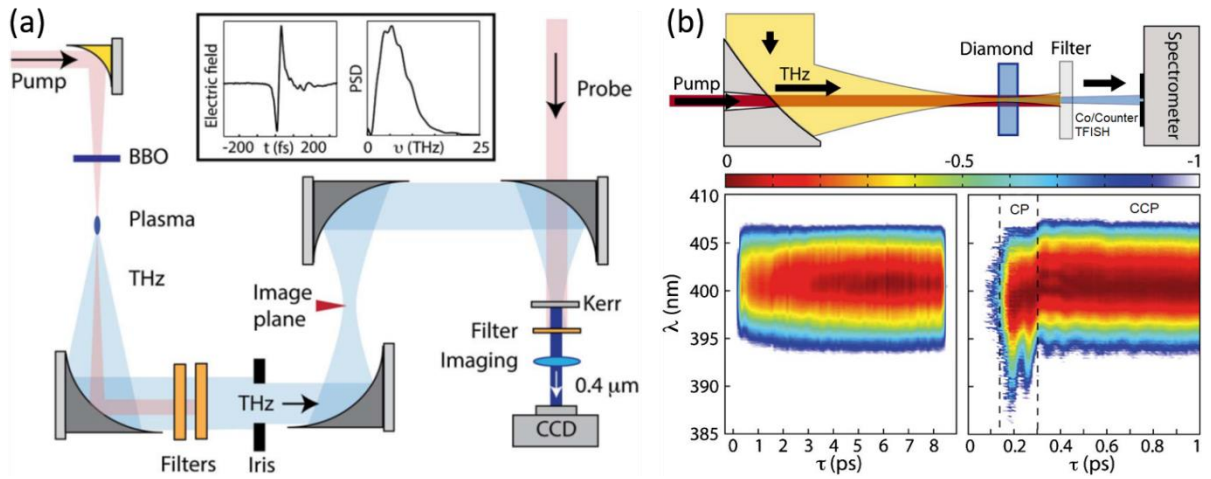


**Figure 3.2.** (a) Sketch of the experimental set-up employed to study the nonlinear interaction between ultra-broadband THz (generated by a two-color plasma source) and collimated NIR beams in diamond samples. The SH signal (0.4  $\mu\text{m}$ ) emerging from the crystal is separated from the fundamental beam by means of a proper filter and it is then sent to a CCD camera. The inset shows the single-cycle pulse and the corresponding spectrum associated to the THz pulses. (b) Top: particular of the detection stage. Bottom left: spectrogram showing the retrieved signal as a function of time and frequency. The signal is composed by two components, as better depicted in the zoom on the bottom right: one very short (around 200 fs) which is featured by a blue-shift spectrum due to the main TFISH term, and a second, long lasting (around 8 ps) term, which possesses a slightly red-shifted spectrum and it is ascribed to the counter-propagating interaction between THz and probe beams. (Figures adapted from Ref [87]).

incoherent TFISH, because of the inability of biasing the NIR-THz interaction inside the diamond crystal with an external AC electric field. Indeed, an important aspect to consider is the integration of metallic structures with the material so to directly deliver the bias voltage

necessary to carry out the heterodyne detection. Moreover, it is worth mentioning that, for relatively long crystals, part of the THz beam reflected back by the rear of the crystal, counter-propagates and interacts again with the probe beam (because of the high refractive index gap at the diamond/air interface). This further interaction gives rise to a second TFISH beam, which is featured by a long-lasting waveform (a few picoseconds), as shown in the spectrogram in Fig. 3.2(b), due to the nearly perfect phase-matching condition which THz and NIR beams satisfy in the case of counter-propagating nonlinear interaction. Since the second TFISH beam also travels towards the forward direction, it interferes with the main TFISH, thus preventing the potential implementation of an ultra-broadband detection scheme via this configuration. More generally, it can be shown that such an undesired counter-propagating effect is common for those materials, the THz refractive indices of which are relatively close in value to those at optical frequencies. One possible solution could then be the use of very thin crystals, the thickness of which is chosen in such a way that the pulse duration of the THz transient is longer than the time the pulse would take to complete a round-trip propagation inside the material, so not to give rise to any back propagating echo. However, besides the lower conversion efficiency achievable with smaller crystal thicknesses (i.e., reduced interaction length among all beams), the main drawback is that this choice would result in crystals as thick as a few tens of micrometers, which are quite fragile and difficult to handle, hampering the realization a practical and portable device.

### **3.3 A CMOS process-compatible material: Silica**

In order to address all the issues briefly discussed in the previous subsection, we have exploited the potentiality of the CMOS manufacturing process, i.e. a well-known fabrication technology, commonly employed in the realization of integrated electronic circuits. The CMOS process allows for the epitaxial growth of a number of dielectric materials, such as amorphous silicon, polysilicon, silicon dioxide and silicon nitride [89]. Since the enormous effort made in the development of such a technology, which is nowadays recognized to be the state-of-the-art for either micro- or nano-fabrication devices, the CMOS process represents a unique tool aimed at the realization of reliable and affordable integrated components. Another noticeable advantage of the CMOS process is that it enables the possibility to deposit metallic structures over the

dielectric material, e.g. with the shape of two metal pads separated by a single slit aperture, which can be directly exploited for the delivering of the bias voltage to operate the heterodyne scheme. Incidentally, we anticipate that the slit size can be made very narrow with a sub-micrometric precision, thus resulting in a peculiar interaction with the THz electric field, which can favor the TFISH generation, as will be detailed throughout the next Chapter. Therefore, the CMOS process-compatibility of our classes of detectors opens up to the simple implementation of the SSBCD technique by means of planar structures relatively easy to fabricate in large quantities, which also allows to cut down the cost of each finalized device. More in details, the

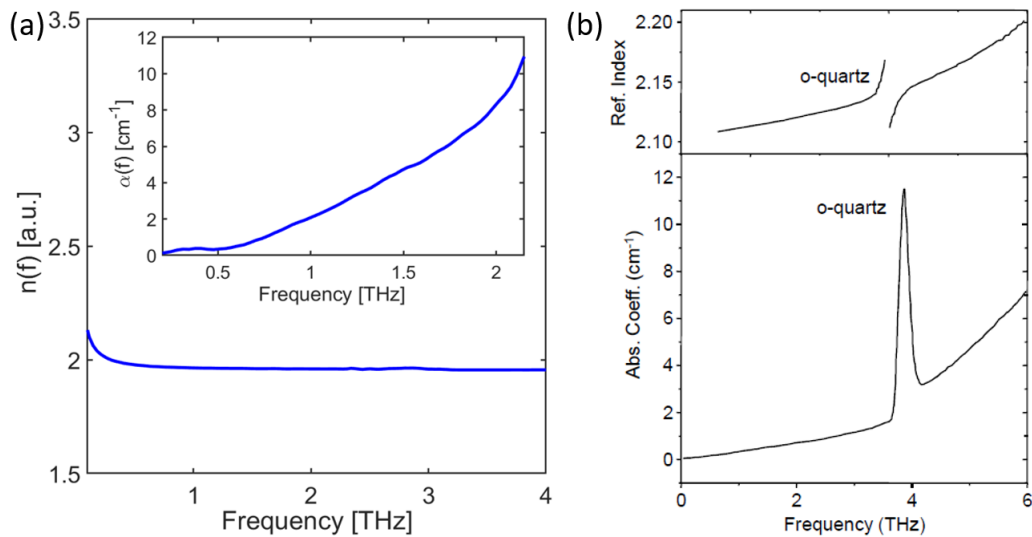


**Figure 3.3.** Comparison between refractive index and absorption coefficient of (a) fused silica and (b) UV-graded quartz (data taken from Ref [90]). The THz window is shortened to roughly 2 THz for the absorption coefficient of fused silica, because of the poor SNR, which prevents an accurate estimation of the losses beyond 2.2 THz.

first generation of SSBCD devices has been based on an epitaxial layer of amorphous silicon dioxide (silica), deposited via plasma-enhanced chemical-vapor-deposition technique (PEVCD), on a thick substrate of UV-fused silica. Before passing to the detailed description of the device structure, it is worth mentioning that silica has been already successfully employed in the THz range. For example, single (narrowband) or multilayer (broadband) interference films of silica have been employed as antireflection coatings in order to improve the THz emission from PC antennas realized on germanium or gallium arsenide substrate [91]–[93], the refractive indices of which ( $n_{Ge} = 4$  and  $n_{GaAs} = 3.63$ , respectively) are close enough to the square

of the corresponding value for silica ( $n_{SiO_2} = 1.95$ ) [94]. Figure 3.3 shows a comparison between the optical properties of fused silica and quartz, which are the amorphous and crystalline forms, respectively, of the same substance, i.e. silicon dioxide ( $SiO_2$ ). In particular, the data shown in Fig. 3.3(a) have been retrieved from a 2-mm-thick sample of fused silica, by means of our THz-TDS set-up involving OR and EOS in ZnTe crystals, whereas the curves in Fig. 3.3(b) have been taken from Ref. [90]. We notice that the low refractive index of silica with respect to that of high resistivity silicon ( $n_{Si} = 3.41$ ) is actually achieved at the price of higher absorption, above all in the high-frequency range (not shown in the plot). It is interesting to note that the absorption coefficient for silica is slightly higher than that of quartz, since, for the former material, the absence of an ordered structure facilitates the coupling of the THz frequencies with multi-mode lattice vibrations [1]. However, as it will be explained in the following sections, the thickness of the layer of silica deposited onto our devices is in the order of micrometers only, hence the losses due to the absorption in such a subwavelength-sized film may be completely neglected. Conversely, we stress that quartz cannot be practically employed in our case, because it is affected by a strong absorption line around 3.87 THz, which prevents its use for ultra-broadband applications [90]. As a nonlinear material, silica possesses a third-order susceptibility ( $\chi_{SiO_2}^{(3)} \sim 2 \times 10^{-22} \text{ m}^2/\text{V}^2$  [63], [95]), that is around three orders of magnitude higher than that of air ( $\chi_{air}^{(3)} \sim 1.68 \times 10^{-25} \text{ m}^2/\text{V}^2$  [82]) and other similar gases. However, such a high value does not simply correspond to a six orders of magnitude higher ( $I_{TFISH} \propto (\chi^{(3)})^2$ ) TFISH intensities, as one would expect compared to ABCD. At first instance, this is because silica cannot withstand the same optical beam intensities employed in standard ABCD. In addition, the length of the interaction region between THz and the probe beams in silica cannot be extended to the same sizes of the air case (i.e., few millimetres, limited by the THz Rayleigh length), because of some strict constraints, mainly related to the larger dispersion associated to silica, which affects the phase-matching condition in the FWM process. On the other hand, we highlight that the dielectric strength of UV fused silica is  $\sim 30 \text{ MV/cm}$  [89], [96], that is definitely higher than the low value of  $30 \text{ kV/cm}$  in air. This means that it is possible to apply elevated bias electric fields to the interaction before breakdown in the material occurs, so to significantly amplify the heterodyne signal and consequently improve the DR.

### 3.3.1 Simulations of the static electric field

As already mentioned above, one of the main advantages of any class of the SSBCD device is that it confines the bias electric field inside the slit region when the voltage is applied to the gold electrodes. Since the size of the slit is in the order of a few micrometers, the resulting bias field can reach very high values. On the one hand, this feature can effectively enhance the amplitude response of the heterodyne detection mechanism occurring in the SSBCD. On the other side, we have to guarantee that the bias electric field does not spread too much inside the

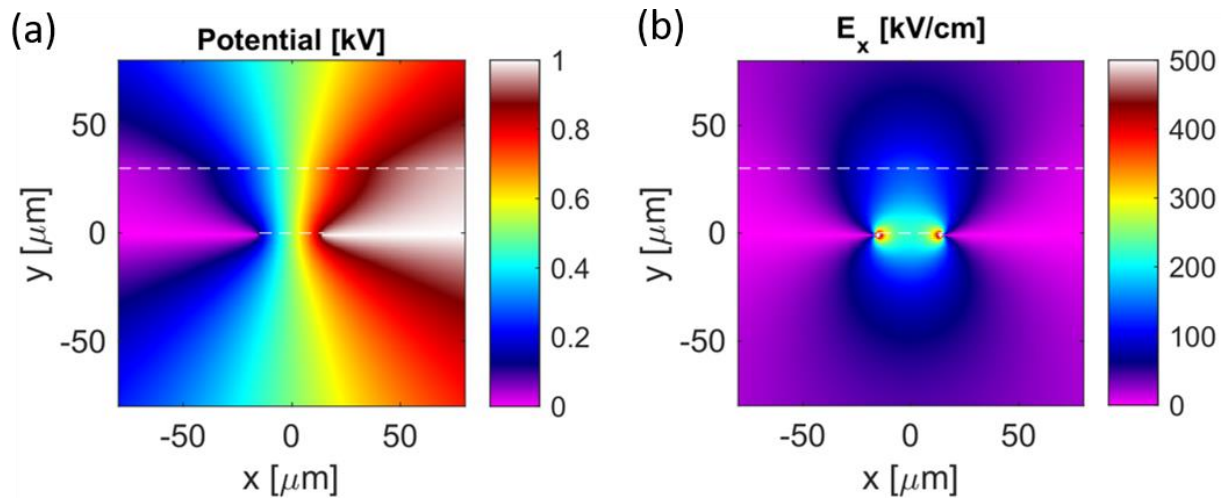


**Figure 3.4.** Simulations of the bias electric field distribution via a Finite Difference Method algorithm. The Laplace’s equation is solved for the static voltage in the case of the 30- $\mu\text{m}$ -wide slit biased with 1 kV, applied to the contacts. The static potential is shown in (a), whereas the static electric field along the x-axis (calculated as the gradient of static potential in (a)) is plotted in (b). The latter reveals that the bias field is mainly confined across the slit embedded in the silica cover layer (the dashed white lines indicate the interface between silica and air).

air immediately above the silica cover layer, which otherwise would trigger discharge, already at relatively low bias fields, thus nullifying the benefit brought about by the higher dielectric strength of silica. At first instance, the thicker the cover layer, the higher the voltage we can apply to the contacts. However, we have to keep in mind that the cover layer is detrimental for the THz field, since it first induces reflection losses (of around 10% in terms of power) and also, among others, limits the capability of the metallic slit to gather the THz beam, as will be better

described later in the text. Therefore, in order to investigate the distribution of the applied bias field across the micro slit device and establish an optimum value for the cover layer thickness, we numerically solved Laplace's equation for the bias potential via a finite difference method (FDM) [97]. In particular, in our simulations, we used a  $150 \times 150 \mu\text{m}^2$  domain surrounded by perfectly matched layers to cancel out spurious reflections from the boundaries. Since we are treating a simple DC case, we considered the gold electrodes, 160-nm-thick and separated by a 30- $\mu\text{m}$ -wide pure silica gap, to be featured by an infinite conductivity, whereas we neglected the presence of the Cr layer. We also assumed that the gold pads were biased with a voltage equal to 1 kV, still quite close to values commonly used for the ABCD case. We then carried out some simulations by varying the thickness of the silica cover layer, the dielectric constant of which was fixed at  $\epsilon_{\text{SiO}_2} = 3.5$ , that is a typical value for PECVD-grown silica [89]. The result of such an investigation is shown in Fig. 3.4, where a 30- $\mu\text{m}$ -thick silica layer was used. The distribution of the static potential and the corresponding bias electric field calculated as the gradient of the potential are reported in Fig. 3.4(a) and (b) respectively. One can note that the bias electric field is indeed strongly localized across the slit gap and is mainly x-polarized, i.e. parallel to both the THz and the optical probe polarizations. However, the field also extends some tens of micrometers along the y-axis, until the border between silica and air, highlighted by the white dashed line. We note that the electric field values immediately above the air interface are slightly lower than 100 kV/cm, which means that the voltage of 1 kV would theoretically result in discharge in air, for this set of layout parameters. Indeed, this type of simulation is only accounting for linear effects, while the breakdown of a material is a highly nonlinear effect, which cannot be predicted under these simplifications. We stress the fact that this circumstance does not affect the device itself, since it essentially occurs outside the device, but prevents its normal operating conditions, because the white light generated by the discharge would blind the photomultiplier tube downstream. However, we note that the electric field values within the silica region in between the metal pads are extremely high, approaching 500 kV/cm and remaining of the same order of magnitude all around the slit edge. Such values are more than 20 times higher than those applicable in air. Moreover, since we are no longer interested in employing bias voltages as high as those seen for standard ABCD, this simulation suggests that we can relax the requirements for the high voltage amplifier, limiting the bias

voltage in the order of hundreds of volts. For this reason, we ended up with a sort of rule of thumb for the design of our device, which establishes that the *slit width (gap size) must have a value equal to the cover thickness*. Indeed, the results of the simulation are scalable with the size of the slit. For example, by shrinking the size of the slit to only 3  $\mu\text{m}$ , the cover silica layer can be reduced to the same thickness value, maintaining an high electric field close to the slit, by applying even lower bias voltages. This choice enables to still operate the SSBCD with high bias electric field, yet avoiding the ionization of the overhead air region.

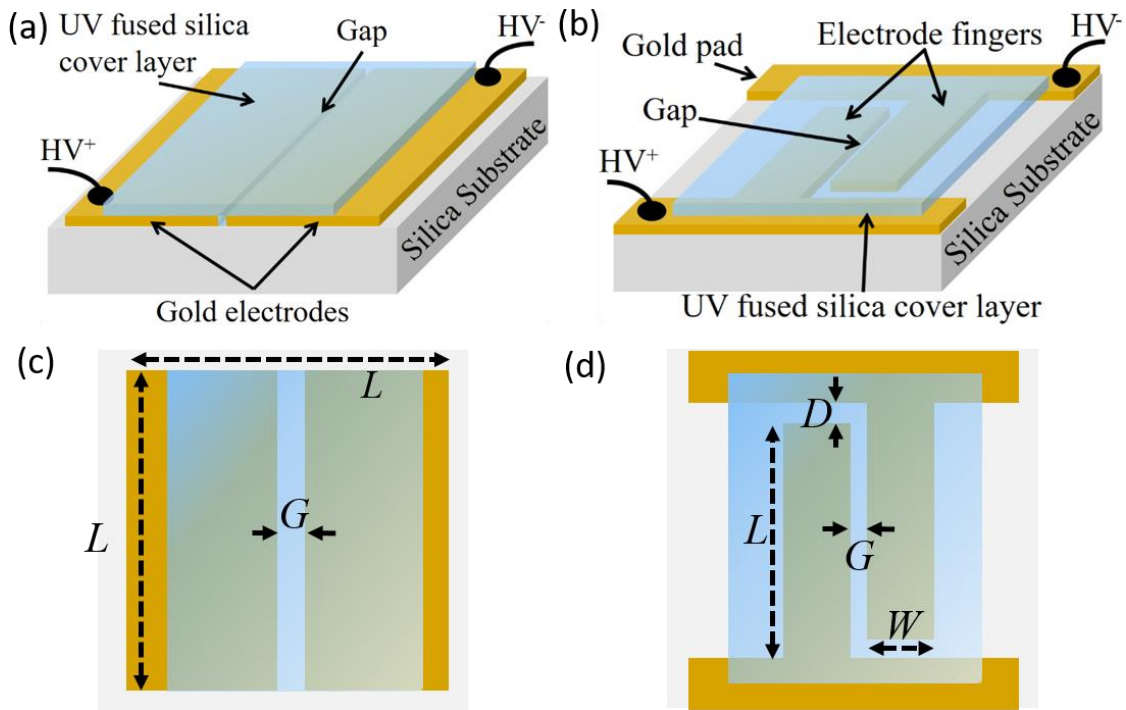


**Figure 3.5.** 3D Sketch of the (a) first and (b) second generation of the SSBCD devices based on silica films; (c) and (d) are the top views of the structures in (a) and (b), respectively, showing all the design parameters (see also the main text). The first generation consists of a single 30- $\mu\text{m}$ -wide slit ( $G$ ) between two longitudinally infinitive (very large  $L \gg \lambda$ ) gold contacts, covered by a 30- $\mu\text{m}$ -thick silica cover layer. The second generation consists of an interdigitated metallic structure, made up by two gold fingers, whose width ( $W$ ) is a parameter of study, as well as the gap size corresponding to the subwavelength slit ( $G$ , in the order of  $\sim \mu\text{m}$ ). The length of each finger ( $L$ ) is fixed at 2 mm for each configuration, whereas  $D$  corresponds to the distance between the finger and the opposite contact. This is equal to 10  $\mu\text{m}$ , for every layout, in order to be larger than any gap size. Both classes of devices are biased with a bipolar High Voltage (HV) source.

### 3.3.2 SSBCD device microfabrication

In light of these introductory considerations, we have designed the two main structures depicted in Fig. 3.5, which have been fabricated within the facilities of the Laboratoire de Micro et Nanofabrication (LMN), located at the Institute National de la Recherche Scientifique – Énergie Matériaux et Telecommunications (INRS-EMT). In particular, based on their dimensions, we refer to the first-generation device as micro-slit (Fig. 3.5(a)), whereas the second generation has been named “sub-wavelength ( $\lambda$ ) slit” (Fig. 3.5(b)). The micro-fabrication process for both the

Generation	Electrodes type	Slit width (silica gap size)	Cover layer thickness	Electrodes size
First (micro-slit)	Pads	30 $\mu\text{m}$	30 $\mu\text{m}$	5x5 mm <sup>2</sup>
Second (sub- $\lambda$ slit)	Fingers	3, 4, 5 $\mu\text{m}$	3 $\mu\text{m}$	2 mm x 10 $\mu\text{m}$ 2 mm x 100 $\mu\text{m}$

**Table 3.1.** Layout parameters featuring the first and second generation of silica-based SSBCD devices.

devices is similar. The micro-slit consists in the sputtering deposition on a 2-mm-thick UV graded fused silica substrate of a 30-nm-thick layer of chromium (Cr) followed by 100-nm-thick layer of gold and another 30-nm-thick layer of chromium. Such Cr layers are essential to ensure a proper adherence of the metallic pads to the bottom and top silica material (substrate and subsequently deposited layer). The electrodes are then defined by direct-write laser lithography and wet etching techniques, in order to form a gap between them, being their width  $30 \pm 3 \mu\text{m}$ . Subsequently, a 30- $\mu\text{m}$ -thick layer of fused silica is deposited by PECVD within the gap and over part of the electrodes (with a thickness tolerance of around 10%). The pads intended for connection of the system to the voltage source are covered with pieces of silicon during PECVD deposition in order to leave them intact. The sub-wavelength slits feature a slightly different fabrication step. Its electrodes and smaller gaps are patterned using direct-write laser lithography on a 1.5- $\mu\text{m}$ -thick photoresist, followed by a standard lift-off process instead of wet-etching (Cr/Au/Cr layers of 15nm/90nm/15nm, respectively, are deposited by e-beam evaporation and samples are soaked into a solvent for few hours to fabricate the

interdigitated electrodes). The silica cover layer is only 3- $\mu\text{m}$ -thick in this case. Three devices, featured by 2-mm-long, 10- $\mu\text{m}$ -wide fingers and different gap sizes of 3, 4, 5  $\mu\text{m}$ , have been fabricated and tested. The fourth sample, featured by 2-mm-long, 100- $\mu\text{m}$ -wide fingers and a gap of 3  $\mu\text{m}$  has also been characterized. In all samples, the distance between the tip of the gold finger and the contact pad of the other electrode is fixed at 10  $\mu\text{m}$ , larger than any other gap size. Table 3.1 briefly summarizes all the types of fabricated SSBCD devices.

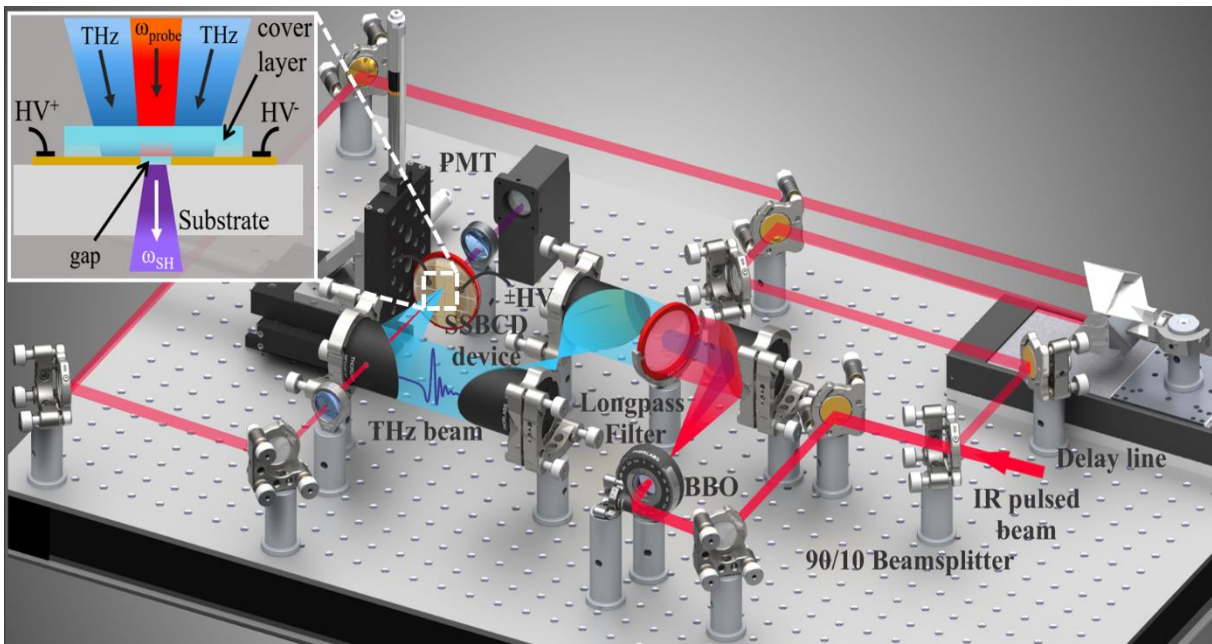


**Figure 3.6.** Sketch of the ultra-broadband THz-Time-Domain Spectroscopy set-up operating in the ultra-broadband regime. THz pulses are obtained via a two-color plasma technique, i.e. by mixing the pump beam and its SH (obtained from a BBO crystal) at the air plasma channel. A 90° off-axis parabolic mirror collimates the THz beam, whereas a high resistivity 0.5-mm-thick silicon wafer acts as long pass filter, blocking the residual SH and IR beams. THz radiation is then focused along with the probe beam into the SSBCD device, the latter placed on the focal plane of the last parabolic mirror. Detection is performed by mixing the temporally overlapped THz and probe pulses. According to the SSBCD paradigm, an SH beam proportional to the THz electric field strength is detected by a PMT, connected to a lock-in amplifier synchronized with the modulation frequency of the bias voltage. The whole set-up is purged with nitrogen. The inset shows in details the focusing of the probe and THz beams.

### 3.4 Ultra-broadband THz time-domain spectroscopy set-up

With the aim of demonstrating the potential of the SSBCD detector in the ultra-broadband regime, we carried out several characterizations via our THz-TDS set-up [98], shown in Fig.3.6 and featuring a 10-THz-wide source. In this case, ultrashort, high-energy THz pulses have been generated via an ultrafast laser-induced two-plasma technique (see Appendix A for a detailed description of the generation mechanism). The experiment implies the use of a train of NIR pulses (800 nm, 160 fs, 2.2 mJ, 1 kHz) generated by a Ti:Sapphire regenerative amplifier laser system (Spitfire Pro, Spectra-Physics). The pump and probe beams are obtained by means of a

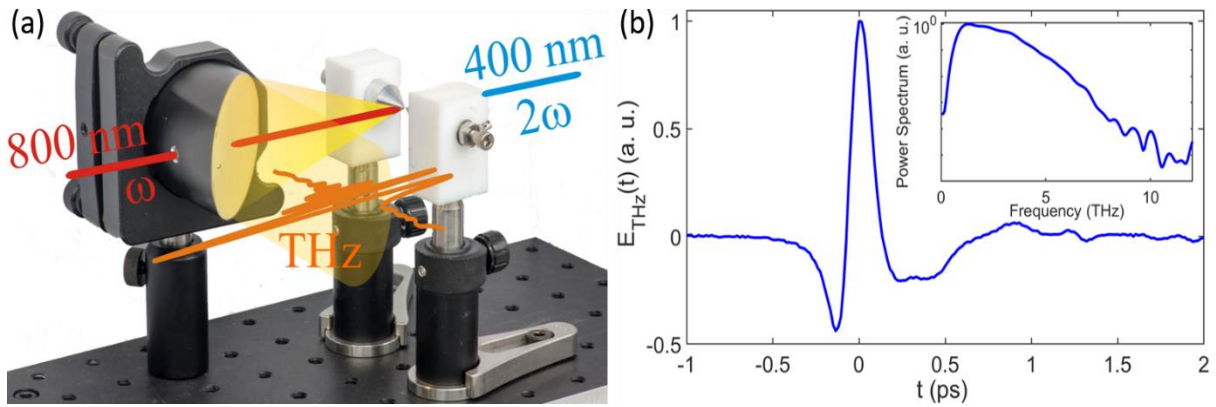


**Figure 3.7.** (a) Pictorial representation of the implementation of the ABCD technique in our ultra-broadband THz-TDS set-up. The probe beam passes through a hole made in the center of the parabolic mirror and it is focused together with the THz beam. Two metallic tips connected to the high voltage source, bias the nonlinear interaction and the generated SH travels towards the optical detector (PMT). (b) Typical THz waveform recorded via ABCD when a two-color plasma source is employed.

90/10 beam splitter. On one arm, THz pulses are emitted by the transient photocurrents excited with a two-color field [99]–[102]. The latter is generated by focusing the 1-mJ-pump beam through a 4-inch silver off-axis parabolic mirror, spatially and temporally overlapped with its SH. To this purpose, frequency doubling of the pump beam is obtained via a 100- $\mu\text{m}$ -thick type-I beta barium borate ( $\beta$ -BBO) crystal placed about 1 cm in front of the laser spot where the plasma is formed. The longitudinal position and the angle of the BBO crystal have been experimentally adjusted in order to maximize the generation yield. A 500- $\mu\text{m}$ -thick high-resistivity ( $>10\text{ k}\Omega$ ) silicon wafer is inserted in the THz path, acting as a long pass filter so to reject both the residual near IR pump and second harmonic. A series of 90° off-axis parabolic

mirrors manage the THz beam so to have a first focus point suitable for spectroscopic applications, while the second focus position is exploited for detection. On the other arm, the 100- $\mu$ J-probe travels through a back-reflector mounted on a motorized delay line, which is moved in order to change the delay between THz and probe pulses. We first carried out THz detection via standard ABCD by focusing the probe beam by means of a 150-mm-lens, placed behind the last 2-inch parabolic mirror provided with a 5-mm-hole on its center, so to ensure the spatial overlap between THz and probe beams, as shown in Fig. 3.7(a). This allows avoiding the use of a 45°-tilted pellicle for inserting the probe beam in the THz path, since such a configuration often introduces fluctuations of the probe intensity due to the high sensitivity of the 4- $\mu$ m-thick pellicle to environmental turbulences. The focal spot of the probe beam was estimated to have a  $1/e^2$  diameter of around 36  $\mu$ m. The bias electric field was applied to the focal region by means of two tip electrodes separated by an air gap of 1.5 mm and connected to an AC modulated (square wave), bipolar high voltage source (HVA series from Advanced Energy), providing a 2.5 kV peak-to-peak square wave. The nonlinear interaction causes the generation of the SH signal, which travels towards a photomultiplier tube (PMT) provided with a bandpass filter centered at 400 nm (necessary to filter out the residual NIR probe beam). The electric signal is then acquired by a lock-in amplifier synchronized with the bias modulation frequency (500 Hz, i.e. half of the THz repetition rate), which rejects the incoherent terms. The measurements were carried out by scanning the relative delay between the THz and optical probe beams, which led to a noticeable change of the SH signal once temporally overlapped. We used a customized software, running in MATLAB© environment, to drive the delay line. The reconstructed quasi single-cycle THz waveform is shown in Fig. 3.7(b), whose envelope lasts around 240 fs. The inset shows the FFT-evaluated power spectral density (PSD), which demonstrates an ultra-broadband capability up to 10 THz. For the above experimental conditions, the DR was estimated to be around 500. We have also measured the THz electric field peak at the detector position, by adopting the technique suggested in [98], [103], i.e. by using the following formula:

$$E_{THz}(t) = \frac{E_m(t)}{\max(|E_m(t)|)} \sqrt{\frac{2\eta_0 U}{\int_{-\infty}^{\infty} G(x,y) dx dy \int_{-\infty}^{\infty} \frac{|E_m(t)|^2}{\max(|E_m(t)|^2)} dt}} \quad (3.59)$$

where  $E_m(t)$  is the THz waveform in Fig. 3.7(b),  $G(x,y)$  is the transversal profile of the THz beam on the focal plane and  $U$  is the energy carried by the THz pulse. The THz spot was imaged by means of a THz camera (MICROXCAM-384I-THz), whereas the recorded data were fitted through a 2D Gaussian profile, which reads as:

$$G(x,y) \propto \exp\left(-\frac{x^2}{w_x^2}\right) \exp\left(-\frac{y^2}{w_y^2}\right) \quad (3.60)$$

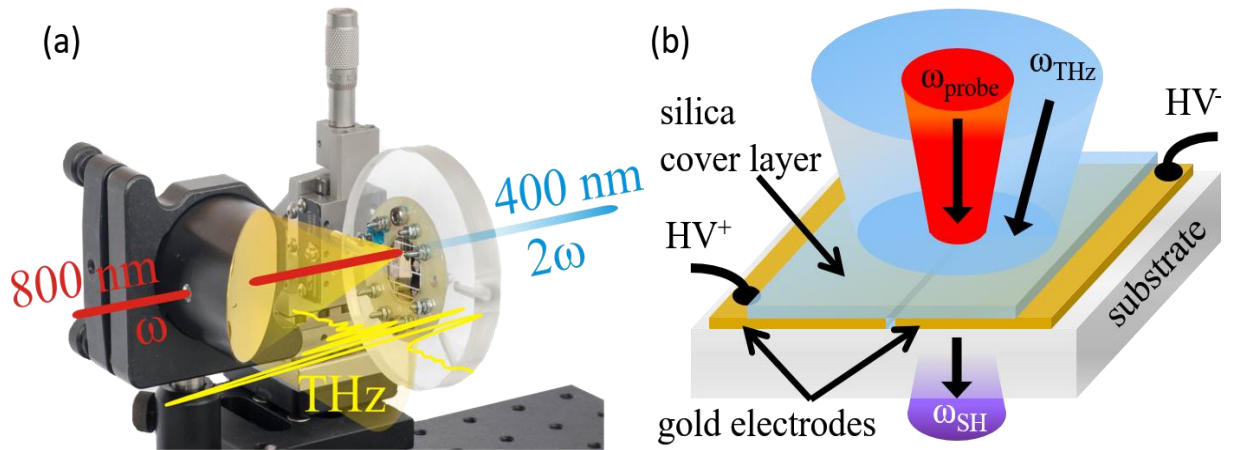


**Figure 3.8** (a) Pictorial representation of the SSBCD device at the detector position in our ultra-broadband THz-TDS set-up. A 3D translation stage allows for the correct alignment of the micro-slit in the focal plane of the parabolic mirror. (b) Operating principle of the SSBCD device: both THz and probe beams are focused onto the silica gap in between the two biased gold electrodes. The generated SH beam is emitted from the region where THz, probe, and bias electric fields interact, eventually emerging from the rear of the SSBCD device.

where  $\eta_0$  is the vacuum impedance ( $377 \Omega$ ), the two waist sizes were estimated to be  $w_x = 115 \pm 35 \mu\text{m}$  and  $w_y = 145 \pm 35 \mu\text{m}$  (see Appendix A). The energy was estimated to be  $U = 10 \pm 1 \text{ nJ}$ , by means of THz bolometer (THZ5I-BL-BNC). By inserting this data into Eq. (3.60), we have estimated a THz electric field peak of  $E_{THz}^{peak} \approx 50 \text{ kV/cm}$  at the detector position.

### 3.5 Characterization of the first generation of SSBCD devices

For the operation of the SSBCD technique, we have replaced the two tip electrodes with our device, as shown in Fig. 3.6, and attenuated the probe power in order not to damage the device. In particular, we recall that for ABCD the average probe power was fixed at 100 mW, whereas for SSBCD it has now been lowered to 100  $\mu$ W. Those values correspond to an energy of 100  $\mu$ J and 100 nJ, respectively, for a laser repetition rate of 1 kHz. We highlight that we have left the same focusing lens for the probe beam in order to better compare SSBCD and ABCD performance, under the same focusing geometry. The whole wafer that we have investigated consisted of a stack of micro-slits, and was mounted on the holder shown in Fig. 3.8(a). The holder, in turn, has been placed on a 3D mechanical translation stage in order to finely adjust the position of the micro-slit on the mirror focal plane. Figure 3.8(b) represents the operating principle underlying the SSBCD method. The co-propagating THz and probe beams are focused onto the slit between the two metal pads. The alignment of the two spots is achieved by independently adjusting the 3D stage holding the SSBCD sample and the focusing lens of the probe beam, along the three directions. We note that the spot of the THz is strongly frequency-dependent, as longer wavelengths are being focused on larger spot sizes [104], which are always larger than for the probe beam. Therefore, the behavior of the slit is slightly different whether illuminated by the THz or probe beam. Indeed, for the latter, the spot size has comparable size with the slit ( $\sim 30$   $\mu$ m) used in the first-generation set of samples, thus the probe beam passes through the device with minimum perturbation. Instead, after passing through the silica cover layer, the larger THz beam mostly impinges on the metal pads, which behave as a mirror, reflecting back a significant amount of the THz power. However, since the THz wave polarization is orthogonal to the long side of the slit (L), the THz beam is somewhat gathered within the silica filling the slit, thus inducing EFISH generation. We stress that the THz and bias electric field polarizations must be parallel to efficiently operate the SSBCD technique. Since the metal pad geometry automatically sets the orientation of the bias field (i.e. orthogonal to the internal walls of the gold electrodes), the THz polarization has to be adjusted accordingly. The gold electrodes of the slit device are then connected to the bias voltage generator to create the heterodyne signal. Finally, the SH beam emerging from the rear of the device is collimated

by a 2-inch-UV-fused silica lens (as shown in Fig. 3.6) and sent to the PMT, as for the ABCD case. We have studied the time and frequency response of our detector, by recording the THz transients as a function of the bias voltage and the probe energy.

### 3.5.1 Bias voltage dependence

The dependence of the SSBCD amplitude response in the time domain upon the bias voltage is shown in Fig. 3.9. In particular, we have fixed the probe energy at 500 nJ and applied a bipolar square wave voltage oscillating at 500 Hz, with the half peak ranging between 50-1050 V. Bipolar voltages are preferred against unipolar waves in order to decrease as much as possible the static ionization of air, which otherwise would result in a noisy offset term in the recorded

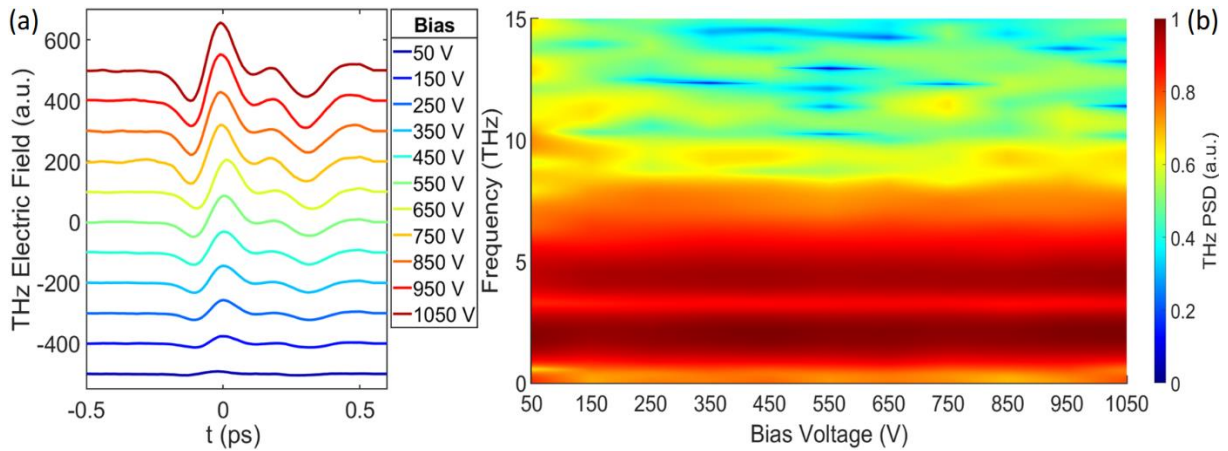


**Figure 3.9.** (a) THz waveforms recorded for the first generation of SSBCD devices as a function of the bias voltage in the range 50-1050 V. The curves are shifted along the y-axis for sake of clarity. (b) 2D color map reporting the THz bandwidth corresponding to the transients in (a), as a function of the bias voltage. The spectrum extends approximately until 10 THz. A frequency modulation is revealed at around 3 THz, where a notch featuring a relatively wide stopband appears, consistently with the multi-cycle nature of the THz pulses observed in (a).

waveform. Voltage values lower than 50 V did not allow to resolve the THz transient from the noise floor. The waveforms shown in Fig. 3.9(a) demonstrate that the effect of the bias electric field is to simply amplify the heterodyne signal, without distorting the shape of the THz pulses. We note that, conversely to what predicted by the simulations shown in section 3.4, we have been able to apply bias voltage slightly higher than 1000 V, before triggering discharge in the air above the slit. This is likely due to either the tolerance in the thickness of the deposited cover

layer or a different distribution of the electric field close to the silica-air interface, which could result in the lowering of the effective electric field outside the dielectric material. We would like to mention that after the occurring of the discharge (above 1100 V), we have checked the device by means of an optical microscope and no damage was observed over the whole structure. However, we have not tested the device at voltages higher than 1200 V, which could instead result in higher order breakdown phenomena and possibly have permanent detrimental effects onto either the silica layer or the metal structure.

The THz pulse retrieved via the first generation of SSBCD devices features a multi-cycle shape that is different from the ABCD reference (see Fig. 3.7(a)), and reflects into the modulation of the FFT-evaluated spectrum, shown as a color map in Fig. 3.9(b) for each bias voltage. We can notice the presence of a notch frequency around 3.3 THz. This can be easily ascribed to an etalon effect establishing between the silica-air interface and the metal pads underneath, acting as a mirror. As a matter of fact, the time interval taken by the main pulse to travel one way through the silica thickness is around 200 fs, which is shorter than its pulse duration. Hence, the silica cover layer acts as a cavity. We recall that the thickness of such a layer is around  $T = 30 \mu\text{m}$  in this case and is comparable with the wavelength of the THz radiation in silica (i.e.,  $\lambda_{\text{SiO}_2} = \lambda_{\text{vacuum}} / n_{\text{SiO}_2}$ ). Hence, by taking into account that the slit is completely buried into the silica cover layer, with a refractive index  $n_{\text{SiO}_2} \sim 1.95$  at THz frequencies (see section 3.3), we find out that a resonance builds up at the wavelength fulfilling the following phase relation in a complete round-trip:

$$\frac{2\pi}{\lambda_{\text{SiO}_2}} T = \pi \Rightarrow \lambda_{\text{etalon}} = 2n_{\text{SiO}_2} T \approx 117 \pm 12 \mu\text{m}, \quad (3.61)$$

where we have also considered the 10% of tolerance affecting the layer thickness value. Such an etalon wavelength indeed corresponds to a frequency of approximately 2.7 THz, in good agreement with what observed on the PSD curves in Fig. 3.9(b). More in detail, a closer look at Fig. 3.9(a) reveals that the waveforms can be regarded as the merge of a first main pulse (similar to the quasi single-cycle retrieved for the ABCD) and its delayed echo that has a flipped shape, consistent with a  $\pi$  phase change induced by the reflection occurring at the metal pads. This also explains the relatively large linewidth of the notch as a spectral artefact due to one single

repetition of the waveform in the time domain. In order to better highlight the dependence of the detected SH signal on the bias voltage, we have taken the peak of each curve in Fig. 3.9(a) and evaluated the corresponding DR, according to Eq. (3.61). The results of this investigation are reported in Fig. 3.10(a) and (b), respectively. The peak trend confirms the linear dependence on the bias voltage predicted by Eq. (3.61), in the whole investigated range. The ratio between the maximum and the minimum peak values is around 18 and represents a measure of the full dynamics of this device. The absence of a saturation effect approaching the maximum applicable voltage proves that the limiting factor is only due to the air discharge and not to the silica itself. On the other hand, Fig. 3.10(b) shows that the DR initially increases, reaching a peak around 450 V and then slowly decays, as the bias voltage spans the whole investigated

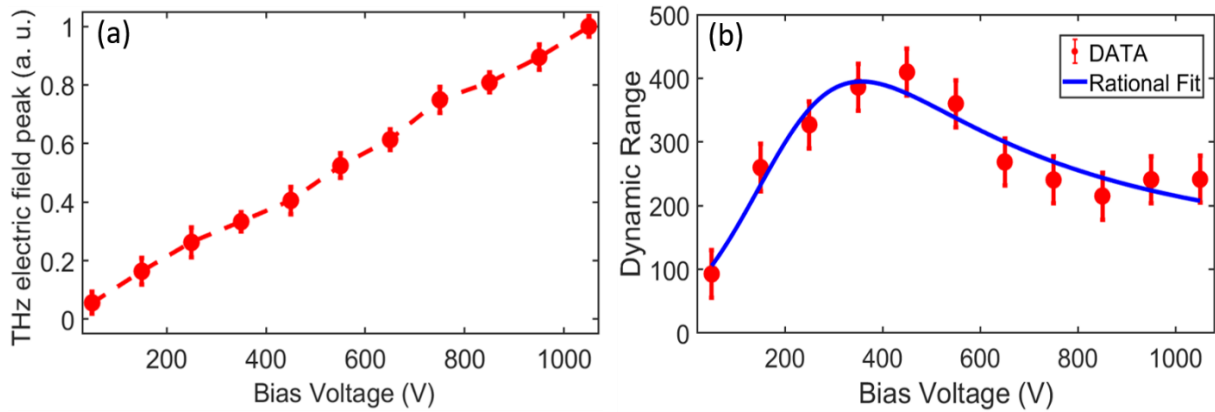


**Figure 3.10** (a) THz electric field peak as a function of the bias voltage. The trend perfectly reproduced the linear dependence predicted by Eq. (3.61). (b) Dynamic range (DR, red dots) evaluated for each data point in (a). The non-monotonic states in subdivision into two different noise regimes. The blue solid curve represents the best fit performed with a rational function, similar to Eq. (3.61). The error bars in both the plots are related to the SNR of the detection method.

range. This behavior somehow resembles the analytical dependence expressed by Eq. (3.61), as pointed out by the rational fit (blue solid line). Therefore, we can establish that for values lower than approximately 450 V, the noise is dominated by the NEP of the PMT. For higher values, the noise introduced by the high voltage amplifier takes over the other contributions, causing a noticeable decrease of the DR. To the best of our knowledge, this is the first experimental demonstration of the model analytically described by Eq. (3.61), since ABCD does not allow to apply enough bias voltage to cause the trend inversion observed in Fig. 3.10(b). The maximum

DR is around 400, which is close to that achieved for the ABCD case, under the same probe focusing condition and by employing the same voltage amplifier. It is worth mentioning that even if we are not exploiting the total THz power focused onto the SSBCD device (due to the 10% Fresnel losses and the narrow-slit aperture), the noise performance are not significantly degraded with respect to the ABCD technique, due to the strong amplification performed by the higher bias electric fields. Indeed, we notice that for a bias voltage of, e.g.,  $V_{bias} = 500$  V, the corresponding electric field across the slit is  $E_{bias}^{slit} = V_{bias} / G\epsilon_{SiO_2} \approx 48$  kV/cm, being  $\epsilon_{SiO_2} \approx 3.9$  the relative permittivity of fused silica [89] and assuming that the simple capacitor model holds for the real slit. Such a bias field value is indeed higher than that applicable in air ( $< 20$  kV/cm). Incidentally, we note that bias voltages in the order of 50 V already allowed to distinguish the

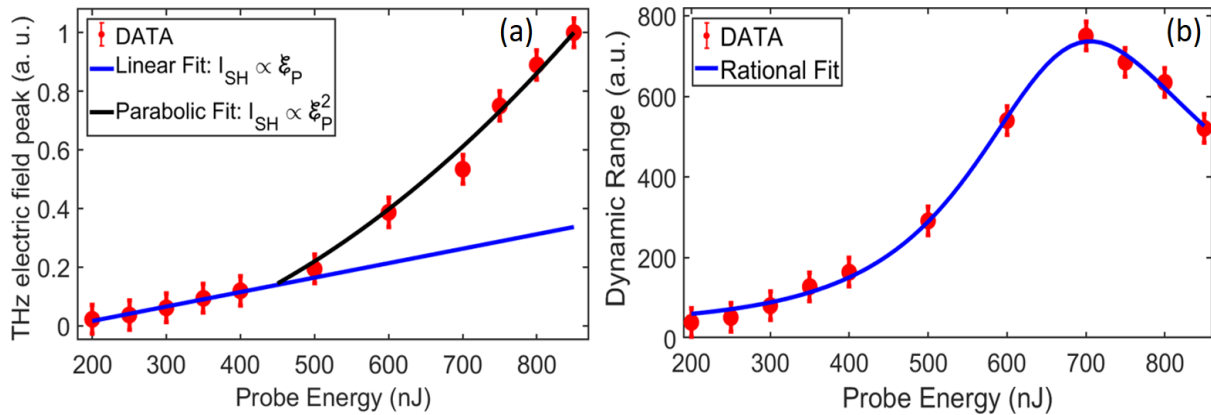


**Figure 3.11.** (a) THz electric field peak and (b) DR trends as a function of the probe energy. The blue solid line in (a) represents the linear fit for the data below threshold. The parabolic curve (black solid line) well fits the data once the FWM takes place (probe energy greater than 500 nJ). The THz peak values are normalized with respect to their maximum. The DR quickly increases as the energy overcome the threshold values, reaching 750, which was our best value for the first generation of SSBCD devices.

heterodyne signal from the noise floor, yet representing the first significant improvement of the SSBCD technique in terms of demanded electrical power.

### 3.5.2 Probe energy dependence

We have investigated the behavior of the SSBCD device in the probe energy range of 200-850 nJ, while fixing the bias voltage at 500 V. Similarly to what has been shown in the previous

subsection, for each reconstructed THz waveform we have taken its peak and evaluated the DR. The results are reported in Fig. 3.11(a) and (b). The first graph reveals an overall trend (red dots) that is not simply increasing with the second power of the probe energy, as it should be for the case of pure FWM ruled by Eq. (3.61). Rather, it can be divided into two regions, as pointed out by the two fitting curves. The black solid line reproduces the linear scaling of the THz signal with the probe energy until approximately 450 nJ, whereas the second-order polynomial curve fits well only the data retrieved for higher probe energies. This behavior was reproducible in several consecutive recorded datasets, hence we can ascertain that is not due to systematic errors in either measuring the employed probe energy or carrying out the detection mechanism. We believe that the reason behind this type of dependence could be ascribed to a sort of threshold, which the peak of the probe beam intensity has to overcome in order to

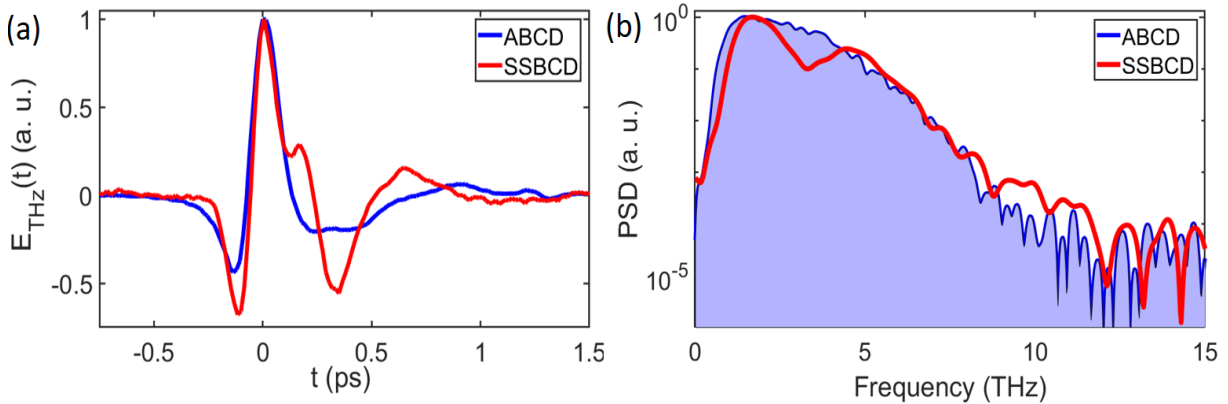


**Figure 3.12.** Comparison between the (a) THz electric field waveforms and (b) the Power Spectral Density (PSD), detected and evaluated for the case of ABCD (blue curves) and the first generation of SSBCD devices (red curves).

properly trigger FWM. For this type of SSBCD device, such a threshold is in the order of 500 nJ for a laser pulse duration of 160 fs, which is  $\sim 200$  times lower than that needed to operate the ABCD technique under the same focusing conditions of the probe beam (150- mm-lens). Since the resulting probe spot ( $\sim 36 \mu\text{m}$ ) on the focal plane is larger than the slit itself, we expect that by employing shorter focal length it would be possible to further relax the probe energy requirement and decrease the energy threshold. The DR trend shows that the noise performance strongly improves after crossing the probe energy threshold, reaching its peak of 750 around 700 nJ. The latter hence represents the optimum energy value in order to operate the SSBCD

with the best performance. The overall trend is quite similar to that seen in Fig. 3.9(b) for the bias voltage. However, here the degradation of the DR for relatively high energies is most likely due to the generation of white light in the silica cover layer, which represents an additional source of noise for the PMT and the contribution of which is not included in Eq. (3.61). On one side, higher probe energies resulted in the generation of randomly pulsing white light (supercontinuum generation [88]), visible to the naked eye, which completely hide the heterodyne signal within the highly unstable spike fluctuations. We mention that the exposition to energies higher than  $1.2 \mu\text{J}$  has completely damaged the gold metal pads and made a burned spot in the silica within the slit. On the other hand, energy values lower than  $200 \text{ nJ}$  have not allowed extracting the signal from the noise floor. Finally, Fig. 3.12(a) and (b) report an overall comparison between the results in terms of temporal transients and spectra achieved whether the THz pulse is reconstructed with either ABCD (blue curves) or the first generation of SSBCD device (red curves). Clearly, such a figure suggests that some issues are still present and that have to be properly addressed. However, we stress again that the first generation can be considered as a non-optimized prototype, being our goal the demonstration of the proof of concept underlying our detection technique. Indeed, as will be described later, the second generation has been designed with the aim of solving most of the limitations highlighted so far.

### **3.6 Characterization of the second generation of SSBCD devices**

The results achieved with the first device generation have revealed some crucial aspects that it is worth briefly summarizing in the following points, in order to better illustrate out the strategy we have subsequently followed to realize optimized (second generation) devices:

- 1) In order to properly detect ultra-broadband THz pulses, the thickness of the silica cover layer must be chosen sufficiently thin so to prevent the establishment of etalon echoes due to reflection from the metal pads, which otherwise would also appear in the detected waveform. This essentially means that the cover layer must feature sub-wavelength sizes.
- 2) The presence of a threshold energy is actually an undesirable condition, which can be easily overcome by tightly focusing the probe beam to smaller spot sizes.

- 3) The overall performance was only just comparable to that achieved via the ABCD technique, mainly due to the higher bias electric fields. Still, the benefit due to the higher nonlinearity of silica was not properly exploited. This arises from the fact that the optimum probe energy was just  $\sim 150$  times lower than that employed in the optimized ABCD case. However, the ratio between the third-order susceptibilities of silica and air is greater than three orders of magnitude ( $\sim 10^{-22}/10^{-25}$ ). This means that there is still room for improvement to attain higher conversion efficiencies.

Regarding the first point, the choice of a narrower cover layer thickness in the order of few microns accordingly implies the shrinking of the slit width  $G$ , so to fulfill the empirical rule that we have introduced in section 3.2. A narrower slit can be easily biased with high electric fields at lower bias voltage than those employed so far. As a first approximation, the bias electric field inversely scales with the slit width ( $E_{bias} \propto V_{bias} / G$ ). However, the effective area illuminated by the probe beam will also linearly decrease since we are acting on only one dimension ( $A_{SiO_2} = L * G$ ). This results in lower total SH power generated and emerging from the rear of the device. Hence, there should be a trade-off between the two conditions. This is the reason why we have realized and studied three types of SSBCD devices for the second generation, featuring different slit sizes. Moreover, since the interaction region is strictly confined to a sub-wavelength size, the particular interplay between the Rayleigh lengths of both THz and probe beam governed by Eq. (3.61) is no longer valid. Indeed, since the THz pulse cannot cross the focal plane along propagation when the SSBCD device is exactly aligned on the focus of the parabolic mirror, the THz beam does not experience a further  $\pi$  phase rotation due to the Gouy phase shift, allowing for a tighter focusing of both beams. However, while the focused THz spot size is ultimately limited by the large diffraction limit affecting long wavelengths, the probe focusing is eventually limited by the physical dimension of the 2-inch-diameter parabolic mirror. For this reason, the minimal focal length we have been able to employ for the next experiments was 10 cm, resulting in an optical spot size whose  $1/e^2$  diameter was around  $20 \mu\text{m}$ . Particular attention has to be paid instead to the issue implied by the third point. Until now, we have simply assumed that the FWM process occurring for the air case could be explained in terms of the same equations for the case of silica. However, this is only partially true, since the non-negligible

dispersion of silica (resulting in different refractive indexes at each optical wavelength) may significantly affect the phase-matching condition underlying the up-conversion process, as will be detailed in the following subsection.

### 3.6.1 Four-wave mixing in silica with THz radiation

We recall that, theoretically, the FWM interaction ruling the EFISH generation can give rise to two processes, namely sum-frequency (SFG) and difference-frequency (DFG) generation, which origin two new beams featuring a central frequency slightly higher and lower than the second harmonic (SH) of the probe beam, respectively:

$$\begin{aligned} DFG: \omega_{DFG} + \omega_{THz} &= 2\omega_P \\ SFG: \omega_{SFG} &= 2\omega_P + \omega_{THz} \end{aligned} \quad (3.62)$$

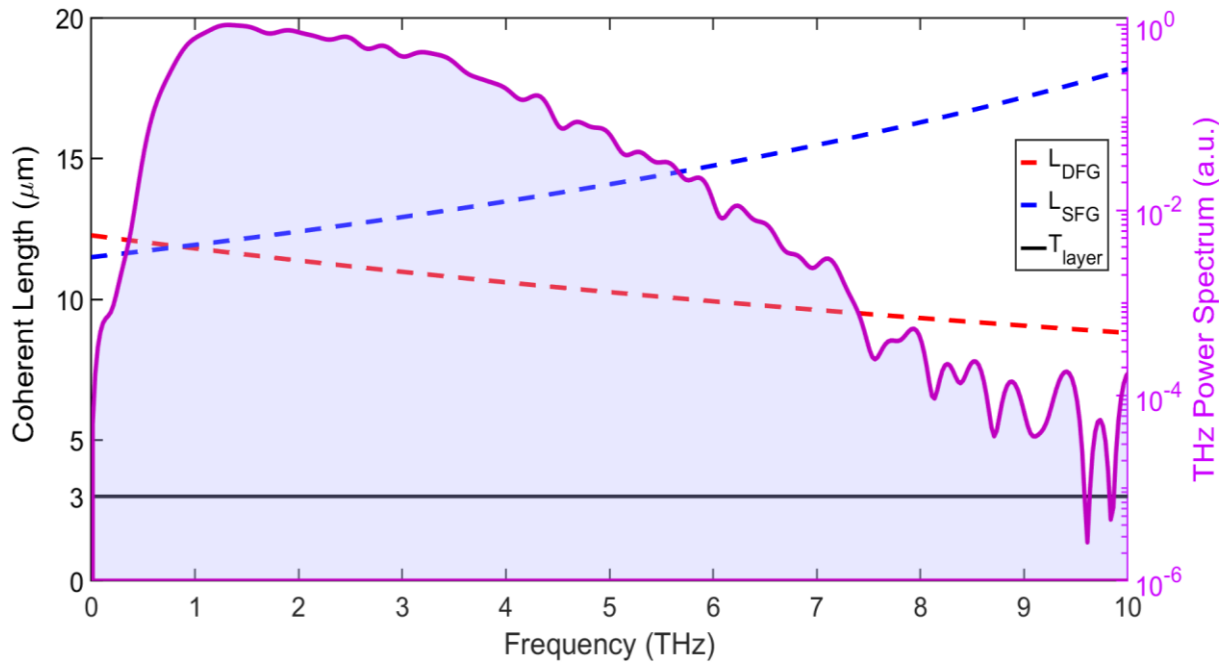


**Figure 3.13.** Coherent length curves corresponding to the four-wave mixing processes taking place in silica for the case of co-propagating THz and probe beam. The red dashed line depicts the difference-frequency generation (DFG) process, whereas the blue dashed line indicates the sum-frequency generation (SFG) process. For comparison purposes, the THz bandwidth reconstructed via the ABCD technique is plotted in purple, showing that the coherence length of both DFG and SFG is only  $\sim 12 \mu\text{m}$ , where the THz spectrum reaches its maximum. The black solid line indicates the thickness of the silica

cover layer ( $T_{\text{layer}}$ ) for the second-generation devices. The overlap length ( $OL \approx 123.4 \mu\text{m}$ ) between the two beams is two orders of magnitude longer than  $T_{\text{layer}}$  and is not shown for sake of simplicity.

We have established that for the ABCD case, the phase-matching condition associated to tightly focused Gaussian beams, favored the DFG process only. Instead, for the SSBCD case, we have to consider both the processes, because the interaction is happening very close to the focal plane, along a region much shorter than the Rayleigh length of both beams. Considering the case of a collinear interaction of planar monochromatic waves, the phase-matching condition reduces to a scalar equation for the involved wave-vectors, which are written as:

$$\begin{aligned} k_{SFG} &= 2k_P + k_T \Rightarrow \Delta k_{SFG} = k_{SFG} - 2k_P - k_T \\ k_{DFG} + k_T &= 2k_P \Rightarrow \Delta k_{DFG} = k_{DFG} - 2k_P + k_T \end{aligned} \quad (3.63)$$

where the subscripts  $P$  and  $T$  stand for the probe and terahertz frequency, respectively. As mentioned above, since silica is a dispersive medium, the two mismatch terms  $\Delta k_{DFG/SFG}$  are not the same, because the corresponding  $f_{DFG}$  and  $f_{SFG}$  are nominally different (by a factor dictated by the THz bandwidth). If we evaluate the coherence length defined as the ratio  $L_{coh} = \pi/|\Delta k_{DFG/SFG}|$  vs the THz frequency, we obtain the plot shown in Fig. 3.13, where the trend for the DFG and SFG processes are reported in red and blue dashed lines, respectively. It is well-known that  $L_{coh}$  expresses the maximum propagation length by which the energy from the fundamental beam is transferred to the new one generated by the nonlinear process. Beyond such a value, the process is reversed and the energy from the new beam is being transferred back to the fundamental one [63]. In other words,  $L_{coh}$  could be regarded as a figure of merit of the process. Notably, the SFG and DFG processes have a comparable coherent length in the case of co-propagating THz and probe beams, hence both coexist in silica. Here, the temporal phases are determined by  $2\phi_P + \phi_T$  and  $2\phi_P - \phi_T$ , respectively [87]. Therefore, the total signal generated by pure four-wave mixing process is generally given by the beating of the two DFG and SFG waves [87]. However, we note that  $L_{coh}$  for all the cases is always lower than  $20 \mu\text{m}$ , meaning that propagation lengths longer than such a value do not result in good conversion efficiencies. In light of this outcome, it is then clear the reason why the micro-slit covered by a  $30\text{-}\mu\text{m}$ -silica layer has not resulted in an optimum nonlinear interaction among the beams.

Another important fact that generally has to be considered is that the THz and probe beams are not continuous-wave, but pulsed. As such, they occupy a finite region in both space and time and travel at different group velocities, due to the different refractive indexes. This phenomenon is called *temporal walk-off* and is well-known in ultrafast Optics [63], [105]–[107]. In other words, such an effect indicates that two beams traveling in a dispersive medium will remain temporally overlapped only for a short time interval. This related overlap length (OL) can be evaluated by calculating the cross-correlation of the two pulses co-propagating inside silica. This calculus leads to the following analytical expression [87]:

$$OL = \frac{c\tau_T}{n_{g,T} - n_{g,P}} \quad (3.64)$$

where  $\tau_T$  is the THz pulse duration (defined as the full-width half maximum of the pulse envelope),  $c$  the speed of light and  $n_{g,T}$  and  $n_{g,P}$  the group refractive index at THz and probe frequency, respectively. The physical meaning of Eq. (3.64) is that after a propagation distance equal to OL, the pulses are no longer overlapped in time and, consequently, the nonlinear interaction stops, even in the case of infinitive coherent length. In our experimental conditions, the two-color plasma source emits THz pulses lasting around  $\tau_T = 240$  fs (recorded by ABCD techniques). From the data shown in Fig. 3.3, it is possible to recover the group refractive index at THz frequencies ( $\sim 2.05$ ), while the dispersion relation featuring fused silica in the optical domain can be easily found in literature, e.g. [108]. Therefore, by putting all those data in Eq. (3.64), it results that  $OL = 123.4 \mu\text{m}$ , which is much longer than the coherent lengths of both DFG and SFG process. This means that the temporal walk-off issue is not affecting our device, since the cover layer must have a thickness at least one order of magnitude narrower than the relative OL, in order to properly operate the SSBCD technique.

Finally, the main constraint in the design of the cover layer thickness is the etalon effect, which cannot be easily removed by keeping this type of layout. Indeed, antireflection (AR) coatings at THz frequencies are quite thick, in the order of tens of micrometers or more, because of the long wavelengths. Moreover, such coating layers are usually narrowband, which would result in an unwanted modulation of the SSBCD device frequency response. Broadband AR coating can be theoretically realized by growing a stack of dielectric materials with slightly different

refractive indexes [1]. Nevertheless, this condition does not meet the requirement imposed by the coherence length of the nonlinear process. However, since our goal is to achieve unperturbed, gap-free detection at least in a two decade-wide THz spectral windows, we have finally chosen a value of  $T = 3 \mu\text{m}$  only, for every device belonging to the second generation. This would eventually result in cavity resonances at frequencies  $>25 \text{ THz}$ , thus perfectly accomplishing the ultra-broadband capability of the structure. A photograph of the finalized structure is shown in Fig. 3.14(a).

### 3.6.2 Dependence on the slit width and electrode size

With respect to the device of the first SSBCD generation, we have fabricated several variants of the second generation, as summarized in Table 3.1. In order to establish the best combination

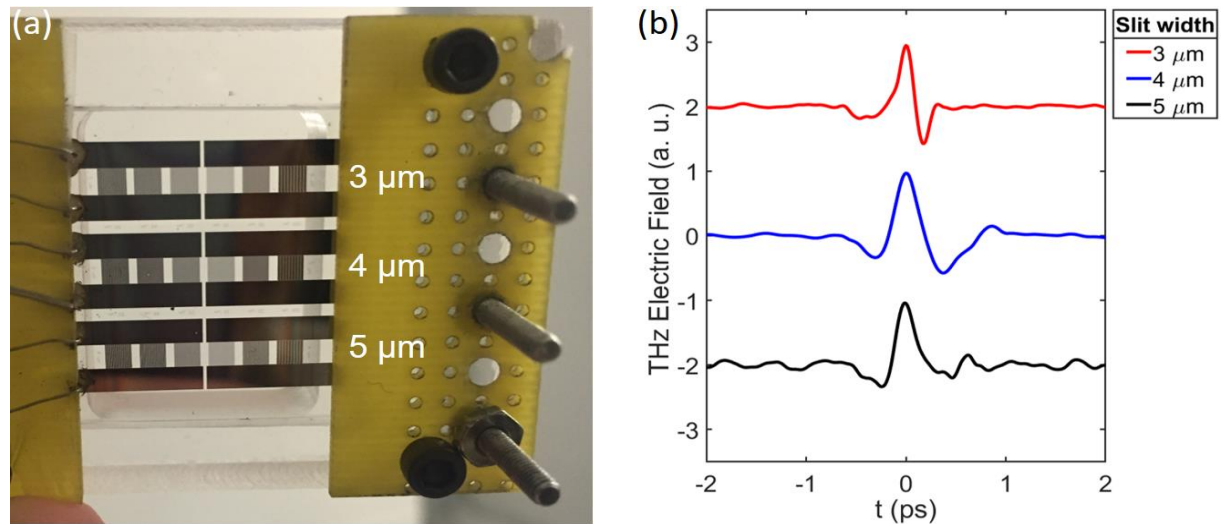


**Figure 3.14.** (a) Photograph showing the second-generation device realized on a silica wafer and mounted on a customized holder, which also serves to deliver the bias voltage. We fabricated 18 samples, each one featured by a different slit width, i.e. 3, 4 and 5  $\mu\text{m}$  from top to bottom, as indicated in the figure, whereas the silica cover layer was equal to 5  $\mu\text{m}$  for all of them. Since the sub-wavelength slits are realized with electrodes displaced as an interdigitated structure, we have realized an array structure, so as to have a larger number of slits to test. (b) THz waveforms recorded as a function of the slit width, for a fixed bias voltage and probe energy of 200 V and 100 nJ, respectively. Each curve is normalized to its own maximum and shifted along the y-axis for clarity.

among the main parameters for the sub-wavelength slits (silica gap and finger size), we compared the performance achieved by using the mentioned above four types of devices. At first, we studied the temporal response as a function of the slit width (i.e. silica gap), for the devices featuring 10- $\mu\text{m}$ -finger electrodes, while keeping the bias voltage at 200 V. The main results are shown in Fig. 3.14(b). We note that the waveforms do not show the same shape. Such a discrepancy could be ascribed to a different reshaping of the THz pulse due to the different periods of the array structure, resulting from joining several slits, which have a different width for each device. In particular, the pulse reconstructed for the 5- $\mu\text{m}$ -slit (black curve) shows a significant noise floor, likely due to the lower bias fields which decreases moving from the 3- $\mu\text{m}$  to the 5- $\mu\text{m}$ -slit case. We mention that the amplitude values recorded for the 5- $\mu\text{m}$ -slit were twice the case of the 4- $\mu\text{m}$ -slit and up to 5 times higher than that of the 3- $\mu\text{m}$ -slit (not shown in the figure). This suggests that the larger silica area illuminated by the same probe beam energy resulted in a higher SH intensity yield. However, the DR evaluated for the 3- $\mu\text{m}$ -slit was more than 20 times higher than that evaluated for the 5- $\mu\text{m}$ -slit case (as can be qualitatively seen in Fig. 3.14(b)), which has to be ascribed to the higher amplification of the signal performed by a stronger bias electric field induced for the same applied voltage. Since further amplifications are still possible with the 3- $\mu\text{m}$ -slit so to easily achieve the same strengths observed in the other two more noisy waveforms, we concluded that the performance of such a device resulted to be best among the others. Therefore, from now on, we will only investigate the dependence on the remaining parameters, by keeping fixed the slit width at 3- $\mu\text{m}$ -slit. The second step was then to study the sub-wavelength slit behavior by varying the electrode finger size, i.e. either 10 or 100  $\mu\text{m}$ . We have performed such an investigation by tuning the bias voltage in the range 50-600 V. Because of the high voltage amplifier employed to perform these experiments, we have not been able to apply lower bias values, since we were limited by the minimum of the output dynamics of such an instrument. However, we would like to mention that by using another low voltage amplifier with maximum output voltage equal to 70 V, we evaluated a minimum bias of 30 V required to extract the signal from the noise. Nevertheless, due to the different specifications of the second amplifier in terms of noise, we have not reported these data in Fig. 3.15(a). On the other hand, higher voltage values resulted in discharge in air, again without damaging any part of the device. It is worth highlighting that, for these devices, the voltage values mentioned above

correspond to bias electric fields one order of magnitude higher than those generated within the slit of the first generation. For example, a voltage of 300 V induces an electric field of  $\sim 250$  kV/cm across the 3- $\mu\text{m}$ -slit, a significantly high strength that the device can sustain due to the high dielectric strength of silica. Moreover, since the external discharge happened for higher AC electric field strengths than those of the first generation, it turned out that the confinement induced by the tinier structure is more effective, which potentially enhances the detection performance. Figure 3.15(a) shows the comparison between the temporal amplitude peaks as a function of the bias voltage. We note a slightly different behavior in the two cases. The measured signal is amplified up to a voltage of 500 V, in the case of the 10- $\mu\text{m}$ -wide electrode finger device. Higher bias values result in a degradation of the signal. This might be ascribed to pre-breakdown phenomena occurring inside the silica for very high electric fields ( $V_{bias} = 600$  V  $\Rightarrow E_{bias} > 500$  kV/cm), distorting the AC electric field distribution between the electrodes

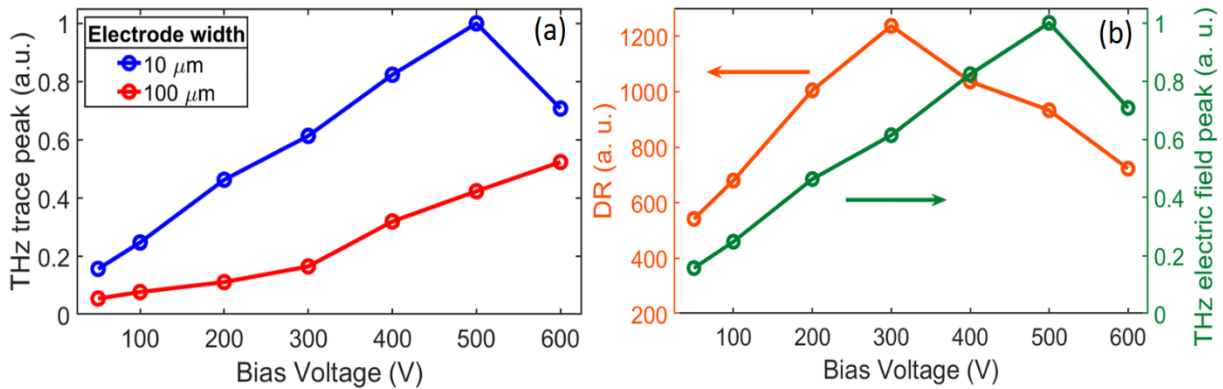


**Figure 3.15.** (a) Comparison between the THz transient peaks trends recorded for device configurations featured by a 3- $\mu\text{m}$ -wide slit as well as 10-(blue dots) and 100-(red dots)- $\mu\text{m}$ -wide electrode fingers, as a function of the bias voltage. (b) DR trend (orange dots) compared to the corresponding THz peak trend (green dots) as a function of the bias voltage for the 3- $\mu\text{m}$ -slit, 10- $\mu\text{m}$ -finger device. The maximum DR value is not aligned with the maximum peak.

and eventually lowering the detection efficiency [109]. Nevertheless, such an effect is absent in the 100- $\mu\text{m}$ -finger trend and we are still debating the origin of this difference. We also note that the higher signal strengths achieved in the 10- $\mu\text{m}$ -finger configuration with respect to the 100- $\mu\text{m}$ -counterpart, regardless of the bias voltage applied, could be ascribed to fringing effects across the metal contacts. Indeed, it is known that narrower electrodes (with sizes comparable

to the gap in between) generate a wider effective bias electric field along the longitudinal direction [73], thus resulting in an enlarged biased region where the probe and THz beams interact. Such results suggest that the proper mathematical relation between the bias voltage and the THz strength may not be exactly linear for the case of such narrow finger electrodes, as in Eq. (3.64), where, instead, we had simply modeled the slit as a two parallel plate capacitor. Rather, it might be reformulated as:

$$I_{DFG}^{readout} \approx 2(\chi^{(3)} I_P)^2 E_{THz} E_{bias}^{eff} (w, G) \quad (3.65)$$

where  $E_{bias}^{eff} (w, G)$  is the *effective* electric field generated in between the electrodes and where we highlight a dependence on both finger width and gap size. Keeping in consideration only the 10- $\mu\text{m}$ -finger device, we have evaluated the DR for each applied voltage and compared it with the corresponding peak amplitude trend, as shown in Fig. 3.15(b). The optimal DR ( $>1200$ ) is

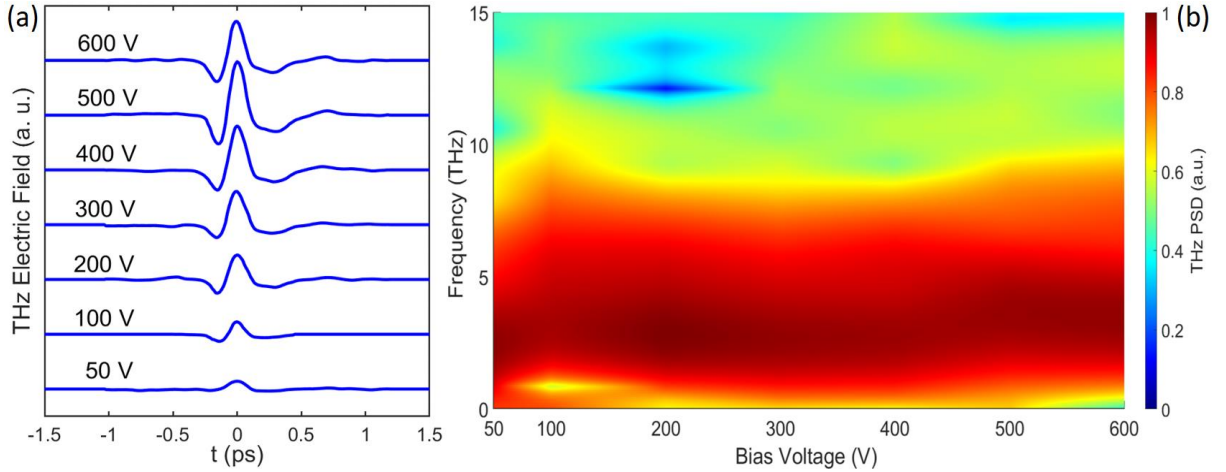


**Figure 3.16.** (a) THz waveforms recorded via the second generation of SSBCD device featured by a 3- $\mu\text{m}$ -wide slit and two 10- $\mu\text{m}$ -wide electrode finger, as a function of the bias voltage in the range 50-600 V. The curves are shifted along the y-axis for the sake of clarity. (b) 2D colormap reporting the THz bandwidth (PSD) corresponding to the transients in (a), as a function of the bias voltage. The continuous spectrum extends approximatively up to 10 THz. No frequency notches are observed, consistently with the quasi single-cycle nature of the THz pulses in (a).

achieved for the bias voltage of 300 V, which however does not correspond to the maximum THz amplitude, reached at 500 V. Actually, even for the 100- $\mu\text{m}$ -wide finger device, we have found an optimal DR ( $\sim 500$ ), yet at the higher voltage of 400 V (not shown in the figure and

different from the corresponding maximum peak). Interestingly, the non-monotonic trend of the DR curve allows distinguishing, once again, two different noise regimes as already seen in Fig. 3.10(b). As the bias electric field increases, the DR improves, since the NEP of the PMT and the laser fluctuations essentially dominates the noise. However, at a certain point, the noise introduced by the switching of elevated bias voltages contributes to increase the noise floor, thus degrading the overall DR. The reason why the turning point occurs for lower AC bias voltages compared to the first generation, is likely due to the fact such a narrower slit not only results in the generation of very AC high electric fields, but also quickly amplifies the noise fluctuations due to the switching mechanism (at 500 Hz) of the high voltage amplifier. Besides these effects, it is worth noting that the DR achieved with this SSBCD device configuration is double of that attained with the first generation, and yet, at a much lower bias voltage.

### 3.6.3 Spectral response

The full THz transients recorded as a function of the bias voltage is reported in Fig. 3.16(a). Differently from the previous generation, here the reconstructed THz pulses feature a quasi single-cycle shape for each bias value with a full width half maximum duration of around 240 fs, thus confirming that the only 3- $\mu\text{m}$ -thick cover layer does not result in secondary echoes. The dynamics of the amplification, i.e. the ratio between the lowest and highest peak values is around 12. Such a value is somewhat lower than that retrieved for the first generation. This means that the slope of the green line fitting the data in Fig. 3.15(b) is smaller than that in Fig. 3.10(a), since the ratios between the voltage values at the edges of the investigated ranges in the two generations are similar ( $1050/50 \approx 600/30$ ). This could be due to the lower THz electric field effectively funneled in the slit array with respect to the single-slit case of the first generation devices [110], which may change the coefficient in Eq. (3.65), and accordingly the slope. The THz spectra evaluated via Fourier transformation of the pulses in Fig. 3.16(a), are shown in the 2D colormap of Fig. 3.16(b), revealing a continuous, gap-free behavior up to roughly 10 THz, thus accomplishing the goal of ultra-broadband detection. Notably, the central frequency is not altered by higher voltages, meaning that no parasitic modulations of the refractive index are induced by the high static electric field. Finally, Fig. 3.17(a) and (b) report the comparison between the THz waveforms and bandwidths retrieved via ABCD (blue curves)

and the second generation of the SSBCD devices (red curves), respectively. We note that the pulse shapes and spectra are essentially the same, demonstrating that the frequency response of the two techniques is quite similar. However, we reiterate that the operating conditions are totally different for the two cases: while for ABCD we have employed a probe energy and bias voltage of 100  $\mu$ J and 2.5 kV, respectively, the same parameters were only 100 nJ and 300 V for the optimal operation of the SSBCD technique. Such values are three and one orders of magnitude lower, respectively, [111] and are record-breaking in the area of the ultra-broadband coherent detection of THz pulses. Finally, Table 3.2 summarizes the main characteristics of the first and second generation SSBCD devices.

Generation	Bias Voltage range	Optical probe energy	Maximum DR (optimum bias)	Spectral response
30- $\mu$ m-slit (first)	50-1050 V	200-850 nJ	> 400	notch @ 3 THz
3- $\mu$ m-slit (second)	50-600 V	down to 100 nJ	> 1200	notch-free

**Table 3.2.** Comparison between the first and second generation of silica-based SSBCD devices.

### 3.7 Comparison between SSBCD and EOS

Until now, we have compared the SSBCD technique with the ABCD method, since the latter has so far represented the benchmark in the area of the ultra-broadband THz detection, according to the definition given in Chapter 1. The up-converting process (from the THz to the optical domain) underlying the two schemes is similar and involves the third-order susceptibility of the nonlinear medium (air and silica). Therefore, the direct comparison between the two techniques is easily interpreted.

Additionally, it is equally interesting to compare the effectiveness of the SSBCD technique against other solid-state techniques, such as EOS. However, we should briefly clarify some important points, before proceeding to the presentation of this type of results, in order to fairly interpret the data. EOS is a balanced technique based on the Pockels effect occurring in second-

order materials, such as ZnTe and GaP. Although the detection mechanism is completely different, EOS possesses the same advantage of the balanced ABCD, as, for the former, the optical probe beam is split into two arms and sent to a balanced optical detector, after having interacted with the THz pulse. The differential scheme of EOS brings about a great improvement in terms of noise performance. Technically, the SSBCD method can be implemented in a differential form, similarly to the ABCD counterpart. However, we have preferred to maintain the single-ended scheme, since it is a “plug and play” scheme, whereas the differential geometry would have implied the realization of an *ad hoc* mechanical holder enabling the rotation of the device in a plane orthogonal to the propagation direction, so to find the angle which allows to fulfill Eq. (3.65). Furthermore, since EOS involves a lower-order nonlinear phenomenon,

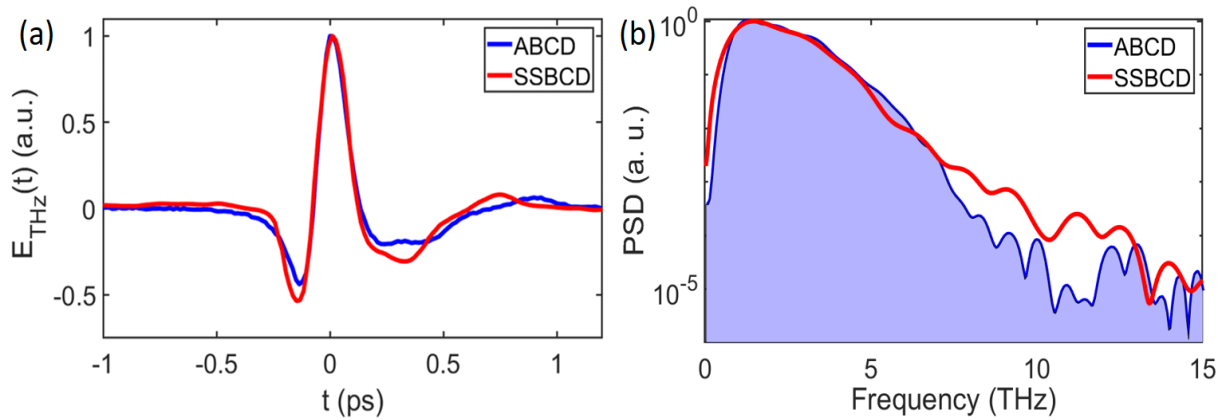


**Figure 3.17.** Comparison between the (a) THz electric field waveforms and (b) the Power Spectral Density (PSD), detected and evaluated for the case of ABCD (blue curves) and the second generation of SSBCD devices (red curves).

the probe energy required to achieve a good amplitude response, is still lower ( $< 1$  nJ) than that employed in the SSBCD case, yet further decreasing the contribution of the laser fluctuation to the total noise. Finally, we should also mention that in EOS, a pair of standard photodiodes are used as an optical balanced detector, since after the interaction with the THz wave, its energy content is carried by the probe beam itself, which only rotates the polarization of the optical beam. Differently, in the SSBCD technique, the THz information is transferred to the third beam resulting from the FWM process (i.e. the DFG beam), whose intensity is proportional to the third-order nonlinear coefficient and therefore only readable by employing a PMT. The NEP associated with a photodiode is lower than that featuring PMTs [112], which in turn results in

expected lower noise floors for the EOS case. Besides, the expected better noise performance which inherently underlies the EOS technique, we will see how the ultra-broadband frequency response represents the unique and characteristic advantage of the proposed SSBCD technique. With this in mind, we now show two types of comparison: once employing a <110>-oriented 20- $\mu\text{m}$ -thick ZnTe crystal grown on a 500- $\mu\text{m}$ -thick <100> ZnTe substrate, which represents the most common material used with Ti:Sapphire lasers, and then by replacing ZnTe with a 500- $\mu\text{m}$ -thick GaP crystal. For the first case, the THz pulses and spectra recorded via either SSBCD or EOS are shown in Fig. 3.18(a) and (b), respectively. More in details, for both the measurements we employed the same amplified laser system and experimental set-up mentioned above, completely purged with nitrogen to avoid water absorptions, which might

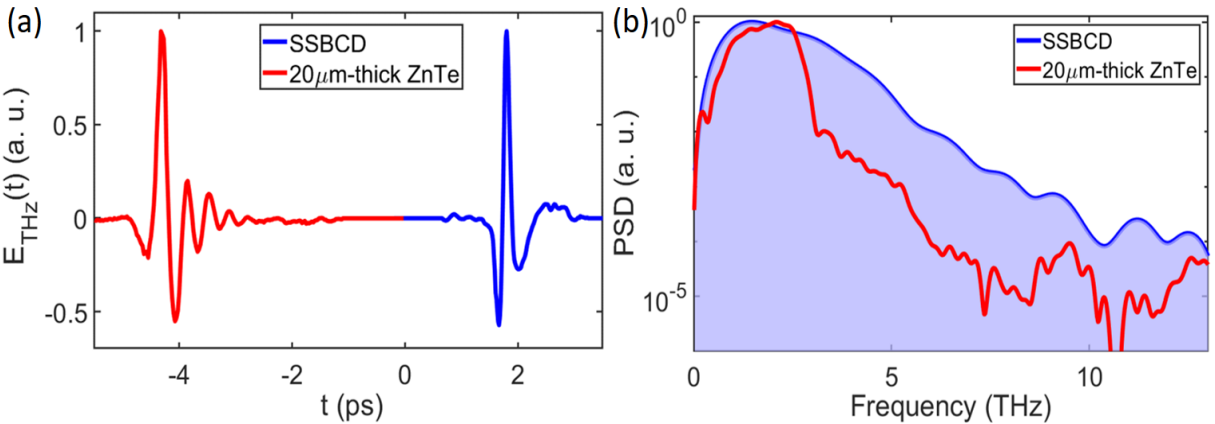


**Figure 3.18.** (a) THz transients and (b) FFT-evaluated spectra retrieved via EOS in a 20- $\mu\text{m}$ -thick ZnTe crystal (red solid lines) and SSBCD (blue solid lines). The pulses in (a) are shifted along the x-axis for clarity. The curves in (b) are normalized with respect to their own maxima.

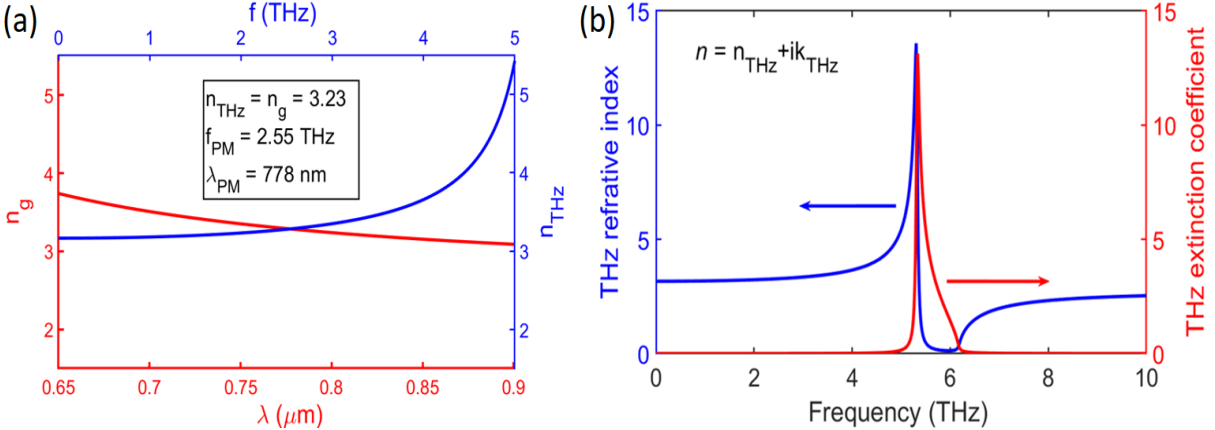


**Figure 3.19.** (a) Phase-matching condition between NIR (red curve) and THz (blue curve) pulses for the case of a ZnTe crystal.  $f_{PM}$  and  $\lambda_{PM}$  are the phase-matched THz frequency and optical wavelength, respectively. (b) Complex refractive index expressed as the sum of the real index (blue curve) and extinction ratio (red curve, proportional to the absorption coefficient) as a function of the THz frequency. The phonon resonance at 5.32 THz induces a rapid increase of both the indexes, thus canceling the phase-matching condition beyond 3 THz, and making the crystal extremely opaque in the 5-6 THz window.

make more difficult the interpretation of the data. In the case of SSBCD, we fixed the probe energy and the 500-Hz-square-wave bias voltage to 100 nJ and 300 V (half peak), respectively. To carry out EOS, we simply replaced the SSBCD device with the ZnTe crystal and decreased the probe energy down to 1 nJ. For the latter case only, we also chopped the THz beam by means of a mechanical chopper rotating at the frequency of 500 Hz, driven by a controller phase-locked to the TTL reference signal generated within the laser system. The electric signal coming from either the PMT (SSBCD) or the balanced photodiodes (EOS) was acquired by a lock-in amplifier (LIA), which was synchronized at a reference frequency of 500 Hz in both cases (corresponding to either the frequency of the mechanical chopper for EOS or the bias modulation rate for SSBCD). For both types of detection, we have set an averaging time of 300 ms. We highlight that in the case of SSBCD, the THz beam was not chopped at 500 Hz, because the detection mechanism exploits the heterodyne scheme to isolate the term in the TFISH intensity that is linearly proportional to the THz electric field strength. Conversely, for EOS, the detection complies with a homodyne scheme, since the LIA reference frequency is the same as the THz chopping frequency. The results collected with the two detection methods are compared in Fig. 3.19(a) and (b), showing the THz transients and the corresponding PSDs, respectively. We note that, while the THz pulse reconstructed via SSBCD (blue curve) is quasi-single cycle and is featured by a spectrum extending up to 10 THz, the same pulse retrieved via EOS (red curve) exhibits a long-lasting multi-cycle shape and its bandwidth is heavily modulated by some inherent effects related to the lattice structure of the semiconductor. Indeed, the lack of the frequencies beyond 3 THz in the spectrum detected via EOS is due to the significant phase-mismatch induced by the strong dispersion of ZnTe approaching the transversal phonon resonance at 5.32 THz [82], [113], as shown in Fig. 3.19(a). More in details, at the probe wavelength of 800 nm, the phase-matching is achieved around 2.5 THz. However, for higher

THz frequencies, the corresponding refractive index quickly increases with respect to the optical group index, due to the phonon resonance. This results in the steep roll off observed in the EOS spectrum in Fig. 3.18(b). Moreover, the ZnTe crystal becomes particularly opaque (giant absorption) in the window between 5 and 6 THz, as pointed out by the sudden increase of the extinction coefficient (the imaginary part of the refractive index) in Fig. 3.19(b), which explains the further increase of the negative slope in the EOS spectrum in that frequency range. For thicker ZnTe crystals, these effects become even more significant. Hence, regardless the laser pulse duration, if EOS is employed, the largest bandwidth suitable for real applications is around 3 THz, since the issues highlighted here are only related to the nonlinear crystal and are

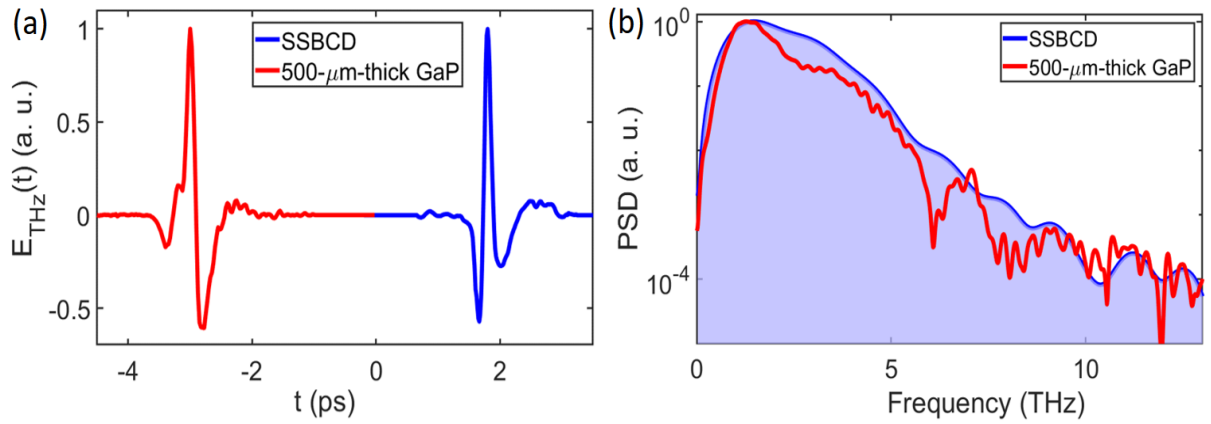


**Figure 3.20.** (a) THz transients and (b) FFT-evaluated spectra retrieved via EOS in a 500- $\mu\text{m}$ -thick GaP crystal (red solid lines) and SSBCD (blue solid lines). The pulses in (a) are shifted along the x-axis for clarity. The curves in (b) are normalized with respect to their own maxima.

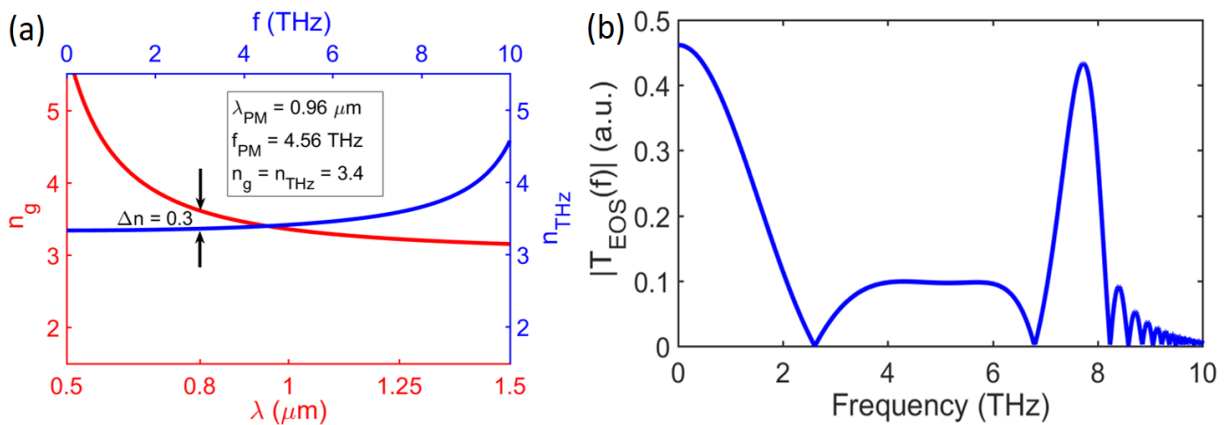


**Figure 3.21.** (a) Phase-matching condition between NIR (red curve) and THz (blue curve) pulses for the case of a GaP crystal.  $f_{PM}$  and  $\lambda_{PM}$  are the phase-matched THz frequency and optical wavelength, respectively. The refractive mismatch at  $0.8 \mu\text{m}$  is relatively high, thus preventing a good efficiency in a collinear geometry. (b) Frequency response of the  $500\text{-}\mu\text{m}$ -thick GaP crystal employed as a THz sensor in the EOS detection. The poor phase-matching results in a heavily modulated response with several zeros within the  $10\text{-THz}$ -wide range.

absent in the SSBCD device. On a final note, as expected, the noise floor for EOS is around one order of magnitude lower than that of SSBCD due to the benefit of the balanced scheme. For the second type of comparison, we replaced the ZnTe crystal with the GaP one and performed the EOS detection under the same experimental conditions. The relative temporal waveform and power spectrum are shown and compared to the homologous retrieved via SSBCD the technique in Fig. 3.20(a) and (b), respectively. We have chosen GaP because its first phonon resonance falls higher in the spectrum, around  $11 \text{ THz}$  [20], [82], thus being potentially suitable for larger detection bandwidth. It is worth mentioning that the GaP crystal is not naturally phase-matched in a collinear geometry, when the excitation optical wavelength is  $\lambda_P = 0.8 \mu\text{m}$ , and its Pockels coefficient ( $\sim 1 \text{ pm/V}$ ) is four times lower than that of ZnTe (that means lower EOS efficiency). This is the reason why GaP is conveniently used in combination with an intense broadband THz source driven by Ti:Sapphire lasers [114], so to obtain a good estimation of the emitted THz electric field peak by minimizing the saturation effects (nonlinear response and overrotation), affecting the EOS detection when the THz electric field becomes so high that the approximation of a linear response is no longer valid [1], [115]. Incidentally, we note that the SSBCD technique does not show any saturation effect as the THz electric field increases, because Eq. (3.65) inherently scales linearly with the THz electric field, in the whole range of operation of the SSBCD device. We note that, in the case of GaP-based EOS, the recorded THz pulse duration is much shorter than that obtained via ZnTe crystals, and its shape resembles that recorded via SSBCD. Correspondingly, the EOS spectrum covers a larger frequency range and is mostly overlapped to the SSBCD one, yet affected by some artefacts around  $2.5$ ,  $6$  and  $8 \text{ THz}$ , as shown in Fig. 3.20(b) (red curve). Again, the latter is due to a severe limitation imposed by the phase-matching condition for such a long crystal, which alters the original form of the spectrum [20]. Indeed, we recall that while propagating inside the crystal, the THz and

optical probe beams experience a group-velocity mismatch which leads to a temporal delay  $\delta(\omega_{\text{THz}})$ , given by:

$$\delta(\omega_{\text{THz}}) = \frac{n_g(\lambda_p) - n(\omega_{\text{THz}})}{c} d \quad (3.66)$$

where,  $n_g(\lambda_p)$  is the group refractive index evaluated at the probe wavelength,  $n(\omega_{\text{THz}})$  the THz refractive index,  $d$  the length of the crystal and  $c$  the speed of light. The dispersion relations of  $n_g(\lambda)$  and  $n(\omega_{\text{THz}})$  are plotted in Fig. 3.21(a). The total electro-optic modulation induced by the THz pulse on the probe beam is then calculated as [9]:

$$T_{\text{EOS}}(\omega_{\text{THz}}) = \frac{t(\omega_{\text{THz}})}{\delta(\omega_{\text{THz}})} \int_0^{\delta(\omega_{\text{THz}})} \exp(i\omega_{\text{THz}}t) dt = \exp\left(i \frac{\delta(\omega_{\text{THz}})}{2}\right) t(\omega_{\text{THz}}) \frac{\sin(\delta(\omega_{\text{THz}})/2)}{\delta(\omega_{\text{THz}})/2} \quad (3.66)$$

where  $t(\omega_{\text{THz}})$  is the transmission coefficient, expressed according to the Fresnel formulation [104], and where we have assumed that the probe pulse duration is much shorter than that of the THz pulse. Figure 3.21(b) shows the absolute value of  $T_{\text{EOS}}$  as a function of the frequency for the case of a 500- $\mu\text{m}$ -thick GaP crystal. The overall trend accurately reproduces the spectral features of the THz spectrum retrieved via GaP-based EOS (red curve in Fig. 3.19(b)). Although phase-match significantly limits detection performances, the THz electric field peak measured via EOS in the GaP crystal was almost twice higher than that measured by means of the same technique operated with the ZnTe crystal, where instead the phase-matching condition is much better fulfilled. This implies that the part of the ultra-broad spectrum undetected by the ZnTe crystal carries a significant amount of the whole THz power, which is totally lost, thus resulting in an underestimation of the real THz electric field strength. This circumstance is intuitively correct if we consider the graphs in Fig. 3.18(b), where the EOS spectrum experiences a sudden drop of more than two orders of magnitude beyond 3 THz, where there is no longer overlap between SSBCD and EOS spectra. We will see in section 4.4.3 that, even though the SSBCD is a single-ended technique, it still allows to estimate the THz electric field peak by performing two consecutive measurements, with and without a bias voltage applied. Another advantage of the SSBCD technique against the EOS method that we want to highlight is the absence of echoes in the detected waveforms for the former case. Indeed, the THz pulses could undergo several

reflections inside the detection crystal, which appear as repetitions of the main trace, limiting the width of the suitable time window and, in turn, the frequency resolution for spectroscopic applications. Some solutions have been adopted to alleviate this issue, such as the employment of wedge-shaped crystals [43], [116], the deposition of metallic thin film (few tens of nanometers) on the rear of the crystals [117], [118], and other more recently strategies based on periodic structures [91]. However, in the SSBCD, the refractive index of the silica is much lower than that of many semiconductor materials, thus resulting in a lower reflection coefficient. Moreover, the cover layer has been designed in such a way to have a sub-wavelength size so to prevent the etalon effect from taking place. Behind the slit, the generated TFISH beam, traveling

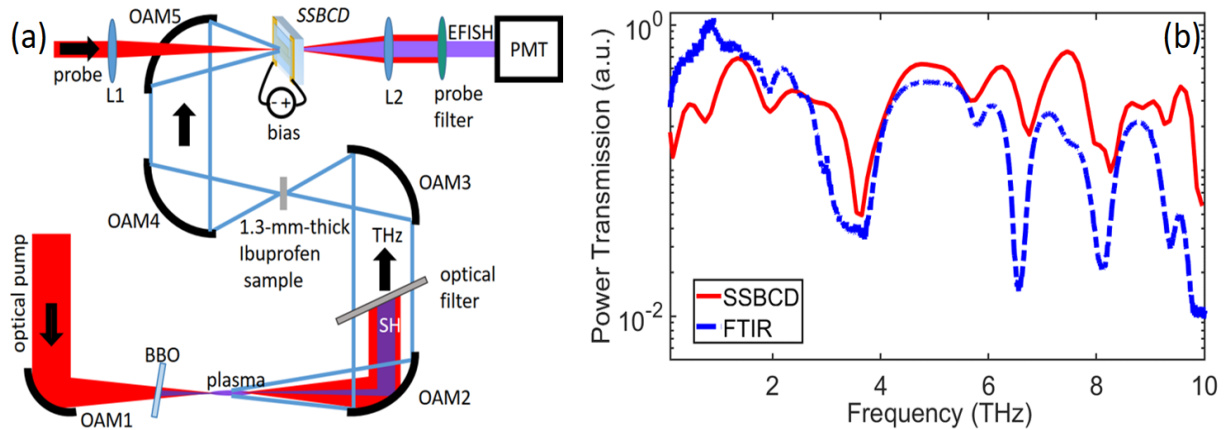


**Figure 3.22.** (a) Sketch of the ultra-broadband THz Time-Domain Spectroscopy set-up. THz pulses are obtained from a plasma source. Detection is carried out through the SSBCD technique. THz radiation is handled by off-axis mirrors only, whereas the sample is placed at the first focus along the propagation direction of the THz transients. (b) Transmission spectra for a 1.3-mm-thick pellet of ibuprofen retrieved via SSBCD (red solid curve) and for a 0.6-mm-thick pellet via FTS (blue dashed curve). Curves are shifted along the y-axis for clarity.

towards to the opposite facet of the silica substrate, experiences a negligible reflection at the interface with air, which does not lead to any spurious repetition. Therefore, if we neglect the THz pulse replicas due to the silicon wafer employed as long pass filter in the THz-TDS set-up (which could be easily removed by replacing it with a stack of long-pass multimesh filters), the SSBCD-detected temporal waveform reproduces the main THz pulse only.

### 3.8 Application: Ultra-broadband Time-Domain Spectroscopy

As a proof of the ultra-broadband detection capability featuring our SSBCD method, we carried out a spectroscopic investigation on a 1.3-mm-thick pellet of ibuprofen (>98%, Sigma-Aldrich). Ibuprofen is a common anti-inflammatory drug, and it is recognized to possess diverse absorption lines in the THz range, due to its long molecule composed of several organic groups [30]. Therefore, we employed the same ultra-broadband set-up presented in Fig. 3.6, where the pellet sample was placed at the first focus of the THz beam, as pointed out in the simplified sketch of Fig. 3.22(a). We recorded both the reference signal (in nitrogen) and the transmitted signal through the sample, and calculated the ratio of the two power spectra, obtaining the transmission curve reported in Fig. 3.20(b). Typical spectral features due to vibrational modes of the crystalline structure of ibuprofen, are easily recognized in the range 0.6-9.0 THz, which manifest as dips in the transmission spectrum. We note that the measurements have demonstrated how the SSBCD technique is able to resolve notches as deep as one order of magnitude in terms of power. We have also retrieved the spectral transmission of a 0.6-mm-thick sample of ibuprofen (same density) by means of a traditional Fourier-Transform Spectroscopy (FTS) method, which is shown as a blue dashed curve in Fig. 3.21(b). The use of a thinner sample was constrained by the low peak power emitted by the incoherent THz thermal source, mounted into the spectrometer, above all in the spectral range below 2 THz. The good alignment between the frequency dips evaluated in the two cases, demonstrates the effectiveness of the SSBCD technique acting as a detector in an ultra-broadband THz spectrometer.

# Chapter 4

## **Beyond silica: Silicon nitride-based solid-state-biased coherent detection**

The results presented in the previous Chapter have demonstrated that the SSBCD technique based on the silica platform brought about an important breakthrough in the area of THz coherent detection, as it cuts down the requirement of probe energy and bias voltage by orders of magnitude with respect to the ABCD technique, yet maintaining an ultra-broadband ( $> 10$ -THz-wide) response. Furthermore, being a solid-state method, it has also a superior frequency response with respect to EOS, overcoming some of its limitations, such as distortion of the actual shape of the THz pulse, absence of pulse echoes (which limit the temporal window), limited range of linear response with respect to the THz electric field (resulting in THz strength under-estimation). These preliminary conclusions lead to the possibility of integrating our SSBCD detectors in compact and portable THz systems, which then gain an ultra-broadband spectral response, as the final detector no longer exhibits bottlenecks and affects the outcomes of measurements concerning, e.g. spectroscopy and hyperspectral imaging. Nevertheless, there

is still room for improvement, so to make the SSBCD technique really competitive in those applications where EOS and PCS currently dominate. This is mainly due to the extremely low laser power and bias voltage required by the latter techniques ( $< 1$  nJ,  $\sim 10$  V), while also being more appealing in both industrial and academic environments. In this fourth Chapter, we will present a new class of SSBCD detectors, based on a micron-sized metallic slit and embedded in a thin film of amorphous silicon nitride, acting as the nonlinear medium. Due to this revised configuration, we show that the new device generation allows for remarkable ultra-broadband detection capabilities, by now using extremely low bias voltages ( $< 10$  V) and probe energies in the order of 10 nJ only.

Material	Nonlinear susceptibility $\chi^{(3)}$	Dielectric Strength	CMOS process compatibility	Thickness deposition
SiO <sub>2</sub>	$2 \times 10^{-22} \text{ m}^2/\text{V}^2$	$> 8 \text{ MV/cm}$	✓ (PECVD)	$> 30 \text{ }\mu\text{m}$
SiN	$8 \times 10^{-21} \text{ m}^2/\text{V}^2$	$1 \div 6 \text{ MV/cm}$	✓ (PECVD)	$\sim 1 \text{ }\mu\text{m}$

**Table 4.1.** Comparison of the silica and silicon nitride physical properties.

#### 4.1 SiN properties: differential THz-time domain spectroscopy

Silicon nitride (SiN) has been already exploited extensively for decades in nonlinear integrated optics [119]–[121], due to its higher nonlinearity with respect to silica, while being fully compatible with the CMOS process [89]. This essentially has allowed the efficiency enhancement of the most common nonlinear phenomena occurring in optical integrated structures [122]. In particular, the main parameters of its amorphous form (deposited via plasma-enhanced chemical vapor deposition (PECVD), and therefore often referred as *plasma nitride*), are shown in Table 4.1 (where they are compared with silica). We note that the third-order susceptibility of SiN is one order of magnitude higher than that of silica [123] and its dielectric strength is comparable. Those are two very encouraging properties for our purposes. However, because of the relatively high strain associated with thin films grown in presence of large lattice mismatch, the maximum thickness that is possible to deposit is approximately equal to one micrometer only. Few works available in literature report data for frequencies between

20 THz and the near infrared region [124]. Such a lack of information has to be ascribed to the fact that the 0.1-10 THz frequency range corresponds to wavelengths much longer than the effective thickness of standard SiN films. This means that most of the common THz-TDS systems are not able to provide the required sensitivity to perform measurements on such thin films. Therefore, in order to properly design our SiN-based device, we had to first characterize the PECVD-grown SiN in terms of refractive index and absorption via a more sophisticated method. To this end, we have deposited a 10- $\mu\text{m}$ -thick film of SiN onto a 4-inch-diameter, 500- $\mu\text{m}$ -thick wafer of silica, as sketched in Fig. 4.1(a). We have carefully adjusted the parameters of the deposition, in order to minimize the strain and avoid the formation of scratches over the film, as well as to avoid lift-off of the film itself from the silica wafer. Then, we have employed a differential algorithm (DTDS) [52] to the data acquired from this sample. This because the propagation of the THz pulse inside a film which is too thin prevents a conventional TDS system to effectively sense the path difference with respect to the case of propagation through the substrate only. In particular, from Fig. 4.1(a), it results that when the input THz field  $E_{THz}^{input}$  travels directly through the silica wafer, we can write:

$$E_{THz}^{ref}(\omega) = t_{air \rightarrow SiO_2} E_{THz}^{input}(\omega) \exp\left(i\omega \frac{d}{c}\right) \quad (5.1)$$

where  $t_{air \rightarrow SiO_2}$  is the Fresnel transmission coefficient from air to silica and  $c$  is the speed of light. We note that Eq. (5.1) also accounts for the propagation of the pulse across a layer of air as thick as the SiN film (the thickness of which is  $d$ ). On the other hand, when the pulse travels through the film, it can undergo multiple reflections (especially if the film refractive index is higher than that of the substrate), therefore the corresponding THz electric field can be written as:

$$E_{THz}^{film}(\omega) = \frac{t_{air \rightarrow SiN} t_{SiN \rightarrow SiO_2} \exp[i\delta(\omega) - \alpha(\omega)d]}{1 - r_{SiN \rightarrow air} r_{SiN \rightarrow SiO_2} \exp[2i\delta(\omega) - 2\alpha(\omega)d]} E_{THz}^{input}(\omega), \quad (5.2)$$

where  $\alpha(\omega)$  is the absorption coefficient of the film and  $\delta(\omega)$  is phase retardation induced by the film refractive index  $n_{SiN}(\omega)$ , i.e.:

$$\delta(\omega) = n_{SiN}(\omega) \omega \frac{d}{c}. \quad (5.3)$$

Now, instead of using  $E_{THz}^{ref}(\omega)$  and  $E_{THz}^{film}(\omega)$  as reference and sample signals, in the THz-DTDS technique we evaluate the differential sample signals as:

$$E_{THz}^{diff}(\omega) = E_{THz}^{film}(\omega) - E_{THz}^{ref}(\omega). \quad (5.4)$$

However, if the film thickness is so small that it satisfies the condition:  $d \ll c/\omega$ , it follows that  $\delta(\omega) \ll 1$ , and the ratio between  $E_{THz}^{diff}(\omega)$  and  $E_{THz}^{ref}(\omega)$  simplifies as:

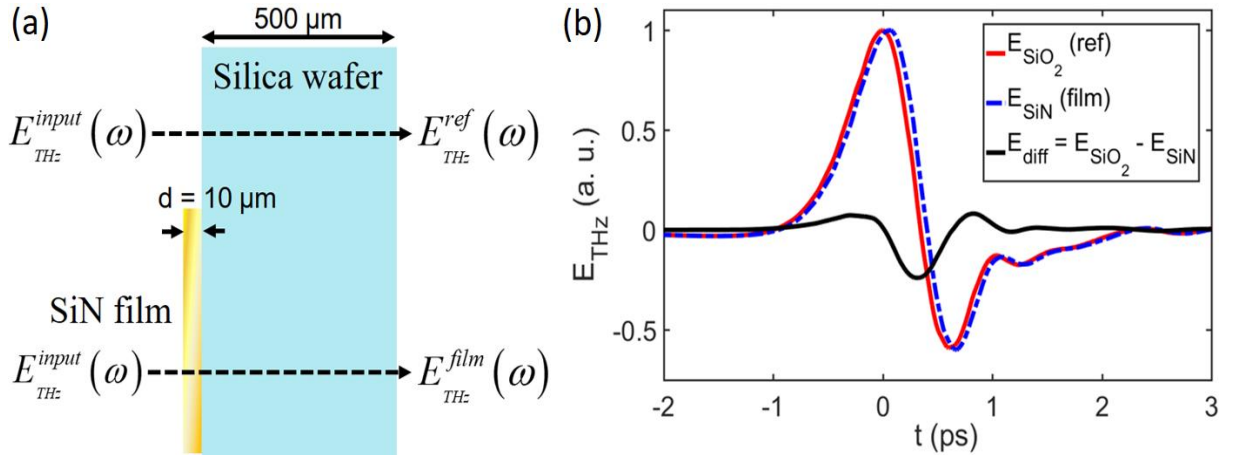


**Figure 4.1** (a) Sketch of a silica wafer, half covered with a 10- $\mu$ m-thick SiN film. The reference signal is measured by letting the THz pulse traveling through the substrate (silica), where the differential signal is calculated as the difference between the pulse passing through the stack of SiN film and silica substrate and the reference. (b) THz waveforms corresponding to the reference pulse (red solid curve) and the pulse traveling through the film (blue dashed line). The differential signal resolved from the noise and shown as the black solid line.

$$\frac{E_{THz}^{diff}}{E_{THz}^{ref}}(\omega) \approx i \frac{\omega}{c} d \left[ n_{SiN} - 1 + \frac{(n_{SiN} - n_{air})(n_{SiN} - n_{SiO_2})}{n_{SiO_2} + n_{air}} \right] - \alpha d \left[ 1 + \frac{(n_{SiN} - n_{air})(n_{SiN} - n_{SiO_2})}{n_{SiO_2} + n_{air}} \right] \quad (5.4)$$

Finally, by imposing  $R(\omega) = \frac{E_{THz}^{diff}}{E_{THz}^{ref}}(\omega)$  and inverting Eq. (5.4), it is found out:

$$\begin{aligned}
n_{SiN}(\omega) &= \sqrt{1 + \frac{c}{\omega d} (1 + n_{SiO_2}) \text{Im}(R(\omega))} \\
\alpha_{SiN}(\omega) &= -\frac{(1 + n_{SiO_2}) \text{Re}(R(\omega))}{d \left[ (n_{SiO_2} + 1)(1 - n_{SiN}) + n_{SiN}^2 + n_{SiO_2} \right]}.
\end{aligned} \tag{5.5}$$

Equation (5.5) can be effectively employed only when the TDS system is able to discriminate with good fidelity the differential signal (i.e. high SNR). In a conventional TDS system, the problem is related to the fact that the signal fluctuations due to the noise in the system are inversely proportional to the film-induced phase change  $\phi(\omega) = [n_{SiN}(\omega) - 1] \omega d / c$ , which

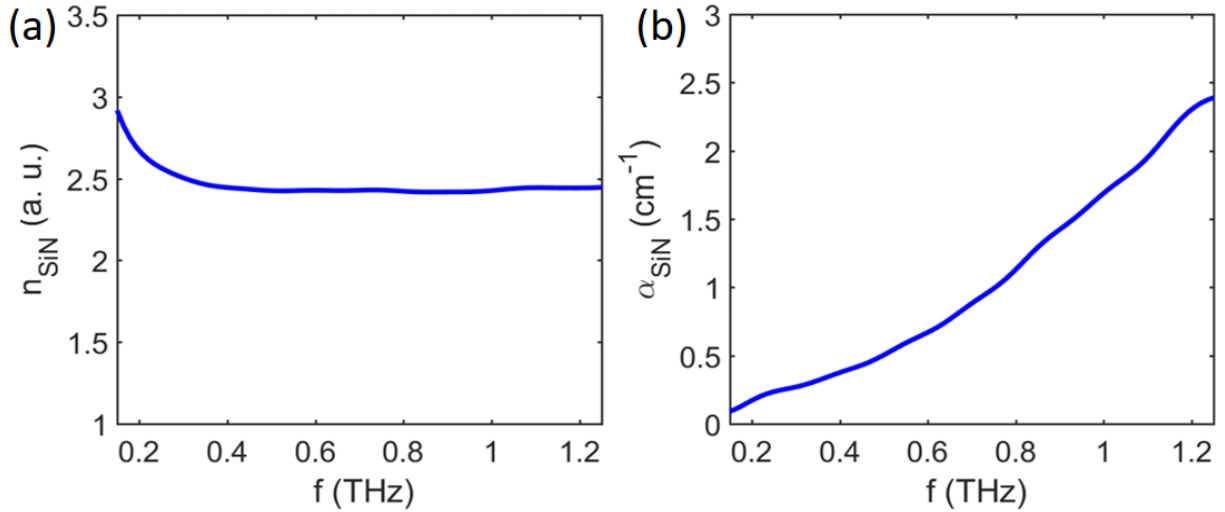


**Figure 4.2.** (a) THz refractive index and (b) power absorption coefficient as a function of the frequency, evaluated via a DTDS algorithm.

can be significantly small when the film thickness is very thin compared to the wavelength, thus resulting in a differential signal indistinguishable from the noise floor. Therefore, one way to overcome such an issue is to maximize the SNR of the whole system. To this end, we have employed a customized hybrid THz-TDS set-up, where the source was a PC antenna, whereas detection was carried out via EOS in a 3-mm-thick ZnTe crystal, both fed by a Ti:Sapphire oscillator operating at 80 MHz repetition rate. In this way, we have joined the valuable stability of a laser oscillator (which in turn results in a good peak stability of the THz signal emitted by the PC antenna) with the very good noise rejection capability of the EOS method. The measurement was carried out by applying a 30 kHz, 70 V<sub>pp</sub> square wave voltage to the PC

antenna. We used the same modulation frequency as a reference for the lock-in amplifier, the time constant of which was set at 1 s. The time step was set to 15 fs, in order to be able to appreciate the delay between the reference and film THz transients. The acquisition of the reference and sample signals led to the THz waveforms shown in Fig. 4.1(b). As it is clear, the phase change induced by the film is so small that is barely detectable (corresponding to around 50 fs of temporal shift). However, the SNR was high enough to allow the calculation of the differential signal, clearly distinguishable from the noise. We note that its amplitude is one order of magnitude lower than that of the two main pulses and, interestingly, it is approximately proportional to the first derivate of the reference pulse. This has to be expected since, in the case of negligible absorption coefficient, the relation expressed in Eq. (3.4) reveals a  $\pi/2$  phase difference between the two pulses, which is a further proof of the effectiveness of our differential scheme. Finally, by applying Eq. (5.5), we have retrieved the THz refractive index and absorption coefficient of the SiN film as a function of the frequency, as shown in Fig. 4.2(a) and (b). The average  $n_{SiN} = 2.45$  is consistent with a static dielectric constant of around 7 for the case of the PECVD-grown film [89]. The absorption coefficient is on the same order of that of silica, which however is of less interest for our purpose, due to the sub-wavelength size of the cover layer employed in the SSBCD device. The graphs in Fig. 4.2(a) and (b) extend until 1.2 THz, as result of the concomitant effects between the limited THz bandwidth detectable via the 3-mm-thick ZnTe crystal ( $< 2$  THz) and the further spectral shrinkage due to the DTDS scheme. The ultra-broadband THz set-up shown several times throughout this thesis, is not suitable for this type of application, because the THz pulses fluctuations due to the plasma source (carrier-envelope instability [125]), do not allow to significantly increase the SNR of the measurements by simply adjusting the lock-in parameters. However, we know that the stoichiometric silicon nitride ( $Si_3N_4$ ) does not present any lattice resonance at least up to 15 THz [124], therefore, it is reasonable that for the amorphous material this feature still holds.

## 4.2 Four-wave mixing in silicon nitride

We recall that in order to properly design the cover layer thickness in our SSBCD devices, the main constraint is the phase-matching condition underlying the FWM process, which takes place between THz and probe beams traveling inside the nonlinear material. Therefore, we have

followed the same strategy presented in section 3.8.1, evaluating the coherence length  $L_{coh} = \pi/|\Delta k_{DFG}|$  for the case of SiN. With regards to the values of the refractive index in the optical domain, we used the set of data provided by the supplier of the material (i.e., LMN at INRS-EMT), who carried out the device fabrication and the characterization of the SiN film via an ellipsometry technique, the results of which are shown in Fig. 4.3(a). In order to also retrieve the value of the refractive index in the shortest wavelength range of the visible domain, we fitted the data with a Sellmeier equation (red curve in Fig. 4.3(a)), which can be modeled as:

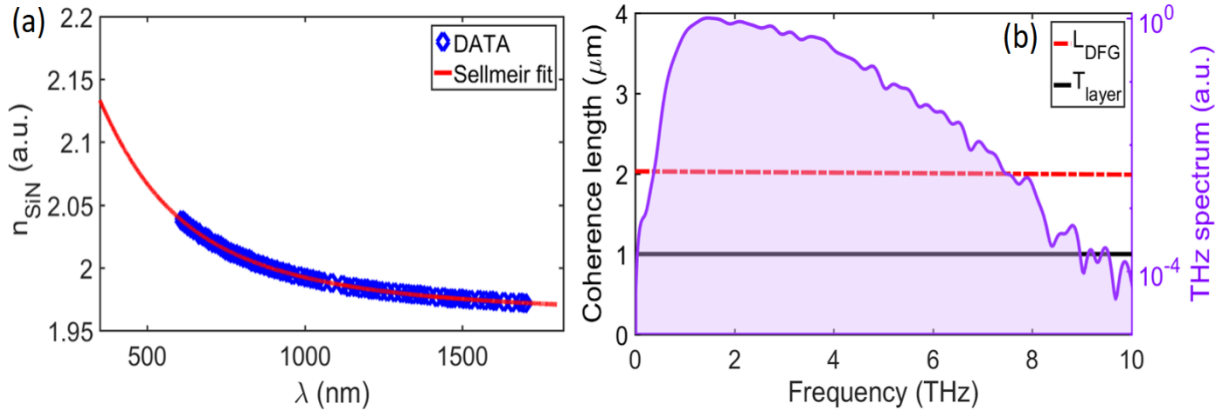


**Figure 4.3.** (a) Optical refractive index of the particular type of SiN film grown by PECVD at the LMN. (b) Coherent length for the FWM process taking place in SiN for the case of co-propagating THz and probe beam. The red dashed line depicts the difference-frequency generation (DFG) process, whereas the black solid line indicates the thickness of the SiN cover layer ( $T_{layer}$ ). For comparison purposes, the THz bandwidth reconstructed via the ABCD technique is plotted in purple, showing that  $T_{layer} = 1 \mu\text{m}$  satisfies the phase-matching condition for the whole THz spectrum.

$$n_{SiN}^{visible}(\lambda) = \sqrt{1 + \frac{A\lambda^2}{\lambda^2 - B^2} + \frac{C\lambda^2}{\lambda^2 - D^2}} \quad (5.6)$$

where  $\lambda$  is the optical wavelength expressed in nanometers and the fitting parameters are:  $A = 15.06$ ;  $B = 283.1 \text{ nm}$ ;  $C = -12.22$ ;  $D = 298.1 \text{ nm}$ . Therefore, by inserting all the proper values in Eq. (5.6), we drew the graph in Fig. 4.3(b). The main result is that the coherence length is only  $2 \mu\text{m}$ , i.e. much shorter than for the silica case. This is essentially due to the higher dispersion (by one order of magnitude [126]) affecting SiN in the UV range. Therefore, by also taking into account a technical constraint concerning the resolution of the fabrication process, as detailed

in the following sections, we finally chose a SiN cover layer as thick as  $T = 1 \mu\text{m}$ , as well as a slit width ( $G = T$ ) of the same size.

#### 4.2.1 Fabrication of the SiN-based SSBCD device

The layout of the sub- $\lambda$  SSBCD device is presented in Fig. 4.4(a) and essentially resembles the structure reported in Fig. 3.5(a). It consists in the deposition on a 1.5-mm-thick fused quartz substrate of a 30 nm-thick layer of chromium (Cr) followed by a 100-nm-thick layer of aluminum and another 30-nm-thick Cr-layer. The Cr layers ensure the proper adhesion of the

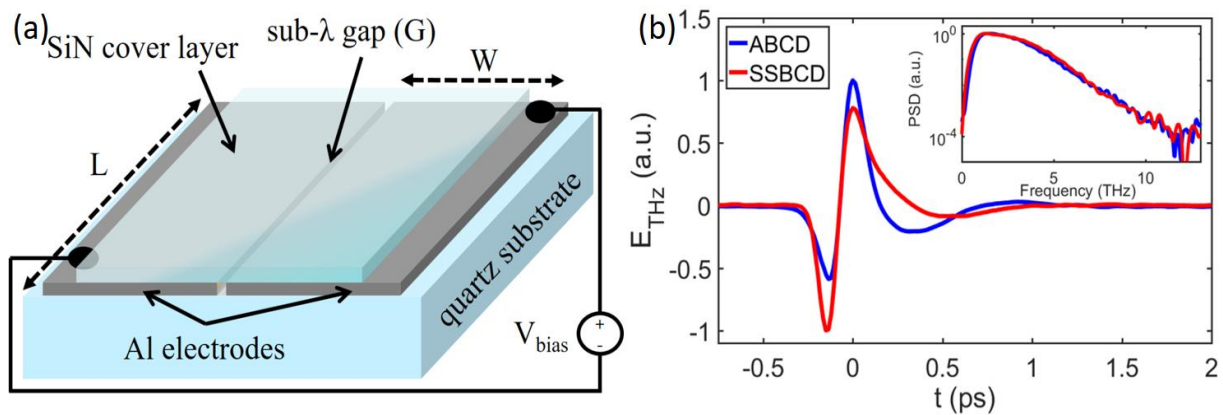


**Figure 4.4.** (a) 3D sketch of the deep subwavelength slit device embedded in a thin layer ( $T$ ) of SiN, deposited on a quartz substrate.  $L$  and  $W$  are the length and the width of the metal pads, respectively. (b) Comparison between the THz waveforms recorded via ABCD (blue curve) and SSBCD (red curve). The inset shows the corresponding Fourier-transformed spectra of the two pulses.

dielectric materials over the aluminum (Al). Two electrodes are then defined by direct-write laser lithography and wet etching techniques, in order to form a  $1.0 \pm 0.1 \mu\text{m}$ -wide gap ( $G$ ) between them. Aluminum has a melting temperature ( $\sim 660 \text{ }^\circ\text{C}$ ) twice lower than that of gold, yet with respect to the latter, Al deposition is much faster and cost-effective [89]. Moreover, since we expected to employ lower probe energies than those used with the previous generation devices featuring gold electrodes, the risk of damaging the Al contacts (burning or ablating) is basically negligible. Subsequently, a 1- $\mu\text{m}$ -thick SiN cover layer is deposited via PECVD over part of the electrodes, thus also completely filling the slit. The aluminum pad sizes have been chosen as  $W = L = 2 \text{ mm}$  in order to maximize the THz energy retrieval. Since the slit width is

much smaller than the THz wavelength in SiN ( $\lambda_{\text{THz}}/n_{\text{SiN}}$ ), we called this third generation of SSBCD devices “*deep sub-wavelength ( $\lambda$ ) slit*”.

### 4.3 Comparison with the ABCD technique

First, we tested the new detector via the same ultra-broadband THz-TDS system introduced in the previous sections. However, this time the experiments implied the use of a two-color plasma source driven by a 2.2 mJ, 800 nm, 140 fs, 1 kHz Ti:Sapphire amplified laser, emitting THz pulses with a bandwidth exceeding 11 THz. We measured a peak value of  $43.8 \pm 1.2$  kV/cm at the detector position, via EOS in a 500- $\mu\text{m}$ -thick GaP crystal. We started the characterization by comparing the spectral response of the device against standard ABCD, the latter performed by focusing the THz and the 50- $\mu\text{J}$ -probe beam together in air through a 2-inch-parabolic mirror and a 100-mm-lens, respectively. While the THz spot size was frequency-dependent (with an average  $1/e^2$  diameter of 150  $\mu\text{m}$ ), the  $1/e^2$  diameter of the 50- $\mu\text{J}$ -probe beam was fixed at approximately 16  $\mu\text{m}$ , in the focal plane. For ABCD, we biased the interaction with a 1.5 kV AC (square wave) bias voltage at 500 Hz. For the case of SSBCD, we maintained the same focusing conditions for both the beams and decreased the probe energy to 100 nJ, and the bias voltage to 100 V, respectively. The waveforms acquired via both techniques are shown in Fig. 4.4(b), whereas the corresponding Fourier-transformed spectra are displayed in the inset. It is interesting to observe that, even though the detected transients in the two cases have roughly the same bandwidth ( $> 10$  THz), the SSBCD spectrum manifests a slight red-shift, which corresponds to a different pulse shape. Such a reshaping is due to the particular frequency response of the deep sub-wavelength slit, as it will be detailed in the following section. However, we stress that the single-cycle nature of the pulse is preserved, thus demonstrating the ultra-broadband capabilities of the SiN-based detectors.

## 4.4 Characterization of the SiN-based SSBCD devices

### 4.4.1 Simulation of the field enhancement

With respect to the previous version of SSBCD devices, the layout of the new structure takes advantage of the THz electric field enhancement induced by a metallic sub- $\lambda$  slit, which funnels the THz radiation in the space between the two metal contacts. Indeed, when a THz wave

impinges orthogonally on a freestanding metallic slit, it gives rise to a carrier current density, the fast transients of which induces accumulation of the carriers at the edges of the metal pads. This mechanism enhances the THz electric field within the slit [127]. Such carriers are gathered from a neighbor region which linearly scales with the wavelength of the incident radiation [110]. Therefore, the field enhancement (FE) due to the funneling effect shows a broad resonance-free  $1/f$ -dependence, where  $f$  is the frequency of the impinging electromagnetic wave, in the case of a laterally infinitive slit, with width much narrower than the metal pad thickness [128]. This intriguing feature works well with the ultra-broadband operating regime of our detector, since it can significantly increase the efficiency of the TFISH generation occurring within the slit, without introducing spectral artefacts. It was shown that FE can reach values up to 100 at 1 THz, as the slit width is reduced to 70 nm, even for the case of gold plates as thin as 60 nm, i.e. approximately the skin depth of gold at that frequency [127]. However, a too narrow slit could significantly limit the active area illuminated by the spot size of the optical probe beam (typically in the order to a few tens of microns), thus degrading the overall TFISH efficiency, in a similar way to what seen when we compared the performance of the devices featuring 3, 4 or 5  $\mu\text{m}$  slit widths (see section 3.8.2). Therefore, a trade-off between these two concurrent effects should be found. Practically, the design parameters were constrained by the minimum resolution allowed by the fabrication process, thus resulting in a slit width of 1  $\mu\text{m}$ , which is the narrowest allowed via the direct laser writing technique. However, the funneling effect through narrow slits has been mostly investigated in relatively low ranges of frequencies, mainly between 0.1 and 1.6 THz, where the enhancement is the highest [129], [130]. For our purpose, it is essential to study the behavior of the sub- $\lambda$  slit in a much broader spectral window. Hence, the estimation of the THz FE occurring in the SSBCD device presented here can be performed by properly refining the methodology employed in those numerical works. More in detail, due to the ultra-broadband nature of our THz beam, we can regard it as the superposition of several beams, each of them at a different frequency component. Thus, the frequency-dependent focusing of the whole THz beam onto the slit cannot be neglected. Indeed, on the one hand, considering a fixed diameter for all the spectral beam components, higher frequencies will be tightly focused to smaller spots (resulting in higher peak values on the slit center) with respect to those at lower frequencies. On the other hand, by considering the same peak value for each

frequency, the larger spots associated to the lower frequencies will result in higher FE. These concurrent effects determine the ultimate frequency response of the slit in our context. In addition, the presence of a dielectric material surrounding the slit affects the total FE. To properly model all these effects, we focused the attention on the experimental set-up sketched in Fig. 4.5. The 140-fs-long NIR pump pulsed beam and its second harmonic (generated in a 100- $\mu\text{m}$ -thick BBO crystal) are focused together through a 4", 90° off-axis parabolic mirror, thus generating a plasma channel with length of  $L = 7\text{ mm}$  and  $1/e^2$  radius of  $r = 50\text{ }\mu\text{m}$ , measured by acquiring the fluorescence of the filament by means of a CCD camera (see Appendix A). We assumed that the two-color plasma emits THz pulses with a frequency content spanning

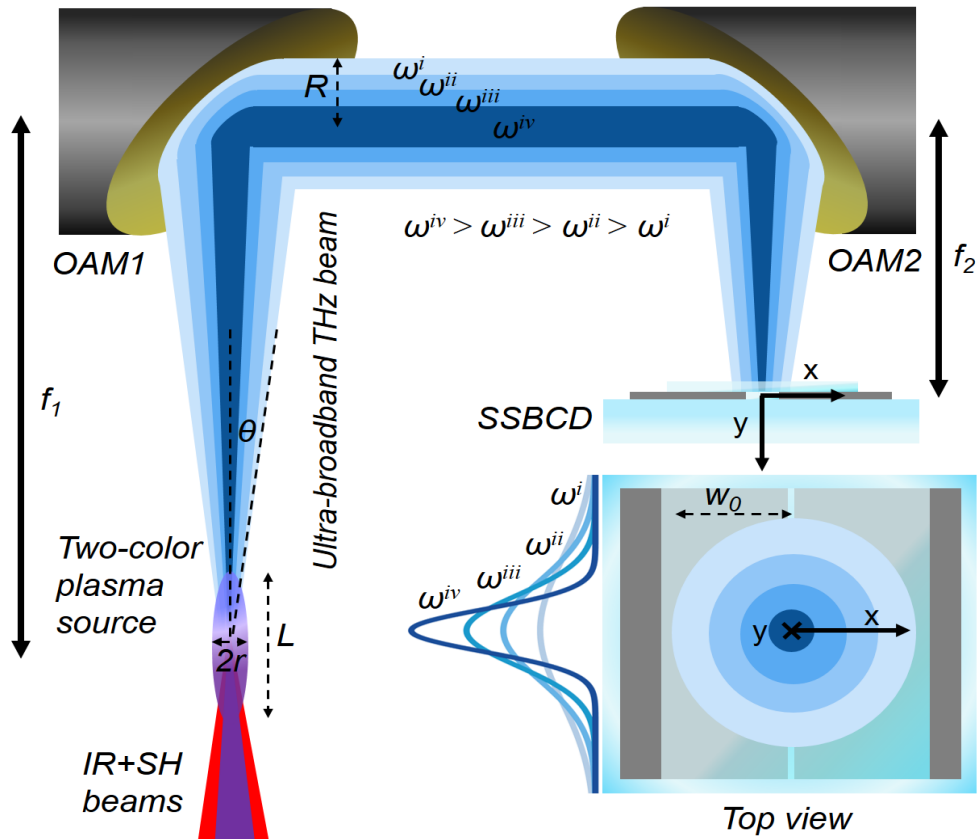


**Figure 4.5.** Geometry of the ultra-broadband THz set-up considered for the modeling of the THz field enhancement. An infrared pulsed beam (IR) and its second harmonic (SH) are focused together in air to generate a two-color plasma channel emitting 10-THz-wide pulses. The THz beam is regarded as the superposition of several frequency components (different shades of blue) featured by different emission cones, with aperture angle  $\theta$ . The first off-axis mirror OAM1, with focal length  $f_1$ , collimates the beam

having radius  $R$ , whereas OAM2 with focal length  $f_2$  focuses the beam into the SSBCD device. The plane associated to the sub- $\lambda$  slit overlaps the focal plane of the OAM1, where each frequency component of the THz beam features a waist size  $w_0$ . The inset shows an example of the different field profiles focused onto the top of the device and associated to each frequency component of the whole beam (darker shades of blue correspond to higher frequencies).

approximately the 0.1-10 THz range. Each component diffracts with an angular distributed interference pattern, the frequency-dependent maxima of which are formed at different angles  $\theta$ , estimated with the aid of the following formula [131]:

$$\theta(\omega) \approx \sqrt{\frac{\lambda}{L}} = \sqrt{\frac{2\pi c}{\omega L}}, \quad (5.7)$$

where  $\lambda$  is the THz wavelength in vacuum,  $\omega$  the THz angular frequency and  $c$  the speed of light. Equation (5.7) states that the higher the frequency, the smaller the emission angle, as sketched in Fig. 4.5, where darker shades of blue correspond to higher frequencies. The first 90° off-axis mirror OAM1 collects and collimates the THz beam, with frequency-dependent radius  $R$  evaluated as:

$$R(\omega) \approx \min \left[ \frac{D}{2}, f_1 \tan(\theta(\omega)) + r \right], \quad (5.8)$$

where  $D$  and  $f_1$  are the diameter and the effective focal length of the mirror, respectively and, for sake of completeness, we took into account the possibility that some frequency components ( $< 0.5$  THz) could result in beam diameters wider than the mirror clear aperture. The collimated THz beam is then focused by a second 90° off-axis mirror (OAM2) -with effective focal length  $f_2$ - the spot size of which results to have a frequency-dependent waist  $w_0$ , evaluated as [113]:

$$w_0(\omega) \approx \frac{\lambda f_2}{\pi R(\omega)} = \frac{2c f_2}{\omega R(\omega)}. \quad (5.9)$$

Equation (5.9) represents the case of a beam focused in the air. For the case of the SSBCD device placed at the detection position, we assumed that the plane of the slit overlaps the mirror focal plane. This means that the THz beam propagates inside the 1- $\mu\text{m}$ -thick SiN cover layer while being focused, before reaching the metal contacts. However, due to the subwavelength

thickness of the cover layer, we neglected the extremely small deviation, which the THz wave experiences due to refraction of the beam at the air/SiN interface (evaluated to be only a few hundreds of nanometers at 10 THz and diminishing as the frequency decreases). The knowledge of  $w_0$  serves to evaluate the initial condition which must be to each beam component profile in order to properly model the focusing onto the slit. In particular, in our simulations, we considered a 2D  $x$ - $y$  reference system with origin on the center of the slit, where  $x$  is the transverse axis and  $y$  is the propagation direction axis (see Fig. 4.5). In this way, by noting that the system made up by the two off-axis mirrors is actually a telescope with magnification  $f_2/f_1 < 1$ , the transverse profile of each THz electric field component, impinging on the device, assumes the form:

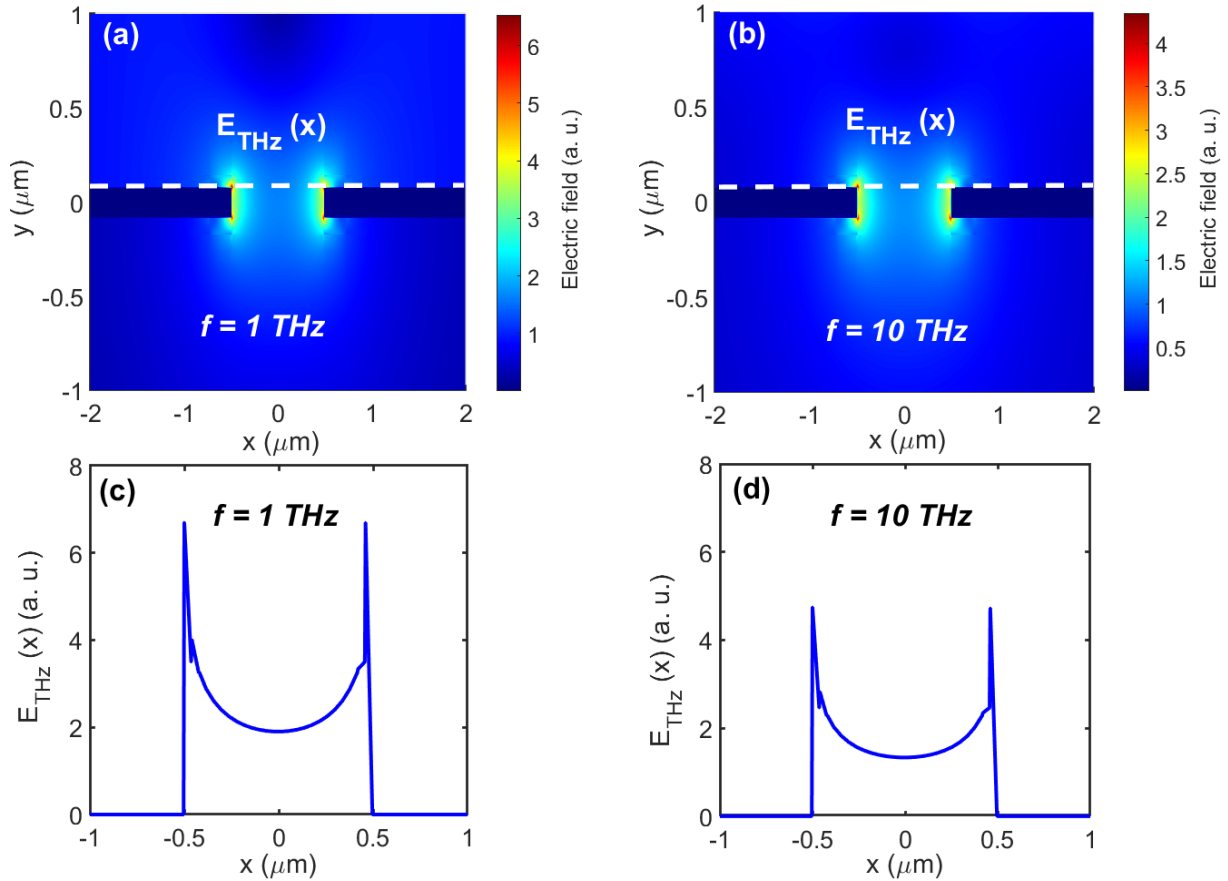


**Figure 4.6.** 2D distribution of the THz electric field in the slit for the frequency component of (a) 1 THz (a) and (b) 10 THz. Corresponding profiles of the THz electric fields at (c) 1 THz and (d) 10 THz, evaluated along the white dashed lines indicated in (a) and (b).

$$E_{THz}(x, \omega) \propto \frac{r}{w_0(\omega)} \exp\left[-\left(\frac{x}{w_0(\omega)}\right)^2\right] \quad (5.10)$$

Equation (5.10) represents the input condition for the simulations of the THz electric field propagating inside the device. The metal pads of the slit were modeled as a  $2 \times 2 \text{ mm}^2$  stack of metal sheets, consisting of a 100-nm-thick aluminum layer sandwiched between two 30-nm-thick layers of chromium. In the calculations, we accounted for the real spectral response of the two metals in the whole THz range, by evaluating its complex frequency-dependent dielectric parameter by means of the Drude model [132], [133]. We recall that the FE is evaluated as the ratio between the THz electric field within the slit aperture and the background field, i.e. the

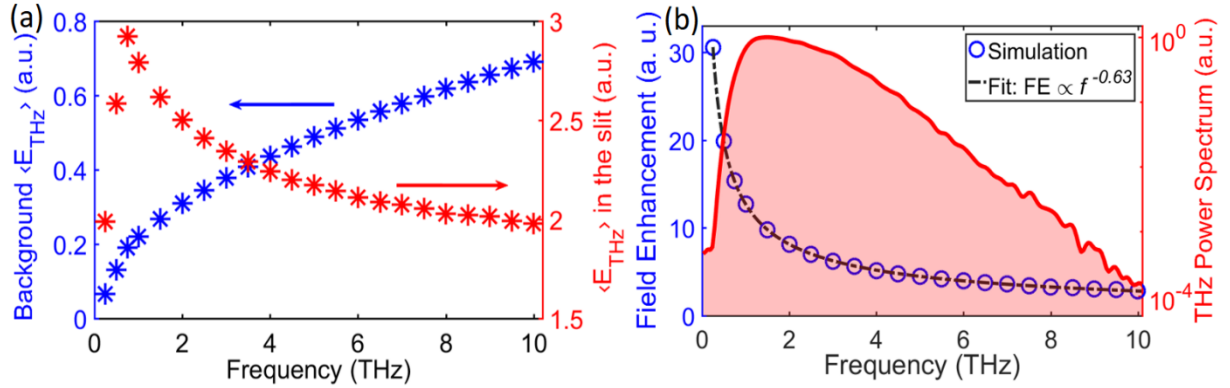


**Figure 4.7.** (a) Comparison between the average THz electric field calculated for the background case  $E_{THz}^{back}$  and THz electric field  $E_{THz}^{slit}$  inside the slit as a function of the frequency. (b) Calculated field enhancement values (blue stars) induced by the metallic slit on a focusing ultra-broadband THz beam, as a function of the frequency, in the 0.25-10 THz range. For comparison purposes, the red area represents the THz spectrum emitted by the two-color plasma source and acquired via ABCD.

expected value of the field in a plain layer of SiN, without the surrounding metal pads. Therefore, we performed two sets of simulations in the 0.25-10 THz range (with a step of 0.25 THz in the 0.25-1 THz range, and a step of 0.5 THz beyond 1 THz), evaluating the THz electric field at its focus, once for the case of a unique layer of SiN (background field) and then in the presence of the metallic slit. In Fig. 4.6(a) and (b), we report the 2D field distribution calculated at 1 THz and 10 THz, respectively, when the metallic slit is present. In particular, Fig. 4.4(c) and (d) show the transverse profiles of the THz electric field evaluated along the white dashed

lines (5 nm above the metal pad edge) in (a) and (b), respectively. We notice a significant confinement of the electric field within the slit (centered on the origin of the  $x$ -axis), which is stronger close to edges of the metal pads. Therefore, we calculated a mean value of the THz electric field by integrating its transverse profile (see Fig. 4.6(c) and (d)) over the  $x$  coordinate, for a region as wide as the slit extension, either with ( $E_{THz}^{slit}$ ) or without ( $E_{THz}^{back}$ , background field) the metallic slit. These values are plotted in Fig. 4.7(a). Finally, the FE is evaluated, for each frequency component, as the ratio between the two average fields:

$$FE(\omega) = \frac{\langle E_{THz}^{slit}(\omega) \rangle}{\langle E_{THz}^{back}(\omega) \rangle}. \quad (5.11)$$

The FE calculated according to Eq. (5.11) as a function of the frequency is shown in Fig. 4.7(b) together with the best fit, which demonstrates a  $\sim 1/f^{0.63}$  dependence upon the frequency. Such spectral behavior is slightly different with respect to the  $1/f$ -trend found in the literature under the hypothesis of an unlimited slit uniformly illuminated by a plane wave [128]. The main reason behind such a difference has to be ascribed to the frequency-dependent focusing of the THz beam. Moreover, in our work, the real dimensions of the device (gap size of 1  $\mu\text{m}$  and metal pad thickness of 160 nm) actually define a completely different geometrical regime with respect to that in [134] (where, instead, the gap size was assumed to be much smaller than the metal pad thickness). The frequency-weighted mean value of FE is equal to 6.1 (evaluated as the first momentum of the black dashed curved in Fig. 4.7(b)).

#### 4.4.2 Bias voltage dependence

We proceeded in our investigation studying the scaling mechanisms in the THz transients acquired via our device, as a function of both bias voltage and probe energy. Figure 4.8 shows the THz waveforms recorded by varying the bias voltage in the 10-70 V range, while the probe energy was held constant at 100 nJ. We point out that we have used the same low voltage amplifier provided with a commercial TDS system involving PC antennas (EKSPLA THz kit). As mentioned above, it results that the retrieved THz transients are quasi single-cycle with an envelope pulse duration of around  $\tau_{FWHM} = 226$  fs for any bias voltage value, which approximatively corresponds to a bandwidth of 11 THz, as shown in the inset. We highlight the

enormous difference between the operating parameters employed for ABCD and this version of SSBCD. This confirms that dispersion introduced by the sub- $\lambda$  SiN cover layer does not affect the nonlinear frequency mixing and, therefore, the frequency response of the device. In particular, Fig. 4.9(a) illustrates the trend of the THz electric field peak as a function of the bias voltage (blue dotted line, left axis), compared to the dynamic range (DR, red dotted line, right axis), in the 5-100 V range. Lower values did not allow to resolve the signal from the noise, whereas the maximum voltage was limited by the output dynamics of the amplifier. In order to determine the maximum voltage this device could withstand, we used again the high voltage amplifier and observed the discharge occurring at  $\sim 140$  V. However, for consistency, we have not reported the data between 100 and 140 V, since the noise due to the latter type of amplifier

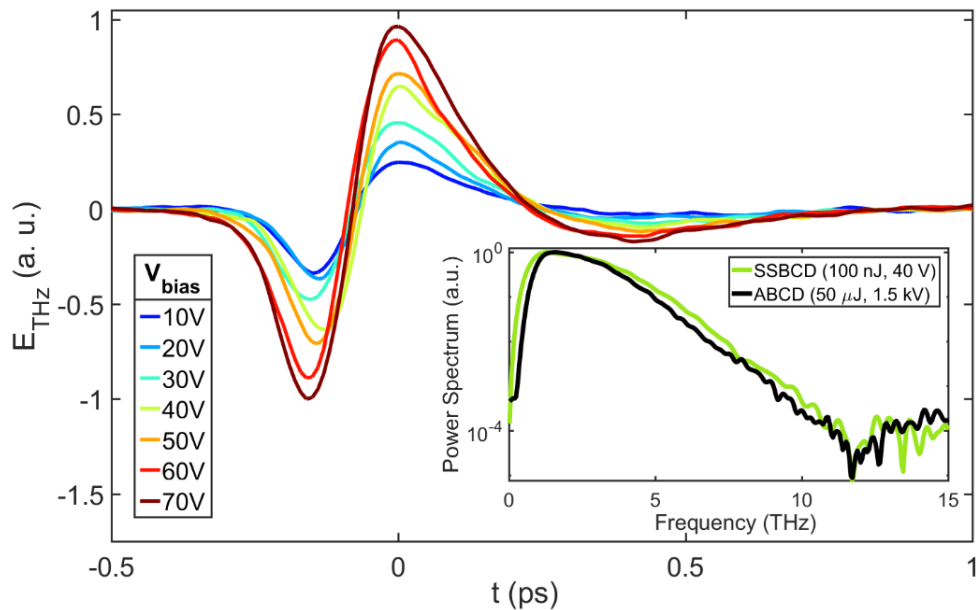


**Figure 4.8.** THz waveforms acquired via SiN-based SSBCD devices (third generation) for different values of the bias voltage in the range 10-70 V. The inset shows the spectrum corresponding to the case of 40 V. Each curve is normalized to the maximum of that retrieved for 70 V. The inset shows the comparison between the THz spectra evaluated for the ABCD case and the SSBCD corresponding at pulse with 40 V bias voltage.

was much higher. We note that the signal, as well as the DR, is linearly proportional to the bias voltage in the whole range, as highlighted by the linear fit (black solid line). Interestingly, the monotonic DR trend is different from the behavior seen for the case of silica-based SSBCD,

where we noticed that for very high bias voltages generated by the relatively noisy kV amplifier, the noise figure eventually worsened. On the contrary, in this case, the absence of the DR deterioration is ascribed to the almost noise-free amplification of the TFISH signal operated by the standard low voltage amplifier, which allows increasing the detection efficiency in a much wider range of bias voltage values, without degrading the DR. We underline that DRs greater than 1000 are easily reached for bias voltages of few tens of volts, while detection can be still carried out for values as low as 5 V. Figure 4.9(b) shows the THz peak trend (blue dotted line) and the related DR (red dotted line) as a function of the probe energy in the 10-200 nJ range. Lower energy values did not allow to extract the signal from the noise floor, whereas higher values caused permanent damage to the aluminum contact pads during long operation.

It is known that in the case of pure four-wave mixing process among fundamental (FH), SH and

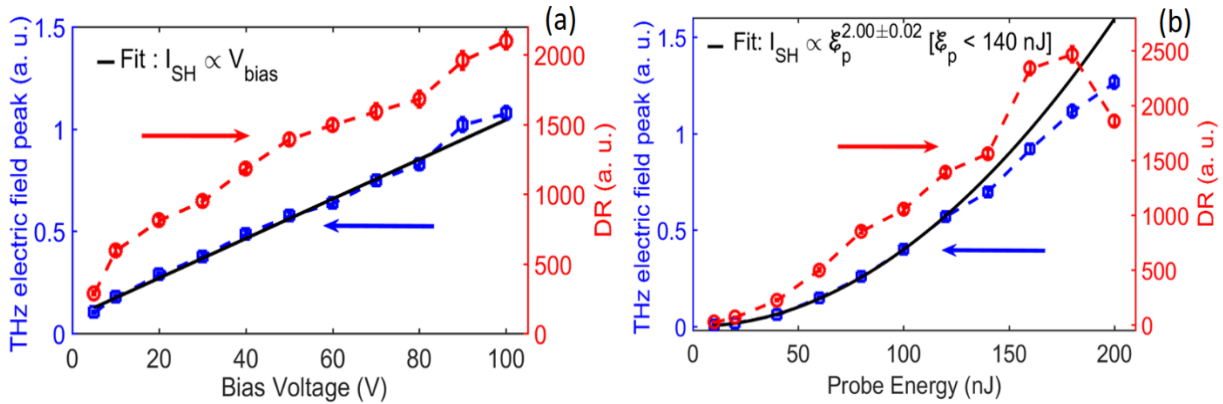


**Figure 4.9.** (a) THz electric field peak (blue dots, left axis) and dynamic (red dots, right axis) trends as a function of the bias voltage. The black solid line represents the linear fit reproducing the THz peak trend all over the bias range. (b) THz electric field peak (blue dots, left axis) and dynamic (red dots, right axis) trends as a function of the probe energy. The black solid line represents the parabolic fit that properly reproduces the THz peak trend in the range 10-140 nJ only.

THz frequencies, the SH intensity as a function of the FH energy follows a quadratic law [65]. Here, the experimental results verify such a trend for probe energies lower than 140 nJ, as highlighted by the quadratic fit (black solid line). For higher values, the data trend shows a slower increasing rate. The reason behind such a behavior is most likely the triggering of other nonlinear phenomena (e.g., nonlinear absorption, broadening of the EFISH bandwidth [88]) occurring in SiN for relatively high probe energies. Furthermore, we report an abrupt drop of

the DR, when approaching 200 nJ, because of an increase of the noise floor, likely due to the generation of white light in the material (supercontinuum generation [88]). Indeed, the DR worsening for higher optical energies was already observed in the air-breakdown coherent detection technique (see Chapter 2), where the elevated probe intensity required to attain quasi-coherent detection also generated a large background noise, strongly degrading the DR [37]. As a final note, it is worth highlighting that we were able to detect the THz signal starting from a probe energy of 10 nJ only, which is the lowest ever employed for this type of coherent detection method.

#### 4.4.3 Direct estimation of the THz electric field peak in the slit

As a further set of measurements, we used our new device as an absolute THz peak meter for ultrashort THz pulses. Indeed, the TFISH process itself occurring in the SSBCD device directly allows probing the THz electric near-field, enhanced by the slit. In particular, we followed the strategy suggested in [135], [136]. We recall that when both the THz ( $E_{THz}$ ) and a generic bias electric field ( $E_{bias}$ ) interact with the probe beam, the total EFISH beam intensity is given by:

$$I_{SH}^{total} \propto (E_{THz})^2 + (E_{bias})^2 \pm 2E_{THz}E_{bias} \quad (5.12)$$

where the double sign depends on the orientation of the bias and THz electric fields, assuming parallel polarization for both fields. In order to carry out the heterodyne detection underlying either standard ABCD or SSBCD, the bias is chosen as an AC modulated voltage wave, typically oscillating at half of the repetition rate of the pulsed THz beam and employed as a reference for the lock-in amplifier. Hence, the two squared terms in Eq. (5.12) are rejected:

$$I_{SH}^{heterodyne} \propto 2E_{THz}E_{bias}^{AC}. \quad (5.13)$$

On the other hand, if we apply a DC (i.e. static) bias field and chop the THz beam, thus acquiring the TFISH signal by synchronizing the lock-in amplifier to the same chopping frequency

(homodyne detection), only the quadratic term dependent on the bias electric field is suppressed in Eq. (5.13), leading to:

$$I_{SH}^{homodyne} \propto (E_{THz})^2 \pm 2E_{THz}E_{bias}^{DC} \quad (5.14)$$

Now, if we consider two measurements carried out via the homodyne scheme, one with ( $I_{SH}^B$ ) and one without ( $I_{SH}^0$ ) static bias voltage applied ( $V_{bias}^{DC}$ ), with the aid of Eq. (5.14), it turns out that the THz electric field can be evaluated as:

$$E_{THz} = \frac{2E_{bias}^{DC}}{\Delta I} \approx \frac{2V_{bias}^{DC}}{\varepsilon_{DC}G\Delta I} \quad (5.15)$$

where  $\overline{\Delta I} = (I_{SH}^B - I_{SH}^0) / I_{SH}^0$  is the relative change of TFISH intensity and where we assumed that

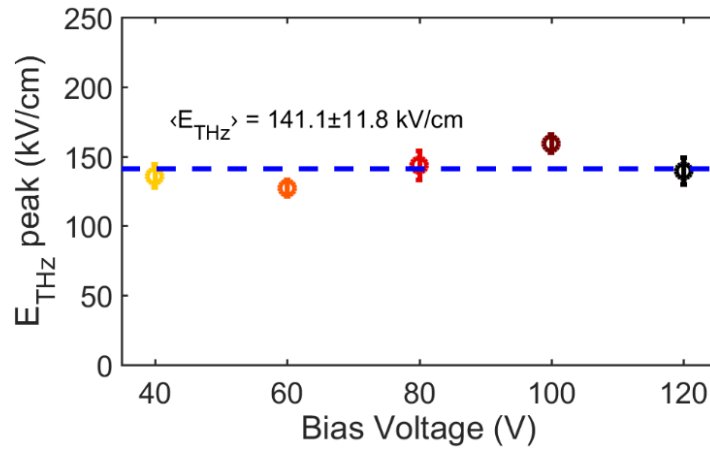


**Figure 4.10.** Evaluation of the THz electric field peak by means of Eq. (5.15), for different values of the bias voltage. The dashed blue line indicates the average THz peak value.

in the framework of simple capacitor model, the bias electric field is equal to the ratio between the effective bias voltage ( $V_{bias}^{DC} / \varepsilon_{DC}$ , being  $\varepsilon_{DC} \approx 7$  the static dielectric constant of PECVD-grown SiN [89]) and the slit width  $G$ . By means of Eq. (5.15), we evaluated the THz electric field in the slit for each bias voltage value and reported the numbers in Fig. 4.10. The average THz electric field peak of all the measurements is  $E_{THz}^{peak} = 142 \pm 12$  kV/cm, as pointed out by the blue dashed line in Fig. 4.10. By considering the Fresnel losses at the interface air/SiN ( $t_{air \rightarrow SiN}$

= 58% in terms of electric field, assuming  $n_{SiN} \approx 2.45$ ) and the previously evaluated FE = 6.1 (see section 4.4.1), such a peak value is consistent with the above-mentioned THz peak value measured in air at the detector position ( $\sim 43$  kV/cm). Incidentally, this value is quite high, meaning that the FE could be potentially exploited to detect low-intensity THz radiation (with electric field peaks  $< 1$  kV/cm), such as the field generated via either OR or PC antennas, which are barely accessible via standard ABCD. We also stress the fact that in order to evaluate the electric field peak strength, we have focused all the THz power into the device, since the only limitation is related to the dielectric strength of SiN ( $> 1$  MV/cm), while for EOS carried out in a 500- $\mu$ m-thick ZnTe, the maximum electric field strength measurable before distortions occur is  $< 20$  kV/cm [1], [115]. We clarify that the DC breakdown in air cannot be triggered by the THz pulse, because its pulse duration is very short ( $< 1$  ps) compared to the repetition rate (1 kHz). Therefore, the average field strength (proportional to the duty cycle,  $\sim 10^{-7}$  %) is very low. Conversely, the impulse breakdown occurs for much more elevated field strengths [137], [138].

# Conclusions

In this thesis, we have presented the very first demonstration of a solid-state technique able to perform the ultra-broadband coherent detection of THz pulses, named the *solid-state-biased coherent detection* (SSBCD) method. Our proposed technique allows for the simultaneous reconstruction of THz radiation amplitude and phase, the bandwidth of which can extend over two decades, i.e. in the 0.1-10 THz range and potentially beyond.

In the first Chapter, we have introduced the reader to the THz domain, i.e. that part of the electromagnetic spectrum ranging between the microwave and the optical domain, which was basically unexplored until some decades ago. The interest in this until now inaccessible spectral window has started to rapidly increase in the 1990s, when the development of the femtosecond (fs) laser technology has been acknowledged to be the perfect launching pad for the

implementation of innovative and promising THz sources and detectors. Indeed, optical downconverting processes have demonstrated higher conversion efficiencies with respect to those achievable from upconverting mechanisms associated to microwaves-based techniques. This is due to the high peak intensity reached by fs optical pulses, which increases the yield of the nonlinear interactions occurring in second- ( $\chi^{(2)}$ ) and third-order ( $\chi^{(3)}$ ) media. We have also introduced three main THz spectral regimes, i.e. CW, broadband and ultra-broadband. While microwaves techniques mainly manage CW radiation, optical techniques allow dealing with THz pulses as well. Nevertheless, there is still a fundamental difference depending on whether the THz pulses features single-cycle shapes or long-lasting transients, which corresponds to the case of either continuous (i.e. gap-free) THz spectra up to 10 THz or bandwidth affected by several spectral artefacts, respectively.

In the second Chapter, we have focused the attention to the current ultra-broadband THz detection techniques, mainly exploiting gas media to accomplish the task of reconstructing unperturbed ultra-wide spectra. Gases have very smooth and ultra-wide frequency responses, since they are not endowed with any lattice structure. Moreover, since gases are continuously renewed, they are not hampered by optical damage thresholds, thus being suitable for high power applications. The nonlinear interaction between THz and optical pulses involves third-order nonlinear effects. Among others, an important  $\chi^{(3)}$ -based process has been called THz-Field Induced Second Harmonic generation (TFISH). Essentially, the THz electric field breaks the symmetry of the gas, thus resulting in a THz-driven second-order behavior, which induces the frequency doubling of an optical probe beam when it is overlapped in time and space with the THz wave. However, in this simple scenario, the TFISH intensity is only proportional to the THz intensity, thus losing the phase information. To overcome this problem, three main methods have been proposed: air-breakdown coherent detection, optically biased coherent detection (OBCD) and air-biased coherent detection (ABCD). In the first method, the coherence is achieved by significantly increasing the probe intensity focused in air, up to values inducing tunneling ionization. The SH component of the white light emitted by the so-generated plasma filament beats with the TFISH beam and gives rise to a term proportional to the THz electric field. Similarly, OBCD exploits the beating between the TFISH beam with the SH of the probe

beam, the latter being properly generated in a second-order crystal, so to be temporally aligned with the TFISH pulse. Conversely to the air-breakdown method, the OBCD technique allows of the reconstruction of the phase of the THz transient (for SH intensity sufficiently high) without the introduction of spectral features, yet requiring a relatively high probe energy. In the ABCD technique, the THz pulse is revealed by exploiting a heterodyne mechanism, where the TFISH beam (at the same repetition rate of the THz pulses) is beaten with a DC electric-field-induced second harmonic (EFISH) term. The latter is generated by applying an external static electric field, according to the same principle of TFISH, yet modulated at a frequency equal to half of the repetition rate of the THz pulses. Therefore, by performing the detection by means of a lock-in amplifier synchronized at the EFISH modulation frequency (heterodyne scheme), only the cross term generated by the beating of the two beams (proportional to the THz electric field) is acquired, with no constraint on either optical energy or DC electric field strength. In particular, we have explored some variants of the ABCD technique in many details, since it has been so far considered the benchmark in the area of THz ultra-broadband coherent detection. We have explained its advantages with respect to other techniques, and highlighted the drawbacks and limitations, addressed while implementing our technique.

In the third Chapter, we have presented our new approach to the ultra-broadband THz coherent detection, called SSBCD technique, which relies on the same operating principle of ABCD. SSBCD is operated via CMOS-compatible devices, as, in the case of the first two generations, they were realized on a silica platform, which features a third-order nonlinear coefficient three orders of magnitude higher than that of air. This means that it is possible to achieve the same TFISH yield, by now using a much lower optical energy and in a more compact, micro-sized structure. Moreover, the CMOS technology allows for the direct deposition of metal contacts on such planar structures, thus easily delivering the bias voltage necessary to operate the heterodyne mechanism. Since the two metal contacts can be realized in such a way to form a slit between them as narrow as few microns or less, which can then be filled with PECVD silica, we have distinguished between first (30- $\mu\text{m}$ -wide slit) and second (3- $\mu\text{m}$ -wide slit) generation devices. One of the main advantages was the possibility to apply extremely high bias electric fields, since the dielectric strength of silica is higher than 10 MV/cm, thus greatly enhancing

the heterodyne signal. We have shown that the main design parameter of these structures was the silica cover layer, which results from the trade-off between the triggering of discharge in the air (happening for too thin layers) and phase-mismatch affecting the pulses propagating in an excessively thick silica slab. By performing static simulations and studying the coherent length of the FWM process giving rise to the TFISH in silica, we have determined the proper value of the silica cover layer. The first structure demonstrated comparable performance with the ABCD, for the same operating conditions (such as THz electric field strength, as well as THz and probe focusing), yet employing half of the bias voltage and more than two orders of magnitude less probe energy. However, its temporal and spectral responses were affected by the appearance of some artefacts (multi-cycle waveform and a large notch around 2.5 THz), which have been ascribed to an etalon resonance occurring inside the 30- $\mu\text{m}$ -thick cover layer. Moreover, such a thickness badly fulfilled the phase-matching condition, thus resulting in a relatively poor TFISH generation. On the other hand, the second generation allowed to achieve a higher dynamic range with respect to that of ABCD, due to the reduced slit width and cover layer thickness, and this without showing any spectral artefact. The best operating condition for this second form of SSBCD devices have been achieved for a bias voltage of 300 V only and an optical energy of 100 nJ, which are one and three orders of magnitude lower than those employed in standard ABCD, respectively. We have also compared the SSBCD second generation with a widely employed solid-state technique, i.e. EOS operated in either GaP or ZnTe crystals, considered the state-of-the-art in the THz coherent detection area. We have shown that, even though the differential scheme underlying EOS offers better noise performance, some inherent detrimental effects involving the lattice structure and dispersion of the Pockels crystals prevent the unaffected detection of THz spectra as wide as 10 THz, regardless of the type of crystal. On the contrary, silica does not show any phononic resonance below 20 THz, thus revealing a quite flat frequency response in the whole THz window.

In the last Chapter, we have shown the implementation of the SSBCD technique operated by means of the third generation devices, fabricated using a deep sub-wavelength thin film of PECVD silicon nitride (SiN). Such a material has a third-order susceptibility more than one order of magnitude higher than that of silica, while maintaining a dielectric strength in the order

of  $\sim$ MV/cm. However, since SiN had never been explored in the THz range, mainly because the thicknesses commonly deposited via PECVD are much smaller than the THz wavelengths, we first managed to measure its refractive index and absorption coefficient, which is a mandatory information to properly design the cover layer of the SSBCD device. To accomplish this task, we have exploited the properties of a differential THz-TDS (DTDS) system. Operatively, a DTDS system is able to resolve the very small phase change induced on the THz waveform by a sub-wavelength thickness of the material under study. Since the measured SiN refractive index was higher ( $\sim$ 2.45) than that of silica ( $\sim$ 2) and the dispersion shown in the optical domain is higher than silica as well, the coherence length for the FWM process resulted to be  $\sim$  2  $\mu$ m only. Therefore, the SiN-based SSBCD device has been endowed with a 1- $\mu$ m-thick SiN cover layer only and, correspondingly, a 1- $\mu$ m-wide slit between two aluminum pads. Such a narrow slit causes a reshaping of the THz transient, because of the non-negligible field enhancement (FE) due to the funneling effect. Hence, we carried out simulations by taking into account the frequency behavior of our experimental ultra-broadband THz set-up, so to estimate an average FE = 6.1. Experimental results demonstrated the functionality of this new structure with bias voltages as low as 10 V, and an optical probe energy down to 10 nJ, both being totally unprecedented for this type of detection mechanism. Moreover, by measuring the THz electric field peak on the slit (near field) and that retrieved via EOS in a GaP crystal placed on the same position of the SSBCD device, we calculated a ratio the value of which is in good agreement with the value of the FE predicted by simulations. Finally, we have shown the possibility to carry out the SSBCD technique with a homodyne scheme, where the lock-in amplifier reference is the same of the THz beam chopping frequency, while the bias voltage is kept constant (DC). As the DC voltage increases, the THz waveform is gradually converted from the incoherent shape to a bipolar transient which resembles the pure coherent THz pulse. A good coherence has been reconstructed for a value of 100 V.

In conclusion, our detectors enable the possibility to operate the SSBCD technique with bias voltage switching at higher frequencies ( $>$  10 kHz), easily provided by cost-effective low voltage amplifiers. This potentially makes the SSBCD technique capable to improve the noise performance of ultra-broadband TDS systems, thus competing with PCSs, which instead suffer

from limited, notch-affected bandwidth responses ( $< 7$  THz). Moreover, the reduced probe power opens up a new scenario of ultra-broadband applications where the optical beam is generated by high repetition rate laser oscillators ( $< 100$  nJ,  $> 1$  MHz), which feature a valuable beam stability and low pulse energy fluctuations, key aspects to boost the performance of low-noise portable THz systems. Finally, the unique advantage of the CMOS compatibility enables the integration of these type of SSBCD devices in a number of diverse applications. To name a few, they can be employed with other type of planar designs, e.g. metamaterial-based, consisting of multi-layer structures that can tune the spectral response, directly realized onto the device, thus adding application-specific features to the device. We envisage that such features will eventually enable the possibility to realize on-chip solutions that can allow for real-time signal processing of the incident THz wave.

# Conclusions

Dans ce travail de thèse, nous avons présenté la toute première démonstration d'une technique à l'état solide capable d'effectuer la détection cohérente d'impulsions THz à bande ultra-large, appelée solid-state-biased coherent detection (SSBCD). Notre technique proposée permet la reconstruction simultanée de l'amplitude et de la phase des rayons THz (d'où le terme «cohérent»), dont la bande passante s'étend sur deux décades, c'est-à-dire entre 0.1-10 THz et même au-delà potentiellement.

Dans le premier chapitre, nous avons présenté au lecteur le domaine THz qui est la partie du spectre électromagnétique comprise entre le domaine des micro-ondes et le domaine optique, qui a été fondamentalement inexploré jusqu'il y a quelques décennies. L'intérêt, pour cette partie jusqu'ici inaccessible du spectre électromagnétique, a commencé à augmenter rapidement dans les années 1990, lorsque le développement de la technologie laser femtoseconde (fs) a été

reconnu comme le tremplin parfait pour la mise en œuvre de sources et de détecteurs à fréquences THz innovants et prometteurs. En effet, les procédés de conversion optique ont montré des rendements de conversion supérieurs à ceux obtenus grâce aux techniques de conversion ascendante des méthodes basées sur les micro-ondes, grâce à l'intensité maximale élevée obtenue par les impulsions optiques femtoseconde, qui augmente le rendement des interactions non-linéaires dans les matériaux du deuxième ( $\chi(2)$ ) et troisième ordre ( $\chi(3)$ ). Nous avons également introduit trois principaux schémas spectraux THz, à savoir CW (continuous-wave), bande large et bande ultra-large. Alors que les techniques de micro-ondes conduisent principalement à la gestion des radiations CW, les techniques optiques permettent également de traiter les impulsions THz. Néanmoins, il existe toujours une différence fondamentale si les impulsions THz présentent des cycles simples ou des états transitoires de longue durée, ce qui correspond respectivement au spectre THz continu (sans espace) jusqu'à 10 THz ou à la bande passante affectée par plusieurs artefacts spectraux.

Dans le deuxième chapitre, nous avons focalisé l'attention sur certaines techniques de détection THz à très haut débit, exploitant principalement les gaz, pour accomplir la tâche de reconstruction de spectres ultra-larges non-perturbés. Les gaz ont des réponses en fréquence graduelles et ultra-larges, puisqu'ils ne sont dotés d'aucune structure cristalline. De plus, comme les gaz sont continuellement renouvelés, ils ne comportent pas de seuils d'endommagement optique, ce qui les rend particulièrement adaptés aux applications à forte puissance. L'interaction non-linéaire entre les impulsions THz et les impulsions optiques implique des effets non-linéaires du troisième ordre. Un tel processus basé sur  $\chi(3)$  a été nommé THz-field-induced-second-harmonic-generation (TFISH). Essentiellement, le champ électrique THz brise la symétrie du gaz, ce qui entraîne un comportement du second ordre lié au THz, qui induit le doublage de fréquence d'un faisceau de sonde optique, lorsqu'il se chevauche avec l'onde THz dans le temps et l'espace. Cependant, dans ce scénario simple, l'intensité du TFISH est seulement proportionnelle à l'intensité THz, perdant ainsi l'information de phase. Pour surmonter ce problème, trois méthodes principales ont été proposées: la air-breakdown coherent detection, optically-biased coherent detection (OBCD) et air-biased coherent detection (ABCD). Dans la première méthode, la cohérence est obtenue en augmentant fortement

l'intensité de la sonde focalisée dans l'air, jusqu'à des valeurs induisant l'ionisation tunnel. La composante SH de la lumière blanche émise par le filament de plasma ainsi généré bat avec le faisceau TFISH et donne lieu à un terme proportionnel au champ électrique THz. De même, l'OBCD exploite le battement entre le faisceau TFISH et le SH du faisceau sonde, ce dernier étant correctement généré pour être aligné temporellement avec l'impulsion TFISH. Contrairement à la méthode de décomposition de l'air, pour une intensité SH suffisamment élevée, la technique OBCD permet de reconstruire la phase de l'état transitoire THz sans l'introduction de caractéristiques spectrales, tout en nécessitant une énergie de sonde relativement élevée. Dans la technique ABCD, l'impulsion THz est révélée en exploitant un mécanisme hétérodyne, où le faisceau TFISH (à la même fréquence de répétition des impulsions THz) est amené à se battre avec un second terme induit par un champ électrique DC (electric-field-induced second harmonic generation, EFISH), généré selon le même principe de TFISH, mais modulé à une fréquence égale à la moitié de la répétition des impulsions THz. Par conséquent, en effectuant la détection au moyen d'un amplificateur synchronisé avec la fréquence de modulation EFISH (schéma hétérodyne), seul le terme croisé généré par le battement des deux faisceaux (proportionnel au champ électrique THz) est acquis, sans contrainte sur l'énergie optique ou l'intensité du champ électrique continu. En particulier, nous avons exploré certaines variantes de la technique ABCD en détails, puisqu'elle a été jusqu'ici considérée comme la référence dans le domaine de la détection THz à très haut débit cohérent. Nous avons expliqué ses avantages par rapport aux autres techniques, mais aussi mis en évidence les inconvénients et les limites que nous avons réussi à résoudre, aboutissant ainsi à la mise en œuvre de notre technique.

Dans le troisième chapitre, nous avons présenté notre nouvelle approche de la détection cohérente THz à très haut débit, c'est-à-dire la technique SSBCD qui, en première instance, repose sur le même principe de fonctionnement d'ABCD. Le SSBCD est exploité via des dispositifs compatibles avec CMOS, car, dans le cas des deux premières générations, ils ont été construits sur une plate-forme de silice qui présente un coefficient non-linéaire du troisième ordre supérieur de trois ordres de grandeur à celui de l'air. Cela signifie qu'il est possible d'atteindre le même rendement EFISH, en utilisant maintenant une énergie optique beaucoup

moins élevée et dans une structure micro-dimensionnelle plus compacte. Deuxièmement, la technologie CMOS permet le dépôt direct de contacts métalliques sur de telles structures planaires, délivrant ainsi facilement la tension de polarisation nécessaire pour faire fonctionner le mécanisme hétérodyne. Puisque les deux contacts métalliques peuvent être réalisés de manière à former entre eux une fente aussi étroite que quelques microns ou moins et ensuite remplis de silice grandi par PECVD, nous avons distingué une première (fente de 30  $\mu\text{m}$  de largeur) et une seconde (fente de 3  $\mu\text{m}$  de largeur) génération de dispositif. Ceci, à son tour, implique la possibilité d'appliquer un champ électrique de polarisation extrêmement élevé, puisque la rigidité diélectrique de la silice est supérieure à 10 MV/cm, améliorant ainsi le signal hétérodyne. Nous avons montré que le paramètre de conception principal de ces structures était la couche de couverture de silice, qui résulte du compromis entre le déclenchement de décharge dans l'air (se produisant pour des couches trop minces) et le déphasage affectant l'impulsion se propageant dans des plaques de silice trop épaisses. En effectuant des simulations statiques et en étudiant la longueur cohérente du processus FWM donnant lieu à l'EFISH dans la silice, nous avons déterminé la valeur correcte de la couche de couverture de silice. La première structure a démontré des performances comparables à celles de l'ABCD opéré dans les mêmes conditions expérimentales (telles que champ THz, THz et focalisation de la sonde), mais employant la moitié de la tension de polarisation et plus de deux ordres de grandeur de moins que l'énergie de la sonde optique. Cependant, ses réponses temporelles et spectrales ont été affectées par l'apparition de certains défauts (forme d'onde multi-cycle et une grande encoche autour de 2.5 THz), attribués à une résonance d'étalon se produisant à l'intérieur de la couche de couverture de 30  $\mu\text{m}$ . De plus, une telle épaisseur remplissait mal la condition d'adaptation de phase, ce qui entraînait une génération de TFISH relativement médiocre. D'autre part, la seconde génération a permis d'atteindre des performances plus élevées que celles de ABCD en termes de dynamique, grâce à la largeur réduite de la fente et à l'épaisseur de la couche de couverture et sans apparition de défauts spectraux. Les meilleures conditions de fonctionnement pour cette seconde forme de dispositifs SSBCD ont été obtenues pour une tension de polarisation de seulement 300 V et une énergie optique de 100 nJ, qui sont respectivement inférieures d'un et trois ordres de grandeur à celles utilisées dans la norme ABCD. Nous avons également comparé la seconde génération de SSBCD avec l'autre technique connue à l'état

solide, c'est-à-dire EOS, opérée dans des cristaux de GaP ou de ZnTe, considérée comme l'état de l'art dans la zone de détection cohérente THz. Nous avons montré que, bien que le schéma différentiel sous-jacent EOS offre de meilleures performances acoustiques, certains effets néfastes inhérents à la structure réticulaire et à la dispersion des cristaux de deuxième ordre empêchent la détection non-affectée des spectres de 10 THz, quel que soit le type de cristal. Au contraire, la silice ne montre aucune résonance phononique inférieure à 20 THz, révélant ainsi une réponse fréquentielle assez plate dans toute la fenêtre THz.

Dans le dernier chapitre, nous avons montré la mise en œuvre de la technique SSBCD opérée à l'aide d'un dispositif de troisième génération comportant un film profond de sous-longueur d'onde en nitrure de silicium (SiN), grandi par PECVD. Un tel matériau a une susceptibilité de troisième ordre supérieure de plus d'un ordre de grandeur à celle de la silice, tout en maintenant une rigidité diélectrique de l'ordre de  $\sim$ MV/cm. Cependant, puisque le SiN n'a jamais été exploré dans la région THz, principalement parce que les épaisseurs communément déposées par PECVD sont beaucoup plus petites que les longueurs d'onde THz, nous avons d'abord réussi à mesurer son indice de réfraction et son coefficient d'absorption, qui sont des informations obligatoires pour concevoir correctement la couche de couverture du dispositif SSBCD. Pour accomplir cette tâche, nous avons exploité les propriétés d'un système THz-TDS différentiel (DTDS). Fonctionnellement, un système DTDS est capable de résoudre le très petit changement de phase induit sur la forme d'onde THz par une épaisseur de sous-longueur d'onde du matériau étudié. Puisque l'indice de réfraction SiN mesuré était plus élevé ( $\sim$  2.45) que celui de la silice ( $\sim$  2) et que la dispersion dans le domaine optique était plus élevée que celle de la silice, la longueur de cohérence pour le procédé FWM était d'environ 2  $\mu$ m. Par conséquent, le dispositif SSBCD à base de SiN a été recouvert par une couche de SiN de seulement 1  $\mu$ m d'épaisseur et d'une fente de 1  $\mu$ m de large entre deux blocs d'aluminium. Une telle fente étroite provoque une réorganisation de l'état transitoire THz, en raison de l'augmentation du champ non-négligeable dû à l'effet d'entonnoir (FE). Nous avons donc effectué des simulations en prenant en compte du comportement en fréquence de notre configuration expérimentale THz à bande ultra large, afin d'estimer un FE moyen de 6.1. Les résultats expérimentaux ont démontré la fonctionnalité de cette nouvelle structure avec des tensions de polarisation aussi faibles que

10 V et une énergie de sonde optique jusqu'à 10 nJ, les deux résultats étant totalement inédits pour ce type de mécanisme de détection. De plus, en mesurant le pic du champ électrique THz au niveau de la fente (champ proche) et en l'extrayant via EOS dans un cristal GaP placé sur la même position que le dispositif SSBCD, nous avons calculé un ratio en bon accord avec la valeur de la FE prédite par des simulations. Enfin, nous avons montré la possibilité de réaliser la technique SSBCD avec un schéma homodyne, où le signal de référence de l'amplificateur de verrouillage est le même que la fréquence de découpage du faisceau THz, tandis que la tension de polarisation est maintenue constante (DC). Lorsque la tension continue augmente, l'onde THz est progressivement convertie de l'état incohérent en un état transitoire bipolaire qui ressemble à l'impulsion THz cohérente pure. Une bonne cohérence a été reconstruite pour une valeur de 100 V.

En conclusion, nos dispositifs de détection offrent la possibilité de faire fonctionner la technique SSBCD avec une commutation de tension de polarisation à des fréquences plus élevées ( $> 10$  kHz), facilement fournie par des amplificateurs basse tension économiques. Cela rend potentiellement le technique SSBCD capable d'améliorer les performances de bruit des systèmes TDS à très haut débit, rivalisant ainsi avec les PCS, qui eux ont une réponses de bande passante limitée et cisailée ( $< 7$  THz). De plus, la puissance réduite de la sonde ouvre la voie à un nouveau scénario d'applications à ultra-haut débit entièrement pompées par des oscillateurs laser à haut-taux de répétition ( $< 100$  nJ,  $> 1$  MHz), caractérisées par une bonne stabilité du faisceau et de faibles fluctuations en énergie d'impulsion, qui sont des facteurs-clé pour améliorer les performances des systèmes THz portables. Enfin, l'avantage unique de la compatibilité CMOS permet l'intégration de ce type de dispositifs SSBCD dans un certain nombre d'applications diverses. Pour n'en nommer que quelques-uns, il peut être employé avec d'autres types de conceptions planaires, par exemple basées sur des métamatériaux constitués de structures multicouches pouvant ajuster la réponse spectrale, directement réalisée sur le système, ajoutant ainsi des fonctionnalités spécifiques à l'application du dispositif. Nous prévoyons que de telles caractéristiques permettront un jour de réaliser des solutions sur puce pouvant permettre le traitement du signal en temps réel de l'onde THz incidente.

# Appendix A

## Two-color plasma THz sources

The generation of ultrashort THz pulses with bandwidth falling in the 0.1-10 THz (or wider) range, has been lately arousing an ever-increasing interest, since they are particularly suitable for several applications spanning from ultra-broadband THz spectroscopy to novel nonlinear interactions induced by the associated extremely high peak intensities, for instance in graphene or other media [139]–[142]. So far, the most reliable way to achieve such a kind of THz pulses has been based on electron accelerator-based systems [143], [144]. However, those solutions are quite unpractical, mainly because of the large-scale and optical power demand, that are characteristics of such facilities. On the other hand, remarkable ultra-broadband THz emission has been also demonstrated in laser-induced one [102], [145]–[149] or two-color plasma [36], [100], [101], [106], [131], [150]–[152]. In particular, the latter allows for very high conversion efficiencies, in the order of  $10^{-3}$  [98], and results in the generation of highly directional THz radiation. The mechanism that gives rise to the complete THz emission from a two-color filament has been a controversial subject and under debate for a long time. Only recently, it has been fully understood and explained in terms of both simulations and experimental

investigations [100]. Essentially, the THz pulses emitted by a two-color plasma filament are recognized to be due to three different contributions: four-wave rectification (Kerr or bound electron response), tunneling ionization which gives rise to plasma photocurrents, as well as longitudinal and transverse plasma waves. The first term is referred as a contribution from neutrals, whereas the other two are due to charge motions. We recall that while an ultrashort laser pulsed beam is being focused in the air, its intensity peak increases propagating towards the focus, which induces a modulation of the air refractive index, driven by the Kerr nonlinearity. The beam core, more intense than the wings, induces a spatial phase profile

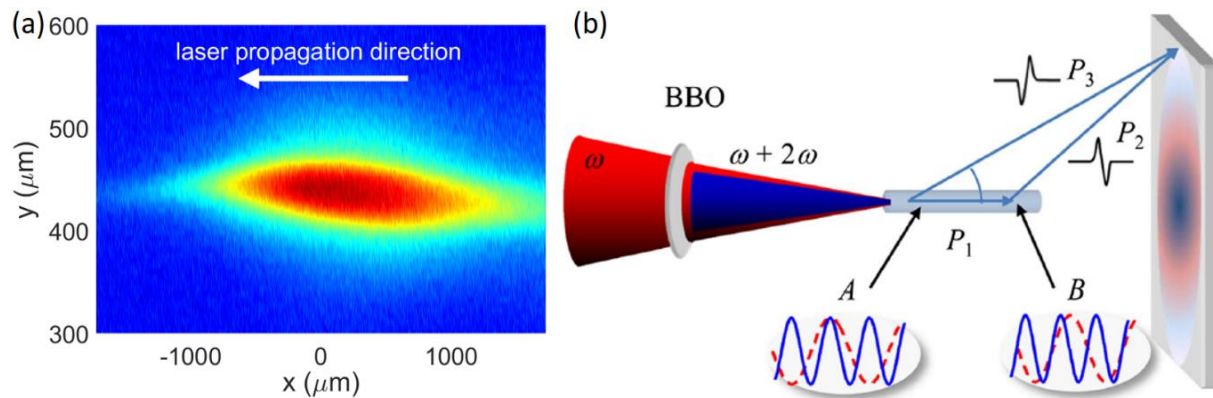


**Figure A.1.** (a) Picture of the fluorescence emitted by a single-color filament generated by a 140 fs, 500  $\mu\text{J}$ , 800 nm pulsed laser, traveling from the right to the left along the x-axis. The image was acquired by means of a CCD camera provided with a 10x objective. (b) Sketch of the generation stage of a typical two-color THz plasma source. The pump beam  $\omega$  is frequency-doubled in a BBO crystal and focused together with its second harmonic to generate a plasma channel (filament). The latter gives rise to a THz radiation with a peak emission direction, which forms the angle  $\theta$  with the propagation axis. (Figure (b) adapted from Ref [101]).

equivalent to that of a focusing lens, resulting in an effect called *self-focusing*, which somewhat speeds up the beam focusing itself. However, at a certain point, the pulse intensity can reach a threshold value, beyond which it starts to ionize air, thus generating a plasma spark. The formation of plasma clamps the peak intensity to approximately the threshold value and tends to hamper the further focusing of the beam, according to a phenomenon known as *de-focusing*. The two concurrent effects counterbalance each other, thus resulting in the so-called plasma filamentation, as shown in Fig. A.1(a). The length of the filament depends on diverse factors,

such as optical energy, focal length, and pulse duration. The longer the focal length, the longer the filament, but the lower its brightness. For a fixed focal length, higher optical energies not always result in a longer filament, as the latter rather tends to grow transversally (volume increase). In the two-color plasma used to generate THz radiation, the fundamental pulse is first traveling through a BBO crystal while is being focused, so to generate a second harmonic beam, which shares the same focal plane of the fundamental beam, as shown in Fig. A.1(b). Moreover, the rotation angle of the BBO crystal can be tuned in order to achieve the proper temporal coherence (i.e., the same arrival time at the focal spot) between the two colors. In light of this

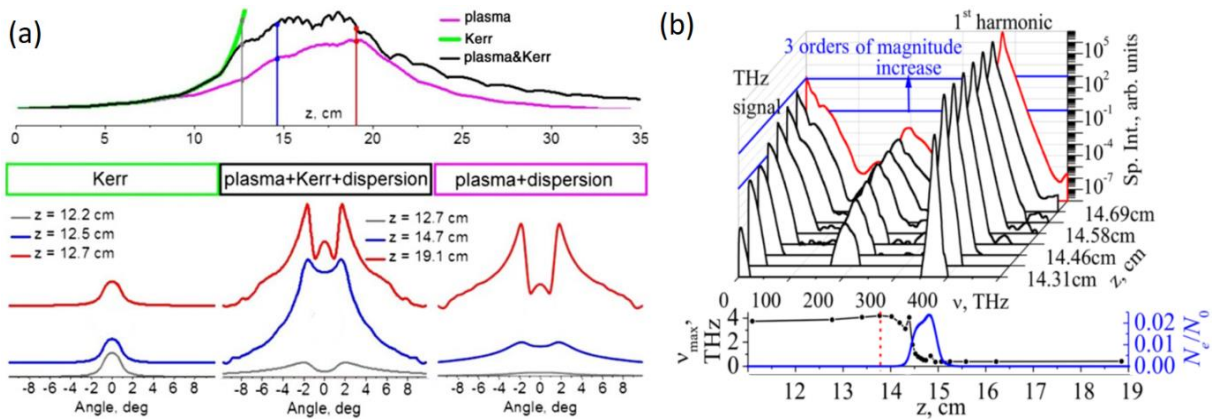


**Figure A.2.** (a) The top subplot shows the simulated intensity trend as the optical beam is being focused by a 20-cm-lens, for the case corresponding to the case of Kerr effect (green line) only, plasma and dispersion only (magenta curve) and all effects together (black line). The laser pulse is characterized by an optical energy of 3.2 mJ and a pulse duration of 54 fs. The three subplots at the bottom show the angular distribution for the THz emission in the three cases at different propagation distances: far from the focus (gray vertical line), close the intensity threshold (blue vertical line) and in front of the focus (red vertical line). (b) The top subplot shows the simulated THz spectra along the propagation axis emitted as the plasma filament is formed. On the wake of the laser pulse, the THz emission driven by the Kerr nonlinearity presents a frequency peak around 4 THz. After the intensity threshold, the power spectrum experiences a sudden increase (as much as three orders of magnitudes) in the low-frequency range, as highlighted by the notch around 25 THz, visible starting at  $z = 12.46$  cm. (Figures adapted from Ref [100]).

brief digression, we can now better understand the origin of the contributions to THz emission stemming from the filament. The top inset in Fig. A.2(a) shows the simulated dynamics of the

intensity increase and plasma formation, respectively, as a 3.2-mJ, 54 fs, NIR beam is focused by a 20-cm-lens. Three cases of (i) pure Kerr effect only (green line), (ii) generation of photocarriers (magenta line), and (iii) both two effects together (black line), are considered [100]. The Kerr effect alone would result in an intensity increase until the so-called catastrophe collapse, which would lead to a virtually infinitive peak energy. The simulation is indeed stopped when the threshold for collapse is reached. Such a level corresponds to the formation of plasma approximately at the beginning of the Rayleigh range. We notice that the actual plasma length is longer than that simulated when the Kerr effect is not taken into account, indicating that the latter plays a crucial role in plasma generation. Indeed, the peak intensity is achieved before the focus, because of the focusing acceleration induced by the Kerr lens. Considering the THz angular emission at three different distances ( $z$ ) indicated by the vertical gray, blue and red lines, the three subplots at the bottom of Fig. A.2(a) can be drawn. Initially, the THz pulse is generated by the neutrals only (Kerr effect) and is completely emitted on axis (the angle indicated in the x-axis is equal to  $\theta$  in Fig. A.1(b)). However, as the plasma defocusing starts to compete with self-focusing, the THz radiation pattern shows two peaks at symmetric positions with respect to the axis, at around  $\theta = \pm 3^\circ$ . In particular, these two peaks are much more intense than the on-axis field. For comparison purpose, the most right subplot shows that, if we neglect the Kerr nonlinearity altogether, the THz emission from the plasma essentially equals the real configuration where both effects take place, confirming that the THz far-field is almost entirely determined by the photocurrent transients. Correspondingly, Fig. A.2(b) shows the THz spectrum evolution as the optical pump beam reaches the focus position. More in detail, the top inset shows that far from the focus, the THz spectrum is resulting from four-wave rectification, with a relatively high-frequency peak of 4 THz (bottom subplot). As the optical beam approaches the focus, the sudden and steep increase of the photocarriers gives rise to plasma THz emission featured by a low-frequency content, which is up to three orders of magnitude higher than the high-frequency contribution due to the neutrals. This causes a dramatic reshaping of the entire THz spectrum and the peak frequency drops to around 0.5 THz, consistent with the plasma frequency  $\omega_{plasma} = \sqrt{e^2 N_e / m \epsilon_0}$ , where  $e$  is the fundamental charge,  $m$  the electronic mass,  $\epsilon_0$  the absolute permittivity and  $N_e$  the typical photocarriers density of

$\sim 10^{16} \text{ cm}^{-3}$  at the pressure of 1 atm. Such a predominant spectral contribution completely hides that generated by the nonlinear polarization (Kerr). The reason behind the low-frequency peak of the plasma contribution is the long-lasting nature of the plasma waves induced by the photoionization of air, in the range of 1 ps [100]. For the sake of completeness, we should say that the plasma waves generate THz radiation even in the transverse direction [149], which however results to be much smaller than that emitted paraxially in the forward direction [100]. The origin of the latter emission peaks can be explained in terms of phase matching condition. Indeed, as the pulse propagates in the plasma channel depicted in Fig. A.1(b), the relative phase retardation  $\phi(\omega)$  between the fundamental ( $\omega$ ) and the second harmonic ( $2\omega$ ) beams is:

$$\phi(\omega) = \omega(n_{\omega} - n_{2\omega})l / c + \phi_0 \quad (\text{A.1})$$

where  $l$  is the filament length and  $\phi_0$  is the relative phase at the starting point of the plasma channel due to both BBO phase-matching condition and the air dispersion. Furthermore,  $n_{\omega, 2\omega}$  are the filament refractive indexes at the two optical frequencies, given by the sum of the refractive indices of air and plasma. We mention that the plasma contribution to the refractive index is purely imaginary for frequencies lower than the plasma frequency, as expressed by the relation  $n_{\text{plasma}, \omega} \approx \sqrt{1 - \omega_{\text{plasma}}^2 / \omega^2}$  [101]. Therefore, since dispersion is not negligible within the plasma, we can define a dephasing length  $l_d$ , which indicates the propagation distance over which the THz pulse does not undergo polarity inversion (i.e.,  $0 \leq \phi \leq \pi$ ):

$$l_d = \frac{\lambda}{2(n_{2\omega} - n_{\omega})} \quad (\text{A.2})$$

where  $\lambda = 2\pi c / \omega$  is the optical wavelength. For example, for the experimental conditions mentioned above, such a value is approximately  $l_d \approx 22$  mm. Therefore, as for any other nonlinear phenomena involving phase-matching condition, the THz yield oscillates in the on-axis direction because of the continuous variation of the diphas in Eq. A.1. Let us consider the points A and B indicated on the plasma channel in Fig. A.1(b), for the case of a filament length  $l \geq l_d$ . Here, given that the distance between A and B approaches  $l_d$ , the THz pulse has a different polarity in the two points. Let us also consider a generic point on a plane orthogonal to the propagation axis and placed in the far field. Here, constructive interference is achieved if the

path difference (expressed in the vectorial form)  $\Delta l = \mathbf{P}_3 - (\mathbf{P}_1 + \mathbf{P}_2)$  is an odd multiple of half the THz wavelength ( $\lambda_{THz}$ ), i.e.:

$$\Delta l = (m + 1/2) \lambda_{THz} \quad (\text{A.3})$$

where  $m$  is an integer. By considering the triangle in Fig. A.1(b), it results that for the zero order of constructive interference, i.e. for  $m = 0$ , the angle  $\theta$  has to satisfy the following condition:

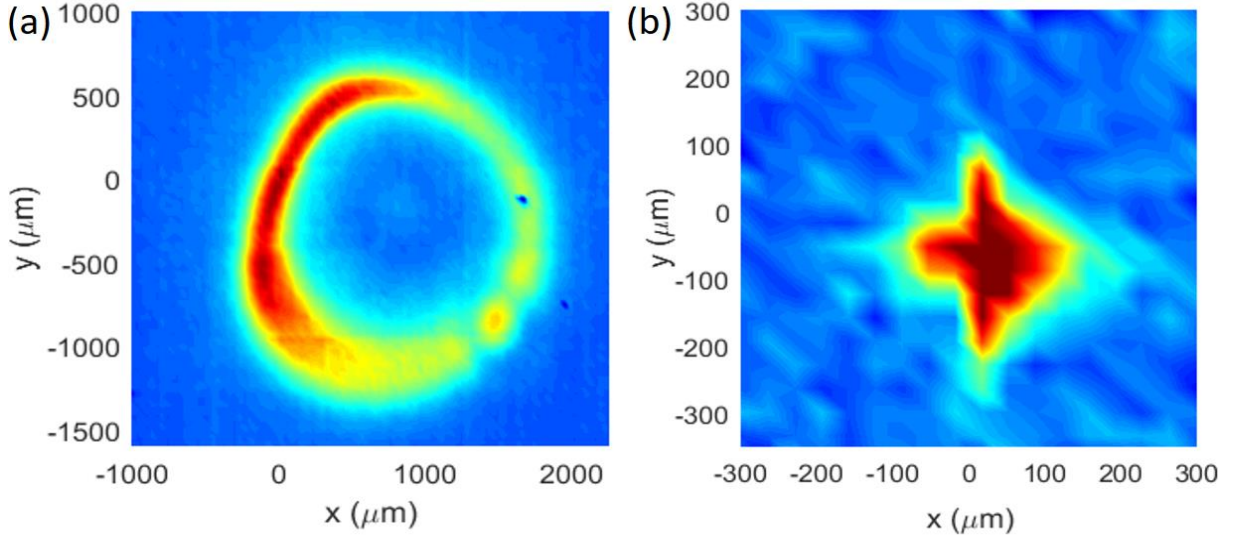


**Figure A.3.** 2D colormaps showing (a) the transversal profile of the THz beam in the far-field region, generated by a two-color plasma driven by a pulsed laser with the same parameters of Fig. A.1(a). Such a profile is acquired approximately 3 cm beyond the plasma spark, in the forward direction. We note the typical donut-shaped as a result of the off-axis phase matching condition. (b) THz beam spot on the focus of a 2-inch 90° off-axis mirror. The typical cross-shape is a consequence of the focusing (spatial Fourier transformation) of the beam profile in (a). The pitch size for both pictures is 35  $\mu\text{m}$ .

$$\cos \theta \approx 1 - \frac{\lambda_{THz}}{2l_d}. \quad (\text{A.4})$$

If we take into account that the angular dispersion is generally smaller than 10° for most of the experimental conditions, we can expand the cosine function in a Taylor series as:

$$\cos \theta \approx 1 - \frac{\theta^2}{2} = 1 - \frac{\lambda_{THz}}{2l_d} \Rightarrow \theta \approx \sqrt{\frac{\lambda_{THz}}{l_d}} \quad (\text{A.5})$$

which has the form of the angular-dependent radiation pattern employed in section 4.4.1. Finally, we mention that this type of phase-matching condition can only hold if the transversal size of the source (filament)  $D$ , its length  $l$  and the THz wavelength fulfill the following relation:

$$D \leq \lambda_{THz} \leq l \quad (\text{A.6})$$

Throughout this thesis, we had  $D = 100 \mu\text{m}$ ,  $l = 7 \text{ mm}$  and  $\lambda_{THz} \approx 300 \mu\text{m}$ , thus certainly complying with the condition in Eq. (A.6). Indeed, Fig. A.3(a) shows the transversal profile of the THz beam, acquired by means of a THz camera (MICROXCAM-384I-THZ) placed  $\sim 3 \text{ cm}$  after the filament and having a spatial resolution of  $35 \mu\text{m} \times 35 \mu\text{m}$  (pixel size). We clearly observe the typical ring shape assumed by the THz beam due to the conical emission, where the on-axis emission is basically negligible [153]. Moreover, the uneven intensity distribution of the intensity around the ring does not seem to be due to a misalignment of the system, since it is also observed in literature and is still under investigation [154]. Finally, Fig. A.3(b) shows the THz spot recorded on the focus of the last 2-inches off-axis mirror in the set-up of Fig. 3.5. We note that the relatively rough resolution does not really allow to properly resolve the 2D Gaussian profile of the spot, since its average FWHM diameters are in the order of  $100 \mu\text{m}$  in both the x- and y-directions, which occupy only 3-4 pixels of the THz camera. We also note that the THz spot better resembles the shape of a cross, which is close to the natural focused form of the beam profile in Fig. A.3(a). Indeed, a better focusing could be possible by replacing the parabolic off-axis mirror with a silicon axicon [155].



# Appendix B

## A.1 List of articles published in scientific journals

1. A. Tomasino, R. Piccoli, Y. Jestin, S. Delprat, M. Chaker, M. Peccianti, M. Clerici, A. Busacca, L. Razzari and R. Morandotti, “*Ultra-broadband terahertz coherent detection via silicon nitride-based deep sub-wavelength metallic slit*”, manuscript accepted (APL Photonics, 2018).
2. A. Tomasino, A. Mazhorova, M. Clerici, M. Peccianti, S. P. Ho, Y. Jestin, A. Pasquazi, A. Markov, X. Jin, R. Piccoli, S. Delprat, M. Chaker, A. Busacca, J. Ali, L. Razzari and R. Morandotti, “*Solid-state-biased coherent detection of ultra-broadband terahertz pulses*”, *Optica* **4**, 1358 (2017).
3. G. Adamo, **A. Tomasino**, A. Parisi, D. Agrò, S. Stivala, L. Curcio, A. Andò, R. Pernice, C. Giaconia, A. C. Busacca, M. C. Mazzillo, D. Sanfilippo, and G. Fallica, “*Electro-optical characterization of new classes of silicon carbide UV photodetectors*”, *IEEE Photon. J.* **6**, 0600707 (2014).

4. G. Adamo, D. Agrò, S. Stivala, A. Parisi, **A. Tomasino**, L. Curcio, C. Giaconia, A. Busacca, and G. Fallica, “*Silicon photomultipliers signal-to-noise ratio in the continuous wave regime*”, IEEE J. Sel. Topics Quantum Electron., **20**, 3804907 (2014).
5. A. C. Busacca, S. Stivala, L. Curcio, **A. Tomasino**, G. Assanto, “*Backward frequency doubling of near infrared picosecond pulses*”, Opt. Express **22**, 7544 (2014).
6. **A. Tomasino**, A. Parisi, S. Stivala, P. Livreri, A. C. Cino, A. C. Busacca, M. Peccianti, R. Morandotti, “*Wideband THz time domain spectroscopy based on optical rectification and electro-optic sampling*”, Sci. Rep. **3**, 3116 (2013).

## A.2 List of conference proceedings

1. **A. Tomasino**, R. Piccoli, Y. Jestin, S. Delprat, M. Chaker, M. Peccianti, M. Clerici, A. Busacca, L. Razzari, and R. Morandotti, “*Deep sub-wavelength SiN-based metallic slit for ultra-broadband THz coherent detection*”, Photonics North 2018, 5-7 June 2018, Montréal, Canada, (oral).
2. G. Balistreri, **A. Tomasino**, V. Aglieri, R. Piccoli, C. Foucher, A. Markov, S. Stivala, A. C. Busacca, R. Carzino, A. Toma, J. Azaña, L. Razzari and R. Morandotti, “*Design and Fabrication of Terahertz Bragg Gratings on Two-Wire Waveguide*”, Photonics North 2018, 5-7 June 2018, Montréal, Canada, (oral).
3. D. Caraffini, **A. Tomasino**, R. Piccoli, Y. Jestin, A. Busacca, L. Razzari, and R. Morandotti, “*Nonlinear frequency mixing between terahertz and optical waves in silica*”, Photonics North 2018, 5-7 June 2018, Montréal, Canada, (oral).
4. **A. Tomasino**, R. Piccoli, Y. Jestin, A. Markov, A. Busacca, L. Razzari, and R. Morandotti, “*Silicon nitride-based deep sub- $\lambda$  slit for ultra-broadband THz coherent detection*”, CLEO: Science and Innovations, 13-18 May 2018, San José, California, USA (oral).
5. **A. Tomasino**, R. Piccoli, D. Caraffini, A. Markov, A. Mazhorova, R. Naccache, F. Vetrone, Y. Jestin, A. Busacca, L. Razzari, and R. Morandotti, “*Ultra-Broadband Terahertz Time Domain Spectroscopy by Solid State Biased Coherent Detection*”, IRMMW 2017, 27<sup>th</sup> Aug – 1<sup>st</sup> September, Cancun, Mexico (oral).
6. **A. Tomasino**, A. Mazhorova, M. Clerici, M. Peccianti, S.-P. Ho, Y. Jestin, A. Pasquazi, A. Markov, X. Jin, R. Piccoli, S. Delprat, M. Chaker, A. Busacca, J. Ali, L. Razzari, and R. Morandotti, “*Coherent Detection of Broadband Terahertz Pulses via CMOS-compatible Solid-State Devices*”, 32nd URSI GASS, 19-26 August 2017, Montréal, Canada (oral).

7. **A. Tomasino**, A. Mazhorova, M. Clerici, M. Peccianti, Y. Jestin, A. Pasquazi, A. Markov, X. Jin, R. Piccoli, S. Delprat, M. Chaker, A. Busacca, L. Razzari, R. Morandotti, “*Ultra-broadband coherent detection of THz pulses via CMOS-compatible devices*”, SIE 2017, 21-23 June 2017, Palermo, Italy (oral).
8. **A. Tomasino**, A. Mazhorova, M. Clerici, M. Peccianti, S.-P. Ho, Y. Jestin, A. Pasquazi, A. Markov, X. Jin, R. Piccoli, S. Delprat, M. Chaker, A. Busacca, J. Ali, L. Razzari, and R. Morandotti, “*Scaling mechanisms in CMOS-compatible sensors for ultra-broadband THz coherent detection*”, Photonics North 2017, 6-8 June 2017, Ottawa, Canada, (poster).
9. G. Balistreri, **A. Tomasino**, S. Stivala, P. Livreri, A. C. Cino and A. Busacca, “*Dependence of Terahertz Emission and Detection in Photoconductive Antennas on Laser Parameters*”, Photonics North 2017, 6-8 June 2017, Ottawa, Canada, (poster).
10. **A. Tomasino**, A. Mazhorova, M. Clerici, M. Peccianti, S.-P. Ho, Y. Jestin, A. Pasquazi, A. Markov, X. Jin, R. Piccoli, S. Delprat, M. Chaker, A. Busacca, J. Ali, L. Razzari, and R. Morandotti, “*Ultra-broadband coherent detection of terahertz pulses via CMOS-compatible solid-state devices*”, CLEO: Science and Innovations, 14-19 May 2017, San José, California, USA (oral).
11. A. Mazhorova, M. Clerici, M. Peccianti, S.-P. Ho, L. Razzari, Y. Jestin, A. Pasquazi, **A. Tomasino**, A. Markov, R. Piccoli, A. Busacca, J. Ali, R. Morandotti, “*Asymmetric Dual-Grating Micro-Slit Configuration for Broadband Solid State Coherent Detection of THz Pulses*”, CLEO: Science and Innovations, 5-10 June 2016, San José, California, USA (oral).
12. **A. Tomasino**, A. Mazhorova, M. Clerici, M. Peccianti, S. P. Ho, L. Razzari, Y. Jestin, A. Pasquazi, A. Markov, A. Busacca, J. Ali, R. Morandotti, “*Ultra-broadband detection of THz pulses via micro-slit array based solid-state device*”, Photonics North 2016, 24-26 May 2016, Québec, Canada, (oral).
13. **A. Tomasino**, A. Mazhorova, M. Clerici, M. Peccianti, S.-P. Ho, L. Razzari, Y. Jestin, A. Pasquazi, A. Markov, R. Piccoli, A. Busacca, J. Ali, R. Morandotti, “*Solid-state broadband detection of THz pulses*”, IONS Québec 2016, 20-22 May 2016, Québec, Canada (poster).
14. **A. Tomasino**, M. K. Mridha, A. Mazhorova, D. Caraffini, H. Breitenborn, M. Clerici, M. Peccianti, L. Razzari, A. C. Cino, S. Stivala, A. Busacca, R. Morandotti, “*Waveguide-Integrated THz Spectral Filter*”, Photonics North 2015, 9-11 June 2015, Ottawa, Canada (oral).
15. **A. Tomasino**, M. K. Mridha, A. Mazhorova, D. Caraffini, H. Breitenborn, M. Clerici, M. Peccianti, L. Razzari, D. Bongiovanni, A. C. Cino, S. Stivala, A. Busacca, R. Morandotti,

- “Two-Wire Waveguide-Based THz Spectral Filter”, FOTONICA 2015, 6-8 May 2015, Turin, Italy (oral).
16. R. Miceli, A. Busacca, V. Rocca, L. Curcio, A. Parisi, A. C. Cino, R. Pernice, A. Ando', G. Adamo, **A. Tomasino**, G. Palmisano, S. Stivala, M. Caruso, G. Cipriani, D. La Cascia, V. Di Dio, G. R. Galluzzo, “*Parametrical study of multilayer structures for CIGS solar cells*”, 3<sup>rd</sup> International Conference on Renewable Energy Research and Applications (ICRERA), 19-22 October 2014, Milwaukee, USA, (oral).
  17. R. Miceli, G. Cipriani, V. Di Dio, C. Spataro, G. R. Galluzzo, V. Rocca, L. Curcio, A. Parisi, A. C. Cino, R. Pernice, A. Andò, G. Adamo, **A. Tomasino**, S. Stivala, A. Busacca, G. Palmisano, D. La Cascia, “*CIGS PV module characteristic curves under chemical composition and thickness variations*”, 3<sup>rd</sup> International Conference on Renewable Energy Research and Applications (ICRERA), 19-22 October 2014, Milwaukee, USA, (oral).
  18. A. C. Busacca, S. Stivala, L. Curcio, **A. Tomasino**, and G. Assanto, “*Backward second-harmonic generation of near infrared picosecond pulses*”, **XX RiNEM (National Meeting of Electromagnetism), 15-18 September 2014, Padova, Italy, (oral)**.
  19. **A. Tomasino**, S. Stivala, A. C. Busacca, M. Peccianti, R. Morandotti, “*Wideband THz time domain spectroscopy set-up based on ultrafast pulsed laser: model and experiments*”, XX RiNEM (National Meeting of Electromagnetism), 15-18 September 2014, Padova, Italy, (poster).
  20. **A. Tomasino**, F. Buccheri, S. Stivala, A. C. Busacca, M. Peccianti, and R. Morandotti, “*A wideband THz time domain spectroscopy table-top system based on ultrafast pulsed laser: model and experiments*”, IRWW-THz (39<sup>th</sup> International Conference on Infrared, Millimeter, and Terahertz Waves), September 14-19, 2014, Tucson, USA, (poster).
  21. D. Agrò, R. Canicattì, M. Pinto, **A. Tomasino**, G. Adamo, L. Curcio, A. Parisi, S. Stivala, N. Galioto, C. Giaconia, A. Busacca “*Design and development of a continuous wave functional near infrared spectroscopy system*”, 3<sup>rd</sup> National Meeting Interaction among Electromagnetic Fields and Biosystems, 2-4 July 2014, Napoli, Italy, (oral).
  22. D. Agrò, G. Adamo, M. Pinto, R. Canicattì, **A. Tomasino**, A. Parisi, S. Stivala, L. Curcio, A. Giordano, C. Giaconia, A. Busacca, “*Design of a portable (CW) fNIRS embedded system*”, SIMAI (Italian Society for the Applied and Industrial Mathematics), Taormina, Italy, July 7-10, 2014 (oral).
  23. D. Agrò, R. Canicattì, **A. Tomasino**, A. Giordano, G. Adamo, A. Parisi, S. Stivala, C. Giaconia, A. C. Busacca, G. Ferla, “*Blood pressure monitoring with a PPG embedded*

- system*”, 46<sup>th</sup> National Meeting of the Italian Electronics Group (GE), June 16-20, 2014, Cagliari, Italy, (oral).
24. D. Agrò, R. Canicattì, M. Pinto, **A. Tomasino**, A. Giordano, N. Galioto, G. Adamo, A. Parisi, S. Stivala, C. Giaconia, A. C. Busacca, “*Development of a CW-fNIRS system for brain monitoring*”, 46<sup>th</sup> National Meeting of the Italian Electronics Group (GE), June 16-20, 2014, Cagliari, Italy, (poster).
  25. G. Adamo, D. Agrò, S. Stivala, A. Parisi, L. Curcio, A. Andò, **A. Tomasino**, C. Giaconia, A.C. Busacca, “*Responsivity measurements of SiC photodiodes*”, 46<sup>th</sup> National Meeting of the Italian Electronics Group (GE), June 16-20, 2014, Cagliari, Italy, (oral).
  26. G. Adamo, D. Agrò, S. Stivala, A. Parisi, **A. Tomasino**, L. Curcio, R. Pernice, C. Giaconia, A.C. Busacca, “*Signal to noise ratio measurements of silicon photomultipliers in the continuous wave regime*”, 46<sup>th</sup> National Meeting of the Italian Electronics Group (GE), June 16-20, 2014, Cagliari, Italy (oral).
  27. **A. Tomasino**, F. Buccheri, S. Stivala, G. Adamo, A. C. Busacca, M. Peccianti, R. Morandotti, “*A wideband THz time domain spectroscopy system based on pulsed laser: model and experiments*”, Photonics North Conference, Montréal, Canada, 28-30 May, 2014, (poster).
  28. G. Adamo, D. Agrò, S. Stivala, A. Parisi, L. Curcio, A. Andò, **A. Tomasino**, C. Giaconia, A.C. Busacca, M. C. Mazzillo, D. Sanfilippo, and G. Fallica “*Electro-optical characterization of silicon carbide schottky photodiodes*”, Photonics North Conference, Montréal, Canada, 28-30 May, 2014, (poster).
  29. G. Adamo, D. Agrò, S. Stivala, A. Parisi, **A. Tomasino**, L. Curcio, R. Pernice, C. Giaconia, A. C. Busacca, and G. Fallica, “*Signal to noise ratio of silicon photomultipliers: a study in the continuous wave regime*”, Photonics North Conference, Montréal, Canada, 28-30 May, 2014, (poster).
  30. A.C. Busacca, S. Stivala, L. Curcio, **A. Tomasino**, G. Assanto, “*Backward second harmonic generation via infrared picosecond pulses*”, 16<sup>th</sup> National Meeting of the Photonic Technologies (FOTONICA2014), 12-14 May 2014, (poster).
  31. G. Adamo, D. Agrò, S. Stivala, A. Parisi, **A. Tomasino**, L. Curcio, R. Pernice, C. Giaconia, A.C. Busacca, G. Fallica, “*Signal to noise ratio measurements of silicon photomultipliers*”, 16<sup>th</sup> National Meeting of the Photonic Technologies (FOTONICA2014), 12-14 May 2014 (oral).

32. G. Adamo, D. Agrò, S. Stivala, A. Parisi, L. Curcio, A. Andò, **A. Tomasino**, C. Giaconia, A.C. Busacca, M. C. Mazzillo, D. Sanfilippo, P. G. Fallica “*Responsivity measurements of SiC schottky photodiodes*”, 16<sup>th</sup> National Meeting of the Photonic Technologies (FOTONICA2014), 12-14 May 2014, (poster).
33. G. Adamo, D. Agrò, S. Stivala, A. Parisi, L. Curcio, A. Andò, **A. Tomasino**, C. Giaconia, A.C. Busacca, M.C. Mazzillo, D. Sanfilippo, and G. Fallica, “*Responsivity measurements of silicon carbide schottky photodiodes in the UV range*”, Third Mediterranean Photonics Conference (MEPHOCO 2014), Trani, Italy, May 7-9, 2014, (oral).
34. G. Adamo, D. Agrò, S. Stivala, A. Parisi, **A. Tomasino**, L. Curcio, R. Pernice, C. Giaconia, A. C. Busacca, and G. Fallica, “*Signal to noise ratio of silicon photomultipliers measured in the continuous wave regime*”, Third Mediterranean Photonics Conference (MEPHOCO 2014), Trani, Italy, May 7-9, 2014, (oral).
35. G. Adamo, D. Agrò, S. Stivala, A. Parisi, L. Curcio, A. Andò, **A. Tomasino**, C. Giaconia; A. C. Busacca, M. C. Mazzillo, D. Sanfilippo, P. G. Fallica, “*Responsivity measurements of 4H-SiC schottky photodiodes for UV light monitoring*”, Proc. SPIE 8990, Silicon Photonics IX, 899017 (2014), (oral).
36. D. Sanfilippo, G. Valvo, M. Mazzillo, A. Piana, B. Carbone, L. Renna, P. G. Fallica, D. Agrò, G. Morsellino, M. Pinto, R. Canicattì, N. Galioto, **A. Tomasino**, G. Adamo, S. Stivala, A. Parisi, L. Curcio, C. Giaconia, A. C. Busacca, R. Pagano, S. Libertino, S. Lombardo “*Design and development of a fNIRS system prototype based on SiPM detectors*”, Proc. SPIE 8990, Silicon Photonics IX, 899016 (2014), (oral).
37. **A. Tomasino**, A. Parisi, S. Stivala, R. Pernice, L. Curcio, A. C. Cino, A. C. Busacca, M. Peccianti, R. Morandotti, “*Analytical Model for wideband THz sources and detectors based on Optical Rectification and Electro-Optic sampling*”, EOS (European Optical Society) Topical Meetings at Capri, 12-14 September 2013, Capri, Italy, (poster).

# References

- [1] Y. S. Lee, *Principles of terahertz science and technology*. Springer, 2009.
- [2] P. H. Siegel, “Terahertz technology,” *IEEE Trans. Microw. Theory Tech.*, vol. 50, no. 3, pp. 910–928, Mar. 2002.
- [3] C. Monte, B. Gutschwager, A. Adibekyan, and J. Hollandt, “A Terahertz Blackbody Radiation Standard Based on Emissivity Measurements and a Monte-Carlo Simulation,” *J. Infrared, Millimeter, Terahertz Waves*, vol. 35, no. 8, pp. 649–658, Aug. 2014.
- [4] H. Li, Y. Zhe, D. Yu, J. Zhou, and H. Yang, “Study on terahertz radiation test of blackbody,” 2012, vol. 8417, p. 841730.
- [5] W. S. Warren and W. S. Warren, “Introduction to Quantum Mechanics,” *Phys. Basis Chem.*, pp. 87–127, Jan. 2001.
- [6] F. Zernike and P. R. Berman, “Generation of Far Infrared as a Difference Frequency,” *Phys. Rev. Lett.*, vol. 15, no. 26, pp. 999–1001, Dec. 1965.
- [7] D. Strickland and G. Mourou, “Compression of amplified chirped optical pulses,” *Opt. Commun.*, vol. 56, no. 3, pp. 219–221, Dec. 1985.
- [8] J.-C. Diels and W. Rudolph, *Ultrashort laser pulse phenomena : fundamentals, techniques, and applications on a femtosecond time scale*. Elsevier/Academic Press, 2006.
- [9] K. Sakai and M. Tani, “Introduction to Terahertz Pulses,” in *Terahertz Optoelectronics*, Berlin/Heidelberg: Springer-Verlag, pp. 1–30.
- [10] C. Rullière, *Femtosecond laser pulses : principles and experiments*. Springer, 2005.

- [11] M. Tonouchi, "Cutting-edge terahertz technology," *Nature Photonics*, vol. 1, no. 2. Nature Publishing Group, pp. 97–105, 01-Feb-2007.
- [12] C. Zandonella, "T-ray specs," *Nature*, vol. 424, no. 6950, pp. 721–722, Aug. 2003.
- [13] B. Ferguson and X.-C. Zhang, "Materials for terahertz science and technology," *Nat. Mater.*, vol. 1, no. 1, pp. 26–33, Sep. 2002.
- [14] D. Dragoman and M. Dragoman, "Terahertz fields and applications," *Prog. Quantum Electron.*, vol. 28, no. 1, pp. 1–66, Jan. 2004.
- [15] D. Smith and A. Belyanin, "Theory and design of Smith-Purcell semiconductor THz sources," in *2011 International Conference on Infrared, Millimeter, and Terahertz Waves*, 2011, pp. 1–2.
- [16] B. S. Williams, "Terahertz quantum-cascade lasers," *Nat. Photonics*, vol. 1, no. 9, pp. 517–525, Sep. 2007.
- [17] A. Nahata, D. H. Auston, T. F. Heinz, and C. Wu, "Coherent detection of freely propagating terahertz radiation by electro-optic sampling," *Appl. Phys. Lett.*, vol. 68, no. 2, pp. 150–152, Jun. 1996.
- [18] Q. Wu and X.-C. Zhang, "Free-space electro-optic sampling of terahertz beams," *Appl. Phys. Lett.*, vol. 67, no. 24, pp. 3523–3525, Dec. 1995.
- [19] Q. Wu and X.-C. Zhang, "Free-space electro-optics sampling of mid-infrared pulses," *Appl. Phys. Lett.*, vol. 71, no. 10, p. 1285, Jun. 1998.
- [20] Q. Wu and X. C. Zhang, "7 terahertz broadband GaP electro-optic sensor," *Appl. Phys. Lett.*, vol. 70, no. 14, pp. 1784–1786, Jun. 1997.
- [21] A. Nahata, A. S. Weling, and T. F. Heinz, "A wideband coherent terahertz spectroscopy system using optical rectification and electro-optic sampling," *Appl. Phys. Lett.*, vol. 69, no. 16, p. 2321, Jun. 1998.
- [22] D. H. Auston, "Picosecond optoelectronic switching and gating in silicon," *Appl. Phys. Lett.*, vol. 26, no. 3, pp. 101–103, Feb. 1975.
- [23] C. H. Lee, "Picosecond optoelectronic switching in GaAs," *Appl. Phys. Lett.*, vol. 30, no. 2, pp. 84–86, Jan. 1977.
- [24] M. Tani, S. Matsuura, K. Sakai, and S. Nakashima, "Emission characteristics of photoconductive antennas based on low-temperature-grown GaAs and semi-insulating GaAs," *Appl. Opt.*, vol. 36, no. 30, p. 7853, Oct. 1997.
- [25] Y. C. Shen *et al.*, "Generation and detection of ultrabroadband terahertz radiation using photoconductive emitters and receivers," *Appl. Phys. Lett.*, vol. 85, no. 2, pp. 164–166, Jul. 2004.

- [26] “Picosecond semiconductor electronic switch controlled by optical means,” Nov. 1974.
- [27] N. Chimot *et al.*, “Terahertz radiation from heavy-ion-irradiated In<sub>0.53</sub>Ga<sub>0.47</sub>As photoconductive antenna excited at 1.55 $\mu$ m,” *Appl. Phys. Lett.*, vol. 87, no. 19, p. 193510, Nov. 2005.
- [28] S. Matsuura, M. Tani, and K. Sakai, “Generation of coherent terahertz radiation by photomixing in dipole photoconductive antennas,” *Appl. Phys. Lett.*, vol. 70, no. 5, p. 559, Jun. 1998.
- [29] M. Beck *et al.*, “Impulsive terahertz radiation with high electric fields from an amplifier-driven large-area photoconductive antenna,” *Opt. Express*, vol. 18, no. 9, p. 9251, Apr. 2010.
- [30] K. J. Kaltenecker, S. Engelbrecht, K. Iwaszczuk, B. M. Fischer, and P. U. Jepsen, “Ultrabroadband THz time-domain spectroscopy of biomolecular crystals,” in *2016 41st International Conference on Infrared, Millimeter, and Terahertz waves (IRMMW-THz)*, 2016, pp. 1–2.
- [31] J. Liu, J. D. J. Dai, S. L. C. S. L. Chin, and X.-C. Zhang, “Broadband terahertz wave remote sensing using coherent manipulation of fluorescence from asymmetrically ionized gases,” *Lasers Electro-Optics Quantum Electron. Laser Sci. Conf. (QELS), 2010 Conf.*, vol. 4, no. July, pp. 627–631, Sep. 2010.
- [32] J. Dai, B. Clough, I.-C. Ho, X. Lu, J. Liu, and X.-C. Zhang, “Recent Progresses in Terahertz Wave Air Photonics,” *IEEE Trans. Terahertz Sci. Technol.*, vol. 1, no. 1, pp. 274–281, Sep. 2011.
- [33] J. LIU, J. DAI, X. LU, I.-C. HO, and X.-C. ZHANG, “BROADBAND TERAHERTZ WAVE GENERATION, DETECTION AND COHERENT CONTROL USING TERAHERTZ GAS PHOTONICS,” *Int. J. High Speed Electron. Syst.*, vol. 20, no. 01, pp. 3–12, Mar. 2011.
- [34] J. Liu, X.-C. Zhang, J. LIU, and X.-C. ZHANG, “Terahertz radiation-enhanced-emission-of-fluorescence,” *Front. Optoelectron.*, vol. 7, no. 2, pp. 156–198, Jun. 2014.
- [35] X. Lu and X.-C. Zhang, “Investigation of ultra-broadband terahertz time-domain spectroscopy with terahertz wave gas photonics,” *Front. Optoelectron.*, vol. 7, no. 2, pp. 121–155, Jun. 2014.
- [36] D. J. Cook and R. M. Hochstrasser, “Intense terahertz pulses by four-wave rectification in air,” *Opt. Lett.*, vol. 25, no. 16, p. 1210, Aug. 2000.
- [37] X. Lu, N. Karpowicz, and X.-C. Zhang, “Broadband terahertz detection with selected gases,” *J. Opt. Soc. Am. B*, vol. 26, no. 9, p. A66, Sep. 2009.
- [38] J. Liu and X.-C. Zhang, “Terahertz-Radiation-Enhanced Emission of Fluorescence from Gas Plasma,” *Phys. Rev. Lett.*, vol. 103, no. 23, p. 235002, Dec. 2009.

- [39] J. Liu, J. Dai, S. L. Chin, and X.-C. Zhang, “Broadband terahertz wave remote sensing using coherent manipulation of fluorescence from asymmetrically ionized gases,” *Nat. Photonics*, vol. 4, no. 9, pp. 627–631, Sep. 2010.
- [40] X. Lu and X.-C. Zhang, “Balanced terahertz wave air-biased-coherent-detection,” *Appl. Phys. Lett.*, vol. 98, no. 15, p. 151111, Apr. 2011.
- [41] J. Dai, J. Liu, and X.-C. Zhang, “Terahertz Wave Air Photonics: Terahertz Wave Generation and Detection With Laser-Induced Gas Plasma,” *IEEE J. Sel. Top. Quantum Electron.*, vol. 17, no. 1, pp. 183–190, Jan. 2011.
- [42] B. Clough, J. Liu, and X.-C. Zhang, “‘All air–plasma’ terahertz spectroscopy,” *Opt. Lett.*, vol. 36, no. 13, p. 2399, Jul. 2011.
- [43] M. Nakajima, M. Tani, and M. Hangyo, “Study of ultrabroadband terahertz radiation from wedge-shaped ZnTe,” in *Infrared and Millimeter Waves, Conference Digest of the 2004 Joint 29th International Conference on 2004 and 12th International Conference on Terahertz Electronics, 2004.*, pp. 161–162.
- [44] Y. C. Shen, P. C. Upadhyaya, E. H. Linfield, H. E. Beere, and A. G. Davies, “Ultrabroadband terahertz radiation from low-temperature-grown GaAs photoconductive emitters,” *Appl. Phys. Lett.*, vol. 83, no. 15, pp. 3117–3119, Oct. 2003.
- [45] S. Kono, M. Tani, P. Gu, and K. Sakai, “Detection of up to 20 THz with a low-temperature-grown GaAs photoconductive antenna gated with 15 fs light pulses,” *Appl. Phys. Lett.*, vol. 77, no. 25, p. 4104, Dec. 2000.
- [46] P. J. Hale *et al.*, “20 THz broadband generation using semi-insulating GaAs interdigitated photoconductive antennas,” *Opt. Express*, vol. 22, no. 21, p. 26358, Oct. 2014.
- [47] Y. Zhang *et al.*, “A Broadband THz-TDS System Based on DSTMS Emitter and LTG InGaAs/InAlAs Photoconductive Antenna Detector,” *Sci. Rep.*, vol. 6, no. 1, p. 26949, Jul. 2016.
- [48] S. Regensburger *et al.*, “Broadband THz detection from 0.1 to 22 THz with large area field-effect transistors &quot; Absorption of terahertz radiation by plasmon modes in a grid-gated double-quantum-well field-effect transistor,” *J. Appl. Phys.*, vol. 23, no. 3556, pp. 89–252, 2007.
- [49] P. Y. Han and X.-C. Zhang, “Free-space coherent broadband terahertz time-domain spectroscopy,” *Meas. Sci. Technol.*, vol. 12, no. 11, pp. 1747–1756, Nov. 2001.
- [50] C.-S. Yang, C.-M. Chang, P.-H. Chen, P. Yu, and C.-L. Pan, “Broadband terahertz conductivity and optical transmission of indium-tin-oxide (ITO) nanomaterials,” *Opt. Express*, vol. 21, no. 14, p. 16670, Jul. 2013.
- [51] J. Takayanagi *et al.*, “High-resolution time-of-flight terahertz tomography using a

- femtosecond fiber laser,” *Opt. Express*, vol. 17, no. 9, p. 7533, Apr. 2009.
- [52] Z. Jiang, M. Li, and X.-C. Zhang, “Dielectric constant measurement of thin films by differential time-domain spectroscopy,” *Appl. Phys. Lett.*, vol. 76, no. 22, p. 3221, May 2000.
- [53] Y. C. Shen, P. C. Upadhyaya, E. H. Linfield, H. E. Beere, and A. G. Davies, “Ultrabroadband terahertz radiation from low-temperature-grown GaAs photoconductive emitters,” *Appl. Phys. Lett.*, vol. 83, no. 15, pp. 3117–3119, Oct. 2003.
- [54] N. Vieweg *et al.*, “Ultrabroadband terahertz spectroscopy of a liquid crystal,” *Opt. Express*, vol. 20, no. 27, p. 28249, Dec. 2012.
- [55] A. G. Davies, A. D. Burnett, W. Fan, E. H. Linfield, and J. E. Cunningham, “Terahertz spectroscopy of explosives and drugs,” *Materials Today*, vol. 11, no. 3. Elsevier, pp. 18–26, 01-Mar-2008.
- [56] R. J. Falconer and A. G. Markelz, “Terahertz Spectroscopic Analysis of Peptides and Proteins,” *J. Infrared, Millimeter, Terahertz Waves*, vol. 33, no. 10, pp. 973–988, Oct. 2012.
- [57] B. M. Fischer, M. Walther, and P. U. Jepsen, “Far-infrared vibrational modes of DNA components studied by terahertz time-domain spectroscopy,” *Phys. Med. Biol.*, vol. 47, no. 21, pp. 3807–3814, Nov. 2002.
- [58] I.-C. Ho, X. Guo, and X.-C. Zhang, “Design and performance of reflective terahertz air-biased-coherent-detection for time-domain spectroscopy,” *Opt. Express*, vol. 18, no. 3, p. 2872, Feb. 2010.
- [59] Y. R. Shen, “Surface properties probed by second-harmonic and sum-frequency generation,” *Nature*, vol. 337, no. 6207, pp. 519–525, Feb. 1989.
- [60] H.-E. Ponath and G. I. Stegeman, *Nonlinear surface electromagnetic phenomena*. North-Holland, 1991.
- [61] O. A. Aktsipetrov, A. A. Fedyanin, V. N. Golovkina, and T. V. Murzina, “Optical second-harmonic generation induced by a dc electric field at the Si–SiO<sub>2</sub> interface,” *Opt. Lett.*, vol. 19, no. 18, p. 1450, Sep. 1994.
- [62] P. Godefroy, W. de Jong, C. W. van Hasselt, M. A. C. Devillers, and T. Rasing, “Electric field induced second harmonic generation spectroscopy on a metal-oxide-silicon structure,” *Appl. Phys. Lett.*, vol. 68, no. 14, p. 1981, Aug. 1998.
- [63] R. W. Boyd, *Nonlinear optics*. Academic Press, 2008.
- [64] M. Naftaly and R. Dudley, “Methodologies for determining the dynamic ranges and signal-to-noise ratios of terahertz time-domain spectrometers,” *Opt. Lett.*, vol. 34, no. 8, p. 1213, Apr. 2009.

- [65] D. J. Cook, J. X. Chen, E. a. Morlino, and R. M. Hochstrasser, "Terahertz-field-induced second-harmonic generation measurements of liquid dynamics," *Chem. Phys. Lett.*, vol. 309, no. 3–4, pp. 221–228, 1999.
- [66] A. Nahata and T. F. Heinz, "Detection of freely propagating terahertz radiation by use of optical second-harmonic generation," *Opt. Lett.*, vol. 23, no. 1, p. 67, Jan. 1998.
- [67] P. A. George, W. Hui, F. Rana, B. G. Hawkins, A. E. Smith, and B. J. Kirby, "Microfluidic devices for terahertz spectroscopy of biomolecules," *Appl. Phys. Lett. Zeon Corp. OSA Opt. EXPRESS Chem. Bov. Serum Albumin Prod. Inf. Sheet Sigma-Aldrich*, vol. 29, no. 16, pp. 187–194, 2003.
- [68] L. Gouy, *Sur une propriété nouvelle des ondes lumineuses*. Paris: Gauthier-Villars, 1890.
- [69] H. Jeffreys and B. S. Jeffreys, *Methods of mathematical physics*. Cambridge University Press, 1999.
- [70] J. Dai, X. Xie, and X. C. Zhang, "Detection of broadband terahertz waves with a laser-induced plasma in gases," *Phys. Rev. Lett.*, vol. 97, no. 10, p. 103903, Sep. 2006.
- [71] C.-Y. Li, D. V. Seletskiy, Z. Yang, and M. Sheik-Bahae, "Broadband field-resolved terahertz detection via laser induced air plasma with controlled optical bias," *Opt. Express*, vol. 23, no. 9, p. 11436, May 2015.
- [72] N. Karpowicz *et al.*, "Coherent heterodyne time-domain spectrometry covering the entire 'terahertz gap,'" *Appl. Phys. Lett.*, vol. 92, no. 1, p. 011131, Jan. 2008.
- [73] H. He and X.-C. Zhang, "Analysis of Gouy phase shift for optimizing terahertz air-biased-coherent- detection," *Appl. Phys. Lett. Addit. Inf. Appl. Phys. Lett. J. Homepage*, vol. 100, 2012.
- [74] A. Farley and R. H. Price, "Electric field outside a parallel plate capacitor," *Am. J. Phys.*, vol. 69, pp. 751–754, 2001.
- [75] X. Lu, N. Karpowicz, and X.-C. Zhang, "Broadband terahertz detection with selected gases," *J. Opt. Soc. Am. B*, vol. 26, no. 9, p. A66, Sep. 2009.
- [76] J. A. Sell and A. Kuppermann, "Angular distributions in the photoelectron spectroscopy of SF<sub>6</sub>," *Chem. Phys.*, vol. 33, no. 3, pp. 379–383, Oct. 1978.
- [77] W. M. Haynes, D. R. Lide, and T. J. Bruno, *CRC handbook of chemistry and physics : a ready-reference book of chemical and physical data*. .
- [78] J. F. Ward and I. J. Bigio, "Molecular second- and third-order polarizabilities from measurements of second-harmonic generation in gases," *Phys. Rev. A*, vol. 11, no. 1, pp. 60–66, Jan. 1975.

- [79] J. F. Ward and C. K. Miller, “Measurements of nonlinear optical polarizabilities for twelve small molecules,” *Phys. Rev. A*, vol. 19, no. 2, pp. 826–833, Feb. 1979.
- [80] R. E. Collin, *Foundations for microwave engineering*. IEEE Press, 2001.
- [81] “Photomultiplier tube basics.”
- [82] M. Bass, G. Li, and E. W. Van Stryland, *Handbook of optics. Volume IV, Optical properties of materials, nonlinear optics, quantum optics*. McGraw-Hill, 2010.
- [83] D. J. Cook, J. X. Chen, E. A. Morlino, and R. M. Hochstrasser, “Terahertz-field-induced second-harmonic generation measurements of liquid dynamics,” *Chem. Phys. Lett.*, vol. 309, no. 3–4, pp. 221–228, Aug. 1999.
- [84] P. Guyot-Sionnest, W. Chen, and Y. R. Shen, “General considerations on optical second-harmonic generation from surfaces and interfaces,” *Phys. Rev. B*, vol. 33, no. 12, pp. 8254–8263, Jun. 1986.
- [85] M. Cornet, J. Degert, E. Abraham, and E. Freysz, “Terahertz-field-induced second harmonic generation through Pockels effect in zinc telluride crystal,” *Opt. Lett.*, vol. 39, no. 20, p. 5921, Oct. 2014.
- [86] M. Clerici *et al.*, “CCD-based imaging and 3D space–time mapping of terahertz fields via Kerr frequency conversion,” *Opt. Lett.*, vol. 38, no. 11, p. 1899, Jun. 2013.
- [87] M. Clerici *et al.*, “Counterpropagating frequency mixing with terahertz waves in diamond,” *Opt. Lett.*, vol. 38, no. 2, p. 178, Jan. 2013.
- [88] M. Petev *et al.*, “Phase-Insensitive Scattering of Terahertz Radiation,” *Photonics*, vol. 4, no. 4, p. 7, Jan. 2014.
- [89] G. S. May and S. M. Sze, *Fundamentals of semiconductor fabrication*. Wiley, 2004.
- [90] E. V. Loewenstein, D. R. Smith, and R. L. Morgan, “Optical Constants of Far Infrared Materials 2: Crystalline Solids,” *Appl. Opt.*, vol. 12, no. 2, p. 398, Feb. 1973.
- [91] Y. W. Chen and X.-C. Zhang, “Anti-reflection implementations for terahertz waves.”
- [92] K. Kawase and N. Hiromoto, “Terahertz-wave antireflection coating on Ge and GaAs with fused quartz,” *Appl. Opt.*, vol. 37, no. 10, p. 1862, Apr. 1998.
- [93] I. Hosako, “Antireflection coating formed by plasma-enhanced chemical-vapor deposition for terahertz-frequency germanium optics,” *Appl. Opt.*, vol. 42, no. 19, p. 4045, Jul. 2003.
- [94] D. Grischkowsky, S. Keiding, M. van Exter, and C. Fattinger, “Far-infrared time-domain spectroscopy with terahertz beams of dielectrics and semiconductors,” *J. Opt. Soc. Am. B*, vol. 7, no. 10, p. 2006, Oct. 1990.

- [95] U. Gubler and C. Bosshard, “Optical third-harmonic generation of fused silica in gas atmosphere: Absolute value of the third-order nonlinear optical susceptibility  $\chi^{(3)}$ ,” *Phys. Rev. B*, vol. 61, no. 16, pp. 10702–10710, Apr. 2000.
- [96] N. P. Bansal and R. H. Doremus, *Handbook of glass properties*. Academic Press, 1986.
- [97] W. H. Press, *Numerical recipes : the art of scientific computing*. Cambridge University Press, 2007.
- [98] M. Clerici *et al.*, “Wavelength scaling of terahertz generation by gas ionization,” *Phys. Rev. Lett.*, vol. 110, no. 25, 2013.
- [99] T. Balčiūnas *et al.*, “CEP-stable tunable THz-emission originating from laser-waveform-controlled sub-cycle plasma-electron bursts,” *Opt. Express*, vol. 23, no. 12, p. 15278, Jun. 2015.
- [100] V. A. Andreeva *et al.*, “Ultrabroad terahertz spectrum generation from an air-based filament plasma,” *Phys. Rev. Lett.*, vol. 116, no. 6, 2016.
- [101] Y. S. You, T. I. Oh, and K. Y. Kim, “Off-Axis Phase-Matched Terahertz Emission from Two-Color Laser-Induced Plasma Filaments,” *Phys. Rev. Lett.*, vol. 109, no. 18, p. 183902, Oct. 2012.
- [102] H. Hamster, A. Sullivan, S. Gordon, and R. W. Falcone, “Short-pulse terahertz radiation from high-intensity-laser-produced plasmas,” *Phys. Rev. E*, vol. 49, no. 1, pp. 671–677, Jan. 1994.
- [103] F. Blanchard *et al.*, “Generation of 1.5  $\mu$ J single-cycle terahertz pulses by optical rectification from a large aperture ZnTe crystal,” *Opt. Express*, vol. 15, no. 20, p. 13212, Oct. 2007.
- [104] B. E. A. Saleh and M. C. Teich, *Fundamentals of Photonics*. New York, USA: John Wiley & Sons, Inc., 1991.
- [105] R. Danielius, P. Di Trapani, C. Solcia, P. Foggi, A. Andreoni, and A. Piskarskas, “Matching of group velocities by spatial walk-off in collinear three-wave interaction with tilted pulses,” *Opt. Lett.*, vol. 21, no. 13, p. 973, Jul. 1996.
- [106] R. J. Gehr, M. W. Kimmel, and A. V. Smith, “Simultaneous spatial and temporal walk-off compensation in frequency-doubling femtosecond pulses in  $\text{BaB}_2\text{O}_4$ ,” *Opt. Lett.*, vol. 23, no. 16, p. 1298, Aug. 1998.
- [107] T. Nishikawa and N. Uesugi, “Effects of walk-off and group velocity difference on the optical parametric generation in  $\text{KTiOPO}_4$  crystals,” *J. Appl. Phys.*, vol. 77, no. 10, pp. 4941–4947, May 1995.
- [108] I. H. Malitson, “Interspecimen Comparison of the Refractive Index of Fused Silica\*,†,” *J. Opt. Soc. Am.*, vol. 55, no. 10, p. 1205, Oct. 1965.

- [109] E. Harari, “Dielectric breakdown in electrically stressed thin films of thermal SiO<sub>2</sub>,” *J. Appl. Phys.*, vol. 49, no. 4, p. 2478, Aug. 1978.
- [110] M. Shalaby *et al.*, “Concurrent field enhancement and high transmission of THz radiation in nanoslit arrays,” *Appl. Phys. Lett.*, vol. 99, no. 4, p. 041110, Jul. 2011.
- [111] A. Tomasino *et al.*, “Solid-state-biased coherent detection of ultra-broadband terahertz pulses,” *Optica*, vol. 4, no. 11, p. 1358, 2017.
- [112] G. P. Agrawal, *Fiber-optic communication systems*. Wiley, 2013.
- [113] A. Tomasino *et al.*, “Wideband THz Time Domain Spectroscopy based on Optical Rectification and Electro-Optic Sampling,” *Sci. Rep.*, vol. 3, no. 1, p. 3116, Dec. 2013.
- [114] T. Bartel, P. Gaal, K. Reimann, M. Woerner, and T. Elsaesser, “Generation of single-cycle THz transients with high electric-field amplitudes,” *Opt. Lett.*, vol. 30, no. 20, p. 2805, Oct. 2005.
- [115] A. Ibrahim, D. Férachou, G. Sharma, K. Singh, M. Kirouac-Turmel, and T. Ozaki, “Ultra-high dynamic range electro-optic sampling for detecting millimeter and sub-millimeter radiation,” *Sci. Rep.*, vol. 6, no. 1, p. 23107, Sep. 2016.
- [116] W. H. Fan, A. Burnett, P. C. Upadhyaya, J. Cunningham, E. H. Linfield, and A. G. Davies, “Far-Infrared Spectroscopic Characterization of Explosives for Security Applications Using Broadband Terahertz Time-Domain Spectroscopy,” *Appl. Spectrosc.*, vol. 61, no. 6, pp. 638–643, Jun. 2007.
- [117] J. Kröll, J. Darmo, and K. Unterrainer, “Metallic wave-impedance matching layers for broadband terahertz optical systems,” *Opt. Express*, vol. 15, no. 11, p. 6552, May 2007.
- [118] Y. Zhou *et al.*, “Terahertz wave reflection impedance matching properties of graphene layers at oblique incidence,” *Carbon N. Y.*, vol. 96, pp. 1129–1137, Jan. 2016.
- [119] J. S. Levy, M. A. Foster, A. L. Gaeta, and M. Lipson, “Harmonic generation in silicon nitride ring resonators,” *Opt. Express*, vol. 19, no. 12, p. 11415, Jun. 2011.
- [120] D. J. Moss, R. Morandotti, A. L. Gaeta, and M. Lipson, “New CMOS-compatible platforms based on silicon nitride and Hydex for nonlinear optics,” *Nat. Photonics*, vol. 7, no. 8, pp. 597–607, Aug. 2013.
- [121] J. S. Levy, A. Gondarenko, M. A. Foster, A. C. Turner-Foster, A. L. Gaeta, and M. Lipson, “CMOS-compatible multiple-wavelength oscillator for on-chip optical interconnects,” *Nat. Photonics*, vol. 4, no. 1, pp. 37–40, Jan. 2010.
- [122] H. Nishihara, M. Haruna, and T. Suhara, *Optical integrated circuits*. McGraw-Hill Book Co, 1989.
- [123] K. Ikeda, R. E. Saperstein, N. Alic, and Y. Fainman, “Thermal and Kerr nonlinear

properties of plasma-deposited silicon nitride/ silicon dioxide waveguides,” *Opt. Express*, vol. 16, no. 17, p. 12987, Aug. 2008.

- [124] J. Kischkat *et al.*, “Mid-infrared optical properties of thin films of aluminum oxide, titanium dioxide, silicon dioxide, aluminum nitride, and silicon nitride,” *Appl. Opt.*, vol. 51, no. 28, p. 6789, Oct. 2012.
- [125] L. Bergé, C.-L. Soulez, C. Köhler, and S. Skupin, “Role of the carrier-envelope phase in laser filamentation,” *Appl. Phys. B*, vol. 103, no. 3, pp. 563–570, Jun. 2011.
- [126] K. Luke, Y. Okawachi, M. R. E. Lamont, A. L. Gaeta, and M. Lipson, “Broadband mid-infrared frequency comb generation in a Si<sub>3</sub>N<sub>4</sub> microresonator,” *Opt. Lett.*, vol. 40, no. 21, p. 4823, Nov. 2015.
- [127] M. A. Seo *et al.*, “Terahertz field enhancement by a metallic nano slit operating beyond the skin-depth limit,” *Nat. Photonics*, vol. 3, no. 3, pp. 152–156, Mar. 2009.
- [128] J.-H. Kang, D.-S. Kim, and M. Seo, “Terahertz wave interaction with metallic nanostructures,” *Nanophotonics*, vol. 7, no. 5, pp. 763–793, 2018.
- [129] X. Lu, R. Wan, G. Wang, T. Zhang, and W. Zhang, “Giant and tunable electric field enhancement in the terahertz regime,” *Opt. Express*, vol. 22, no. 22, p. 27001, Nov. 2014.
- [130] O. K. Suwal, J. Rhie, N. Kim, and D.-S. Kim, “Nonresonant 104 Terahertz Field Enhancement with 5-nm Slits,” *Sci. Rep.*, vol. 7, p. 45638, Apr. 2017.
- [131] C. D. Amico *et al.*, “Forward THz radiation emission by femtosecond filamentation in gases: theory and experiment,” *New J. Phys.*, vol. 10, no. 1, p. 013015, Jan. 2008.
- [132] M. A. Ordal *et al.*, “Optical properties of the metals Al, Co, Cu, Au, Fe, Pb, Ni, Pd, Pt, Ag, Ti, and W in the infrared and far infrared,” *Appl. Opt.*, vol. 22, no. 7, p. 1099, Apr. 1983.
- [133] R. Lovrinčić and A. Pucci, “Infrared optical properties of chromium nanoscale films with a phase transition,” *Phys. Rev. B*, vol. 80, no. 20, p. 205404, 2009.
- [134] J.-H. Kang, D.-S. Kim, and M. Seo, “Terahertz wave interaction with metallic nanostructures,” *Nanophotonics*, vol. 7, no. 5, pp. 763–793, Mar. 2018.
- [135] K. Iwaszczuk, A. Andryieuski, A. Lavrinenko, X.-C. Zhang, and P. U. Jepsen, “Terahertz field enhancement to the MV/cm regime in a tapered parallel plate waveguide,” *Opt. Express*, vol. 20, no. 8, p. 8344, Apr. 2012.
- [136] A. V. Borodin, M. N. Esaulkov, A. A. Frolov, A. P. Shkurinov, and V. Y. Panchenko, “Possibility of direct estimation of terahertz pulse electric field,” *Opt. Lett.*, vol. 39, no. 14, p. 4092, Jul. 2014.

- [137] A. A. Emel'yanov and E. A. Emel'yanova, "A technique for evaluating the pulse breakdown voltage in vacuum," *Instruments Exp. Tech.*, vol. 51, no. 1, pp. 115–118, Jan. 2008.
- [138] M. Liu *et al.*, "Terahertz-field-induced insulator-to-metal transition in vanadium dioxide metamaterial," *Nature*, vol. 487, 2012.
- [139] H. Y. Hwang, N. C. Brandt, H. Farhat, A. L. Hsu, J. Kong, and K. A. Nelson, "Nonlinear THz Conductivity Dynamics in P-Type CVD-Grown Graphene," *J. Phys. Chem. B*, vol. 117, no. 49, pp. 15819–15824, Dec. 2013.
- [140] J. Wang, Y. Hernandez, M. Lotya, J. N. Coleman, and W. J. Blau, "Broadband Nonlinear Optical Response of Graphene Dispersions," *Adv. Mater.*, vol. 21, no. 23, pp. 2430–2435, Jun. 2009.
- [141] K. Tanaka, H. Hirori, and M. Nagai, "THz Nonlinear Spectroscopy of Solids," *IEEE Trans. Terahertz Sci. Technol.*, vol. 1, no. 1, pp. 301–312, Sep. 2011.
- [142] H. Hirori and K. Tanaka, "Nonlinear Optical Phenomena Induced by Intense Single-Cycle Terahertz Pulses," *IEEE J. Sel. Top. Quantum Electron.*, vol. 19, no. 1, pp. 8401110–8401110, Jan. 2013.
- [143] D. Daranciang *et al.*, "Single-cycle terahertz pulses with  $>0.2$  V/Å field amplitudes via coherent transition radiation," *Appl. Phys. Lett.*, vol. 99, no. 14, p. 141117, Oct. 2011.
- [144] Z. Wu *et al.*, "Intense terahertz pulses from SLAC electron beams using coherent transition radiation," *Rev. Sci. Instrum.*, vol. 84, no. 2, p. 022701, Feb. 2013.
- [145] J.-M. Manceau, M. Massaouti, and S. Tzortzakis, "Strong terahertz emission enhancement via femtosecond laser filament concatenation in air," *Opt. Lett.*, vol. 35, no. 14, p. 2424, Jul. 2010.
- [146] J.-M. Manceau *et al.*, "Terahertz pulse emission optimization from tailored femtosecond laser pulse filamentation in air," *Opt. Lett.*, vol. 34, no. 14, p. 2165, Jul. 2009.
- [147] J. Zhao *et al.*, "Simple method to enhance terahertz radiation from femtosecond laser filament array with a step phase plate," *Opt. Lett.*, vol. 40, no. 16, p. 3838, Aug. 2015.
- [148] H. Hamster, A. Sullivan, S. Gordon, W. White, and R. W. Falcone, "Subpicosecond, electromagnetic pulses from intense laser-plasma interaction," *Phys. Rev. Lett.*, vol. 71, no. 17, pp. 2725–2728, Oct. 1993.
- [149] F. Buccheri and X.-C. Zhang, "Terahertz emission from laser-induced microplasma in ambient air," *Optica*, vol. 2, no. 4, p. 366, Apr. 2015.
- [150] T. I. Oh, Y. J. Yoo, Y. S. You, and K. Y. Kim, "Generation of strong terahertz fields

exceeding 8 MV/cm at 1 kHz and real-time beam profiling,” *Appl. Phys. Lett.*, vol. 105, no. 4, p. 041103, Jul. 2014.

- [151] S. L. Chin, S. Yuan, T.-J. Wang, and Y. Chen, “Intense broadband THz generation from femtosecond laser filamentation,” *Chinese Opt. Lett. Vol. 11, Issue 1, pp. 011401-*, vol. 11, no. 1, p. 011401, Jan. 2013.
- [152] K. Liu, A. D. Koulouklidis, D. G. Papazoglou, S. Tzortzakis, and X.-C. Zhang, “Enhanced terahertz wave emission from air-plasma tailored by abruptly autofocusing laser beams,” *Optica*, vol. 3, no. 6, p. 605, Jun. 2016.
- [153] A. Gorodetsky, A. D. Koulouklidis, M. Massaouti, and S. Tzortzakis, “Physics of the conical broadband terahertz emission from two-color laser-induced plasma filaments,” *Phys. Rev. A - At. Mol. Opt. Phys.*, vol. 89, no. 3, 2014.
- [154] P. Klarskov, A. C. Strikwerda, K. Iwaszczuk, and P. U. Jepsen, “Experimental three-dimensional beam profiling and modeling of a terahertz beam generated from a two-color air plasma,” *New J. Phys.*, vol. 15, no. 7, p. 075012, Jul. 2013.
- [155] T. I. Oh, Y. S. You, N. Jhaji, E. W. Rosenthal, H. M. Milchberg, and K. Y. Kim, “Intense terahertz generation in two-color laser filamentation: energy scaling with terawatt laser systems,” *New J. Phys.*, vol. 15, no. 7, p. 075002, Jul. 2013.

# List of Figures

**Figure 1.1** Subdivision of the electromagnetic spectrum. The THz domain is situated between the band of the microwaves and the mid-infrared radiation (photonics). ..... 3

**Figure 1.2.** Chart of the THz generation techniques deployed as a function of the THz spectral emission and available average power. Compact terahertz sources exhibit low power and conversion efficiencies of much less than 1 percent. And in nearly every case, as the frequency rises into the terahertz range, the source output power plummets. Here, the  $Pf^2 = \text{constant}$  line, with P the power and f the frequency, is the power-frequency slope one would expect to see in a more mature RF device, while the  $P\lambda = \text{constant}$  line, with  $\lambda$  the wavelength, is the expected slope for some commercial lasers. Higher frequencies are accessible by means of laser techniques only. Image readapted from [15]..... 4

**Figure 1.3** Subdivisions of the THz generation methods. Continuous wave radiation featured by a multicycle shape can be achieved via either (a) microwave harmonic generation in nonlinear devices (mixer) or (b) integrated devices based on semiconductor nanostructured lattices (QCL). (c) Down-conversion from the optical domain in second-order materials, allow the generation or both pulsed and CW THz radiation. .... 6

**Figure 2.1** (a) Typical THz time domain waveform (blue line) reconstructed as the mean of nine consecutive temporal scans (left vertical axis). The standard deviation of such measurements is plotted as the purple line. The green curve represents the SNR plotted as a function of the time (right vertical axis). (b) DR (blue cure, left vertical axis) and SNR (purple curve, right vertical axis) evaluated in the frequency domain. Note the different scale of the two vertical axes. .... 13

**Figure 2.2** (a) TFISH generation in air: the probe pulse is frequency-doubled when the THz beam is strongly focused around the focal spot of the optical beam. A photomultiplier tube acquires the filtered second harmonic beam. Simplified diagram representing the two possible energy transitions taking place in the four-wave mixing process giving rise to (a) the difference frequency generation (DFG) and (c) sum frequency generation (SFG). ..... 16

**Figure 2.3.** (a) Gouy phase shift experienced by the THz beam while crossing the focal point. The  $\pi$ -rotation results in a flip of the polarity of the THz pulse.  $z_T$  and  $z_R$  are the Rayleigh lengths of THz and probe beam, respectively. Gouy phase shift for the case (b) DFG and (c) SFG generation process, along the propagation direction  $z$  with origin on the focal plane, evaluated for the case of  $z_T = 0.8$  mm and  $z_R = 4.8$  mm. While for the DFG the total phase change (blue curve) never overcomes the value of  $\pm\pi$ , thus promoting the coherent summation of the contributions to the total DFG beam in a wide range of propagation values, for the SFG case, the total phase change overcomes  $\pm\pi$ -rotation for values relatively close to the focus, thus limiting the total conversion efficiency. .... 17

**Figure 2.4** (a) Sketch of the experimental set-up employed in Ref [69]. The THz wave is generated by the nonlinear mixing of the fundamental and its second harmonic beams occurring at the first plasma. A couple of 90 off-axis mirror collimates and, after separation from the optical beams, focuses the THz beam in air together with the probe beam, the latter focused via an optical lens and passing through a hole made in the middle of the mirror. The EFISH beam is hence formed and acquired by a PMT, after filtering the remaining probe power. (b) Time-resolved EFISH transients measured at three different probe intensities (increasing moving from the upper to the lower):  $1.8 \times 10^{14}$  W/cm<sup>2</sup>,  $4.6 \times 10^{14}$  W/cm<sup>2</sup>,  $9.2 \times 10^{14}$  W/cm<sup>2</sup>. Gradual conversion of the transient from unipolar to bipolar is observed. .... 21

**Figure 2.5.** (a) Intensity of the local oscillator  $I_{LO}^{SH}$  as a function of the probe intensity (black dots). Note that both the scales are logarithmic. The corresponding Keldysh parameter is shown on the top x-axis. It is possible to identify three main regions, separated by the vertical dashed lines, which indicate the probe intensity values for which the incoherent, hybrid and coherent detection regime is achieved, respectively. (b) Power spectrum of the THz waveform recorded in a nitrogen environment for a probe intensity of  $9.2 \times 10^{14}$  W/cm<sup>2</sup> and shown in the inset. Some spectral artefacts appear in the spectrum, whose actual origin is not totally understood. .... 22

**Figure 2.6.** (a) Sketch of the experimental set-up implementing the OBCD technique. THz pulses are emitted from the two-color plasma generated by focusing the pump beam and its second harmonic achieved in a BBO crystal. On the detection arm, the probe beam is frequency-doubled in a second BBO crystal and finally focused together with its SH and the THz beam inside a metallic hollow fiber, thus

forming a plasma channel. The nonlinear interaction generates the fourth beam with a central frequency slightly lower than the probe SH, which is proportional to the THz waveform. The output total beam is filtered from the probe fundamental frequency and acquired by a PMT. (b) THz transients recovered via OBCD for the case of  $\Delta\phi = 0$  (black line) and  $\Delta\phi = \pi$  (red line). (c) Corresponding electric field THz spectra of the waveforms in (b)..... 26

**Figure 2.7.** (a) Cross correlation signal  $S(\tau, \Delta\phi)$  measured a function of the delay and the diphas between fundamental and SH probe frequencies in the range  $\Delta\phi = 0-2\pi$ . (b) Comparison between the simulated TFISH spectrum (red dashed line) and that retrieved experimentally (red solid line). The spectrum of the probe SH (local oscillator) is also reported (blue solid line) for comparison purpose. All the curves are normalized to their own maxima..... 28

**Figure 2.8.** (a) Sketch of the ABCD technique. A square wave bias voltage is applied to the focal plane of the off-axis parabolic mirror. The modulation frequency of the voltage is half of the repetition rate of the train of THz pulse. The result of the interaction among the three electric fields is directed towards the photomultiplier. (b) Typical THz spectra acquired via ABCD. The bandwidth depends on the optical pulse duration only. If the probe pulse duration is halved, the bandwidth doubles accordingly. The difference in the noise floor is due to a different repetition rate of the two fs lasers used to carry out the detection via lock-in amplifier. The notch around 18.5 THz in the both the spectra is due to a two-phonon absorption effect in the silicon wafers used to separate the pump and THz beams at the generation stage. .... 30

**Figure 2.9.** Comparison between the THz electric field waveforms (a) and relative FFT-evaluated bandwidth (b) emitted by a two-color plasma source driven by an 85 fs optical pulse and retrieved via EOS in a thin ZnTe crystal (blue curve) and ABCD technique (red curve)..... 31

**Figure 2.10.** (a) Experimental set-up for the study of the Gouy phase shift effect on the ABCD technique. The electrodes consist of as a stair-shaped stack, which is vertically shifted to change the effective width of the biased region. (b) THz electric field strength (red dots) experimentally retrieved as a function of the electrode width for the two cases of 35-mm-diameter (upper curve) and 20-mm-diameter (lower curve) THz beam. The blue solid line shows the simulation results. The dotted black line represents the simulation result for the case of a plane wave. Curves and data are normalized to the corresponding maximum values, respectively. .... 35

**Figure 2.11.** (a) Sketch of the vacuum cell employed in the study of the ABCD performance as a function of the type of gas. The apparatus consists of a stain steel chamber fed by a gas dilution system, which allows varying the gas pressure inside. Two fused quartz windows at the entrance and exit (2 and 3-mm-

thick, respectively) of the cell are relatively transparent to the incoming probe and outgoing second harmonic. THz frequencies beyond 5 THz are highly attenuated by the large thickness of the glass. (b) Second harmonic intensity generated from the ABCD mechanism as a function of the probe energy for two different gases at the pressure of 1 atm (~760 torr): Xenon (red dots) and sulfur hexafluoride (SF<sub>6</sub>, blue dots). The dashed lines are quadratic fits. .... 37

**Figure 2.12** Second harmonic intensity generated from the ABCD mechanism as a function of the bias electric field for three different gases, Xenon (red full dots), sulfur hexafluoride (SF<sub>6</sub>, blue dots), and Air (black diamonds) at the pressure of (a) 1 atmosphere (756 torr) and (b) 100 torr. The dashed lines are quadratic fits. .... 39

**Figure 2.13** Second harmonic intensity generated from the ABCD mechanism as a function of the bias electric field for three different gases, Xenon (red full dots), sulfur hexafluoride (SF<sub>6</sub>, blue dots), and Air (black diamonds) at the pressure of (a) 1 atmosphere (756 torr) and (b) 100 torr. The dashed lines are quadratic fits. .... 41

**Figure 2.14** (a) Sketch of the modified detection stage to operate the balanced ABCD technique. The THz and static electric field polarizations form an angle  $\theta$  with the optical probe beam ( $E_o$ ). A Wollaston prism separates the two orthogonal components, which are then sent to two different PMTs. (b) THz waveforms detected by each single PMT (first and second curve starting from the top). The lowest curve represents the actual signal from the lock-in amplifier, given by the difference of the two curves above. .... 44

**Figure 2.15.** Comparison between conventional ABCD technique and balanced ABCD in terms of (a) waveforms and DR and (b) spectra and SNR. .... 46

**Figure 2.16.** Dependence of the (a) DR and (b) SNR upon the bias electric field. In both the graphs, the red curves indicate the regime of ideal PMT, whereas the blue curves represent the case of NEP comparable with the fluctuation introduced by the laser and bias sources. Note that for the SNR, both the cases of in-phase (solid curves) and out of phase (dashed lines)  $E_{THz}$  and  $E_{DC}$  are depicted. All the curves are normalized to their own maxima. .... 49

**Figure 3.1.** (a) Sketch of the experimental set-up employed to demonstrate TFISH in amorphous silicon. Note in the inset the geometrical orientation of the THz, probe and SH beams. (b) Reconstructed bipolar THz waveform retrieved by means of the set-up in (a), for two different values of the angle  $\theta$ . .... 57

**Figure 3.2.** (a) Pictorial representation of the experimental set-up employed to study the nonlinear interaction between ultra-broadband THz (generated by a two-color plasma source) and collimated NIR

beams in diamond samples. The SH signal (0.4  $\mu\text{m}$ ) emerging from the crystal is separated from the fundamental beam by means of a proper filter and it is then sent to a CCD camera (or a spectrometer, not shown in the figure). The inset shows the single-cycle pulse and the corresponding spectrum featuring the THz pulses. (b) Top: particular of the detection stage. Bottom left: spectrogram showing the retrieved signal as a function of time and frequency. The signal results to be composed by two components, as better depicted in the zoom on the bottom right: one very short (around 200 fs) which owns a blue-shift spectrum and due to the main TFISH term. A second term, long lasting (around 8 ps) possesses a slightly red-shifted spectrum and it is due to the counter-propagating interaction between THz and probe beams..... 59

**Figure 3.3.** Comparison between refractive index and absorption coefficient of (a) fused silica and (b) UV-graded quartz. The THz window is shortened to only 2 THz for the absorption coefficient of fused silica, because of the poor SNR, which prevents an accurate estimation of the losses beyond 2.2 THz. .... 61

**Figure 3.4.** Simulations of the bias electric field distribution via a Finite Difference Method algorithm. The Laplace's equation is solved for the static voltage in the case of the 30- $\mu\text{m}$ -wide slit biased with 1 kV, applied to the contacts. The static potential is shown in (a), whereas the static electric field along the x-axis (calculated as the gradient of static potential in (a)) is plotted in (b). The latter reveals that the bias field is mainly confined across the slit embedded in the silica cover layer (the dashed white lines indicate the interface between silica and air). .... 63

**Figure 3.5.** 3D Sketch of the (a) first and (b) second generation of the SSBCD devices based on silica films; (c) and (d) are the top views of the structures in (a) and (b), respectively, showing all the design parameters (see also the main text). The first generation consists of a single 30- $\mu\text{m}$ -wide slit (G) between two longitudinally infinitive (very large  $L \gg \lambda$ ) gold contacts, covered by a 30- $\mu\text{m}$ -thick silica cover layer. The second generation consists of an interdigitated metallic structure, made up by two gold fingers, whose width (W) is a parameter of study, as well as the gap size corresponding to the subwavelength (in the order of  $\sim \mu\text{m}$ ) slit (G). The length of each finger (L) is fixed at 2 mm for each configuration, whereas D corresponds to the distance between the finger and the opposite contact and is equal to 10  $\mu\text{m}$ , for every layout, in order to be larger than any gap size. Both the classes of device are biased with a bipolar High Voltage (HV) source. .... 65

**Figure 3.6.** Sketch of the ultra-broadband THz-Time-Domain Spectroscopy set-up operating into the ultra-broadband regime. THz pulses are obtained via a two-color plasma technique, i.e. by mixing the pump beam and its SH (obtained from a BBO crystal) at the air plasma channel. A 90° off-axis parabolic

mirror collimates the THz beam, whereas a high resistivity 0.5-mm-thick silicon wafer acts as long pass filter, blocking the residual SH and IR beams. THz radiation is then focused along with the probe beam into the SSBCD device, the latter placed on the focal plane of the last parabolic mirror. Detection is performed by mixing the temporally overlapped THz and probe pulses. According to the SSBCD paradigm, an SH beam proportional to the THz electric field strength is detected by a PMT, connected to a lock-in amplifier synchronized with the modulation frequency of the bias voltage. The whole set-up is purged with nitrogen. The inset shows in details the focusing of the probe and THz beams..... 67

**Figure 3.7.** (a) Pictorial representation of the implementation of the ABCD technique in our ultra-broadband THz-TDS set-up. The probe beam passes through a hole made in the center of the parabolic mirror and it is focused together with the THz beam. Two metallic tips connected to the high voltage source, bias the nonlinear interaction and the generated SH travels towards the optical detector (PMT). (b) Typical THz waveform recorded via ABCD when a two-color plasma source is employed..... 68

**Figure 3.8** (a) Pictorial representation of the positioning of the SSBCD device at the detector position in our ultra-broadband THz-TDS set-up. A 3D translation stage allows for the correct alignment of the micro-slit on the focal plane of the parabolic mirror. (b) Operating principle of the SSBCD device: both THz and probe beams are focused onto the silica gap in between the two biased gold electrodes. The generated SH beam is emitted from the region where THz, probe, and bias electric fields interact, eventually emerging from the rear of the SSBCD device. .... 70

**Figure 3.9.** (a) THz waveforms recorded via the first generation of SSBCD device as a function of the bias voltage in the range 50-1050 V. The curves are shifted along the y-axis for sake of clarity. (b) 2D color map reporting the THz bandwidth corresponding to the transients in (a), as a function of the bias voltage. The spectrum extends approximatively until 10 THz. A frequency modulation is revealed at around 3 THz, where a notch featuring a relatively wide stopband appears, consistently with the multi-cycle nature of the THz pulses observed in (a). .... 72

**Figure 3.10** (a) THz electric field peak as a function of the bias voltage. The trend perfectly reproduced the linear dependence predicted by Eq. (5.15). (b) Dynamic range (DR, red dots) evaluated for each data point in (a). The non-monotonic states in subdivision into two different noise regimes. The blue solid curve represents the best fit performed with a rational function, similar to Eq. (5.15). The error bars in both the plots are related to the SNR of the detection method. .... 74

**Figure 3.11.** (a) THz electric field peak and (b) DR trends as a function of the probe energy. The blue solid line in (a) represents the linear fit for the data below the threshold. The parabolic curve (black solid line) well fits the data once the FWM takes place (probe energy greater than 500 nJ). The THz peak

values are normalized with respect to their maximum. The DR quickly increases as the energy overcome the threshold values, reaching 750, which was our best value for the first generation of SSBCD. .... 75

**Figure 3.12.** Comparison between the (a) THz electric field waveforms and (b) the Power Spectral Density (PSD), detected and evaluated for the case of ABCD (blue curves) and the first generation of SSBCD devices (red curves). .... 76

**Figure 3.13.** Coherent length curves corresponding to the four-wave mixing processes taking place in silica for the case of co-propagating THz and probe beam. The red dashed line depicts the difference-frequency generation (DFG) process, whereas the blue dashed line indicates the sum-frequency generation (SFG) process. For comparison purposes, the THz bandwidth reconstructed via the ABCD technique is plotted in purple, showing that the coherence length of both DFG and SFG is only  $\sim 12 \mu\text{m}$ , where the THz spectrum reaches its maximum. The black solid line indicates the thickness of the silica cover layer ( $T_{\text{layer}}$ ) for the second generation devices. The overlap length ( $OL \approx 123.4 \mu\text{m}$ ) between the two beams is two orders of magnitude longer than  $T_{\text{layer}}$  and is not shown for sake of simplicity. .... 79

**Figure 3.14.** (a) Photograph showing the second generation device realized on a silica wafer and mounted on a customized holder, which also serves to the delivering of the bias voltage. We fabricated 18 samples, each one featuring a different slit width, i.e. 3, 4 and 5  $\mu\text{m}$  from top to bottom, as indicated in the figure, whereas the silica cover layer was equal to 5  $\mu\text{m}$  for all of them. Since the sub-wavelength slits are realized with electrodes displaced as an interdigitated structure, we have realized an array structure, so as to have a larger number of slits for the test. (b) THz waveforms recorded as a function of the slit width, for a fixed bias voltage and probe energy of 200 V and 100 nJ, respectively. Each curve is normalized to its own maximum and shifted along the y-axis for clarity. .... 82

**Figure 3.15.** (a) Comparison between the THz transient peaks trends recorded for device configurations featuring a 3- $\mu\text{m}$ -wide slit and 10 (blue dots) and 100- $\mu\text{m}$ -wide (red dots) electrode fingers, as a function of the bias voltage. (b) DR trend (orange dots) compared to the corresponding the THz peak trend (green dots) as a function of the bias voltage for the 3- $\mu\text{m}$ -slit, 10- $\mu\text{m}$ -finger device. The maximum of the DR is not aligned with the maximum of the peak trend. .... 84

**Figure 3.16.** (a) THz waveforms recorded via the second generation of SSBCD device featuring a 3- $\mu\text{m}$ -wide slit and two 10- $\mu\text{m}$ -wide electrode finger, as a function of the bias voltage in the range 50-600 V. The curves are shifted along the y-axis for sake of clarity. (b) 2D colormap reporting the THz bandwidth (PSD) corresponding to the transients in (a), as a function of the bias voltage. The continuous spectrum extends approximatively up to 10 THz. No frequency notches are observed, consistently with the quasi single-cycle nature of the THz pulses in (a). .... 85

**Figure 3.17.** Comparison between the (a) THz electric field waveforms and (b) the Power Spectral Density (PSD), detected and evaluated for the case of ABCD (blue curves) and the second generation of SSBCD devices (red curves). ..... 88

**Figure 3.18.** (a) THz transients and (b) FFT-evaluated spectra retrieved via EOS in a 20- $\mu\text{m}$ -thick ZnTe crystal (red solid lines) and SSBCD (blue solid lines). The pulses in (a) are shifted along the x-axis for clarity. The curves in (b) are normalized with respect to their own maxima. .... 89

**Figure 3.19.** (a) Phase-matching condition between NIR (red curve) and THz (blue curve) pulses for the case of a ZnTe crystal.  $f_{\text{PM}}$  and  $\lambda_{\text{PM}}$  are the phase-matched THz frequency and optical wavelength, respectively. (b) Complex refractive index expressed as the sum of the real index (blue curve) and extinction ratio (red curve, proportional to the absorption coefficient) as a function of the THz frequency. The phonon resonance at 5.32 THz induces a rapid increase of both the indexes, thus canceling the phase-matching condition beyond 3 THz, and making the crystal extremely opaque in the 5-6 THz window. .... 90

**Figure 3.20.** (a) THz transients and (b) FFT-evaluated spectra retrieved via EOS in a 500- $\mu\text{m}$ -thick GaP crystal (red solid lines) and SSBCD (blue solid lines). The pulses in (a) are shifted along the x-axis for clarity. The curves in (b) are normalized with respect to their own maxima. .... 91

**Figure 3.21.** (a) Phase-matching condition between NIR (red curve) and THz (blue curve) pulses for the case of a GaP crystal.  $f_{\text{PM}}$  and  $\lambda_{\text{PM}}$  are the phase-matched THz frequency and optical wavelength, respectively. The refractive mismatch at 0.8  $\mu\text{m}$  is relatively high, thus preventing a good efficiency in a collinear geometry. (b) Frequency response of the 500- $\mu\text{m}$ -thick GaP crystal employed as a THz sensor in the EOS detection. The poor phase-matching resulting in a heavily modulated response with several zeros within the 10-THz-wide range. .... 92

**Figure 3.22.** (a) Sketch of the ultra-broadband THz Time-Domain Spectroscopy set-up. THz pulses are obtained from a plasma source. Detection is carried out through the SSBCD technique. THz radiation is handled by off-axis mirrors only, whereas the sample is placed at the first focus along the propagation direction of the THz transients. (b) Transmission spectra for a 1.3-mm-thick pellet of ibuprofen retrieved via SSBCD (red solid curve) and for a 0.6-mm-thick pellet via FTS (blue dashed curve). Curves are shifted along the y-axis for clarity..... 94

**Figure 4.1** (a) Sketch of a silica wafer, half covered with a 10- $\mu\text{m}$ -thick SiN film. The reference signal is measured by letting the THz pulse traveling through the substrate (silica), where the differential signal is calculated as the difference between the pulse passing through the stack of SiN film and silica substrate

and the reference. (b) THz waveforms corresponding to the reference pulse (red solid curve) and the pulse traveling through the film (blue dashed line). The differential signal resolved from the noise and shown as the black solid line. .... 99

**Figure 4.2** (a) THz refractive index and (b) power absorption coefficient as a function of the frequency, evaluated via DTDS algorithm. .... 100

**Figure 4.3.** (a) Optical refractive index featuring the particular type of SiN film grown by PECVD at the LMN. (b) Coherent length for the FWM process taking place in SiN for the case of co-propagating THz and probe beam. The red dashed line depicts the difference-frequency generation (DFG) process, whereas the black solid line indicates the thickness of the SiN cover layer ( $T_{\text{layer}}$ ). For comparison purposes, the THz bandwidth reconstructed via the ABCD technique is plotted in purple, showing that  $T_{\text{layer}} = 1 \mu\text{m}$  satisfies the phase-matching condition for the whole THz spectrum. .... 102

**Figure 4.4.** (a) 3D sketch of the deep subwavelength slit device embedded in a thin layer (T) of SiN, deposited on a quartz substrate. L and W are the length and the width of the metal pads, respectively. (b) Comparison between the THz waveforms recorded via ABCD (blue curve) and SSBCD (red curve). The inset shows the corresponding Fourier-transformed spectra of the two pulses. .... 103

**Figure 4.5.** Geometry of the ultra-broadband THz set-up considered for the modeling of the THz field enhancement. An infrared pulsed beam (IR) and its second harmonic (SH) are focused together in air to generate a two-color plasma channel emitting 10-THz-wide pulses. The THz beam is regarded as the superposition of several frequency components (different shades of blue) featured by different emission cones, with aperture angle  $\theta$ . The first off-axis mirror OAM1, with focal length  $f_1$ , collimates the beam having radius R, whereas OAM2 with focal length  $f_2$  focuses the beam into the SSBCD device. The plane of sub- $\lambda$  slit overlaps the focal plane of OAM1, where each frequency component of the THz beam features a waist size  $w_0$ , as indicated in the bottom right inset, which shows an example of the different field profiles assumed by each frequency component of the whole beam (darker shades of blue correspond to higher frequencies). .... 106

**Figure 4.6.** 2D distribution of the THz electric field in the slit for the frequency component of 1 (a) and 10 THz (b). Corresponding profiles of the THz electric fields at 1 THz (c) and 10 THz (d), evaluated along the white dashed lines indicated in (a) and (b). .... 108

**Figure 4.7.** (a) Comparison between the average THz electric field calculated for the background case  $E_{\text{THz}}^{\text{back}}$  and THz electric field  $E_{\text{THz}}^{\text{slit}}$  inside the slit as a function of the frequency. (b) Calculated field enhancement values (blue stars) induced by the metallic slit on a focusing ultra-broadband THz beam,

as a function of the frequency, in the 0.25-10 THz range. For comparison purposes, the red area represents the THz spectrum emitted by the two-color plasma source and acquired via ABCD..... 109

**Figure 4.8.** THz waveforms acquired via SiN-based SSBCD devices (third generation) for different values of the bias voltage in the range 10-70 V. The inset shows the spectrum corresponding to the case of 40 V. Each curve is normalized to the maximum of that retrieved for 70 V. The inset shows the comparison between the THz spectra evaluated for the ABCD case and the SSBCD corresponding at pulse with 40 V bias voltage. .... 111

Figure 4. 9.(a) THz electric field peak (blue dots, left axis) and dynamic (red dots, right axis) trends as a function of the bias voltage. The black solid line represents the linear fit reproducing the THz peak trend all over the bias range. (b) THz electric field peak (blue dots, left axis) and dynamic (red dots, right axis) trends as a function of the probe energy. The black solid line represents the parabolic fit well reproducing the THz peak trend only in the range 10-140 nJ. .... 112

Figure 4. 10Evaluation of the THz electric field peak by means of Eq. (5.15), for different values of the bias voltage. The dashed blue line indicates the average THz peak value. .... 114

**Figure A.1.** (a) Picture of the fluorescence emitted by a single-color filament generated by a 140 fs, 500  $\mu$ J, 800 nm pulsed laser, traveling from the right to the left along the x-axis. The image was acquired by means of a CCD camera provided with a 10x objective. (b) Sketch of the generation stage of a typical two-color THz plasma source. The pump beam  $\omega$  is frequency-doubled in a BBO crystal and focused together with its second harmonic to generate a plasma channel (filament). The latter gives rise to a THz radiation with a peak emission direction which forms the angle  $\theta$  with the propagation axis. .... 129

**Figure A.2.** (a) The top subplot shows the simulated intensity trend as the optical beam is being focused by a 20-cm-lens, for the case corresponding to the case of Kerr effect (green line) only, plasma and dispersion only (magenta curve) and all the effects (black line). The laser pulse is characterized by an optical energy of 3.2 mJ and a pulse duration of 54 fs. The three subplots on the bottom show the angular distribution of the THz emission in the three cases at different propagation distance: far from the focus (gray vertical line), close the intensity threshold (blue vertical line) and in front of the focus (red vertical line). (b) The top subplot shows the simulated THz spectra along the propagation axis emitted as the plasma filament is formed. On the wake of the laser pulse, the THz emission driven by the Kerr nonlinearity manifests a frequency peak around 4 THz. After the intensity threshold, the power spectrum experiences a sudden increase of three orders of magnitudes in the low-frequency range, as highlighted by the notch around 25 THz, visible starting at  $z = 12.46$  cm. .... 130

**Figure A.3.** 2D colormaps showing (a) the transversal profile of the THz beam in the far-field region, generated by a two-color plasma driven a pulsed laser featuring the same parameters of Fig. A.1(a), and acquired approximately 3 cm beyond the plasma spark, in the forward direction. We note the typical donut-shaped as a result of the off-axis phase matching condition. (b) THz beam spot on the focus of a 2-inch 90° off-axis mirror. The typical cross-shape is a consequence of the focusing (spatial Fourier transformation) of the beam profile in (a). The pitch size for both the picture is 35 μm. .... 133

# List of Tables

<b>Table 3.1.</b> Layout parameters featuring the first and second generation of silica-based SSBCD devices. .....	66
<b>Table 3.2.</b> Comparison between the first and second generation of silica-based SSBCD devices.....	87
<b>Table 4.1.</b> Comparison of the silica and silicon nitride physical properties. ....	97